Analysis of Quasistatic MHD Perturbations and Stray Magnetic Fields in a Tokamak Plasma

P. V. Savrukhin

Russian Research Centre Kurchatov Institute, pl. Kurchatova, Moscow, 123182 Russia

Received October 23, 2000; in final form, April 4, 2001

Abstract—Mechanisms for the development of quasistatic MHD perturbations in a viscous rotating tokamak plasma are considered. The influence of stray magnetic fields on the stability of MHD modes in the plasma of the TFTR tokamak is analyzed. © *2001 MAIK "Nauka/Interperiodica".*

1. INTRODUCTION

Recently, the problem of quasistatic MHD perturbations in large tokamaks has attracted considerable interest [1, 2]. An analysis shows that these perturbations can arise either due to the rotation of magnetic islands or due to the destabilization of static (locked) MHD modes. The stopping of rotation is usually accompanied by a rapid increase in the perturbation amplitude and, sometimes, by discharge disruption (see [3]). One of the factors favorable for the development of quasistatic MHD perturbations is the breaking of the symmetry of the tokamak equilibrium magnetic configuration (the generation of stray magnetic fields). The threshold amplitude of the stray magnetic field at which quasistatic MHD perturbations develop decreases substantially as the tokamak size increases, the plasma rotation slows down, and the plasma pressure increases (see [1, 3]). For these reasons, this kind of instability may be dangerous for future tokamak reactors with a slowly rotating plasma under burning conditions [3]. The primary cause for the appearance of stray magnetic fields, which is associated with the imperfect fabrication of the tokamak magnetic system and the nonsymmetric configuration of conductors, can be minimized by improving the accuracy of the device assembly. However, there are a number of factors that are fundamentally unavoidable. First of all, there is the asymmetry of the tokamak mechanical elements (such as the divertor, diagnostic ports, and neutral beam injectors), the inhomogeneity of internal plasma perturbations, and the local character of the interaction of the plasma with the chamber wall during major disruptions (the excitation of halo-currents and the injection of impurities [4]). The diversity of sources exciting inhomogeneous magnetic fields makes it difficult to predict the onset of instabilities and hampers the development of stabilization systems for future experiments.

At present, there are several methods for identifying the structure of stray fields. A direct method is based on the calculations of magnetic fields excited by currents in the tokamak magnetic system. These calculations involve the three-dimensional modeling of magnetic fluxes (including the fluxes induced in the tokamak conductors) at given positions of the controlling coils. Unfortunately, such modeling does not provide the required accuracy in determining the stray fields because of the complicated spatial structure of the induced fluxes and the mechanical deformation of the tokamak construction during the experiment. Another method is the direct measurement of helical perturbations of the magnetic field with the help of magnetic probes and saddle loops. However, under the experimental conditions, magnetic probes are situated outside the plasma (outside the vacuum chamber of the tokamak), which hampers the determination of the local field structure inside the plasma column. Magnetic fields inside the vacuum chamber can be measured if the tokamak is equipped with special movable probes (e.g., in experiments in the DIII-D tokamak [1]). However, such measurements cannot be carried out during the discharge. The accuracy of the measurements of stray magnetic fields can be substantially improved if the tokamak is equipped with additional coils for generating helical magnetic fields with given amplitudes and spatial orientations [2]. In this case, the stray fields can be deduced by analyzing the thresholds for the destabilization of quasistatic MHD perturbations at different amplitudes and phases of the external helical magnetic fields.

Unfortunately, experiments with helical magnetic fields produced by additional coils present serious problems to large tokamaks because of the high equipment cost and the rigorous schedule of the device operation. In such a situation, the stray fields can be deduced by analyzing the dynamics of internal MHD perturbations [5]. In this paper, we describe a procedure of determining the dominant harmonics of external helical perturbations based on the numerical modeling of tearing modes in a viscous rotating plasma. By analyzing internal perturbations in the TFTR plasma as an example, we identify the $m = 2$, $n = 1$ harmonic (where m and n are the transverse and longitudinal wavenum-

bers, respectively), which plays a key role in the initiation of the discharge disruption. In order to improve the accuracy of the analysis, the parameters of the numerical model are determined by comparing the results of calculations with the results of previous experiments in tokamaks equipped with external coils (JET, DIII-D) at prescribed helical perturbations of the magnetic field [5].

2. NUMERICAL MODEL OF MHD PERTURBATIONS CONTROLLED BY EXTERNAL MAGNETIC FIELDS

The evolution of MHD perturbations under the action of external helical magnetic fields is analyzed using a phenomenological model of tearing modes in a viscous rotating plasma [5]. The model is based on the
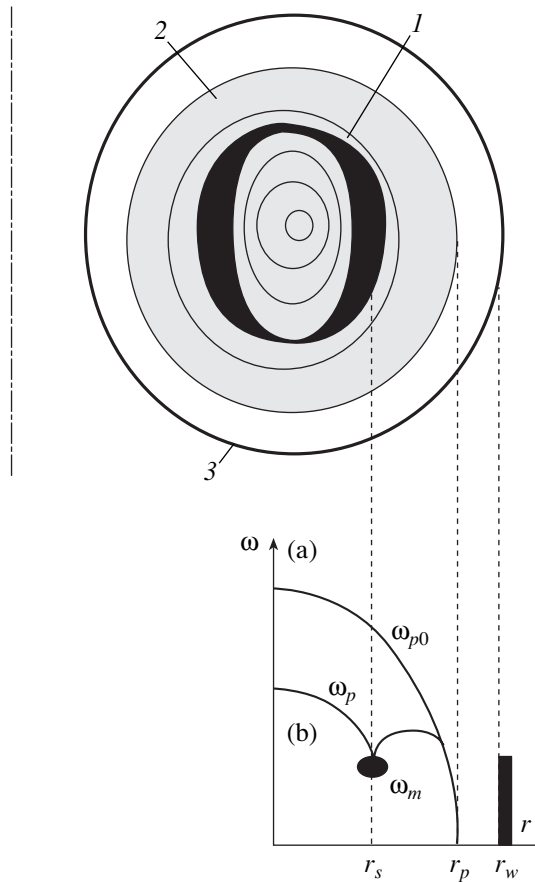
Fig. 1. Schematic illustration of the tearing mode model and the profiles of the angular plasma rotation velocity (a) in a quasi-stable configuration and (b) upon the onset of MHD perturbations. Magnetic islands (*1*) are located in the viscous plasma (*2*) confined in a chamber with conducting walls (*3*). Here, ω_m and ω_p are the instantaneous angular frequencies of the mode and the plasma, respectively; r_s, r_p, and r_w are the minor radii of the resonant magnetic surface, the bulk plasma, and the conducting wall, respectively; and ω_{p0} is the plasma rotation frequency in the absence of tearing modes.

one-fluid MHD theory [6], which describes the electromagnetic effects in a plasma with finite viscosity and inertia. The geometry of the model is shown schematically in Fig. 1.

External magnetic field perturbations and MHD perturbations (modes) are represented in the form of helical harmonics $B_{em} = B_e\exp(jm\chi_e)$ and $B_{rm} = B_r\exp(jm\chi_m)$. Here, $m\chi_m = m\vartheta - n\varphi + \int\omega_m dt$, $m\chi_e = m\vartheta - n\varphi + \int\omega_e dt$ (where χ_m and χ_e are the phases and ω_m and ω_e are the angular frequencies of the modes and external fields, respectively), and θ and ϕ are the transverse (poloidal) and longitudinal (toroidal) coordinates. The amplitude B_r and the instantaneous frequency $\omega_m = d\chi_m/dt$ are described by the equations

$$\sqrt{B_r}dB_r/dt = c_1\Delta'_{frb}B_r$$
$$- c_2B_r(\omega_m\tau_w)^2/(1 + \omega_m^2\tau_w^2) + c_3B_e\cos(\chi_e - \chi_m), \quad (1)$$

$$\sqrt{B_r}d\omega_m/dt = c_4(\omega_p - \omega_m)$$
$$- c_5B_r^2\omega_m\tau_w/(1 + \omega_m^2\tau_w^2) + c_6B_e\sin(\chi_e - \chi_m); \quad (2)$$

where Δ'_{frb} is the stability parameter of the tearing mode in a plasma with a free boundary, τ_w is the time constant of the conducting tokamak chamber, ω_p is the instantaneous rotation frequency of the bulk plasma surrounding the magnetic island, and c_i ($i = 1$–6) are numerical factors calculated using the measured plasma parameters.

MHD perturbations were modeled and stray magnetic fields were then identified using the PLASCON program [5] in the MATLAB programming environment [7]. The block diagram of the program is shown in Fig. 2. The TEARING MODE block models the growth and rotation of MHD perturbations by numerically solving Eqs. (1) and (2) for given values of B_e and χ_e. The stability parameter of the tearing mode Δ'_{frb} is specified using the current density profile calculated with the TRANSP code [4]. The transmission characteristics of the set of magnetic probes (see below) are modeled by the MAGNETIC block. The calculated values of B_r, ω_m (denoted by BR and Ωm), and the signals from magnetic detectors (BR-LMD and BP-MM) are compared with the measured values. The amplitude and phase of external fields are determined by fitting the calculated values to the experimental results.

The instantaneous angular frequency ω_m and the perturbation amplitude B_r depend on the mode phase with respect to the external magnetic field [see Eqs. (1), (2)]. Depending on the phase shift ($\chi_e - \chi_m$), the mode periodically accelerates and decelerates during the rotation period. At large amplitudes of the external field, such nonuniform rotation produces characteristic sawtooth signals from magnetic detectors, which allows us

to identify the phase of the stray field under given experimental conditions.

3. EXPERIMENTAL RESULTS AND COMPARISON WITH CALCULATIONS

The diagnostic complex of the TFTR tokamak [8] makes it possible to identify external and internal MHD perturbations and, concurrently, to measure the plasma parameters used in numerical calculations (see table and Fig. 3). The spatial structure of internal MHD modes (wavenumbers m and n), the angular frequency, and the magnetic island width are measured with the help of two microwave polychromators situated in the cross sections separated by an angle of $126°$ in the toroidal direction. The amplitudes and phases of the quasistatic and rotating perturbations of the magnetic field outside the plasma column were measured with the help of saddle loops and sets of magnetic probes. The plasma rotation velocity was determined from spectroscopic measurements (charge exchange of C^{6+} ions).

Internal MHD perturbations and stray magnetic fields were analyzed under conditions typical of the experiments in the TFTR tokamak described in [9]: the plasma current is $I_p = 2.0$ MA, the magnetic field is $B_t = 5.0$ T, the minor and major plasma radii are $r_p = 0.87$ m and $R_0 = 2.51$ m, and the neutral beam injection (NBI) power is $P_{NB} \sim 24$ MW. Figure 4 shows the time evolution of the plasma parameters in those experiments. The $m = 2$, $n = 1$ perturbations appear after an internal disruption at $t \approx 3.35$ s. The subsequent increase in the mode amplitude is accompanied by a decrease in the rotation frequency up to the full stopping (locking) of MHD perturbations at $t \approx 4.1$–4.2 s. Spectroscopic measurements of the velocity of C^{6+} ions show that the mode grows simultaneously with the slowing-down of the bulk plasma rotation over the entire cross section of the plasma column. A rapid slowing-down of the mode immediately before the rotation stops is explained by the fact that one of the neutral injectors is switched off at $t \approx 4.12$ s. Switching-off is only accompanied by a weak (about 10%) decrease in the total NBI power, which, however, results in the complete disappearance of the rotational moment T_{NBI}, determining the angular plasma motion under these conditions (see Fig. 5,

Experimental data
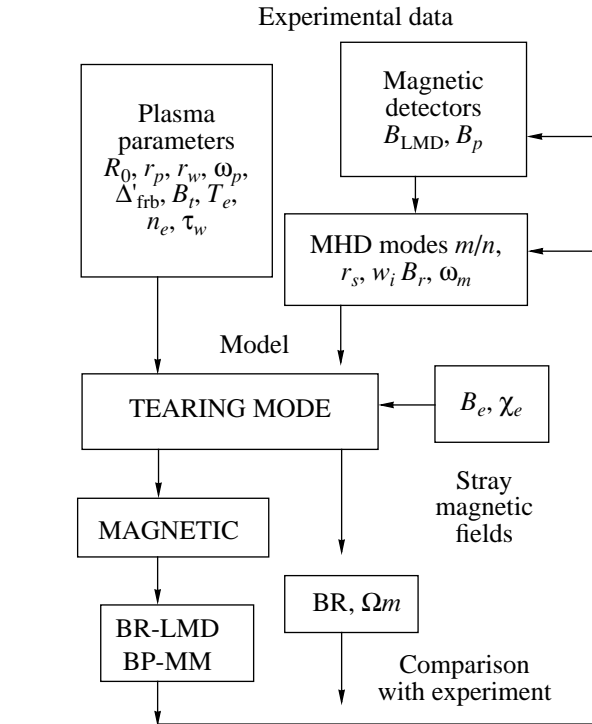
Fig. 2. Block diagram of the PLASCON model used to identify quasistatic MHD modes and stray magnetic fields. The amplitude and phase of the external stray fields (B_e and χ_e) are determined by fitting the calculated amplitude and frequency of MHD perturbations (BR and Ωm) and the signals from magnetic detectors (BR-LMD and BP-MM) to the measured values B_r, ω_m, B_{LMD}, and B_p.

$t \approx 4.12$ s). After several short pulses in the time interval $t \approx 4.18$–4.24 s, the given injector is switched on again and the rotational moment T_{NBI} reaches its initial value at $t \approx 4.27$ s (Fig. 4).

An analysis of electron-cyclotron (EC) emission with the help of polychromators shows that the growth of the $m = 2$, $n = 1$ perturbations is accompanied by the appearance of flattened regions in the radial profile of the electron temperature, which is associated with the formation of magnetic islands. An analysis of the EC emission profile allows us to determine the width (w_i)

Diagnostic systems for the identification of internal and external MHD perturbations

| Plasma parameters		Diagnostics	Notation in Fig. 3
Helical structure of internal modes, the width and angular rotation velocity of magnetic islands	m, n, w_i, ω_m	Microwave polychromators	GPC-1, GPC-2
Amplitude of quasistatic MHD perturbations	B_r	Detectors of locked modes (saddle loops)	LMD-D, LMD-F LMD-N, LMD-P
Helical structure, the amplitude and rotation frequency of external MHD perturbations	m, n, B_p, ω_{ext}	Magnetic probes	Mirnov coils
Plasma rotation	$\omega_p(r)$	Spectroscopy of the charge-exchange C^{6+} ion lines	
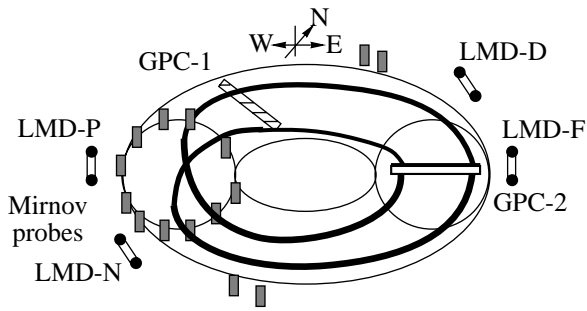
Fig. 3. Arrangement of the TFTR diagnostic systems for studying quasistatic MHD perturbations and stray magnetic fields (see [9]). The amplitude of external MHD perturbations is measured with locked-mode detectors (LMD-D, LMD-P, LMD-N, and LMD-P saddle loops) and magnetic pickup coils (Mirnov probes). The amplitude and frequency of internal plasma perturbations is analyzed with two multichannel polychromators (GPC-1 and GPC-2). The spiral line shows the location of the $m = 2$, $n = 1$ mode, and the arrows W, N, and E show the spatial orientation of the tokamak magnetic system.

and spatial location of magnetic islands. By analyzing the width of a magnetic island together with the signals from external magnetic probes, we can reconstruct the time evolution of the MHD perturbation amplitude (B_r) on the resonant magnetic surface $r = r_s$.

Figure 6 shows the results from the modeling of tearing modes in the TFTR plasma. At the given experimental plasma parameters, the modeling allows us to describe the increase in MHD perturbations and the slowing-down and full stopping of the $m = 2$, $n = 1$ mode rotation. The modeling also allows us to reproduce sawtooth signals from magnetic probes, which reflect the nonuniform rotation of magnetic perturbations during the rotation period, depending on the phase of the stray fields. By comparing the calculated and experimental signals under these conditions, we can determine the spatial orientation (phase) of the $m = 2$ harmonic of the external magnetic field. An analysis shows that the experimentally observed signals correspond to the permanent orientation of the external field, which does not change when the mode amplitude grows nor when MHD perturbations slow down. This indicates that the stray fields in the experiments under study are governed, first of all, by quasistatic inhomogeneities of the tokamak magnetic system, rather than by possible inhomogeneous interaction between the plasma and the limiter (see [9]).

At a specified (using experimental data) time evolution of the amplitude and frequency of MHD perturbations, the calculated time during which the rotation of the mode ($t = t_{lock}$) stops is determined by the amplitude of external stray fields. An analysis shows that the best agreement between the calculated and experimental
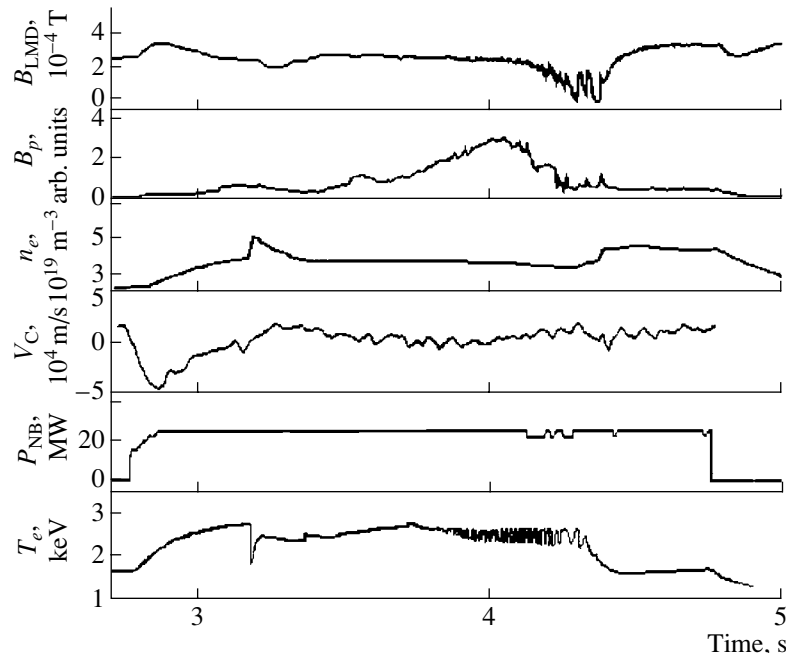
Fig. 4. Time evolution of the plasma parameters in the TFTR experiments [9] with the injection of neutral beams ($t = 2.65$–4.75 s) and a lithium pellet ($t = 3.15$ s). MHD perturbations with $m = 2$ and $n = 1$ arise after internal disruption ($t = 3.35$ s). The subsequent growth of the perturbation amplitude is accompanied by the slowing-down and full stopping of the mode at $t = 4.1$–4.2 s. Here, B_{LMD} and B_p are the amplitudes of the radial and poloidal perturbations of the magnetic field, n_e is the electron density, V_C is the angular rotation velocity of C^{6+} ions, P_{NB} is the total power of neutral beams, and T_e is the electron temperature near the $q = 2$ ($R = 3.1$ m) surface.
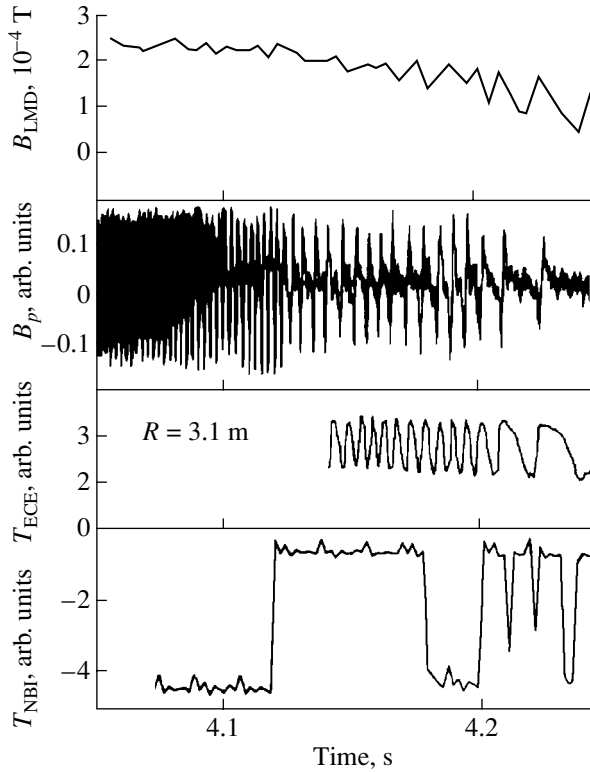
Fig. 5. Time evolution of MHD perturbations in the TFTR plasma: B_{LMD}, and B_p are the signals from a locked-mode detector and magnetic probes, respectively; T_{ECE} is the microwave emission intensity from the plasma near the $q = 2$ ($R = 3.1$ m) surface; and T_{NBI} is the moment of momentum of the injected neutrals.

values of t_{lock} is achieved at the $q = 2$ resonance surface for the amplitude of the $m = 2$, $n = 1$ harmonic of external fields equal to $B_e \approx 7.5 \times 10^{-4}$ T.

4. DISCUSSION OF EXPERIMENTAL RESULTS

An analysis of internal plasma perturbations observed in the TFTR experiments and the numerical modeling of tearing modes allow us to clarify the mechanisms for the growth of quasistatic MHD perturbations in a viscous rotating plasma in the presence of external stray magnetic fields. The developed procedure of comparing the calculated time evolution of tearing modes and the signals from the magnetic detectors with the values measured in the experiment allows us to determine the spatial orientation and amplitude of the dominant $m = 2$ harmonic of external stray fields under conditions typical for experiments in large tokamaks.

The numerical model used in this study was primarily developed for the modeling of the simultaneous development of several MHD harmonics (see [5, 10]). Calculations show, in particular, that the coupled $m = 2$ and $m = 3$ modes stop rotating at a lower amplitude of stray fields in comparison with the single $m = 2$ mode.
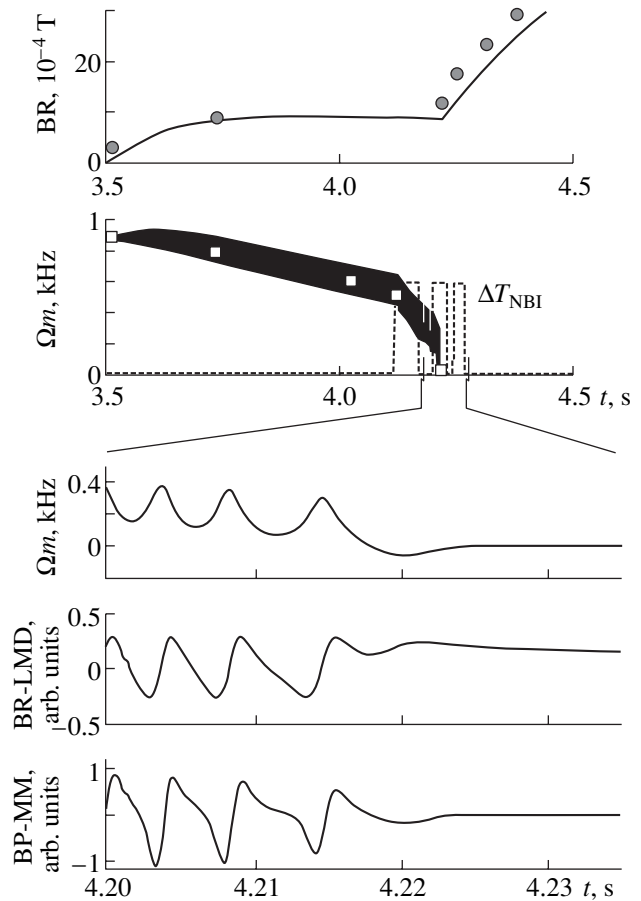
Fig. 6. Results of the numerical modeling of tearing modes in the TFTR plasma. As in the experiment (Fig. 5), after the destabilization (at $t \sim 3.5$ s) and subsequent growth of magnetic perturbations, the rotation of tearing modes slows down and they stop ($t \sim 4.22$ s). Here, BR and Ωm are the calculated amplitude and rotation frequency of the tearing modes, BR-LMD and BP-MM are the calculated signals from magnetic detectors, and ΔT_{NBI} is the change in the moment of momentum of neutrals injected into the plasma. Circles and squares show the amplitude of radial magnetic field perturbations at the $q = 2$ surface and the rotation frequency of the $m = 2$, $n = 1$ mode (both measured with the help of microwave polychromators), respectively.

However, an analysis of signals from the magnetic probes and polychromators showed that, in the TFTR experiments under consideration, no substantial perturbations with the wavenumber $m = 3$ develop. This allows us to ignore the $m = 3$ harmonic when analyzing stray fields in the TFTR. Experiments in the DIII-D, however, demonstrate the significant role of the $m = 3$ harmonic in certain discharge modes [1]. This difference can be attributed to the elongation of the cross section of the plasma column or to the enhanced toroidal effects when the DIII-D operates in modes with a low aspect ratio. To determine the stray fields under these conditions, it is necessary to model the simultaneous time evolution of the $m = 2$ and $m = 3$ modes.

The procedure described in this paper allows us to determine the stray magnetic fields under actual tokamak experimental conditions. Unfortunately, the results of such an analysis depend on the accuracy of the measurements of the plasma discharge parameters (the electron temperature and density, impurity composition, plasma rotation velocity, and current density). For a higher reliability of the determination of stray fields and for the possible compensation of MHD perturbations in future experiments, the tokamak should be equipped with additional external coils.

5. CONCLUSION

An analysis of internal and external MHD perturbations in the TFTR plasma and numerical modeling make it possible to identify the parameters of the dominant $m = 2$, $n = 1$ mode and determine the spatial structure of the stray magnetic fields. In order to more reliably identify the stray fields and to stabilize MHD perturbations, the tokamak should be equipped with additional external coils.

ACKNOWLEDGMENTS

REFERENCES

1. R. S. LaHaye, R. Fitzpatrick, T. C. Hender, *et al.*, Phys. Fluids B **4**, 2098 (1992).

2. A. Santagiustina, S. AliArshad, D. J. Campbell, *et al.*, in *Proceedings of the 22nd European Conference on Controlled Fusion and Plasma Physics, Bournemouth, 1995*; ECA, **19C** (4), 461 (1995).

3. ITER Expert Group on Disruption, Plasma Control, and MHD, ITER Physics Basis Editors, Nucl. Fusion **39**, 2251 (1999).

4. H. Takahashi, E. Fredrickson, K. McGuire, and W. Morris, Rev. Sci. Instrum. **66**, 816 (1995).

5. P. V. Savrukhin, Fiz. Plazmy **26**, 675 (2000) [Plasma Phys. Rep. **26**, 633 (2000)].

6. R. Fitzpatrick, Nucl. Fusion **33**, 1049 (1993).

7. *MATLAB User's Guide / The MathWorks Inc.* (Englewwod Cliffs, Prentice Hall, 1992).

8. G. Taylor, E. Fredrickson, and A. Janos, Rev. Sci. Instrum. **66**, 830 (1995).

9. H. Takahashi, E. Fredrickson, K. McGuire, and A. Ramsey, Bull. Am. Phys. Soc. **41**, 1S27 (1996).

10. P. Savrukhin, D. J. Campbell, M. DeBenedetti, *et al.*, *Numerical Simulation of Feedback Control of Coupled Tearing Modes at JET*, JET Joint Undertaking Report JET-R(95)-06 (1995).

11. F. Karger, H. Wobig, S. Corti, *et al.*, Plasma Phys. Controlled Nucl. Fusion Res. **1**, 207 (1975).

12. A. P. Popryadukhin, Prikl. Fiz., Nos. 3–4, 90 (1995).

Translated by N. F. Larionova

Generation of Large-Scale Structures
by Strong Drift Turbulence

V. P. Lakhin

Nuclear Fusion Institute, Russian Research Centre Kurchatov Institute, pl. Kurchatova 1, Moscow, 123182 Russia
Received January 21, 2001

Abstract—The previously existing quasilinear theory of the generation of a large-scale radial electric field by small-scale drift turbulence in a plasma is generalized for the case of strong turbulence which is usually observed in experiments. The geostrophic equation (i.e., the reduced Charney–Hasegawa–Mima equation) is used to construct a systematic theory in the two-scale direct interaction approximation. It is shown that, as in the quasilinear case, drift turbulence results in a turbulent viscosity effect and leads to the renormalization of the Poisson bracket in the Charney–Hasegawa–Mima equation. It is found that, for strong drift turbulence, the viscosity coefficient is represented as a sum of two parts, which are comparable in magnitude. As in quasilinear theory, the first part is determined by the second-order correlation functions of the turbulent field and is always negative. The second part is proportional to the third-order correlation functions, and the sign of its contribution to the turbulent viscosity coefficient depends strongly on the turbulence spectrum. The turbulent viscosity coefficient is calculated numerically for the Kolmogorov spectra, which characterize the inertial interval of the drift turbulence. © 2001 MAIK "Nauka/Interperiodica".

1. INTRODUCTION

The so-called Charney–Hasegawa–Mima (CHM) model [1, 2] is a simple model for describing both drift turbulence in a magnetized plasma and the turbulence of Rossby waves in the atmospheres of rotating planets. Recently, this model has been used to investigate the effect of small-scale turbulent pulsations on larger-scale perturbations [3, 4]. The study by Gruzinov *et al.* [3] was motivated by experiments on L–H transitions in tokamaks [5, 6]. The authors supposed that a turbulent mechanism may be responsible for the generation of radial electric fields and poloidal sheared flows, which are both observed in the experiments cited. In order to describe this phenomenon, they constructed a simple analytic theory based on the reduced CHM equation— the geostrophic equation. This equation neglects the term that is proportional to the plasma density gradient and accounts for linear waves in the CHM equation. As was noted in [3], neglecting this term is justified only for a strongly nonlinear turbulent regime dominated by the nonlinear interaction of turbulent pulsations (rather than by linear waves). Experimental investigations of drift turbulence in tokamaks show that nonlinear frequency shifts exceed the linear frequencies of the drift waves [7], which provides evidence in support of such a simplification. On the other hand, in [3], the equation describing the evolution of large-scale perturbations due to their interaction with small-scale turbulent pulsations was derived in the quasilinear approximation, which is employed to construct standard turbulent dynamo theories [8, 9]. However, in my opinion, the quasilinear approximation can only be used when the turbulence is governed by the driving force rather than

the nonlinear interaction of self-consistent turbulent pulsations. In [3], it was found that small-scale drift turbulence results in the negative turbulent viscosity in the equations for the large-scale field. This effect is related to the term describing the adiabatic response of the electrons in the Hasegawa–Mima equation. This result agrees well with the conclusion drawn by Montgomery and Hatori [10]: in the two-dimensional incompressible hydrodynamics based on the Euler equation (i.e., in the absence of the above-mentioned term), small-scale turbulence does not give rise to turbulent viscosity. As was mentioned in [3], the instability driven by turbulent viscosity with a negative coefficient causes a spontaneous growth of large-scale perturbations and can serve as a mechanism for the generation of the radial electric fields observed in experiments on L–H transitions.

A primary motivation for the study by Chechkin *et al.* [4] is its application to the physics of the atmosphere and ocean. The analysis carried out in that paper was based on the CHM equation supplemented with the terms describing molecular viscosity and the external force. The role of the latter was merely to maintain turbulence at a steady level. The authors assumed that the amplitude of the small-scale turbulent field is small enough so that the Reynolds number for small-scale perturbations is low and the terms proportional to the squared amplitudes of the small-scale perturbations in the equation for the turbulent field can be neglected. Thus, as in [3], the analysis of [4] also used the quasilinear approximation and revealed the effect of negative turbulent viscosity on large-scale perturbations: the term that reflects this effect originates from the compressibility of fluid and is responsible for the same term

in the CHM equation as the adiabatic term in the equations for drift waves in a magnetized plasma. In [4], it was also shown that small-scale turbulence leads to the renormalization of the coefficient in front of the Poisson bracket, which, as is well known, describes nonlinear effects in the CHM equation.

The purpose of this paper is to generalize the analysis of [3, 4] for the case of strong turbulence, which is more adequate for the experimental observations of drift turbulence in tokamaks [7]. Since this case cannot be described in the quasilinear approximation, we apply the so-called two-scale direct-interaction approximation. The corresponding formalism was developed by Yoshizawa [11] when constructing the theory of hydrodynamic turbulence with sheared flows. As implied by its name, the formalism is based on a combination of the standard technique of multiscale expansions (in the case at hand, a two-scale expansion) and Kraichnan's direct-interaction approximation [12], which is used to calculate statistically averaged quantities. In Section 2, we present a detailed formulation of the problem. We derive an equation for large-scale motions from the geostrophic equation. In accordance with the theory of multiscale expansions, we introduce fast and slow variables. Then, we represent the electrostatic potential as the sum of the mean (large-scale) and random (small-scale) components and solve the equation for the random (turbulent) component by applying the method of expansion in the small parameter—the ratio of the spatial scale of the turbulent motion to that of the mean electrostatic field. Using the direct-interaction approximation, we calculate the mean values of the turbulence-related quantities to arrive at an evolutionary equation for the averaged electrostatic potential expressed in terms of a second-order correlation function and a statistically averaged response function (a Green's function) of the turbulent field. Details of the calculations are given in Appendix A. In Section 3, we obtain expressions for the second-order correlation function and the averaged Green's function of the small-scale drift turbulence. We assume that, in the absence of the mean field, drift turbulence is homogeneous and isotropic. We also assume that the drift turbulence is in a highly nonlinear regime and is described by the second-order correlation function and the averaged Green's function characterizing the inertial interval of the turbulence; i.e., they are independent of both the dissipation and the source of turbulence and are completely determined by the nonlinear interaction of turbulent pulsations. To derive the correlation function and Green's function, we turn to the method based on the analysis of the invariant properties of the geostrophic equation with respect to the scale transformations. We consider two limiting cases in which the characteristic spatial scale of the turbulent motion is either much larger than or much smaller than the natural spatial scale for the geostrophic equation—the ion Larmor radius in terms of the electron temperature. In Section 4, we use the expressions for the second-order correlation function and the averaged Green's function in the inertial interval of turbulence in order to derive analytic expressions for the turbulent coefficients in the evolutionary equation for the large-scale field. Details of the corresponding calculations are given in Appendix B. In this section, we also describe the results of the numerical computation of the turbulent viscosity coefficients with the help of the Mathematica-3 software package. Finally, in Section 5, we discuss the results obtained.

2. EVOLUTIONARY EQUATION FOR THE LARGE-SCALE FIELD

2.1. Basic Equations

We start with the geostrophic equation in dimensionless variables,

$$\frac{\partial}{\partial t}(\lambda\phi - \nabla^2\phi) - [\nabla\phi \times \nabla\nabla^2\phi]_z = 0. \tag{1}$$

Here, $\nabla^2 \equiv \partial^2/\partial x^2 + \partial^2/\partial y^2$; the time is in units of the inverse ion gyrofrequency; the electrostatic potential ϕ is in units of T_e/e; and the spatial variables are normalized to the ion Larmor radius in terms of the electron temperature, $\rho_0 = (T_e/m_i\omega_{Bi}^2)^{1/2}$. The Poisson bracket $[\mathbf{f} \times \mathbf{g}]_z$ denotes the z-component of the vector product. In the above dimensionless variables, the coefficient λ equals unity, $\lambda = 1$. We keep this coefficient merely in order to illustrate how different terms appear in expressions describing the effect of turbulence on large-scale plasma motions (recall that our primary goal here is to calculate these terms). In Eq. (1), the term with the coefficient λ describes the adiabatic perturbation of the electron density. Formally, for $\lambda = 0$, Eq. (1) is a two-dimensional Euler equation for the two-dimensional motions of an incompressible fluid. By its very nature, the geostrophic equation is a simplified version of the Hasegawa–Mima equation, in which, according to the arguments given in the Introduction, the term that stems from the nonuniformity of the equilibrium plasma density and describes the drift waves is neglected.

We represent the electrostatic potential as the sum of the averaged (mean) and random (turbulent) components,

$$\phi = \bar{\phi} + \tilde{\phi}, \quad \bar{\phi} = \langle\phi\rangle, \tag{2}$$

where the angular brackets $\langle...\rangle$ stand for ensemble averaging. We average Eq. (1) in order to obtain the following evolutionary equation for the mean field:

$$\frac{\partial}{\partial t}(\lambda\bar{\phi} - \nabla^2\bar{\phi}) - [\nabla\bar{\phi} \times \nabla\nabla^2\bar{\phi}]_z$$
$$- \langle[\nabla\tilde{\phi} \times \nabla\nabla^2\tilde{\phi}]_z\rangle = 0. \tag{3}$$

If we subtract Eq. (3) from Eq. (1), we find that the turbulent field is described by the equation

$$\frac{\partial}{\partial t}(\lambda\tilde{\phi} - \nabla^2\tilde{\phi}) - [\nabla\tilde{\phi} \times \nabla\nabla^2\bar{\phi}]_z - [\nabla\bar{\phi} \times \nabla\nabla^2\tilde{\phi}]_z$$

$$- [\nabla\tilde{\phi} \times \nabla\nabla^2\tilde{\phi}]_z + \langle[\nabla\tilde{\phi} \times \nabla\nabla^2\tilde{\phi}]_z\rangle = 0. \tag{4}$$

2.2. Introduction of Two Scales

Assuming that the spatial and temporal scales of the mean and turbulent fields are essentially different, we introduce two spatiotemporal scales,

$$\mathbf{x}, \mathbf{X}(= \epsilon\mathbf{x}), \quad t, T(= \epsilon^4 t). \tag{5}$$

In other words, the mean field depends only on the slowly varying variables, while the turbulent field depends on both the rapidly and slowly varying variables because of its interaction with the mean field:

$$\bar{\phi} = \bar{\phi}(\mathbf{X}, T), \quad \tilde{\phi} = \tilde{\phi}(\mathbf{x}, t; \mathbf{X}, T). \tag{6}$$

Transforming the Poisson bracket in an appropriate manner, it is expedient to rewrite Eq. (3) as

$$\frac{\partial}{\partial T}(\lambda\bar{\phi} - \nabla_s^2\bar{\phi}) + \left(\frac{\partial^2}{\partial X^2} - \frac{\partial^2}{\partial Y^2}\right)\left\langle\frac{\partial\tilde{\phi}}{\partial\hat{x}}\frac{\partial\tilde{\phi}}{\partial\hat{y}}\right\rangle$$

$$- \frac{\partial^2}{\partial X\partial Y}\left\langle\left(\frac{\partial\tilde{\phi}}{\partial\hat{x}}\right)^2 - \left(\frac{\partial\tilde{\phi}}{\partial\hat{y}}\right)^2\right\rangle - [\nabla_s\bar{\phi} \times \nabla_s\nabla_s^2\bar{\phi}]_z = 0, \tag{7}$$

where $\hat{\nabla} \equiv \partial/\partial\mathbf{x} + \partial/\partial\mathbf{X}$, $\nabla_s \equiv \partial/\partial\mathbf{X}$, and $\nabla_s^2 \equiv \partial^2/\partial X^2 + \partial^2/\partial Y^2$. In terms of the variables introduced, Eq. (4) for the turbulent field becomes

$$\left(\frac{\partial}{\partial t} + \frac{\partial}{\partial T}\right)(\lambda\tilde{\phi} - \hat{\nabla}^2\tilde{\phi}) - [\nabla_s\bar{\phi} \times \hat{\nabla}\hat{\nabla}^2\tilde{\phi}]_z$$

$$- [\hat{\nabla}\tilde{\phi} \times \nabla_s\nabla_s^2\bar{\phi}]_z - [\hat{\nabla}\tilde{\phi} \times \hat{\nabla}\hat{\nabla}^2\tilde{\phi}] \tag{8}$$

$$+ \langle[\hat{\nabla}\tilde{\phi} \times \hat{\nabla}\hat{\nabla}^2\tilde{\phi}]_z\rangle = 0.$$

For convenience of further analysis, we represent the electrostatic potential of the turbulent field as the Fourier integral over the rapidly varying spatial variable:

$$\tilde{\phi}(\mathbf{x}, t; \mathbf{X}, T) = \int d\mathbf{k}\tilde{\phi}_\mathbf{k}(t; \mathbf{X}, T)e^{i\mathbf{k}\mathbf{x}}$$

$$\equiv \int_\mathbf{k}\tilde{\phi}_\mathbf{k}(t; \mathbf{X}, T)e^{i\mathbf{k}\mathbf{x}}. \tag{9}$$

Note that the Fourier coefficients of the electrostatic potential of the turbulent field depend on the slowly varying spatial variable $\mathbf{X}$. According to Eq. (8), the Fourier coefficients satisfy the equation

$$\frac{\partial}{\partial t}\tilde{\phi}_\mathbf{k}(t)$$

$$- \frac{1}{2}\int\int_{\mathbf{k}_1\mathbf{k}_2}[\mathbf{k}_1 \times \mathbf{k}_2]_z\frac{k_2^2 - k_1^2}{\lambda + k^2}\tilde{\phi}_{\mathbf{k}_1}(t)\tilde{\phi}_{\mathbf{k}_2}(t)\delta(\mathbf{k} - \mathbf{k}_1 - \mathbf{k}_2)$$

$$= \frac{ik^2}{\lambda + k^2}\tilde{\phi}_\mathbf{k}(t)[\mathbf{k} \times \nabla_s\bar{\phi}]_z + \frac{2i(\mathbf{k}\nabla_s)}{\lambda + k^2}\frac{\partial}{\partial t}\tilde{\phi}_\mathbf{k}(t)$$

$$- \int\int_{\mathbf{k}_1\mathbf{k}_2}\frac{i(k_2^2 - k_1^2)}{\lambda + k^2}\tilde{\phi}_{\mathbf{k}_1}(t)[\mathbf{k}_1 \times \nabla_s]_z\tilde{\phi}_{\mathbf{k}_2}(t)\delta(\mathbf{k} - \mathbf{k}_1 - \mathbf{k}_2) \tag{10}$$

$$- \int\int_{\mathbf{k}_1\mathbf{k}_2}\frac{2i}{\lambda + k^2}[\mathbf{k}_1 \times \mathbf{k}_2]_z\tilde{\phi}_{\mathbf{k}_1}(t)(\mathbf{k}_2\nabla_s)\tilde{\phi}_{\mathbf{k}_2}(t)$$

$$\times \delta(\mathbf{k} - \mathbf{k}_1 - \mathbf{k}_2) + \dots,$$

where dots designate the terms of the second order and higher in the expansion in powers of the small parameter ϵ. These terms can be neglected, because they are unimportant when calculating the effect of turbulent viscosity. Here and below, we do not indicate the explicit dependence of the Fourier coefficients of the turbulent field on the slowly varying variables.

2.3. Expansions of the Turbulent Field in the Small Parameter

Let us expand the Fourier coefficients of the electrostatic potential $\tilde{\phi}$ in powers of the small parameter ϵ:

$$\tilde{\phi}_\mathbf{k} = \tilde{\phi}_\mathbf{k}^{(0)}(t) + \epsilon\tilde{\phi}_\mathbf{k}^{(1)}(t; \mathbf{X}, T) + \epsilon^2\tilde{\phi}_\mathbf{k}^{(2)}(t; \mathbf{X}, T) + \dots. \tag{11}$$

Here, the first term is independent of the slowly varying variables and corresponds to a uniform isotropic turbulent field, which is assumed to be generated and maintained at a steady level by small-scale drift instabilities. The remaining terms describe the interaction between a small-scale turbulent field and a large-scale electrostatic field with the averaged potential $\bar{\phi}$.

We substitute Eq. (11) into Eq. (10) and collect terms of different orders in ϵ. As a result, we arrive at the following zero-order equation for the Fourier coefficients of the electrostatic potential of the homogeneous isotropic turbulent field:

$$\frac{\partial}{\partial t}\tilde{\phi}_\mathbf{k}^{(0)}$$

$$- \frac{1}{2}\int\int_{\mathbf{k}_1\mathbf{k}_2}[\mathbf{k}_1 \times \mathbf{k}_2]_z\frac{k_2^2 - k_1^2}{\lambda + k^2}\tilde{\phi}_{\mathbf{k}_1}^{(0)}(t)\tilde{\phi}_{\mathbf{k}_2}^{(0)}(t)\delta(\mathbf{k} - \mathbf{k}_1 - \mathbf{k}_2) = 0. \tag{12}$$

To first order, we obtain

$$\frac{\partial}{\partial t}\tilde\phi_{\mathbf{k}}^{(1)}$$

$$-\iint_{\mathbf{k}_1\mathbf{k}_2}[\mathbf{k}_1\times\mathbf{k}_2]_z\frac{k_2^2-k_1^2}{\lambda+k^2}\tilde\phi_{\mathbf{k}_1}^{(0)}(t)\tilde\phi_{\mathbf{k}_2}^{(1)}(t)\delta(\mathbf{k}-\mathbf{k}_1-\mathbf{k}_2)$$

$$=\frac{ik^2}{\lambda+k^2}\tilde\phi_{\mathbf{k}}^{(0)}[\mathbf{k}\times\mathbf{\nabla}_s\bar\phi]_z. \tag{13}$$

In the second-order approximation, i.e., in the lowest order approximation in which the effect of turbulence on large-scale plasma motions can be described, the equation for the turbulent field has the form

$$\frac{\partial}{\partial t}\left(\tilde\phi_{\mathbf{k}}^{(2)}-\frac{2i(\mathbf{k}\cdot\mathbf{\nabla}_s)}{\lambda+k^2}\tilde\phi_{\mathbf{k}}^{(1)}\right)$$

$$-\iint_{\mathbf{k}_1\mathbf{k}_2}[\mathbf{k}_1\times\mathbf{k}_2]_z\frac{k_2^2-k_1^2}{\lambda+k^2}\tilde\phi_{\mathbf{k}_1}^{(0)}(t)\tilde\phi_{\mathbf{k}_2}^{(2)}(t)\delta(\mathbf{k}-\mathbf{k}_1-\mathbf{k}_2)$$

$$=\frac{ik^2}{\lambda+k^2}\tilde\phi_{\mathbf{k}}^{(1)}[\mathbf{k}\times\mathbf{\nabla}_s\bar\phi]_z$$

$$+\frac{1}{2}\iint_{\mathbf{k}_1\mathbf{k}_2}[\mathbf{k}_1\times\mathbf{k}_2]_z\frac{k_2^2-k_1^2}{\lambda+k^2}\tilde\phi_{\mathbf{k}_1}^{(1)}(t)\tilde\phi_{\mathbf{k}_2}^{(1)}(t)\delta(\mathbf{k}-\mathbf{k}_1-\mathbf{k}_2) \tag{14}$$

$$-\iint_{\mathbf{k}_1\mathbf{k}_2}\frac{i(k_2^2-k_1^2)}{\lambda+k^2}\tilde\phi_{\mathbf{k}_1}^{(0)}(t)[\mathbf{k}_1\times\mathbf{\nabla}_s]_z\tilde\phi_{\mathbf{k}_2}^{(1)}(t)\delta(\mathbf{k}-\mathbf{k}_1-\mathbf{k}_2)$$

$$-\iint_{\mathbf{k}_1\mathbf{k}_2}\frac{2i}{\lambda+k^2}[\mathbf{k}_1\times\mathbf{k}_2]_z\tilde\phi_{\mathbf{k}_1}^{(0)}(t)(\mathbf{k}_2\mathbf{\nabla}_s)\tilde\phi_{\mathbf{k}_2}^{(1)}(t)\delta(\mathbf{k}-\mathbf{k}_1-\mathbf{k}_2).$$

The function describing the response of turbulence to a perturbation (or, equivalently, the Green's function) $\hat{G}_{\mathbf{k}}$ is introduced in a standard way as the solution to the equation

$$\frac{\partial}{\partial t}\hat{G}_{\mathbf{k}}(t,t')$$

$$-\iint_{\mathbf{k}_1\mathbf{k}_2}[\mathbf{k}_1\times\mathbf{k}_2]_z\frac{k_2^2-k_1^2}{\lambda+k^2}\tilde\phi_{\mathbf{k}_1}^{(0)}(t)\hat{G}_{\mathbf{k}_2}(t,t')\delta(\mathbf{k}-\mathbf{k}_1-\mathbf{k}_2) \tag{15}$$

$$=\delta(t-t').$$

Then, the solution to the first-order equation (13) is expressed in terms of $\bar\phi$, the Fourier amplitude $\tilde\phi_{\mathbf{k}}^{(0)}$ of the homogeneous isotropic field, and the Green's function:

$$\tilde\phi_{\mathbf{k}}^{(1)}(t)=\frac{ik^2}{\lambda+k^2}[\mathbf{k}\times\mathbf{\nabla}_s\bar\phi]_z\int_{-\infty}^{t}dt'\hat{G}_{\mathbf{k}}(t,t')\tilde\phi_{\mathbf{k}}^{(0)}(t'). \tag{16}$$

The solution to the second-order equation (14) can be found in an analogous manner: it is expressed in terms of $\bar\phi$, $\tilde\phi^{(0)}$, the Green's function, and the first-order solution:

$$\tilde\phi_{\mathbf{k}}^{(2)}(t)=\frac{2i}{\lambda+k^2}(\mathbf{k}\cdot\mathbf{\nabla}_s)\tilde\phi_{\mathbf{k}}^{(1)}(t)$$

$$+\frac{ik^2}{\lambda+k^2}[\mathbf{k}\times\mathbf{\nabla}_s\bar\phi]_z\int_{-\infty}^{t}dt'\hat{G}_{\mathbf{k}}(t,t')\tilde\phi_{\mathbf{k}}^{(1)}(t')$$

$$+\frac{1}{2}\iint_{\mathbf{k}_1\mathbf{k}_2}\int_{-\infty}^{t}dt'[\mathbf{k}_1\times\mathbf{k}_2]_z\frac{k_2^2-k_1^2}{\lambda+k^2}\delta(\mathbf{k}-\mathbf{k}_1-\mathbf{k}_2)$$

$$\times\hat{G}_{\mathbf{k}}(t,t')\tilde\phi_{\mathbf{k}_1}^{(1)}(t')\tilde\phi_{\mathbf{k}_2}^{(1)}(t') \tag{17}$$

$$-\iint_{\mathbf{k}_1\mathbf{k}_2}\int_{-\infty}^{t}dt'\frac{i}{(\lambda+k^2)(\lambda+k_2^2)}\delta(\mathbf{k}-\mathbf{k}_1-\mathbf{k}_2)\hat{G}_{\mathbf{k}}(t,t')$$

$$\times\tilde\phi_{\mathbf{k}_1}^{(0)}(t')\{2(\lambda+k_1^2)[\mathbf{k}_1\times\mathbf{k}_2]_z(\mathbf{k}_2\cdot\mathbf{\nabla}_s)\tilde\phi_{\mathbf{k}_2}^{(1)}(t')$$

$$+(\lambda+k_2^2)(k_2^2-k_1^2)[\mathbf{k}_1\times\mathbf{\nabla}_s]_z\tilde\phi_{\mathbf{k}_2}^{(1)}(t')\}.$$

Having derived (with the desired accuracy) the corrections to the small-scale turbulent field that come from the interaction with the large-scale field, we can calculate the statistical averages in Eq. (7) and thus analyze the effect of the small-scale drift turbulence on the averaged field.

2.4. Calculation of the Statistical Mean Values

We start by rewriting the averaged quantities in Eq. (7) in terms of the Fourier transformed turbulent field. Taking into account Eqs. (9) and (11) and keeping the terms of the corresponding orders of smallness, we obtain

$$\left\langle\frac{\partial\tilde\phi}{\partial\hat{x}}\frac{\partial\tilde\phi}{\partial\hat{y}}\right\rangle=\iint_{\mathbf{k}_1\mathbf{k}_2}e^{i(\mathbf{k}_1+\mathbf{k}_2)\cdot\mathbf{x}}\left\{-k_{1x}k_{2y}(\langle\tilde\phi_{\mathbf{k}_1}^{(0)}(t)\tilde\phi_{\mathbf{k}_2}^{(0)}(t)\rangle\right.$$

$$+\langle\tilde\phi_{\mathbf{k}_1}^{(1)}(t)\tilde\phi_{\mathbf{k}_2}^{(1)}(t)\rangle)-(k_{1x}k_{2y}+k_{1y}k_{2x})$$

$$\times(\langle\tilde\phi_{\mathbf{k}_1}^{(1)}(t)\tilde\phi_{\mathbf{k}_2}^{(0)}(t)\rangle+\langle\tilde\phi_{\mathbf{k}_1}^{(2)}(t)\tilde\phi_{\mathbf{k}_2}^{(0)}(t)\rangle) \tag{18}$$

$$\left.+i\left(k_{2x}\frac{\partial}{\partial Y}+k_{2y}\frac{\partial}{\partial X}\right)\langle\tilde\phi_{\mathbf{k}_1}^{(1)}(t)\tilde\phi_{\mathbf{k}_2}^{(0)}(t)\rangle\right\},$$

$$\left\langle \left(\frac{\partial \tilde{\phi}}{\partial \hat{x}}\right)^2 - \left(\frac{\partial \tilde{\phi}}{\partial \hat{y}}\right)^2 \right\rangle = \iint\limits_{\mathbf{k}_1 \mathbf{k}_2} e^{i(\mathbf{k}_1 + \mathbf{k}_2) \cdot \mathbf{x}} \left\{ (k_{1y}k_{2y} - k_{1x}k_{2x}) \right.$$

$$\times (\langle \tilde{\phi}^{(0)}_{\mathbf{k}_1}(t)\tilde{\phi}^{(0)}_{\mathbf{k}_2}(t)\rangle + 2\langle \tilde{\phi}^{(1)}_{\mathbf{k}_1}(t)\tilde{\phi}^{(0)}_{\mathbf{k}_2}(t)\rangle$$

$$+ 2\langle \tilde{\phi}^{(2)}_{\mathbf{k}_1}(t)\tilde{\phi}^{(0)}_{\mathbf{k}_2}(t)\rangle + \langle \tilde{\phi}^{(1)}_{\mathbf{k}_1}(t)\tilde{\phi}^{(1)}_{\mathbf{k}_2}(t)\rangle) \qquad (19)$$

$$\left. + 2i\left(k_{2x}\frac{\partial}{\partial X} - k_{2y}\frac{\partial}{\partial Y}\right)\langle \tilde{\phi}^{(1)}_{\mathbf{k}_1}(t)\tilde{\phi}^{(0)}_{\mathbf{k}_2}(t)\rangle \right\}.$$

We use the second-order correlation function and the averaged Green's function as the fundamental statistical characteristics of the turbulent field in the absence of a large-scale perturbation. Under the assumption that turbulence is homogeneous and isotropic, these functions depend only on the magnitude k of the wave vector and are described by the expressions

$$\langle \tilde{\phi}^{(0)}_{\mathbf{k}_1}(t)\tilde{\phi}^{(0)}_{\mathbf{k}_2}(t')\rangle \equiv I(k_1; t, t')\delta(\mathbf{k}_1 + \mathbf{k}_2),$$
$$\langle \hat{G}_{\mathbf{k}}(t, t')\rangle \equiv G(k; t, t'). \qquad (20)$$

It is assumed that the higher order correlation functions can be expressed in terms of functions (20) by using Kraichnan's direct-interaction approximation [12]. In particular, from solution (16), we obtain

$$\langle \tilde{\phi}^{(1)}_{\mathbf{k}_1}(t)\tilde{\phi}^{(0)}_{\mathbf{k}_2}(t)\rangle$$

$$= \frac{ik_1^2}{\lambda + k_1^2}[\mathbf{k}_1 \times \boldsymbol{\nabla}_s\bar{\phi}]_z \int\limits_{-\infty}^{t} dt' \langle \hat{G}_{\mathbf{k}_1}(t, t')\tilde{\phi}^{(0)}_{\mathbf{k}_1}(t')\tilde{\phi}^{(0)}_{\mathbf{k}_2}(t)\rangle$$

$$= \frac{ik_1^2}{\lambda + k_1^2}[\mathbf{k}_1 \times \boldsymbol{\nabla}_s\bar{\phi}]_z \int\limits_{-\infty}^{t} dt' \langle \hat{G}_{\mathbf{k}_1}(t, t')\rangle\langle\tilde{\phi}^{(0)}_{\mathbf{k}_1}(t')\tilde{\phi}^{(0)}_{\mathbf{k}_2}(t)\rangle \qquad (21)$$

$$= \frac{ik_1^2}{\lambda + k_1^2}[\mathbf{k}_1 \times \boldsymbol{\nabla}_s\bar{\phi}]_z \int\limits_{-\infty}^{t} dt' G(k_1; t, t')I(k_1; t', t)\delta(\mathbf{k}_1 + \mathbf{k}_2)$$

and, analogously,

$$\langle \tilde{\phi}^{(1)}_{\mathbf{k}_1}(t)\tilde{\phi}^{(1)}_{\mathbf{k}_2}(t)\rangle$$

$$= -\frac{k_1^2 k_2^2}{(\lambda + k_1^2)(\lambda + k_2^2)}[\mathbf{k}_1 \times \boldsymbol{\nabla}_s\bar{\phi}]_z[\mathbf{k}_2 \times \boldsymbol{\nabla}_s\bar{\phi}]_z$$

$$\times \int\limits_{-\infty}^{t} dt' \int\limits_{-\infty}^{t} dt'' \langle \hat{G}_{\mathbf{k}_1}(t, t')\hat{G}_{\mathbf{k}_2}(t, t'')\tilde{\phi}^{(0)}_{\mathbf{k}_1}(t')\tilde{\phi}^{(0)}_{\mathbf{k}_2}(t'')\rangle \qquad (22)$$

$$= \frac{k_1^4}{(\lambda + k_1^2)^2}[\mathbf{k}_1 \times \boldsymbol{\nabla}_s\bar{\phi}]_z^2 \int\limits_{-\infty}^{t} dt' \int\limits_{-\infty}^{t} dt'' G(k_1; t, t')$$

$$\times G(k_1; t, t'') \times I(k_1; t', t'')\delta(\mathbf{k}_1 + \mathbf{k}_2).$$

The last statistically averaged quantity that is required to calculate the effect of turbulence on the large-scale field in the desired order of smallness can be found by substituting solution (16) into solution (17) and taking into account relationship (21):

$$\langle \tilde{\phi}^{(2)}_{\mathbf{k}_1}(t)\tilde{\phi}^{(0)}_{\mathbf{k}_2}(t)\rangle = -\frac{2k_1^2}{(\lambda + k_1^2)^2}(\mathbf{k}_1 \cdot \boldsymbol{\nabla}_s)[\mathbf{k}_1 \times \boldsymbol{\nabla}_s\bar{\phi}]_z$$

$$\times \int\limits_{-\infty}^{t} dt' G(k_1; t, t')I(k_1; t', t)\delta(\mathbf{k}_1 + \mathbf{k}_2)$$

$$-\frac{k_1^4}{(\lambda + k_1^2)^2}[\mathbf{k}_1 \times \boldsymbol{\nabla}_s\bar{\phi}]_z^2 \int\limits_{-\infty}^{t} dt' \int\limits_{-\infty}^{t'} dt'' G(k_1; t, t')$$

$$\times G(k_1; t', t'')I(k; t'', t)\delta(\mathbf{k}_1 + \mathbf{k}_2)$$

$$+\frac{1}{2}\iint\limits_{\mathbf{q}_1 \mathbf{q}_2}\int\limits_{-\infty}^{t} d\tau \int\limits_{-\infty}^{\tau} dt' \int\limits_{-\infty}^{\tau} dt'' [\mathbf{q}_1 \times \mathbf{q}_2]_z$$

$$\times \frac{q_1^2 q_2^2(q_2^2 - q_1^2)}{(\lambda + k_1^2)(\lambda + q_1^2)(\lambda + q_2^2)}\delta(\mathbf{k}_1 - \mathbf{q}_1 - \mathbf{q}_2) \qquad (23)$$

$$\times [\mathbf{q}_1 \times \boldsymbol{\nabla}_s\bar{\phi}]_z[\mathbf{q}_2 \times \boldsymbol{\nabla}_s\bar{\phi}]_z G(k_1; t, \tau)G(q_1; \tau, t')$$

$$\times G(q_2; \tau, t'')\langle \tilde{\phi}^{(0)}_{\mathbf{q}_1}(t')\tilde{\phi}^{(0)}_{\mathbf{q}_2}(t'')\tilde{\phi}^{(0)}_{\mathbf{k}_2}(t)\rangle$$

$$+\iint\limits_{\mathbf{q}_1 \mathbf{q}_2}\int\limits_{-\infty}^{t} dt' \int\limits_{-\infty}^{t'} dt'' \frac{q_2^2}{(\lambda + k_1^2)(\lambda + q_2^2)^2}\delta(\mathbf{k}_1 - \mathbf{q}_1 - \mathbf{q}_2)$$

$$\times G(k_1; t, t')G(q_2; t', t'')\langle \tilde{\phi}^{(0)}_{\mathbf{q}_1}(t')\tilde{\phi}^{(0)}_{\mathbf{q}_2}(t'')\tilde{\phi}^{(0)}_{\mathbf{k}_2}(t)\rangle$$

$$\times \{2(\lambda + q_1^2)[\mathbf{q}_1 \times \mathbf{q}_2]_z(\mathbf{q}_2 \cdot \boldsymbol{\nabla}_s)[\mathbf{q}_2 \times \boldsymbol{\nabla}_s\bar{\phi}]_z$$

$$+(q_2^2 - q_1^2)(\lambda + q_2^2)[\mathbf{q}_1 \times \boldsymbol{\nabla}_s]_z[\mathbf{q}_2 \times \boldsymbol{\nabla}_s\bar{\phi}]_z\}.$$

We see that relationship (23) contains a third-order correlation function. In the direct-interaction approximation, this third-order correlation function can be expressed in terms of the second-order correlation functions and the averaged Green's function by using the well-known procedure that was described in detail in, e.g., [12, 13]:

$$\langle \tilde{\phi}^{(0)}_{\mathbf{k}_2}(t)\tilde{\phi}^{(0)}_{\mathbf{q}_1}(t')\tilde{\phi}^{(0)}_{\mathbf{q}_2}(t'')\rangle$$
$$= [\mathbf{q}_1 \times \mathbf{q}_2]_z \mathcal{G}(k_2, q_1, q_2; t, t', t'')\delta(\mathbf{k}_2 + \mathbf{q}_1 + \mathbf{q}_2), \qquad (24)$$

where

$$\mathcal{G}(k_2, q_1, q_2; t, t', t'')$$
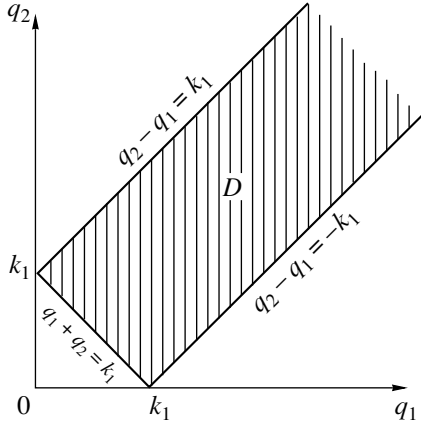
Fig. 1. Region of integration in the space of the absolute values of the wave vectors.

$$= \frac{q_2^2 - q_1^2}{\lambda + k_2^2} \int_{-\infty}^{t} d\tau G(k_2; t, \tau) I(q_1; t', \tau) I(q_2; t'', \tau)$$

$$+ \frac{k_2^2 - q_2^2}{\lambda + q_1^2} \int_{-\infty}^{t'} d\tau G(q_1; t', \tau) I(k_2; t, \tau) I(q_2; t'', \tau) \quad (25)$$

$$+ \frac{q_1^2 - k_2^2}{\lambda + q_2^2} \int_{-\infty}^{t''} d\tau G(q_2; t'', \tau) I(k_2; t, \tau) I(q_1; t', \tau).$$

In expression (23), integration can be carried out over the angles in the spaces of the vectors $\mathbf{q}_1$ and $\mathbf{q}_2$ using the following formulas (the details of their derivation are given in Appendix B):

$$\iint_{\mathbf{q}_1 \mathbf{q}_2} [\mathbf{q}_1 \times \mathbf{q}_2]_z^2 F(q_1, q_2) \delta(\mathbf{k}_1 - \mathbf{q}_1 - \mathbf{q}_2)$$

$$\times [\mathbf{q}_1 \times \nabla_s \bar{\phi}]_z [\mathbf{q}_2 \times \nabla_s \bar{\phi}]_z$$

$$= \iint_D dq_1 dq_2 q_1 q_2 F(q_1, q_2) \frac{\Delta(k_1, q_1, q_2)}{k_1^4} \quad (26)$$

$$\times \{ \Lambda(k_1, q_1, q_2) [\mathbf{k}_1 \times \nabla_s \bar{\phi}]_z^2$$

$$- 16\Delta^2(k_1, q_1, q_2)(\mathbf{k}_1 \cdot \nabla_s \bar{\phi})^2 \},$$

$$\iint_{\mathbf{q}_1 \mathbf{q}_2} [\mathbf{q}_1 \times \mathbf{q}_2]_z F(q_1, q_2) \delta(\mathbf{k}_1 - \mathbf{q}_1 - \mathbf{q}_2)$$

$$\times [\mathbf{q}_1 \times \nabla_s]_z [\mathbf{q}_2 \times \nabla_s \bar{\phi}]_z$$

$$= \iint_D dq_1 dq_2 q_1 q_2 F(q_1, q_2) \frac{4\Delta(k_1, q_1, q_2)}{k_1^4} \quad (27)$$

$$\times (\mathbf{k}_1 \cdot \nabla_s)[\mathbf{k}_1 \times \nabla_s \bar{\phi}]_z,$$

$$\iint_{\mathbf{q}_1 \mathbf{q}_2} [\mathbf{q}_1 \times \mathbf{q}_2]_z^2 F(q_1, q_2) \delta(\mathbf{k}_1 - \mathbf{q}_1 - \mathbf{q}_2)$$

$$\times (\mathbf{q}_2 \cdot \nabla_s)[\mathbf{q}_2 \times \nabla_s \bar{\phi}]_z$$

$$= \iint_D dq_1 dq_2 q_1 q_2 F(q_1, q_2) \frac{4\Delta(k_1, q_1, q_2)}{k_1^4} \quad (28)$$

$$\times [k_1^2 q_2^2 - 8\Delta^2(k_1, q_1, q_2)](\mathbf{k}_1 \cdot \nabla_s)[\mathbf{k}_1 \times \nabla_s \bar{\phi}]_z.$$

The region of integration, D, is shown in Fig. 1: it restricts q_1 and q_2 so that the vectors $\mathbf{k}_1$, $\mathbf{q}_1$, and $\mathbf{q}_2$ form a triangle whose area is equal to

$$\Delta(k_1, q_1, q_2)$$

$$= \frac{1}{4}(2q_1^2 q_2^2 + 2q_1^2 k_1^2 + 2k_1^2 q_2^2 - k_1^4 - q_1^4 - q_2^4)^{1/2}. \quad (29)$$

Also, in formula (26), we introduced the notation

$$\Lambda(k_1, q_1, q_2) = k_1^4 - (q_1^2 - q_2^2)^2. \quad (30)$$

After integration over the angles, Eq. (23) becomes

$$\langle \tilde{\phi}_{\mathbf{k}_1}^{(2)}(t) \tilde{\phi}_{\mathbf{k}_2}^{(0)}(t) \rangle$$

$$= \left[-\frac{2k_1^2}{(\lambda + k_1^2)^2} (\mathbf{k}_1 \cdot \nabla_s)[\mathbf{k}_1 \times \nabla_s \bar{\phi}]_z \int_{-\infty}^{t} dt' G(k_1; t, t') \right.$$

$$\times I(k_1; t', t) - \frac{k_1^4}{(\lambda + k_1^2)^2} [\mathbf{k}_1 \times \nabla_s \bar{\phi}]_z^2$$

$$\times \int_{-\infty}^{t} dt' \int_{-\infty}^{t'} dt'' G(k_1; t, t') G(k_1; t', t'') I(k_1; t'', t)$$

$$- \frac{1}{2} \iint_D dq_1 dq_2 \int_{-\infty}^{t} d\tau \int_{-\infty}^{\tau} dt' \int_{-\infty}^{\tau} dt'' \frac{q_1^3 q_2^3 (q_2^2 - q_1^2)}{k_1^4 (\lambda + k_1^2)(\lambda + q_1^2)}$$

$$\times \frac{\Delta(k_1, q_1, q_2)}{\lambda + q_2^2} \mathcal{G}(k_2, q_1, q_2; t, t', t'') G(k_1; t, \tau)$$

$$\times G(q_1; \tau, t') G(q_2; \tau, t'') \{ \Lambda(k_1, q_1, q_2) [\mathbf{k}_1 \times \nabla_s \bar{\phi}]_z^2$$

$$- 16\Delta^2(k_1, q_1, q_2)(\mathbf{k}_1 \cdot \nabla_s \bar{\phi})^2 \}$$

$$+ \iint_D dq_1 dq_2 \int_{-\infty}^{t} dt' \int_{-\infty}^{t'} dt'' \frac{4q_1 q_2^3 \Delta(k_1 q_1 q_2)}{k_1^4 (\lambda + k_1^2)(\lambda + q_2^2)^2}$$

$$\times \mathcal{G}(k_2, q_1, q_2; t, t', t'') G(k_1; t, t') G(q_2; t', t'')$$

$$\times \{ (\lambda + q_2^2)(q_2^2 - q_1^2)^2 + 2(\lambda + q_1^2)[k_1^2 q_2^2 \quad (31)$$

$$-8\Delta^2(k_1, q_1, q_2)]\}(\mathbf{k}_1 \cdot \boldsymbol{\nabla}_s)[\mathbf{k}_1 \times \boldsymbol{\nabla}_s\bar{\phi}]_z\Big]\delta(\mathbf{k}_1 + \mathbf{k}_2).$$

2.5. Mean-Field Equation

We substitute Eqs. (18) and (19) and relationships (21), (22), and (31) into Eq. (7) and use the formulas

$$\int d\mathbf{k}\, k_i k_j F(k) = \pi\delta_{ij}\int_0^\infty k^3 F(k)\,dk,$$

$$\int d\mathbf{k}\, k_i k_j k_l k_m F(k) \qquad (32)$$

$$= \frac{\pi}{4}(\delta_{ij}\delta_{lm} + \delta_{il}\delta_{jm} + \delta_{im}\delta_{jl})\int_0^\infty k^5 F(k)\,dk$$

in order to carry out integration over the angles in the vector space $\mathbf{k}_1$. As a result, we arrive at the final form of the evolutionary equation for the large-scale field:

$$\frac{\partial}{\partial T}(\lambda\bar{\phi} - \boldsymbol{\nabla}_s^2\bar{\phi})$$

$$\qquad\qquad (33)$$

$$-(1 - \beta_T)[\boldsymbol{\nabla}_s\bar{\phi} \times \boldsymbol{\nabla}_s\boldsymbol{\nabla}_s^2\bar{\phi}]_z + \nu_T\boldsymbol{\nabla}_s^4\bar{\phi} = 0,$$

where

$$\nu_T = -\int_0^\infty dk\,\frac{\pi\lambda k^5}{(\lambda + k^2)^2}\int_{-\infty}^t dt'\,G(k; t, t')I(k; t', t)$$

$$-\int_0^\infty dk\iint_D dk_1 dk_2\int_{-\infty}^t dt'\int_{-\infty}^{t'} dt''\,\frac{2\pi k k_1 k_2^3 \Delta(k, k_1, k_2)}{(\lambda + k^2)(\lambda + k_2^2)^2} \qquad (34)$$

$$\times \mathcal{G}(k, k_1, k_2; t, t', t'')G(k; t, t')G(k_2; t', t'')$$

$$\times \{(\lambda + k_2^2)(k_2^2 - k_1^2)^2 + (\lambda + k_1^2)[k^2 k_2^2 - 8\Delta^2(k, k_1, k_2)]\}$$

is the turbulent viscosity coefficient and

$$\beta_T = \int_0^\infty dk\,\frac{\pi k^9}{2(\lambda + k^2)^2}\int_{-\infty}^t dt'$$

$$\times\left[\int_{-\infty}^t dt''\,G(k; t, t')G(k; t, t'')I(k; t', t'')\right.$$

$$\left. -2\int_{-\infty}^{t'} dt''\,G(k; t, t')G(k; t', t'')I(k; t'', t)\right]$$

$$-\int_0^\infty dk\iint_D dk_1 dk_2[\Lambda(k, k_1, k_2) + 16\Delta^2(k, k_1, k_2)] \quad (35)$$

$$\times \frac{\pi k k_1^3 k_2^3 (k_2^2 - k_1^2)}{2(\lambda + k^2)(\lambda + k_1^2)}\frac{\Delta(k, k_1, k_2)}{\lambda + k_2^2}$$

$$\times \int_{-\infty}^t d\tau\int_{-\infty}^\tau dt'\int_{-\infty}^\tau dt''\,G(k; t, \tau)G(k_1; \tau, t')$$

$$\times G(k_2; \tau, t'')\,\mathcal{G}(k, k_1, k_2; t, t', t'').$$

Expression (34) implies that, if the third-order correlations (the second term on the right-hand side) are negligible, then the coefficient ν_T is determined by the first term and is nonzero only when $\lambda \neq 0$, i.e., when the adiabatic response of the electrons is important. The third-order correlation functions can be neglected only in the case of drift turbulence, which is dominated by the source of turbulence rather than by the nonlinear interaction of turbulent pulsations. As was mentioned above, this case can be described in the quasilinear approximation. It is not surprising that the conclusion that the electron adiabatic term is responsible for turbulent viscosity agrees with the results obtained in [3, 4]. Since the Green's function G and the spectral density I of turbulent pulsations are both positive, the second-order correlation functions always make a *negative* contribution to the turbulent viscosity coefficient ν_T. On the other hand, even in the limiting case described by the two-dimensional Euler equation ($\lambda = 0$), taking into account third-order correlations in a strongly turbulent regime leads to a nonzero turbulent viscosity coefficient, whose sign is very sensitive to both the turbulence spectrum and the Green's function of the turbulent field. Below, we will be interested in turbulent pulsations whose energy is concentrated in the wavenumber range corresponding to the inertial interval of turbulence. In the next section, we will attempt to find adequate expressions for the functions characterizing drift turbulence in this case.

3. TURBULENCE SPECTRA IN THE INERTIAL INTERVAL

In the inertial interval of turbulence, the turbulent spectra are universal in the sense that they are governed by the nonlinear interaction of turbulent pulsations and are insensitive to dissipation and the sources of turbulence. The shape of the turbulent spectrum in the inertial interval can be determined using the method based on the scaling symmetries of the geostrophic equation (1) describing the drift turbulence. In the general case ($\lambda \simeq \boldsymbol{\nabla}^2$), this equation admits only one scaling symmetry, which is characterized by the infinitesimal operator $X_1 = t\partial/\partial t - \phi\partial/\partial\phi$. This operator implies that Eq. (1) is invariant under the following one-parameter scale transformation with the parameter α:

$$t' = \alpha t, \quad \mathbf{x}' = \mathbf{x}, \quad \phi' = \alpha^{-1}\phi. \qquad (36)$$

In the two limiting cases under analysis, the geostrophic equation admits additional scaling symmetries. Specifically, when the adiabatic electron response is negligible ($\lambda \ll \nabla^2$, which corresponds to the two-dimensional Euler equation), the additional scaling symmetry is characterized by the infinitesimal operator $X_2 = \mathbf{x}\partial/\partial\mathbf{x} + 2\phi\partial/\partial\phi$, and the two-parameter group of scale transformations is defined as

$$t' = \alpha t, \quad \mathbf{x}' = \beta\mathbf{x}, \quad \phi' = \alpha^{-1}\beta^2\phi. \tag{37}$$

In the opposite limit ($\lambda \gg \nabla^2$), the geostrophic equation admits the additional scaling symmetry $X_3 = \mathbf{x}\partial/\partial\mathbf{x} + 4\phi\partial/\partial\phi$ and is thus invariant under the two-parameter scale transformation

$$t' = \alpha t, \quad \mathbf{x}' = \beta\mathbf{x}, \quad \phi' = \alpha^{-1}\beta^4\phi. \tag{38}$$

The geostrophic equation possesses two quadratic integral invariants: the energy integral

$$W \equiv \int w\,d\mathbf{x} = \frac{1}{2}\int[\lambda\phi^2 + (\nabla\phi)^2]\,d\mathbf{x} \tag{39}$$

and the enstrophy integral

$$U \equiv \int u\,d\mathbf{x} = \frac{1}{2}\int[\lambda(\nabla\phi)^2 + (\nabla^2\phi)^2]\,d\mathbf{x}. \tag{40}$$

If there is a source of turbulence that injects energy and enstrophy, then, as a result of the nonlinear interaction of turbulent pulsations (see, e.g., [14]), the energy cascades toward large scales (an inverse cascade), while the enstrophy cascades toward small scales (a direct cascade). The correlators and spectra of turbulence that correspond to a constant energy flux or to a constant enstrophy flux can be found from the scaling properties of the geostrophic equation by applying the P theorem, which was proved as early as 1914 by Buckingham [15]. Thus, for a constant rate ε of the energy density transfer along the spectrum, the second-order two-time two-point correlation function of a steady uniform isotropic turbulence in the inertial interval can depend only on three quantities: $\tau = |t_1 - t_2|$, $r = |\mathbf{x}_1 - \mathbf{x}_2|$, and ε. Consequently, in the most general form, the second-order correlation function can be written as

$$\langle\phi(\mathbf{x}_1, t_1)\phi(\mathbf{x}_2, t_2)\rangle = \sum_{a, b, c} C_{abc}\varepsilon^a\tau^b r^c, \tag{41}$$

where C_{abc} are arbitrary tensor coefficients. Taking into account the relationship $\varepsilon \propto dw/dt$, we find that the scale transformation (36) converts the quantity ε according to the law

$$\varepsilon' = \alpha^{-3}\varepsilon, \tag{42}$$

so that the second-order correlation function (41) transforms to

$$\langle\phi(\mathbf{x}_1, t_1)\phi(\mathbf{x}_2, t_2)\rangle$$
$$= \sum_{a, b, c} C_{a, b, c}\alpha^{3a-b}(\varepsilon')^a(\tau')^b(r')^c \tag{43}$$
$$\equiv \alpha^{3a-b}\langle\phi'(\mathbf{x}_1', t_1')\phi'(\mathbf{x}_2', t_2')\rangle.$$

On the other hand, the scale transformation (36) implies that

$$\langle\phi(\mathbf{x}_1, t_1)\phi(\mathbf{x}_2, t_2)\rangle = \alpha^2\langle\phi'(\mathbf{x}_1', t_1')\phi'(\mathbf{x}_2', t_2')\rangle. \tag{44}$$

We equate the powers of α in relationships (43) and (44) to obtain $a = 2/3 + b/3$. Inserting this equality into formula (41), we see that the second-order correlation function of turbulence is an arbitrary function of the two parameters:

$$\langle\phi(\mathbf{x}_1, t_1)\phi(\mathbf{x}_2, t_2)\rangle = \varepsilon^{2/3}\hat{F}(\varepsilon^{1/3}\tau, r). \tag{45}$$

Taking into account the relationship

$$I(k; t_1, t_2) = \int\langle\phi(\mathbf{x}_1, t_1)\phi(\mathbf{x}_1 + \mathbf{r}, t_2)\rangle e^{-i\mathbf{k}\cdot\mathbf{r}}\,d\mathbf{r}, \tag{46}$$

we can see that the spectral function of the drift turbulence should have the general form

$$I(k; t_1, t_2) = \varepsilon^{2/3}F_1(\varepsilon^{1/3}\tau, k), \tag{47}$$

where F_1 is an arbitrary function. The Green's function of turbulence can be found in an analogous way. It should have the form

$$G(k; t_1, t_2) = R_1(\varepsilon^{1/3}\tau, k). \tag{48}$$

For a constant density η of the enstrophy flux along the spectrum, we can also apply the above procedure. As a result, we find that the turbulence is described by the spectral function and Green's function as follows:

$$I(k; t_1, t_2) = \eta^{2/3}F_2(\eta^{1/3}\tau, k),$$
$$G(k; t_1, t_2) = R_2(\eta^{1/3}\tau, k). \tag{49}$$

In the two limiting cases under analysis, additional scaling symmetries imply that the spectral function and Green's function are both arbitrary functions of only one parameter. In the limit $\lambda \ll \nabla^2$, which is described by the Euler equation, we arrive at the following spectra corresponding to the constant energy and enstrophy fluxes:

$$I(k; t_1, t_2) = \varepsilon^{2/3}k^{-14/3}F_1(\varepsilon^{1/3}k^{2/3}\tau),$$
$$G(k; t_1, t_2) = R_1(\varepsilon^{1/3}k^{2/3}\tau), \tag{50}$$

$$I(k; t_1, t_2) = \eta^{2/3}k^{-6}F_2(\eta^{1/3}\tau),$$
$$G(k; t_1, t_2) = R_2(\eta^{1/3}\tau). \tag{51}$$

The Kolmogorov energy spectra that correspond to the spectral functions (50) and (51) have the form (see, e.g., [14])

$$E(k) \sim \varepsilon^{2/3} k^{-5/3}, \quad E(k) \sim \eta^{2/3} k^{-3}. \qquad (52)$$

Analogously, in the opposite limit ($\lambda \gg \nabla^2$), we obtain

$$I(k; t_1, t_2) = \varepsilon^{2/3} k^{-14/3} F_1(\varepsilon^{1/3} k^{8/3} \tau),$$
$$G(k; t_1, t_2) = R_1(\varepsilon^{1/3} k^{8/3} \tau), \qquad (53)$$

$$I(k; t_1, t_2) = \eta^{2/3} k^{-6} F_2(\eta^{1/3} k^2 \tau),$$
$$G(k; t_1, t_2) = R_2(\eta^{1/3} k^2 \tau). \qquad (54)$$

The Kolmogorov energy spectra that correspond to the spectral functions (53) and (54) have the form

$$E(k) \sim \varepsilon^{2/3} k^{-11/3}, \quad E(k) \sim \eta^{2/3} k^{-5}. \qquad (55)$$

In the next section, we follow [11, 14] and set the arbitrary functions in formulas (50)–(54) to be exponential, so that

$$I(k; t_1, t_2) = \sigma(k) \exp(-\omega(k)|t_1 - t_2|) H(k - k_c),$$
$$G(k; t_1, t_2)$$
$$= \exp(-\omega(k)(t_1 - t_2)) H(t_1 - t_2) H(k - k_c), \qquad (56)$$

where $H(t)$ is the Heaviside step function and k_c is the length of the wave vector of the largest scale vortices in the inertial interval of turbulence. The one-moment ($t_1 - t_2 = 0$) spectral function $\sigma(k)$ of turbulence and the nonlinear frequency $\omega(k)$ are determined by the corresponding equations presented above and have the form

$$\sigma(k) = \begin{cases} \sigma_1 \varepsilon^{2/3} k^{-14/3} & \text{for the spectrum with a constant} \\ & \text{energy flux} \qquad (57) \\ \sigma_2 \eta^{2/3} k^{-6} & \text{for the spectrum with a constant} \\ & \text{enstrophy flux,} \end{cases}$$

$$\omega(k) = \begin{cases} f_1 \varepsilon^{1/3} k^{\alpha} & \text{for the spectrum with a constant} \\ & \text{energy flux} \qquad (58) \\ f_2 \eta^{1/3} k^{\beta} & \text{for the spectrum with a constant} \\ & \text{enstrophy flux,} \end{cases}$$

where the exponents α and β differ between the two limiting cases of drift turbulence (in which the characteristic spatial scales are much larger than or much smaller than the ion Larmor radius in terms of the electron temperature):

$$\alpha = \begin{cases} 2/3 & \text{for} \quad \lambda \ll k_c^2 \\ 8/3 & \text{for} \quad \lambda \gg k_c^2, \end{cases} \qquad (59)$$

$$\beta = \begin{cases} 0 & \text{for} \quad \lambda \ll k_c^2 \\ 2 & \text{for} \quad \lambda \gg k_c^2. \end{cases} \qquad (60)$$

4. TURBULENT COEFFICIENTS IN THE CASE OF STRONG DRIFT TURBULENCE

Here, we consider the turbulent coefficients ν_T and β_T in the particular case of strong turbulence such that the spectral function and Green's function are independent of both the source of turbulence and the dissipation mechanism (the inertial interval). The calculation of the turbulent coefficients is straightforward but rather lengthy. Substituting relationships (56) into formula (34) yields the following expression for the turbulent viscosity coefficient (see Appendix B for details):

$$\nu_T = -\int_{k_c}^{\infty} dk \frac{\pi \lambda k^5 \sigma(k)}{2(\lambda + k^2)^2 \omega(k)}$$

$$- \int_{k_c}^{\infty} dk \iint_D dk_1 dk_2 \frac{\pi k k_1 k_2^3 \Delta(k, k_1, k_2)}{(\lambda + k^2)(\lambda + k_2^2)^2}$$

$$\times \frac{\sigma(k)\sigma(k_1)\sigma(k_2)}{\omega(k)\Omega^2} \{ (\lambda + k_2^2)(k_2^2 - k_1^2)^2$$

$$+ 2(\lambda + k_1^2)[k^2 k_2^2 - 8\Delta^2(k, k_1, k_2)] \} \qquad (61)$$

$$\times \left\{ \frac{k_1^2 - k^2}{\lambda + k_2^2} \frac{1}{\sigma(k_2)} + \frac{k^2 - k_2^2}{\lambda + k_1^2} \frac{1}{\sigma(k_1)} \left(1 + \frac{\Omega}{2\omega(k_2)} \right) \right.$$

$$\left. + \frac{k_2^2 - k_1^2}{\lambda + k^2} \frac{1}{\sigma(k)} \left(1 + \frac{\Omega}{\omega(k_2)} \right) \right\} H(k_1 - k_c) H(k_2 - k_c),$$

where $\Omega \equiv \omega(k) + \omega(k_1) + \omega(k_2)$. On the other hand, by inserting relationships (56) into formula (35), we can see that the first two terms in the resulting expression cancel each other by virtue of the equality

$$\int_{-\infty}^{t} dt' \int_{-\infty}^{t} dt'' G(k; t, t') G(k; t, t'') I(k; t', t'')$$

$$= 2 \int_{-\infty}^{t} dt' \int_{-\infty}^{t'} dt'' G(k; t, t') G(k; t', t'') I(k; t'', t) \qquad (62)$$

$$= \frac{\sigma(k)}{2\omega^2(k)}.$$

Hence, in our model, in which the spectral functions and Green's functions depend exponentially on $t_1 - t_2$, the turbulent coefficient β_T, which corresponds to the turbulence-related renormalization of the Poisson

bracket, is nonzero only at the expense of the third-order correlation function:

$$\beta_T = \int_{k_c}^{\infty} dk \iint_{D} dk_1 dk_2$$

$$\times \frac{\pi k k_1^3 k_2^3 (k_1^2 - k_2^2) \Delta(k, k_1, k_2) \sigma(k) \sigma(k_1) \sigma(k_2)}{2(\lambda + k^2)(\lambda + k_1^2)(\lambda + k_2^2) \omega(k) \Omega^3}$$

$$\times [\Lambda(k, k_1, k_2) + 16\Delta^2(k, k_1, k_2)]$$

$$\times \left\{ \frac{k_2^2 - k_1^2}{\lambda + k^2} \frac{1}{\sigma(k)} \left[1 + \frac{\Omega}{4} \left(\frac{1}{\omega(k_1)} + \frac{1}{\omega(k_2)} \right) \right. \right.$$

$$\left. + \frac{\Omega^2}{4\omega(k_1)\omega(k_2)} \right] + \frac{k^2 - k_2^2}{\lambda + k_1^2} \frac{1}{\sigma(k_1)} \left[1 + \frac{\Omega}{4\omega(k_2)} \right]$$

$$+ \frac{k_1^2 - k^2}{\lambda + k_2^2} \frac{1}{\sigma(k_2)} \left[1 + \frac{\Omega}{4\omega(k_1)} \right] \right\} H(k_1 - k_c) H(k_2 - k_c). \quad (63)$$

In both limits $\lambda \ll k_c^2$ and $\lambda \gg k_c^2$, the coefficient β_T for a constant energy (enstrophy) flux along the spectrum is independent of k_c and the energy flux density ε (the enstrophy flux density η):

$$\beta_T = \frac{\sigma_i^2}{f_i^4} \int_1^{\infty} dx \iint_{\tilde{D}} dy dz \frac{\pi \Delta(x, y, z)(y^2 - z^2)}{x^{a+2} y^a z^a \hat{\Omega}^3}$$

$$\times [2y^2 z^2 + x^2 y^2 + x^2 z^2 - x^4 - z^4]$$

$$\times \left\{ (z^2 - y^2) x^b \left[(yz)^c + \frac{\hat{\Omega}}{4} (y^c + z^c) + \frac{\hat{\Omega}^2}{4} \right] \right. \quad (64)$$

$$\left. + (x^2 - z^2) y^{b+c} \left[z^c + \frac{\hat{\Omega}}{4} \right] + (y^2 - x^2) z^{b+c} \left[y^c + \frac{\hat{\Omega}}{4} \right] \right\}$$

$$\times H(y - 1) H(z - 1).$$

Here, $\hat{\Omega} = x^c + y^c + z^c$; the region of integration, $\tilde{D}$, is analogous to D and restricts y and z in such a way that x, y, and z form a triangle; and the subscript $i = (1, 2)$ refers to the spectra with a constant energy flux and constant enstrophy flux, respectively. For the spectra with a constant energy flux, the exponents a, b, and c are equal to

$$a = 13/3, \quad b = \begin{cases} 8/3 & \text{for} \quad \lambda \ll k_c^2 \\ 14/3 & \text{for} \quad \lambda \gg k_c^2, \end{cases} \quad (65)$$

$$c = \alpha,$$

and, for the spectra with a constant enstrophy flux, they are equal to

$$a = 5, \quad b = \begin{cases} 4 & \text{for} \quad \lambda \ll k_c^2 \\ 6 & \text{for} \quad \lambda \gg k_c^2, \end{cases} \quad c = \beta. \quad (66)$$

As for the turbulent viscosity coefficient, it depends on both the quantity k_c and the energy (enstrophy) flux density. Let us determine this coefficient in the two limiting cases in question.

4.1. The Limit $\lambda \ll k_c^2$

In this limit, the terms λ can be neglected in all combinations of the form $\lambda + k^2$ in the integrands, so that the turbulent viscosity coefficients for the spectra with a constant energy and constant enstrophy flux density are described by relatively simple expressions.

4.1.1. Spectrum with a constant energy flux. We substitute the spectrum determined by relationships (57)–(59) into formula (61) to obtain the following expression for the turbulent viscosity coefficient:

$$\nu_T = \varepsilon^{1/3} k_c^{-4/3} (\kappa_1 \lambda / k_c^2 + \kappa_2), \quad (67)$$

where

$$\kappa_1 = -3\pi\sigma_1/20 f_1, \quad (68)$$

and the coefficient κ_2 is represented in integral form,

$$\kappa_2 = \frac{\pi\sigma_1^2}{f_1^3} \int_1^{\infty} dx \iint_{\tilde{D}} dy dz \frac{\Delta(x, y, z)}{(xz)^{19/3} y^{11/3}} \frac{1}{(x^{2/3} + y^{2/3} + z^{2/3})^2}$$

$$\times \{ y^6 + z^6 + x^4 y^2 - 2x^2 y^4 - y^4 z^2 - x^2 z^4 \}$$

$$\times \left\{ (x^2 - y^2) z^{10/3} + \frac{1}{2} (z^2 - x^2) y^{8/3} (x^{2/3} + y^{2/3} + 3z^{2/3}) \right. \quad (69)$$

$$\left. + (y^2 - z^2) x^{8/3} (x^{2/3} + y^{2/3} + 2z^{2/3}) \right\} H(y - 1) H(z - 1).$$

Expression (67) implies that the contribution of the second-order correlations to the turbulent viscosity coefficient is formally as small as λ/k_c^2; however, with the possible case $\kappa_2 \ll \kappa_1$ in mind, we retain this contribution in the expression for the viscosity coefficient.

Since the coefficient κ_2 is impossible to determine analytically because of the very complicated integrand, it was calculated by the Monte Carlo method with the help of the Mathematica-3 software package. By truncating the turbulence spectrum at the upper limit (e.g., by taking into account collisional dissipation), the numerical scheme was made convergent, and it was found that $\kappa_2 = -0.17\pi\sigma_1^2/f_1^3$ for $k_{max}/k_c = 10$ and

$\kappa_2 = -0.23\pi\sigma_1^2/f_1^3$ for $k_{max}/k_c = 20$. We thus see that the third-order correlations of the turbulent field, like the second-order correlations, make a negative contribution to the turbulent viscosity coefficient. With an infinite integration domain and different numbers of iterations, the integral was always found to be finite and negative. On the other hand, in the standard iteration method, the step-by-step process of numerical integration converges very slowly because of the nontrivial integrand, which makes it impossible to complete the iteration procedure and thus necessitates the use of another numerical scheme. Since the details of the turbulence spectrum (i.e., the coefficients σ_1 and f_1) are still unknown, the most important point here is to determine the sign of the integral, so that we restrict ourselves to the results presented above.

Hence, in the case at hand, the turbulent viscosity coefficient is negative, so a spontaneous amplification of the large-scale perturbations should take place. As the amplitude of these perturbations increases due to the instability, nonlinear effects come into play (i.e., the nonlinear term in the evolutionary equation for the large-scale field becomes important). Presumably, it is these effects that cause the instability to saturate at a certain level and the system to relax to a certain steady state. To answer this question, it is necessary to numerically solve Eq. (33) for the large-scale field.

4.1.2. Spectrum with a constant enstrophy flux. For the turbulence spectrum with a constant enstrophy flux, we obtain

$$\nu_T = \eta^{1/3}k_c^{-2}(\kappa_3\lambda/k_c^2 + \kappa_4),\tag{70}$$

where

$$\kappa_3 = -\pi\sigma_2/8f_2,\tag{71}$$

and the coefficient κ_4 has the form

$$\kappa_4 = \frac{\pi\sigma_2^2}{9f_2^3}\int_1^\infty dx\iint_{\tilde{D}}dydz\frac{\Delta(x,y,z)}{(xz)^7y^5}\{y^6 + z^6 + x^4y^2$$

$$- 2x^2y^4 - y^4z^2 - x^2z^4\}\left\{(x^2 - y^2)z^4 + \frac{5}{2}(z^2 - x^2)y^4\right.\tag{72}$$

$$\left. + 4(y^2 - z^2)x^4\right\}H(y-1)H(z-1).$$

Numerical integration shows that, for infinite integration limits, the quantity κ_4 diverges, $\kappa_4 \longrightarrow \infty$, so that the integral should be truncated at the upper limit. As an upper limit in the wavenumber, it is natural to choose the reciprocal of the scale length of the collisional viscosity–related dissipation, which is neglected in our analysis. With the integral truncated in such a way, numerical calculations yielded the expressions $\kappa_2 =$

$2.73\pi\sigma_2^2/f_2^3$ for $k_{max}/k_c = 10$ and $\kappa_2 = 11.86\pi\sigma_1^2/f_1^3$ for $k_{max}/k_c = 20$. Consequently, in the case at hand, the third-order correlations of the turbulent field make a positive contribution to the turbulent viscosity coefficient, thereby canceling the negative contribution of the second-order correlations. That is why, in order to determine the sign of the turbulent viscosity coefficient, it is necessary to know the exact spectrum of the small-scale drift turbulence. However, because of the weighting factor λ/k_c^2, the contribution of the second-order correlations is small; therefore, it is highly probable that the total turbulent viscosity coefficient will be positive and the spontaneous perturbations of the averaged field will be damped.

4.2. The Limit $\lambda \gg k_c^2$

In this limit, the integrands can be simplified by neglecting the terms k^2 in all combinations of the form $\lambda + k^2$. The turbulent viscosity coefficients for the spectra with a constant energy and constant enstrophy flux density can be calculated in the same way as in Section 4.1.

4.2.1. Spectrum with a constant energy flux. Using relationships (57)–(59) and formula (61), we obtain the following expression for the turbulent viscosity coefficient:

$$\nu_T = \varepsilon^{1/3}k_c^{-4/3}(\gamma_1 + \gamma_2),\tag{73}$$

where

$$\gamma_1 = -3\pi\sigma_1/8f_1\lambda,\tag{74}$$

and the coefficient γ_2 is represented in integral form,

$$\gamma_2 = \frac{\pi\sigma_1^2}{\lambda^3 f_1^3}\int_1^\infty dx\iint_{\tilde{D}}dydz\frac{\Delta(x,y,z)}{x^{19/3}y^{11/3}z^{13/3}}\frac{1}{(x^{8/3} + y^{8/3} + z^{8/3})^2}$$

$$\times\{2y^4 + 2z^4 + x^4 - 2x^2y^2 - 4y^2z^2\}\left\{(x^2 - y^2)z^{22/3}\right.\tag{75}$$

$$\left. + \frac{1}{2}(z^2 - x^2)y^{14/3}(x^{8/3} + y^{8/3} + 3z^{8/3}) + (y^2 - z^2)x^{14/3}\right.$$

$$\left. \times(x^{8/3} + y^{8/3} + 2z^{8/3})\right\}H(y-1)H(z-1).$$

Numerical integration over an unbounded domain showed that the coefficient γ_2 is infinite, so that a physically reasonable result can only be obtained by truncating the turbulence spectrum at a large value of k. As an upper limit in the wavenumber, it is natural to choose the reciprocal of the ion Larmor radius, i.e., to set

$k_{max}^2 = \lambda$, in which case numerical calculations give the following expressions: $\gamma_2 = 9.10\pi\sigma_1^2/\lambda^3 f_1^3$ for $k_{max}/k_c = 10$ and $\kappa_2 = 40.54\pi\sigma_1^2/f_1^3$ for $k_{max}/k_c = 20$. Consequently, the third-order correlations of the turbulent field make a positive contribution to the turbulent viscosity coefficient, thereby canceling the negative contribution of the second-order correlations. Hence, in order to determine the sign of the turbulent viscosity coefficient, it is necessary to know the exact spectrum of the drift turbulence.

4.2.2. Spectrum with a constant enstrophy flux. We insert relationships (57), (58), and (60) into formula (61) to obtain

$$\nu_T = \eta^{1/3} k_c^{-2}(\gamma_3 + \gamma_4). \qquad (76)$$

Here, the coefficient γ_3 is determined by the second-order correlations,

$$\gamma_3 = -\pi\sigma_2/2\lambda f_2, \qquad (77)$$

and the contribution γ_4 of the third-order correlations is represented in integral form,

$$\gamma_4 = \frac{\pi\sigma_2^2}{\lambda^3 f_2^3}\int_1^\infty dx \iint_{\tilde{D}} dy\,dz \frac{\Delta(x,y,z)}{x^7 y^5 z^5} \frac{1}{(x^2+y^2+z^2)^2}$$

$$\times \{2y^4 + 2z^4 + x^4 - 2x^2y^2 - 4y^2z^2\}\Bigg\{(x^2-y^2)z^8$$

$$+ \frac{1}{2}(z^2-x^2)y^6(x^2+y^2+3z^2) + (y^2-z^2)x^6 \qquad (78)$$

$$\times (x^2+y^2+2z^2)\Bigg\}H(y-1)H(z-1).$$

As in the case of the spectrum with a constant energy flux for $\lambda \ll k_c^2$, the integral in expression (78) converges even when the integration domain is unbounded. With different numbers of iterations, the integral was always found to be negative. On the other hand, because of the nontrivial integrand, attempts to make the iteration process of numerical integration convergent were unsuccessful. For this reason, we restrict ourselves to the results obtained for a bounded region of integration, specifically, $\gamma_4 = -0.47\pi\sigma_2^2/f_2^3\lambda^3$ for $k_{max}/k_c = 10$ and $\gamma_4 = -0.86\pi\sigma_2^2/f_2^3\lambda^3$ for $k_{max}/k_c = 20$. We see that the third-order correlations of the turbulent field, like the second-order correlations, make a negative contribution to the turbulent viscosity coefficient. Hence, we can conclude that, in the case at hand, small-scale drift turbulence on the whole gives rise to turbulent viscosity with a negative coefficient. In turn, the instability driven by this turbulent viscosity causes the spontaneous growth of large-scale perturbations.

5. DISCUSSION OF THE RESULTS

A systematic theory of the generation of large-scale perturbations by the small-scale drift turbulence in a plasma has been constructed by applying a geostrophic equation (a simplified version of the Hasegawa–Mima model) and the two-scale direct interaction approximation technique. Thus, the previously existing theory, which is based on the quasilinear approximation and, strictly speaking, is valid when the Reynolds number is low (i.e., when the collisional dissipation dominates over the nonlinear interaction of turbulent pulsations) or when the turbulence spectrum is determined by the source of turbulence, has been extended to the case of strong drift turbulence, whose spectrum is governed by the nonlinear interaction of turbulent pulsations and is insensitive to dissipation and the source of turbulence. It has been shown that, as in quasilinear theory, accounting for small-scale drift turbulence gives rise to a turbulent viscosity effect and leads to renormalization of the nonlinear term with the Poisson bracket in the evolutionary equation for the large-scale (mean) field. However, for the regime of strong drift turbulence under consideration, the turbulent viscosity coefficient and renormalization coefficient are both represented as a sum of two parts, which are comparable in magnitude. As in the quasilinear approximation, the first part is determined by the second-order correlations and is nonzero merely because the geostrophic equation incorporates the adiabatic electron response. The contribution of the second-order correlations to the turbulent viscosity coefficient is negative regardless of the turbulence spectrum. In the limiting case corresponding to the two-dimensional incompressible hydrodynamics described by the Euler equation, the second-order correlations do not contribute to the turbulent viscosity coefficient. The sign of the second part, which is associated with the third-order correlations of the turbulent field, depends on the spectral properties of turbulence.

Explicit expressions for the turbulent viscosity coefficient and renormalization coefficient have been derived for the model Kolmogorov spectra of drift turbulence, which are thought to be characteristic of the inertial interval of turbulence. For the model used in the analysis, the renormalization of the Poisson bracket is completely governed by the third-order correlations, because the contribution of the second-order correlations is identically zero. For $\lambda \ll k_c^2$ (the case of turbulence described by the two-dimensional Euler equation) and for the Kolmogorov spectrum with a constant energy flux, the contribution of the third-order correlations to the turbulent viscosity coefficient is negative. Accordingly, the turbulent viscosity coefficient is also negative, which indicates the growth of large-scale per-

turbations. For the Kolmogorov spectrum with a constant enstrophy flux, the contribution of the third-order correlations is positive, so that the determination of the sign of the turbulent viscosity coefficient requires a knowledge of the exact turbulence spectrum. Moreover, since the weighting factor λ/k_c^2 of the contribution of the second-order correlations is small, it can be expected that the resulting turbulent viscosity coefficient will be positive.

The results obtained for $\lambda \gg k_c^2$ differ radically from those obtained in the opposite limit. For the spectrum with a constant energy flux, the contribution of the third-order correlations to the turbulent viscosity coefficient is positive, so that the sign of this coefficient cannot be determined without knowing the details of the turbulence spectrum. On the other hand, for the spectrum with a constant enstrophy flux, the contribution of the third-order correlations to the turbulent viscosity coefficient is negative, so that the coefficient itself is also negative, which indicates the instability of large-scale perturbations.

The results obtained in this study may be of interest in solving the problems of L–H transitions in tokamaks and the generation of large-scale vortices in the ocean and in the atmospheres of rotating planets.
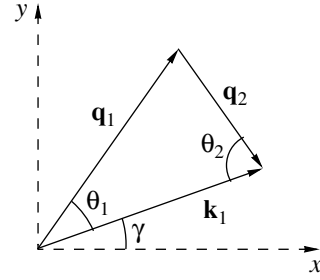
ACKNOWLEDGMENTS

APPENDIX A

Derivation of Formulas (26)–(28)

We illustrate the method for deriving formulas (26)–(28) by calculating as an example the integral in expression (28). In the geometry shown in Fig. 2, this expression can be rewritten in the form

$$J = \iint_{\mathbf{q}_1\mathbf{q}_2} [\mathbf{q}_1 \times \mathbf{q}_2]_z^2 F(q_1, q_2)\delta(\mathbf{k}_1 - \mathbf{q}_1 - \mathbf{q}_2)$$

$$\times (\mathbf{q}_2 \cdot \mathbf{V}_s)[\mathbf{q}_2 \times \mathbf{V}_s \bar{\phi}]_z$$

Fig. 2. Geometry of the fundamental triad of the wave vectors.

$$= \int_0^\infty q_1 dq_1 \int_0^\infty q_2 dq_2 \int_0^{2\pi} d\theta_1 \int_0^{2\pi} d\theta_2 k_1^2 q_2^4 \sin^2\theta_2 F(q_1, q_2)$$

$$\times \left[(\cos^2(\theta_2 - \gamma) - \sin^2(\theta_2 - \gamma))\frac{\partial^2\bar{\phi}}{\partial X\partial Y} \right.$$

$$\left. + \sin(\theta_2 - \gamma)\cos(\theta_2 - \gamma)\left(\frac{\partial^2\bar{\phi}}{\partial X^2} - \frac{\partial^2\bar{\phi}}{\partial Y^2}\right) \right]$$

$$\times \delta(k_1 - q_1\cos\theta_1 - q_2\cos\theta_2)\delta(q_1\sin\theta_1 - q_2\sin\theta_2). \tag{A.1}$$

Since, in the presence of the second δ function, the integral over the angles is nonzero only when the functions $\sin\theta_1$ and $\sin\theta_2$ have the same sign, the integral (A.1) can be represented as

$$\int_0^{2\pi} d\theta_1 \int_0^{2\pi} d\theta_2(\ldots)$$

$$= \int_0^\pi d\theta_1 \int_0^\pi d\theta_2(\ldots) + \int_\pi^{2\pi} d\theta_1 \int_\pi^{2\pi} d\theta_2(\ldots). \tag{A.2}$$

After the replacements $\theta_1^* = 2\pi - \theta_1$ and $\theta_2^* = 2\pi - \theta_2$ in the second integral in (A.2), we obtain

$$J = \int_0^\infty dq_1 \int_0^\infty dq_2 k_1^2 q_1 q_2^5 F(q_1, q_2)$$

$$\times \int_0^\pi d\theta_1 \int_0^\pi d\theta_2 \sin^2\theta_2\left[\left(\cos[2(\theta_2 - \gamma)]\right.\right.$$

$$+ \cos[2(\theta_2 + \gamma)])\frac{\partial^2\bar{\phi}}{\partial X\partial Y} + \frac{1}{2}(\sin[2(\theta_2 - \gamma)]$$

$$\left.\left. - \sin[2(\theta_2 + \gamma)])\left(\frac{\partial^2\bar{\phi}}{\partial X^2} - \frac{\partial^2\bar{\phi}}{\partial Y^2}\right)\right]\right] \tag{A.3}$$

$$\times \delta(k_1 - q_1\cos\theta_1 - q_2\cos\theta_2)\delta(q_1\sin\theta_1 - q_2\sin\theta_2)$$

$$= \int_0^\infty dq_1 \int_0^\infty dq_2 k_1^2 q_1 q_2^5 F(q_1, q_2) \int_0^\pi d\theta_1 \int_0^\pi d\theta_2 \sin^2\theta_2 \cos 2\theta_2$$

$$\times \left[2\cos 2\gamma \frac{\partial^2 \bar\phi}{\partial X \partial Y} - \sin 2\gamma \left(\frac{\partial^2 \bar\phi}{\partial X^2} - \frac{\partial^2 \bar\phi}{\partial Y^2} \right) \right]$$

$$\times \delta(k_1 - q_1 \cos\theta_1 - q_2 \cos\theta_2)\delta(q_1 \sin\theta_1 - q_2 \sin\theta_2).$$

In (A.3), we carry out integration over the angles θ_1 and θ_2 and take into account the relationships $\cos\gamma = k_{1x}/k_1$ and $\sin\gamma = k_{1y}/k_1$. As a result, we arrive at expression (28). Formulas (26) and (27) can be derived in a similar way.

APPENDIX B

Calculation of the Integrals over Time in the Expressions for ν_T and β_T

As an example, we turn to the second term in expression (34) for ν_T. In the triple integral over time, we calculate the part containing the first of the three terms in formula (25) for $\mathcal{G}$:

$$F \equiv \int_{-\infty}^{t} dt' \int_{-\infty}^{t'} dt'' \int_{-\infty}^{t} d\tau\, G(k; t, t') G(k_2; t', t'')$$

$$\times G(k_2; t, \tau) I(k_1; t', \tau) I(k_2; t'', \tau)$$

$$= \sigma(k_1)\sigma(k_2) \int_{-\infty}^{t} dt' \int_{-\infty}^{t'} dt'' \int_{-\infty}^{t} d\tau\, H(t - t') \quad (B.1)$$

$$\times H(t' - t'') H(t - \tau)$$

$$\times \exp[-\omega(k)(2t - t' - \tau) - \omega(k_1)|t' - \tau|$$

$$- \omega(k_2)(t' - t'' + |t'' - \tau|)].$$

The interval of integration over time can be divided into the following three subintervals:

$$\int_{-\infty}^{t} d\tau\, H(t - t') H(t' - t'') H(t - \tau)$$

$$\times \exp[-\omega(k)(2t - t' - \tau) - \omega(k_1)|t' - \tau|$$

$$- \omega(k_2)(t' - t'' + |t'' - \tau|)]$$

$$= \int_{-\infty}^{t''} d\tau \exp[-\omega(k)(2t - t' - \tau)$$

$$- (\omega(k_1) + \omega(k_2))(t' - \tau)]$$

$$+ \int_{t''}^{t'} d\tau \exp[-\omega(k)(2t - t' - \tau) - \omega(k_1)(t' - \tau)$$

$$- \omega(k_2)(t' + \tau - 2t'')] + \int_{t'}^{t} d\tau \exp[-\omega(k)(2t - t' - \tau)$$

$$- \omega(k_1)(\tau - t') - \omega(k_2)(t' + \tau - 2t'')] \quad (B.2)$$

$$= \frac{1}{\Omega} \exp[-\omega(k)(2t - t' - t'') - (\omega(k_1) + \omega(k_2))(t' - t'')]$$

$$+ \frac{1}{\omega(k) + \omega(k_1) - \omega(k_2)} \{ \exp[-2\omega(k)(t - t')$$

$$- 2\omega(k_2)(t' - t'')] - \exp[-\omega(k)(2t - t' - t'')$$

$$+ (\omega(k_1) - \omega(k_2))(t' - t'')] \} + \frac{1}{\omega(k) - \omega(k_1) - \omega(k_2)}$$

$$\times \{ \exp[-(\omega(k) + \omega(k_1))(t - t') - \omega(k_2)(t + t' - 2t'')]$$

$$- \exp[-2\omega(k)(t - t') - 2\omega(k_2)(t' - t'')] \}.$$

Inserting integral (B.2) into expression (B.1) and integrating over t' and t'', we find

$$F = \frac{\sigma(k_1)\sigma(k_2)}{2\omega(k)\Omega} \left[\frac{1}{\Omega} + \frac{1}{\omega(k_2)} \right]. \quad (B.3)$$

Analogously, we can obtain

$$\int_{-\infty}^{t} dt' \int_{-\infty}^{t'} dt'' \int_{-\infty}^{t'} d\tau\, G(k; t, t') G(k_2; t', t'')$$

$$\times G(k_1; t, \tau) I(k; t, \tau) I(k_2; t'', \tau) \quad (B.4)$$

$$= \frac{\sigma(k)\sigma(k_2)}{2\omega(k)\Omega} \left[\frac{1}{\Omega} + \frac{1}{2\omega(k_2)} \right],$$

$$\int_{-\infty}^{t} dt' \int_{-\infty}^{t'} dt'' \int_{-\infty}^{t''} d\tau\, G(k; t, t') G(k_2; t', t'')$$

$$\times G(k_2; t, \tau) I(k; t, \tau) I(k_1; t', \tau) = \frac{\sigma(k)\sigma(k_1)}{2\omega(k)\Omega^2}. \quad (B.5)$$

Integration over time in formula (35) gives

$$\int_{-\infty}^{t} d\tau \int_{-\infty}^{\tau} dt' \int_{-\infty}^{\tau} dt''\, G(k; t, \tau)$$

$$\times \int_{-\infty}^{t} d\tau' G(k; t, \tau) G(k_1; \tau, t') G(k_2; \tau, t'')$$

$$\times G(k; t, \tau') I(k_1; t', \tau') I(k_2; t'', \tau')$$

(B.6)

$$= \frac{\sigma(k_1)\sigma(k_2)}{\Omega\omega(k)} \left[\frac{1}{\Omega^2} + \frac{1}{4\omega(k_1)\omega(k_2)} + \frac{1}{4\Omega}\left(\frac{1}{\omega(k_1)} + \frac{1}{\omega(k_2)}\right) \right],$$

$$\int_{-\infty}^{t} d\tau \int_{-\infty}^{\tau} dt' \int_{-\infty}^{\tau} dt'' G(k; t, \tau)$$

$$\times \int_{-\infty}^{t'} d\tau' G(k; t, \tau) G(k_1; \tau, t') G(k_2; \tau, t'')$$

$$\times G(k_1; t', \tau') I(k; t, \tau') I(k_2; t'', \tau')$$

(B.7)

$$= \frac{\sigma(k)\sigma(k_2)}{\Omega^2\omega(k)} \left[\frac{1}{\Omega} + \frac{1}{4\omega(k_2)} \right],$$

$$\int_{-\infty}^{t} d\tau \int_{-\infty}^{\tau} dt' \int_{-\infty}^{\tau} dt'' G(k; t, \tau)$$

$$\times \int_{-\infty}^{t''} d\tau' G(k; t, \tau) G(k_1; \tau, t') G(k_2; \tau, t'')$$

$$\times G(k_2; t'', \tau') I(k; t, \tau') I(k_1; t', \tau')$$

(B.8)

$$= \frac{\sigma(k)\sigma(k_1)}{\Omega^2\omega(k)} \left[\frac{1}{\Omega} + \frac{1}{4\omega(k_1)} \right].$$

Substituting relationships (B.6)–(B.8) into formula (35), we arrive at expression (63).

REFERENCES

1. J. G. Charney, J. Mar. Res. **14**, 477 (1955).
2. A. Hasegawa and K. Mima, Phys. Fluids **21**, 87 (1978).
3. A. V. Gruzinov, P. H. Diamond, and V. B. Lebedev, Phys. Plasmas **1**, 3148 (1994).
4. A. V. Chechkin, M. I. Kopp, V. V. Yanovsky, and A. V. Tur, Zh. Éksp. Teor. Fiz. **113**, 646 (1998) [JETP **86**, 357 (1998)].
5. F. Wagner, G. Becker, K. Behringer, *et al.*, Phys. Rev. Lett. **49**, 1408 (1990).
6. R. J. Groebner, Phys. Fluids B **5**, 2343 (1993).
7. P. C. Liewer, Nucl. Fusion **25**, 543 (1985).
8. S. I. Vainstein, Ya. B. Zel'dovich, and A. A. Ruzmaikin, *Turbulent Dynamo in Astrophysics* (Nauka, Moscow, 1980), p. 208.
9. H. K. Moffat, *Magnetic Field Generation in Electrically Conducting Fluids* (Cambridge Univ. Press, Cambridge, 1978; Mir, Moscow, 1980).
10. D. Montgomery and T. Hatori, Plasma Phys. Controlled Fusion **26**, 717 (1984).
11. A. Yoshizawa, J. Phys. Soc. Jpn. **46**, 669 (1979).
12. R. H. Kraichnan, J. Fluid Mech. **5**, 497 (1959).
13. R. H. Kraichnan, Phys. Fluids **6**, 1603 (1963).
14. J. A. Krommes, in *Basic Plasma Physics*, Ed. by A. A. Galeev and R. N. Sudan (Énergoatomizdat, Moscow, 1984; North-Holland, Amsterdam, 1984), Vol. 2.
15. E. Buckingham, Phys. Rev. **4**, 345 (1914).

Translated by I. A. Kalabalyk

High-Current Plasma Channel Produced with a Narrow Gas Column

V. F. Basmanov, G. V. Karpov, B. I. Model', S. T. Nazarenko, V. A. Savchenko, A. N. Subbotin, A. S. Fedotkin, and F. G. Shalata

*All-Russia Research Institute of Experimental Physics, Russian Federal Nuclear Center, Sarov,
Nizhni Novgorod oblast, 607188 Russia*
Received January 25, 2001; in final form, April 1, 2001

Abstract—A new method for creating high-current plasma channels is developed. The method uses a narrow gas column formed by the leading particles of a nonsteady gas jet outflowing into a vacuum. An electric discharge device with a system for the formation of a narrow gas column is experimentally studied. The parameters of emission from the plasma channel are measured. © *2001 MAIK "Nauka/Interperiodica"*.

1. INTRODUCTION

The development of the methods for generating current pulses with an amplitude of 10 MA and a rise time of ~100 ns [1] motivated considerable interest in the problem of producing self-contracted plasma channels (such as high-temperature Z-pinches) [2]. Among the methods for solving this problem, we mention the following: (i) the use of multiwire metal arrays [3–5], (ii) pulsed gas puffing [6–8], and (iii) the electric explosion of a frozen deuterium fiber [9] or deuterium-containing fiber [10]. The latter method is of special importance in thermonuclear fusion research because it enables one to obtain high energy densities in a stable channel with an anomalously long lifetime [9]. Probably, this channel would be even more stable if there were no instabilities leading to the formation of waists, which, according to calculations [11], start to develop well before the evaporation of the frozen deuterium is completed. The studies of the electric explosion of a hydrocarbon fiber with a preformed neck [12] provide indirect evidence in favor of this assumption. Hence, it is of interest to change the initial conditions so as to achieve higher stability of the channel. An appropriate method for solving this problem is to use a strongly nonisothermal plasma ($T_e \gg T_i$) produced from the initial gas channel under conditions such that the ion heating is slower than the electron Joule heating.

Let us assume that, instead of a frozen deuterium fiber, we have a narrow uniform gas column. In a discharge, the released Joule energy is spent mainly on electron heating. Due to the high thermal conductivity, the electron temperature rapidly equalizes throughout the channel cross section. Hence, if the current increases rapidly and the initial diameter of the gas column is small enough, then the magnetic pressure can only be balanced by the electron thermal pressure. The ions remain cold and immobile until they are heated via either collisional or collisionless mechanisms. Colli-

sionless heating requires high electron current velocity (at least higher than the ion acoustic speed). However, in a self-contracted channel with a high electron density n_e, the electron current velocity may remain lower than the ion acoustic speed. Thus, in a channel whose radius is comparable to the skin depth, the electron current velocity will always be less than the ion acoustic speed if the electron linear density N_e exceeds a certain critical value, $N_e > N_0 = 2m_i c^2 e^{-2}$. In particular, in a 1-mm-diameter deuterium channel with the electron density $n_e = 10^{19}$ cm^{-3} ($N_e = 8 \times 10^{16}$ cm^{-1}, $N_0 = 2.6 \times 10^{16}$ cm^{-1}), the electron current velocity is approximately two times lower than the ion acoustic speed. In this case, collisional heating is the only mechanism for ion heating; its rate can be estimated by the time of heat exchange between the plasma components, $\tau = 17 A T_e^{3/2} n^{-1}$ [13]. In a deuterium channel ($A = 2$) at a temperature of $T_e = 10^7$ K, we have $\tau > 100$ ns. Hence, if the current rise time is on the order of 100 ns, we can expect that T_e will grow faster than the ion temperature, which results in the higher stability of the channel. The necessary condition for this is a rapid (in the limiting case, synchronous with the magnetic pressure at the channel boundary) increase in the electron thermal pressure at the channel axis. Otherwise, the radial charge separation field inevitably arises, in which the ions can be accelerated toward the axis up to high energies. The only way to exclude or diminish the radial plasma implosion is to decrease the initial diameter of the gas column. The question as to which parameters of the gas column are achievable still remains open because nobody has yet dealt with the problem of completely excluding radial plasma implosion in gas puffs.

In this study, a new method for creating a narrow gas column is developed. An electric discharge device in which the plasma channel is produced using such a column is experimentally studied.

2. FORMATION OF A NARROW GAS COLUMN

When a gas that was initially at rest expands through a long channel into a vacuum, the longitudinal velocity of the leading portion of the gas flow is several times higher than the speed of sound in an unperturbed gas and the gas temperature here is nearly zero [14]. Therefore, after escaping from the channel into free space, the leading gas particles have high longitudinal and low transverse velocities, thus forming a gas jet with an extremely low divergence. If the channel is sufficiently narrow, the jet has the shape of a column whose diameter is much less than its length. The schematic of a gas-dynamic gas puff experiment based on the above consideration is shown in Fig. 1. The gas is separated from the vacuum by an aluminum foil 15 μm thick. The foil is broken by an electric discharge in a time $\Delta t \sim 1$ μs, which is much shorter than the time t_s it takes for the leading particles to pass along the channel length l_0: $\Delta t \ll t_s$. By virtue of this inequality, the gas flow is nonsteady, which distinguishes our device from gas puff systems used in high-current plasma facilities [6–8]. The maximum initial gas pressure is less than 1 atm, which is determined by the foil breaking strength. The instant at which the gas appears at the channel exit, $t = t_s$ is indicated by the electric breakdown of an auxiliary spark gap. The time t_s depends on the gas species, initial pressure, channel length, etc.; under our conditions, it is on the order of 100 μs.

In experiments, we encountered the problem of the visualization of the gas jet. Attempts to visualize the gas jet using laser techniques failed because of the low gas density and the small radius of the jet. Visualization with the help of a short low-current discharge along the flow did not provide the required image contrast. It was found that nitrogen, atmospheric air, and, particularly, oxygen jets are self-luminous; this property was employed for the jet visualization. The glow starts at $t = t_s$ and lasts for several tens of microseconds. The high-speed photography reveals no appreciable radial shift in the boundary of the glow region. The shape of the glowing gas column is adequately displayed by the time-integrated photographs. Figure 2 shows the time-integrated photograph obtained with atmospheric air puffing. It can be seen that the column diameter is nearly constant and coincides with the channel diameter, which is equal to 3 mm. The glow is the most intense and contrasted at the channel outlet. Downstream from the outlet, the glow intensity decreases and the radial boundary of the column becomes smeared. Perhaps, this is related to the axial inhomogeneity of the gas density in the column, which, in turn, is due to the highly nonuniform distribution of the gas density in the channel. It was found theoretically [14] that, in a nonsteady gas flow escaping into a vacuum through a long channel, the speed of sound is equal to $c_s = 0$ at the flow front and increases linearly along the channel as it approaches the unperturbed gas. The gas density n also
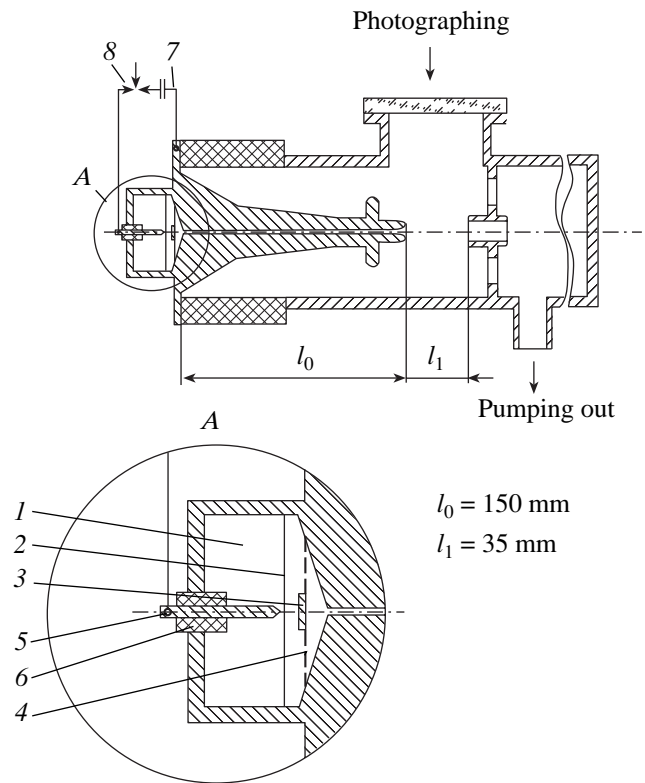
Fig. 1. Schematic of the narrow gas column formation: (1) gas volume ($V \approx 10$ cm³), (2) 15-μm-thick Al foil, (3) 0.5-mm-thick Ta disk 10 mm in diameter, (4) stainless steel grid, (5) needle electrode, (6) insulator, (7) capacitor ($C = 0.8$ μF, $U = 30$ kV), and (8) controlled discharge gap.

$l_0 = 150$ mm

$l_1 = 35$ mm
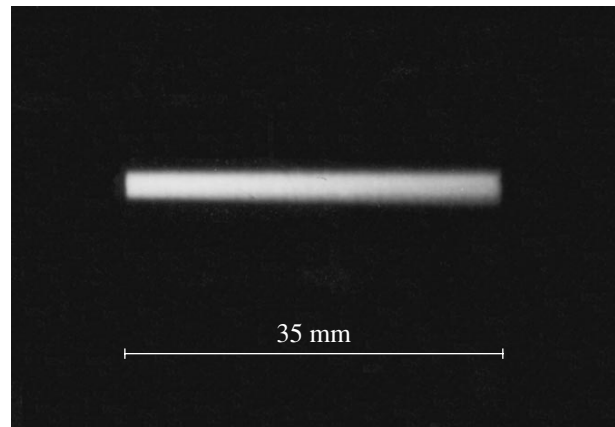
Fig. 2. Photograph of the glowing atmospheric air column.

varies strongly along the channel. Thus, for a diatomic gas, we have $n \sim c_s^5$.

The detailed diagnostics of the column are still difficult to perform. Nevertheless, the results obtained

enabled us to carry out plasma experiments with a narrow gas column and to plan subsequent steps in improving the system for gas puffing. These future improvements include (i) a decrease in the axial non-uniformity of the column by increasing the ratio of the channel length l_0 to the column length l_1; (ii) the use of much higher initial pressures and, consequently, gas densities in the column; and (iii) a decrease in the diameters of the channel and gas column to less than 1 mm.

3. EXPERIMENTAL SETUP

The plasma experiments were carried out in an experimental stand (Fig. 3) with a capacitive energy storage of 24 kJ at a charge voltage of 100 kV. The storage bank consists of twelve IK-100-04 capacitors connected in parallel; each of them is triggered by its own gas-filled discharge gap. The capacitors and gaps are placed in a metal tank filled with transformer oil. The discharge chamber is mounted on the tank lid and is connected to the energy storage bank via a low-inductance cable line. In the chamber, there are two electrodes: a high-voltage anode and a grounded cathode. The distance between the electrodes along the chamber axis is $l_1 = 35$ mm. The discharge chamber is preevacuated to 10^{-4} torr. The gas is injected into the chamber through the anode along a central channel with a diameter of 3 mm and length of $l_0 = 15$ cm. The foil separating the working gas from the vacuum chamber is broken by the electric discharge of two IK-100-04 capacitors connected in parallel and charged to 30 kV. The delay time t_c of triggering the energy storage bank with respect to triggering the controlled discharge gap in the foil-break circuit (Fig. 1) is regulated with an accuracy no worse than 0.1 μs. The working gas was alternatively deuterium, helium, nitrogen, oxygen, atmo-

spheric air, neon, argon, or xenon. The initial gas pressure was less than 1 atm.

X-ray emission was measured using spectrometers with silicon semiconductor detectors equipped with various absorbing filters. The signals from seven detectors placed inside the discharge chamber near its axis at a distance of ~60 cm from the anode were recorded simultaneously. X radiation fell onto the detectors through a central 8-mm-diameter hole in the cathode. We alternatively used spectrometers designed for measuring either soft (up to 10 keV) or hard (higher than 10 keV) X radiation. In each of these spectrometers, one of the channels was the same to ensure the matching of the measurements in the soft and hard X-ray spectral ranges. Soft X radiation was measured with SPPD-11 silicon detectors designed at the Research Institute of Pulsed Technologies (Moscow). A characteristic feature of these detectors is the small thickness of both the entrance window (the total thickness of the electrical contact and dead layer is less than 1 μm) and the sensitive region (~50 μm). Hard X radiation was measured with silicon detectors based on sensitive elements designed at the Research Institute of Pulsed Technologies. The spectral sensitivity of the detectors was calculated using the Monte Carlo method with allowance for the transport of γ radiation, electrons, and positrons [15]. To attenuate the recorded radiation, each detector was equipped with its own aperture diaphragm with diameters of 2 to 9 mm. The time resolution of the different detectors varied from 1.5 to 20 ns. An assembly of the thermoluminescent dosimeters made of 0.2- and 1-mm-thick IS-7 glass plates [16] were used to measure the integral dose and to estimate the effective energy of X-ray photons. A stack of five to ten glass plates was placed in a hollow Al cylinder with a 5-mm-thick wall and was oriented so as to ensure the nearly normal incidence of radiation. From the source side, the glass plates were covered with a mylar film either with or without aluminum deposition. The opposite end of the cylinder was closed with a 5-mm-thick Al cap. After being irradiated, the glass plates were tested with a standard IKS-A dosimeter. The location of the X-ray source was determined from X-ray photos obtained using several pinhole cameras with different absorbing filters. The signals from several semiconductor detectors that simultaneously recorded X-ray emission from different regions of the interelectrode gap were also used for this purpose. Both the hard X radiation with the photon energy above 100 keV and the neutron flux were recorded with an SSDI-8 detector [17] consisting of a plastic scintillator block with a photomultiplier. The time resolution of the detector was ~5 ns. To distinguish between the neutron and X-ray pulses, several detectors were set at different distances from the discharge chamber. The integral neutron yield was determined by the activation of an Ag foil placed in a paraffin moderator. In all discharges, the plasma channel current was recorded with a time resolution no worse than 10 ns.
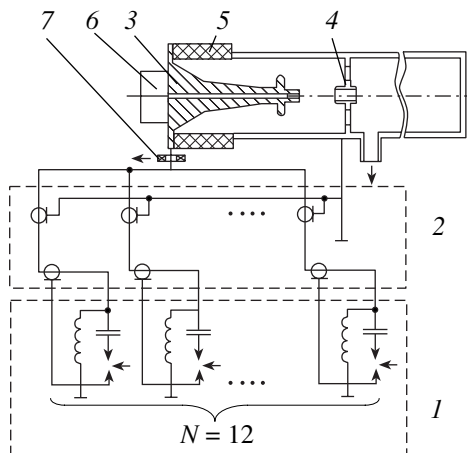
Fig. 3. Schematic of the experimental facility: (*1*) capacitive energy storage, (*2*) feed cable line, (*3*) anode, (*4*) cathode, (*5*) insulator, (*6*) pulsed valve, and (*7*) current detector.

4. EXPERIMENTAL RESULTS

The electric breakdown of the gas column leads to the formation of a plasma current channel with a current rise time of several hundred nanoseconds. Due to the plasma processes in the channel, its resistance sharply increases. As a result, in the current oscillogram, the increase in the current is finished with a singularity in the shape of a kink. The current singularity, which is observed in all of the gases, is accompanied by an X-ray burst. For light gases, the burst duration is ~50 ns; for deuterium, neutron emission with an integral yield of 10^8 neutrons per pulse is also recorded.

Figure 4 shows the waveforms of the current and the signals from the SSDI-8 detector for helium at an initial pressure of 1 atm. The maximum current in the channel depends on the initial gas pressure and the delay time t_c of the triggering of the energy storage bank. As t_c and the gas pressure increase, the time during which the current grows also increases; as a result, the current attains a higher value before the singularity occurs. It can be seen in Fig. 4 that the increase in t_c by 5 μs increases the discharge current by a factor larger than 1.5. The further increase in t_c provides a severalfold increase in the current by the instant of the kink; however, in this case, the reproducibility of the radiation parameters substantially decreases.

Semiconductor detector measurements show that the shortest X-ray pulses are generated when light gases are used. A comparison of the detector signals obtained in the different spectral ranges during one discharge reveals the following feature characteristic of all the gases. Namely, the X-ray pulses show a double-humped shape which is most pronounced in the hard X-ray spectral range. The signals from the detectors recording X-ray photons with a lower energy also demonstrate the double-humped shape, but it is less pronounced. As the photon energy decreases, the signal maxima merge into one maximum. Such behavior was observed throughout the entire spectral range that was studied with semiconductor detectors, i.e., in the 1- to 100-keV spectral range.

Figure 5 shows the waveforms of double-humped X-ray pulses recorded in air and helium plasma channels. We chose the most representative waveforms with sufficiently long time intervals between the maxima in order to reliably resolve them in time. The semiconductor detectors were also used to locate the X-ray source; for this purpose, several identical detectors recorded the emission from different regions of the plasma channel. It is found that the main fraction of radiation with a photon energy of ~10 keV and higher is generated near the anode edge. When a cap was put on the anode, the X-ray source was located at the cap edge, which was in contact with the plasma. This is also confirmed by X-ray photographs of the radiating region. In experiments, we used thin lead caps with a wall thickness of ~0.05 mm, which were evaporated during a single pulse. Figure 6 shows the schematic of pinhole mea-
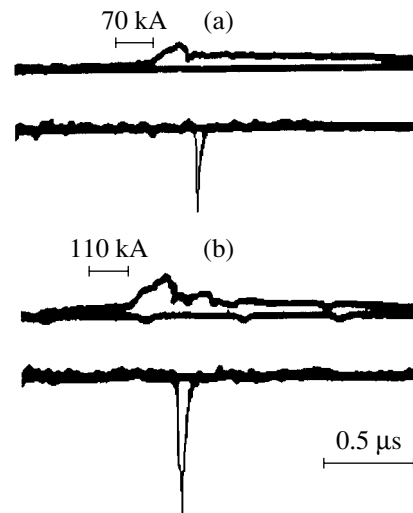

Fig. 4. Waveforms of the current and the signals from an SSDI-8 detector for different delay times t_c of triggering the capacitive storage: (a) 90 and (b) 95 μs; the working gas is helium at an initial pressure of 1 atm.

surements and pinhole images of the X-ray source obtained in a helium plasma channel with the use of a lead cap. In photo II (Fig. 6b), a metal grid welded into the side window of the discharge chamber casts a shadow on the image of the lead cap emitting X-rays.

The efficiency of the electric discharge X-ray source was estimated based on the dose measured by thermoluminescent dosimeters. The maximum dose recorded behind a 20-μm-thick mylar film with Al deposition (~1 μm) at a distance of 5.5 cm from the source was 3×10^3 rad. The dose of radiation passed through the central hole in the cathode along the chamber axis and measured behind a 20-μm-thick Al foil at a distance of 55 cm from the anode edge was 20 rad. The spectral distribution of the radiant energy was estimated based on the measurements of both the distribution of the absorbed dose in the stack of IS-7 glasses and the signals from semiconductor detectors. Nearly one-half of the energy falls in the photon energy range of up to 10 keV, the spectral intensity being maximum at 3 keV. Almost all of the remaining energy falls in the range 10–60 keV.

When operating with light gases, a short (~20 ns) pulse of extremely hard X-ray radiation is observed. Since this pulse can be recorded (with the SSDI-8 detector) at a distance of up to 20 m from the source behind a metal shield with a thickness of more than 5 mm, it should contain megaelectronvolt photons.

Finally, it should be noted that, in the plasma channel, a rather intense axial plasma flow is produced, which extends beyond the interelectrode gap through the central hole in the cathode. The presence of the plasma flow is indicated by the destruction of the films and foils placed on the axis behind the discharge gap. The flow divergence, which was determined from the
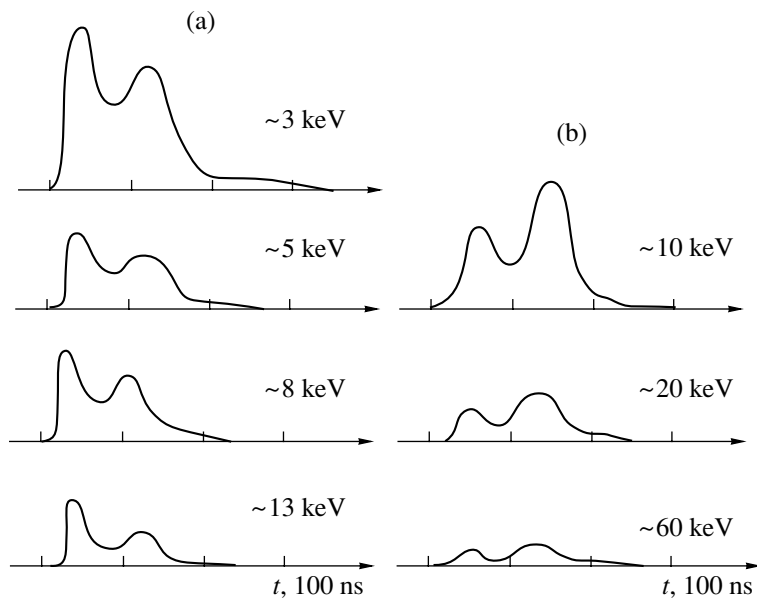
Fig. 5. Double-humped X-ray pulses recorded in different photon energy ranges in (a) an air plasma channel and (b) a helium plasma channel.
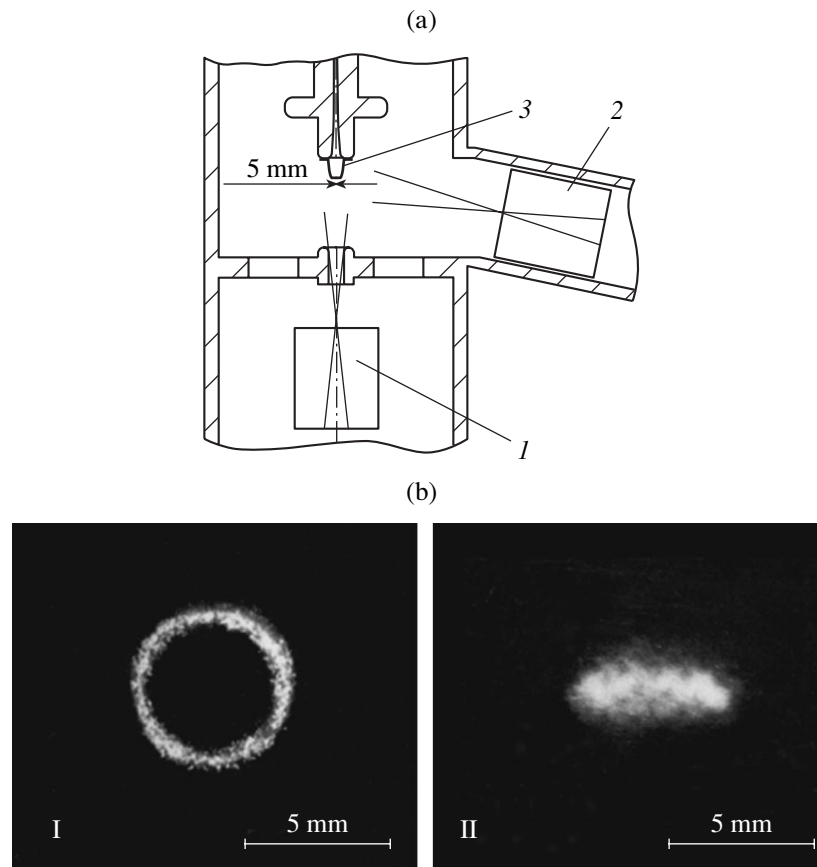
Fig. 6. (a) Schematic of pinhole measurements: (*1*) pinhole camera I, (*2*) pinhole camera II, and (*3*) lead cap. (b) Pinhole images of the X-ray source.

flow imprints, was about one degree for deuterium or helium. The maximum flow velocity, which was estimated by the instant of the flow appearance at a distance of ~50 cm behind the cathode flange, was equal to ~10^8 cm/s.

5. CONCLUSION

A new method for creating a plasma current channel has been developed. For this purpose, a 35-mm-long 3-mm-diameter gas column formed by the leading particles of a nonsteady gas jet outflowing into a vacuum is used. For all the gases under study (deuterium, helium, nitrogen, oxygen, atmospheric air, neon, argon, and xenon), the waveforms of the current in the channel resemble those in Z-pinches [2]. The increase in the current is finished with a singularity in the shape of a kink. The stable operation of the plasma channel lasts for several hundred nanoseconds until the singularity occurs; this time is longer than the duration of a stable plasma channel in experiments with a frozen deuterium fiber [9]. The current singularity is accompanied by an X-ray burst; for deuterium, neutron emission with an integral yield of 10^8 neutrons per pulse is also recorded. The instant of the singularity can be controlled by either changing the initial pressure of the working gas or varying the delay time of applying the high-voltage pulse to the gas column. The highest yield of X radiation, which lasts for ~50 ns, is attained with light gases. A significant fraction of radiation falls into the 10–60 keV photon energy range. The X-ray source is located near the anode edge. The maximum dose measured at a distance of 5.5 cm from the anode is 3 krad. At the instant of the current singularity, the axial plasma flow directed away from the anode is generated in the channel; its velocity attains 10^8 cm/s.

In order to further develop the proposed method for creating the current plasma channel and perform experiments with currents as high as 1 MA, a system for gas puffing with a 2–3 orders of magnitude higher initial gas pressure must be designed. These experiments will make it possible to draw the final conclusion about the influence of the initial discharge conditions on the stability of the plasma channel.

REFERENCES

1. J. J. Ramírez, IEEE Trans. Plasma Sci. **25**, 155 (1997).
2. V. A. Burtsev, V. A. Gribkov, and T. I. Filippova, Itogi Nauki Tekh., Ser. Fiz. Plazmy **2**, 80 (1981).
3. W. Clark, M. Gersten, J. Katzenstein, *et al.*, J. Appl. Phys. **53**, 4099 (1982).
4. C. Deeney, T. J. Nash, R. B. Spielman, *et al.*, Phys. Rev. E **56**, 5945 (1997).
5. T. W. L. Sanford, T. J. Nash, R. C. Mock, *et al.*, Phys. Plasmas **4**, 2188 (1997).
6. J. Shiloh, A. Fisher, and N. Rostoker, Phys. Rev. Lett. **40**, 515 (1978).
7. W. Clark, R. Richardson, J. Brannon, *et al.*, J. Appl. Phys. **53**, 5552 (1982).
8. A. V. Batyunin, A. N. Bulatov, V. D. Vikharev, *et al.*, Fiz. Plazmy **16**, 1027 (1990) [Sov. J. Plasma Phys. **16**, 597 (1990)].
9. J. D. Sethian, A. E. Robson, K. A. Gerber, and A. W. De Silva, Phys. Rev. Lett. **59**, 892 (1987).
10. W. Kies, G. Decker, M. Mälzig, *et al.*, J. Appl. Phys. **70**, 7261 (1991).
11. I. R. Lindemuth, Phys. Rev. Lett. **65**, 179 (1990).
12. L. E. Aranchuk, S. A. Dan'ko, A. V. Kopchikov, *et al.*, Fiz. Plazmy **23**, 215 (1997) [Plasma Phys. Rep. **23**, 194 (1997)].
13. L. A. Artsimovich, *Controlled Thermonuclear Reactions*, Ed. by A. Kolb and R. S. Pease (Fizmatgiz, Moscow, 1961; Gordon and Breach, New York, 1964).
14. K. P. Stanyukovich, *Nonsteady Motions of Continuous Media* (Gostekhteorizdat, Moscow, 1955), p. 154.
15. E. N. Donskoĭ, Vopr. At. Nauki Tekh., Ser. Mat. Model. Fiz. Protsessov, No. 1, 3 (1993).
16. I. A. Bochvar, T. I. Gimadova, I. B. Keirim-Markus, *et al.*, *Methods of Individual-Control-Glass Dosimetry* (Atomizdat, Moscow, 1977), p. 65.
17. A. I. Veretennikov and K. N. Danilenko, *Diagnostics of Single-Pulse Radiation* (AT, Moscow, 1999), p. 45.

Translated by N. N. Ustinovskiĭ

Calculation of One-Dimensional Plasma Flows with Allowance for the Kinetics of Ion Collisions

P. D. Gasparyan and N. V. Ivanov

All-Russia Research Institute of Experimental Physics, Russian Federal Nuclear Center,
Sarov, Nizhni Novgorod oblast, 607190 Russia

Received November 13, 2000

Abstract—The influence of kinetic effects on the generation of line X radiation during the spherical implosion of a laser corona plasma with two ion species is studied under the conditions prevailing in experiments with thin-wall spherical targets in the Iskra-5 laser facility of the All-Russia Research Institute of Experimental Physics (Sarov, Russia). Kinetic processes occurring in a multicharged plasma are investigated using a specially devised code for solving one-dimensional Landau equations for a nondegenerate multicomponent plasma by the Monte Carlo method (the KIN-MC code). The code was developed using the quasineutral plasma approximation under the assumption that the electron distribution function is locally equilibrium. The model equations are presented, the scheme of numerical solution is described, and the calculated results are discussed. © 2001 MAIK "Nauka/Interperiodica".

1. INTRODUCTION

The development of the theory of nonequilibrium processes in high-temperature multicharged plasmas is motivated by diverse practical and theoretical applications. Such plasmas are created by the interaction of ultrashort laser pulses with solid bodies and other objects in experiments aimed at investigating various targets used in laser fusion, inertial confinement fusion (ICF), and laboratory X-ray lasers [1–3].

In particular, in experiments on the laser irradiation of targets, it is of considerable interest to study the interaction of counterstreaming flows of a laser corona plasma, because, in the interaction region, the temperature and density of the plasma and its lifetime can increase substantially. This makes it possible to significantly extend laboratory experiments to such issues of high-temperature plasma physics as (i) the emissivity of a multicharged plasma, (ii) the capability of a plasma to decelerate fast ion beams, and (iii) reaction rates in a plasma.

The interaction of counterstreaming flows of a laser corona plasma can be studied in experiments with various types of one-dimensional and two-dimensional laser targets irradiated by laser light in different ways (see, e.g., [4–11] and other related papers). Estimates show that, in the region where the flows of a laser corona plasma interact with each other, it is easy to achieve conditions under which the mean free paths of multicharged plasma ions are comparable to or even larger than the characteristic dimensions of the flows. Under these conditions, the gas-dynamic approximation, which is usually used to calculate the plasma parameters and to analyze them theoretically, may turn out to be inaccurate; consequently, the physical processes in the region where the plasma flows interact should be studied using numerical methods based on kinetic plasma models [7–10].

Note that the plasma-related kinetic problems are too complicated to be investigated numerically in full formulation, i.e., to simultaneously solve nonlinear Boltzmann equations for all subsystems of particles in the plasma (photons, electrons, and ions) even in a one-dimensional approximation. For this reason, we will apply an approach based on the solution of simplified physical problems.

Here, we study the violation of the gas-dynamic approximation in the model of a nondegenerate plasma with constant ion charge. The ion plasma component is described by the kinetic equation with the Landau collision integral. The electron plasma component is assumed to be equilibrium and to obey a locally Maxwellian velocity distribution function. We use the quasineutral plasma approximation and neglect electron inertia. An analogous model of the nonequilibrium plasma dynamics was applied in [7, 8] when studying the role of kinetic effects in the dynamics of laser fusion targets. In our approach, the kinetic equations reduce to a set of the modified nonlinear Landau kinetic equations for ion plasma components and the electron energy balance equation. In the combined method developed for solving this set of equations numerically, the kinetic equations are solved by the Monte Carlo (MC) method and the energy balance equation is solved in finite differences. The combined method was implemented as the one-dimensional KIN-MC code.

When solving the nonlinear Boltzmann equations in finite differences, the plasma flows are especially difficult to calculate for ions with short mean free paths. The method developed here is based on the MC method

for solving kinetic equations and requires approximately the same amounts of computational resources for ions with short and long mean free paths. The proposed approach can also be applied to solving more complicated problems, including those in which account should be taken of, e.g., the nonequilibrium nature of plasma electrons, the kinetics of fusion reaction, the non-Maxwellian character of ion distribution functions, and ion diffusion in a multicomponent plasma. For problems in kinetic formulation, the results of calculations of the dynamics of a simple plasma can be used to analyze the accuracy of some other approximations applied in the numerical modeling of the plasma processes, e.g., the multistream gas-dynamic plasma approximation [7, 12].

The physical formulation of the dynamic plasma problems under consideration and the model equations are presented in Section 2. The numerical method and the potentialities of the KIN-MC code are described in the Appendix, in which we also illustrate the results from test simulations of plasma flows in planar geometry (the problem of the interaction of unloading waves). In Section 3, we discuss numerical results obtained with the KIN-MC code when simulating the implosion of a laser corona plasma in experiments with thin-wall spherical targets with an internal input of the laser energy [11, 13]. We analyze how the collisional kinetics of the ions manifests itself in the spherical implosion of a laser corona. We numerically investigate the influence of kinetic effects on the resonant X-ray emission of the He_α-line of Fe ions (the Fe He_α-line) in a nonequilibrium high-temperature multicharged plasma under the conditions prevailing in experiments with thin-wall spherical targets in the Iskra-5 laser facility of the All-Russia Research Institute of Experimental Physics (Sarov, Russia).

2. PROBLEM FORMULATION AND MODEL EQUATIONS

We consider an ideal two-component plasma in which the ions of different species have a constant charge. In planar geometry, the Landau–Vlasov kinetic equations for the ion distribution function $f_i(t, x, v)$ in the absence of a magnetic field have the form [14, 15]

$$\frac{\partial f_i}{\partial t} + v_1 \frac{\partial f_i}{\partial x} + \frac{eZ_iE}{m_i}\frac{\partial f_i}{\partial v_1} = \sum_{j=1}^{2} J_{ij} + J_{ie}; \qquad (1)$$

where $E(t, x)$ is the electric field and the integrals J_{ii} and J_{ie} describe ion–ion and ion–electron Coulomb collisions, respectively. The Landau collision integrals accounting for ion–ion collisions are represented as

$$J_{ij} = \frac{m_{ij}^2}{m_i}\frac{\partial}{\partial v_k}\int\frac{A_{kl}^{ij}}{2}\left[\frac{f_j(\mathbf{c})}{m_i}\frac{\partial f_i(\mathbf{v})}{\partial v_l} - \frac{f_i(\mathbf{v})}{m_j}\frac{\partial f_j(\mathbf{c})}{\partial u_l}\right]d\mathbf{c}, (2)$$

where $m_{ij} = \dfrac{m_im_j}{m_i + m_j}$ is the reduced mass, $A_{kl}^{ij} = \dfrac{4\pi e^4 Z_i^2 Z_j^2 \Lambda_{ij}}{m_{ij}^2 g^3}(g^2\delta_{kl} - g_kg_l)$ is the diffusion tensor, $\mathbf{g} = \mathbf{v} - \mathbf{c}$ is the relative velocity, and Λ_{ij} are Coulomb logarithms for ion–ion collisions.

Using the approximation of a small electron-to-ion mass ratio m_e/m_i and assuming that the electrons obey a Maxwellian distribution function with a shifted argument, we can write the ion–electron collision integral as [14]

$$J_{ie} = \nu_{ie}\left[\frac{T_e}{m_e}\Delta f_i + \frac{m_i}{m_e}\frac{\partial}{\partial \mathbf{v}}(\mathbf{v} - \mathbf{u}_e)f_i\right]; \qquad (3)$$

where $\mathbf{u}_e = (u_e, 0, 0)$ is the mean electron velocity vector, $\nu_{ie} = \dfrac{4\sqrt{2\pi}}{3}\dfrac{e^4 Z_i^2 L_{ei}n_e}{m_i^2}\left(\dfrac{m_e}{T_e}\right)^{3/2}$ is the ion–electron collision frequency, and Λ_{ie} are Coulomb logarithms for ion–electron collisions. Note that expression (3) can easily be generalized to arbitrary electron distribution functions, in particular, the bi-Maxwellian distribution functions [16] used to describe fast electrons in the two-component diffusion approximation or even more general nonequilibrium electron distribution functions used in nonlocal extensions of plasma gas-dynamic theories [17, 18]. In such generalizations, the coefficients in front of the diffusion term and the term with a shifted argument in the ion–electron collision integral in expression (3) should be changed.

We assume that the electron distribution function is locally equilibrium. This allows us to apply the kinetic description solely to the ion plasma component. We also assume that the electrons obey a Maxwellian function described by the number density $n_e(t, x)$, mean velocity $u_e(t, x)$, and temperature $T_e(t, x)$, which is determined from the electron energy balance equation

$$\frac{\partial}{\partial t}(n_eT_e) + \frac{\partial}{\partial x}(u_en_eT_e)$$
$$= -\frac{2}{3}n_eT_e\frac{\partial u_e}{\partial x} + \frac{\partial}{\partial x}\lambda_e\frac{\partial T_e}{\partial x} + 2\sum_{i=1}^{2}\frac{m_i}{m_e}\nu_{ie}n_i(T_i - T_e) + Q, \qquad (4)$$

where λ_e is the electron thermal diffusivity, ν_{ie} is the ion–electron collision frequency, and the term Q describes an additional electron energy source.

Below, we restrict ourselves to considering a currentless plasma, which corresponds to quasineutral plasma motions. The conditions for the two-component plasma to be quasineutral and to carry no current have the form

$$n_e = Z_1n_1 + Z_2n_2, \qquad (5)$$

$$n_eu_e = Z_1n_1u_1 + Z_2n_2u_2; \qquad (6)$$

where Z_i, n_i, and u_i are the charges, densities, and mean velocities of the ions.

To describe the plasma flows completely, we are left with the problem of determining the electric field $E(t, x)$. We consider the following electron momentum transport equation with allowance for the ion plasma component:

$$m_e\left(\frac{\partial u_e}{\partial t} + u_e\frac{\partial u_e}{\partial x}\right) = -\frac{1}{n_e}\frac{\partial P_e}{\partial x} + eE + m_e(R_{e1} + R_{e2}); \quad (7)$$

where $P_e = n_e T_e$ is the electron pressure and $R_{ei} = \nu_{ei}(u_i - u_e)$ is the deceleration force exerted on the electrons by the ions. The electron–ion collision frequency ν_{ei} can be reduced to the form

$$\nu_{ei} = \frac{4\sqrt{2\pi}}{3}\frac{e^4 Z_i^2 L_{ei} n_i}{m_e^2}\left(\frac{m_e}{T_e}\right)^{3/2}, \quad (8)$$

in which we took into account the smallness of the electron mass. We force m_e in Eq. (7) to zero and retain the terms proportional to $\sqrt{m_e}$ to arrive at the following expression for the electric field:

$$E = \frac{1}{en_e}\frac{\partial P_e}{\partial x} - m_e(R_{e1} + R_{e2}). \quad (9)$$

Equations (1) and (4) and expression (9) provide a complete mathematical description of the plasma flows under consideration. Note that, in Eqs. (1), the collision integrals (3) are written in a frame of reference moving with velocity u_e. However, for the numerical solution of the problem, it is convenient to transform them to a frame moving with the mean ion velocity u_i. In the latter frame, the expression $\frac{eZ_i}{m_i}E\frac{\partial f_i}{\partial v_1} - \nu_{ie}\frac{m_i}{m_e}\frac{\partial}{\partial \mathbf{v}}(\mathbf{v} - \mathbf{u}_e)f_i$ becomes

$$F_i\frac{\partial f_i}{\partial v_1} - \nu_{ie}\frac{m_i}{m_e}\frac{\partial}{\partial \mathbf{v}}(\mathbf{v} - \mathbf{u}_i)f_i,$$

where

$$F_i = -\frac{eZ_1}{m_1 n_e}\frac{\partial P_e}{\partial x} + \nu_{1u}(u_2 - u_1),$$

$$F_2 = -\frac{Z_2}{m_2 n_e}\frac{\partial P_e}{\partial x} - \nu_{2u}(u_2 - u_1),$$

$$\nu_{iu} = \frac{4\sqrt{2\pi}e^4 Z_1^2 Z_2^2}{3m_e^2}\frac{L_{e2}n_1 + L_{e1}n_2}{n_e}\frac{m_e}{m_i}\left(\frac{m_e}{T_e}\right)^{3/2}n_i. \quad (11)$$

Consequently, in the moving frame, the kinetic equations for the ion distribution functions have the form

$$\frac{\partial f_i}{\partial t} + v_1\frac{\partial f_i}{\partial x} + F_i\frac{\partial f_i}{\partial v_1} = \sum_{j=1}^{2}J_{ij} + J_{ie}, \quad (12)$$

where the collision integrals J_{ij} are given by relationships (2) and $J_{ie} = \nu_{ie}\left[\frac{T_e}{m_e}\Delta f_i + \frac{m_i}{m_e}\frac{\partial}{\partial \mathbf{v}}(\mathbf{v} - \mathbf{u}_i)f_i\right]$.

The electron thermal diffusivity in Eqs. (4) is calculated from the interpolation formula [19, 20]

$$\lambda_e = \frac{aT_e^{5/2}}{(Z + 3.44)\Lambda_{ie}}.$$

The Coulomb logarithms are calculated from the expressions

$$\Lambda_{ii} = \max\left\{1, \ln\left(\frac{a_i T}{Z^2}\sqrt{\frac{TT_e}{n_e(T + ZT_e)}}\right)\right\},$$

$$\Lambda_{ie} = \max\left\{1, \ln\left(a_e T_e\sqrt{\frac{T_e}{n_e(T + ZT_e)}}\right)\right\};$$

where a, a_i, and a_e are constants.

The method for the numerical solution of the set of kinetic equations (4) and (12) and the results of comparative test numerical calculations are presented in the Appendix.

3. SIMULATIONS OF THE SPHERICAL IMPLOSION OF A LASER CORONA PLASMA

In order to investigate nonequilibrium physical processes that occur during the implosion of a multicharged plasma, Gasparyan et al. [11] considered a thin-wall spherical target (TST), shown schematically in Fig. 1.

A two-layer TST is a substrate plastic thin-wall spherical shell whose inner surface is coated with a thin layer of the material to be investigated. Laser light is fed into the target at an angle to the normal to the target surface through several entrance holes that are, on average, distributed uniformly over the surface. Inside the target, laser light is absorbed by the laser corona plasma. The symmetry of the laser energy absorption inside the target is ensured by such factors as the minimum area of the holes, the focusing of laser light as it passes through the holes, and multiple internal reflections of the light until it is completely absorbed. The thickness of the inner coating was chosen in such a way that the coating material completely evaporates during laser light absorption. The material of the spherical shell is chosen to be transparent to X radiation generated within a TST. When the laser pulse is short, the target goes through two stages: first; the formation of the internal laser corona during laser light absorption and, second, the implosion of a laser corona plasma toward the target center followed by the formation of a shock wave reflected from the center. Gas-dynamic simulations show that it is the second stage in which the plasma temperature is maximum (several times the ini-

tial temperature of the laser corona) and the density of the hot plasma is highest (higher than the critical density of the initial corona by a factor of about 10 to 100). Hard X radiation is generated throughout both of the stages. Since the plasma inside the TST is relatively transparent to X radiation, the overall picture of the physical processes occurring during plasma implosion can be reconstructed from the measurements of the spatial and temporal evolutions of the X-ray spectra, thereby providing an interesting diagnostic tool for studying radiational and collisional kinetics of the plasma.

The parameters of a TST and X-ray spectra were calculated using the CC-9 code [21] based on a non-equilibrium radiative gas-dynamic model in which the radiative–collisional kinetics of the ion level populations was described either by a chemical approach [21] or by using the mean ion approximation [22, 23]. For the conditions of experiments carried out in the Iskra-5 laser facility with Fe-coated TSTs [6], ideal spherically symmetric simulations showed that the maximum plasma density at the target center amounted to 0.1–0.2 g/cm^3, the plasma temperature being about 3 keV.

The related experiments with Fe-coated TSTs in the Iskra-5 device were carried out in 1997 [13]. The TSTs were made of substrate spherical CH shells with the radius $R_{CH} = 1$ mm and thickness $\Delta_{CH} = 5$ μm ($\rho\Delta_{CH} = 5 \times 10^{-4}$ g/cm^2). The thickness of Fe coatings on the inner surfaces of the TSTs was about $\Delta_{Fe} \sim 0.26$ μm ($\rho\Delta_{Fe} = 2 \times 10^{-4}$ g/cm^2). The plasma inside the TSTs was created by light pulses with a total energy of about 7 kJ and duration $\tau_{0.5} \sim 0.3$–0.4 ns from an iodine laser operating at the fundamental frequency ($\lambda = 1.315$ μm). The total area of six holes for launching laser light into a TST was about 7% of the total area of the target surface. The results from measurements of the integral spectra of X-ray photons in the energy range $\nu > 6$ keV and of the spatial region where X radiation was generated in the experiments were found to differ strongly from the related numerical results obtained with the CC-9 code. As an example, the calculated diameter of the region of resonant X-ray emission of the Fe He$_\alpha$-line ($\nu \sim 6.8$ keV) was about $D_{calc} \sim 300$ μm, while the measured diameter was substantially larger, $D_{exp} \sim 450$–500 μm. One possible reason for such a large discrepancy between the theoretical and experimental results is that the gas-dynamic approximation may fail to describe the spherical implosion of the plasma in the TST [13]. In fact, estimates show that, by virtue of the strong velocity dependence of the ion mean free paths ($\sigma_{ii} \sim Z^4/v^{-4}$) and the low density of a laser corona plasma, the ion mean free paths in the interaction of the counterstreaming ion flows in the central region are comparable with the initial dimensions of the target, in which case the gas-dynamic description of the implosion stage in a TST may be inexact. In order to estimate the accuracy of the gas-dynamic approximation and to analyze how the kinetics of ion–ion collisions affects the resonant
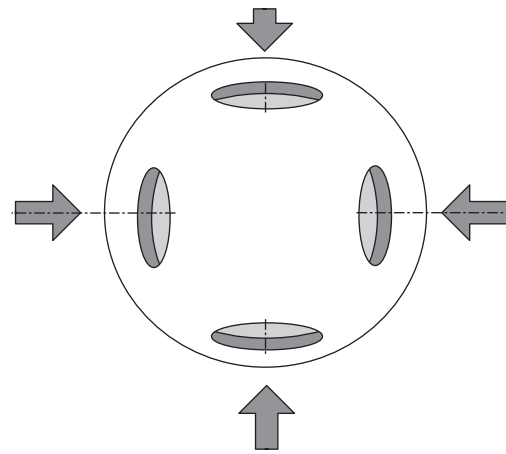

Fig. 1. Schematic of a TST with internal input of the laser energy.

X-ray emission of the Fe He$_\alpha$-line, we simulated the implosion of a laser corona plasma in a TST using the KIN-MC code.

Since ion kinetic effects play an insignificant role in the formation of a laser corona in the first stage of the TST dynamics (see the Appendix), we run the KIN-MC code only to simulate the second stage. In the experiments with TSTs in Iskra-5, the first stage comes to an end when the laser pulse terminates, i.e., by the time $t_1 \sim 0.8$ ns. By this time, about 4–5 kJ of the laser energy is absorbed within a TST, the Fe coating of the target is heated to a temperature of about 1–1.5 keV, and the tail of the unloading wave of a laser corona plasma approaches the radius $R_1 \sim 200$–300 μm. The profiles of the plasma velocity, plasma density, and electron and ion temperatures obtained by the time $t_1 \sim 0.8$ ns through the gas-dynamic calculations with the CC-9 code served as the initial conditions for kinetic simulations with the KIN-MC code.

We used the KIN-MC code to simulate the dynamics of only the Fe coating of a TST, assuming that the plastic spherical shell is immobile. The initial distribution of the ions was modeled by a locally Maxwellian distribution. The ion composition of the plasma was assumed to be constant, the ion charge number being 24, which corresponds to the results obtained with the CC-9 code when calculating the degree of ionization of Fe atoms in the tail of the unloading wave of a laser corona plasma in a TST by the time $t_1 \sim 0.8$ ns and in the region where the counterstreaming ion flows interact. The boundary conditions imposed at the left and right boundaries of the computation region for the kinetic equation assumed ideal ion reflection. The boundary conditions imposed on the electron thermal diffusivity assumed zero electron heat fluxes at the boundaries of the Fe coating. Calculations with the CC-9 code showed that, in the course of plasma implosion in a TST, all these boundary conditions are approximately satisfied over the time interval $0.8 < t < 3$ ns.

As the integral characteristic for gas-dynamic and kinetic simulations of plasma implosion in a Fe-coated TST, we chose the emissivity of the Fe He_α-line in a plasma, because this line makes the main contribution to hard (for $\nu > 6$ keV) X radiation. The choice of this line was dictated by the ion composition of the compressed plasma and the transparency of the target wall to Fe He_α-line radiation [13]. In the KIN-MC code, calculations are carried out on a mixed Eulerian–Lagrangian spatial grid consisting of $N_X = 80$ mesh points in space. The run time of the code was chosen to be about 2 ns, which is close to the time at which the pulse of resonant Fe He_α-line radiation comes to an end. During this time, the shock wave reflected from the center travels a distance approximately equal to one-half of the initial target radius and the thermal and gas-dynamic perturbations that propagate from the inner surface of the target approach the shock front. The computation time over which the laser corona plasma arrives at the target center is about 1 ns, which coincides with the beginning of the pulse of the resonant Fe He_α-line radiation. The resonant X radiation is most intense at a time of about $t_{max} \sim 1.5$–1.7 ns.

In the KIN-MC code, the effects of radiation from the plasma are described by the model of internal radiative losses. The power of the internal radiative losses was calculated by the CC-9 code [21–23] in the corona approximation from the formula $Q(\rho, T_e) = \text{const} \times \rho^2 F_1(\rho, T_e)$, in which the function F_1 was interpolated using tabulated values at the mesh points. The internal radiative losses were incorporated into the KIN-MC code as a negative source term in the electron energy balance equation. The specific power of the resonant Fe He_α-line radiation was interpolated in a similar way: $J_\alpha(\rho, T_e) = \text{const} \times \rho^2 F_2(\rho, T_e)$. The integral power and the energy of the resonant Fe He_α-line radiation in the stage of implosion of a laser corona plasma were calculated from the electron density and temperature profiles with the help of the above expression for the specific power of the resonant X radiation:

$$J_\alpha(R, t) = 4\pi \int_0^R \rho^2(r, t) F_2(\rho, T_e) r^2 dr \times 10^7 \ [\text{J/ns}],$$

$$JT_\alpha(R, t)$$

$$= 4\pi \int_{0.8}^t dt \int_0^R \rho^2(r, t) F_2(\rho, T_e) r^2 dr \times 10^7 \ [\text{J}].$$

The distribution $J_\alpha(R, t)$ makes it possible to estimate the radius of the region where the resonant Fe He_α-line radiation is generated during the implosion of a laser corona plasma and to analyze the relative influence of the kinetic effects of the delocalization of mass and heat transfers on the shape of the pulse of the resonant Fe He_α-line radiation and the radiation energy.

We carried out the following three series of simulations with the KIN-MC code: in the first series, we used the collisionless approximation, in which the ion–ion collision integral was artificially set to zero (the f version); in the second series, we modeled ion–ion collisions in full measure (the c version); and, in the third series, we used the gas-dynamic approximation with a Maxwellian ion distribution function (the m version).

Numerical results from these three versions are illustrated in Figs. 2–6.

In Figs. 2–4, one can clearly see that the stage of reflection of the shock wave from the center of a TST is well described in all calculation versions. Among the three versions, the collisionless f version gives the maximum density (about 1 g/cm^3) to which the Fe plasma is compressed, while the gas-dynamic m version gives the highest ion temperature. The c version yields parameter values intermediate between those obtained in the f and m versions. In Fig. 3, we can see that, in the stage of maximum compression, the kinetics of Fe ions in the central region is essentially collisionless. This conclusion is evidenced by the fact that the wide leading edge of the ion heat wave extends to a radius of about 200 μm and significantly overtakes the jump in density in the reflected shock wave. In the f version, the leading edge of the ion heat wave is double-humped, which corresponds to the flows of high-energy ions that are scattered and unscattered near the target center. An analysis of the ion density in phase space shows that, in the f and c versions, the ion distribution function within the leading edge of the ion heat wave is far from being locally Maxwellian. At the time at which the reflected shock wave forms, the ion distribution function over the radial velocities is nonmonotonic: the beam component of the function contains about 10–20% of the ions in the region $R \leq 130$–200 μm. Such a significant beam component of the distribution function facilitates the onset of various ion instabilities in the plasma and may hinder the implosion of a laser corona plasma even when the initial spherical plasma flow is ideally symmetric.

Although simulations with and without allowance for collisions show distinctly different dynamics of the plasma implosion, this difference has only a minor effect on the calculated electron temperature and the calculated integral energy yield in the Fe He_α-line (Figs. 5, 6) and, for the conditions under consideration, results in discrepancies no higher than ~5%. The reasons for such a slight effect lie in the strong influence of the shape of the ion distribution function on the electron temperature, strong coupling between the electron and ion plasma densities, high electron thermal conductivity, and the functional dependence of the intensity of the resonant Fe He_α-line emission in the corona approximation.

Let us give a clearer insight into one of these factors. The plasma differs radically from a system of individual particles in that the electron and ion plasma components are strongly coupled to one another. In our model,
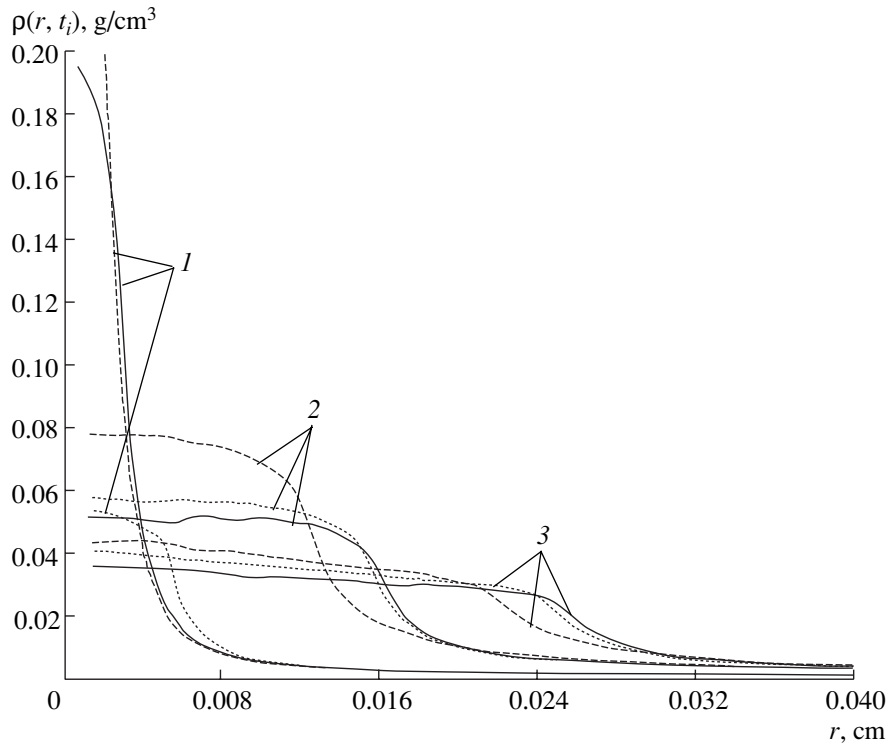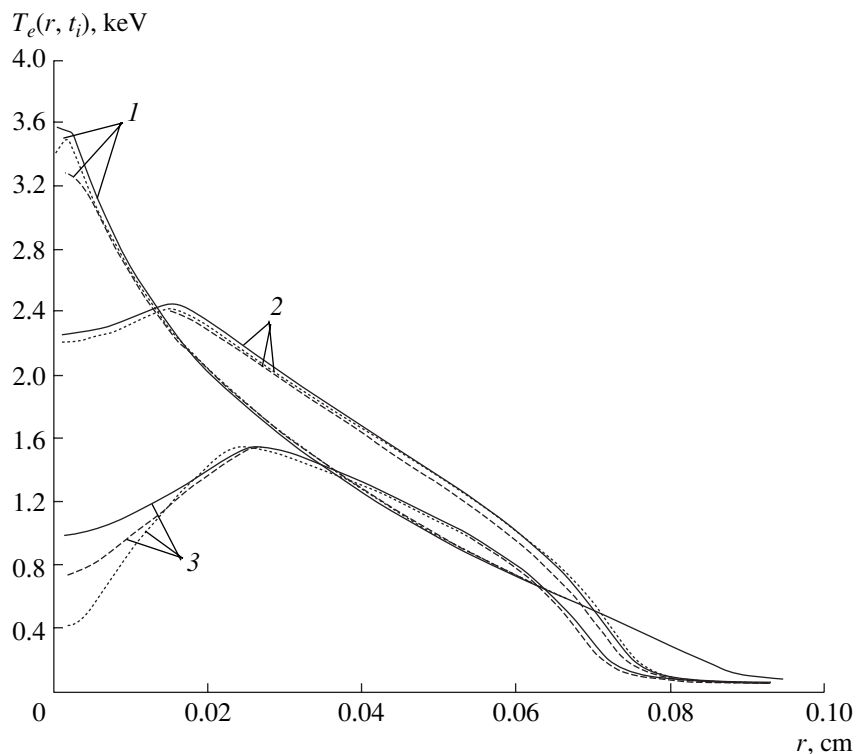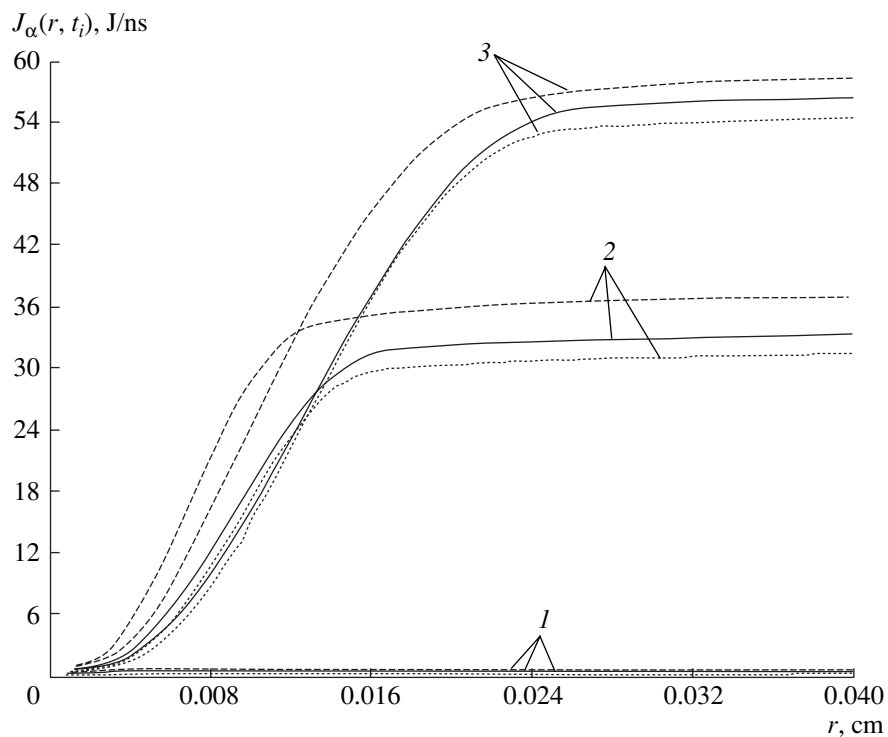
Fig. 2. Density profiles $\rho(r, t_i)$ computed at the times $t_i = $ (*1*) 1.1, (*2*) 1.6, and (*3*) 2 ns using the KIN-MC code. The solid curves are from the collisional *c* version, the dashed curves are from the collisionless *f* version, and the dotted curves are from the gas-dynamic *m* version.
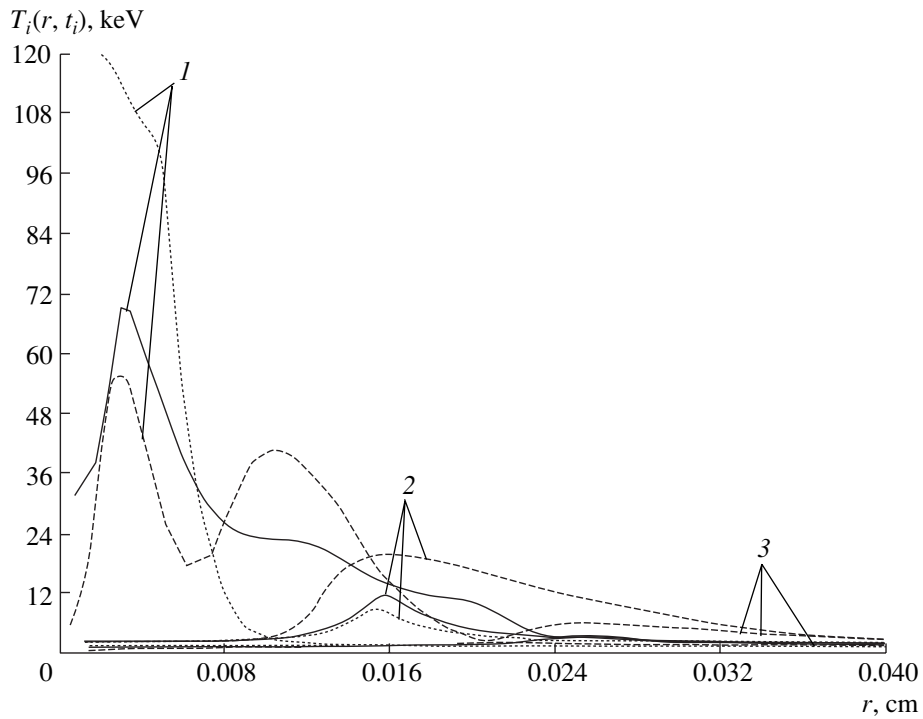
Fig. 3. Ion temperature profiles $T_i(r, t_i)$ computed at the times $t_i = $ (*1*)1.1, (*2*) 1.6, and (*3*) 2 ns using the KIN-MC code. The solid curves are from the collisional *c* version, the dashed curves are from the collisionless *f* version, and the dotted curves are from the gas-dynamic *m* version.

Fig. 4. Electron temperature profiles $T_e(r, t_i)$ computed at the times t_i = (*1*) 1.1, (*2*) 1.6, and (*3*) 2 ns using the KIN-MC code. The solid curves are from the collisional *c* version, the dashed curves are from the collisionless *f* version, and the dotted curves are from the gas-dynamic *m* version.


Fig. 5. Profiles of the integral (over space) power $J_\alpha(r, t_i)$ of the resonant X radiation emitted from the sphere of radius *R*, computed at the times t_i = (*1*) 1.1, (*2*) 1.6, and (*3*) 2 ns using the KIN-MC code. The solid curves are from the collisional *c* version, the dashed curves are from the collisionless *f* version, and the dotted curves are from the gas-dynamic *m* version. At the time t_1 = 1.1 ns, the power J_α is nearly zero (the corresponding curves are close to the abscissa) because of the small mass of the hot plasma.
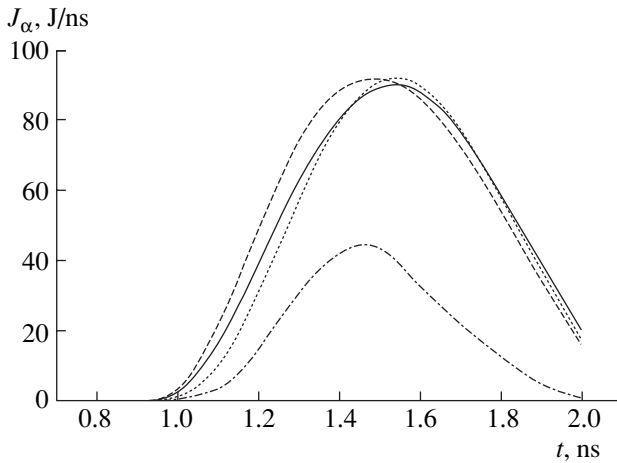
Fig. 6. Shape of the pulse of the integral energy flux $J_\alpha(t)$ of the resonant Fe He$_\alpha$-line radiation from a TST, computed using the KIN-MC code. The solid curve is from the collisional c version, the dashed curve is from the collisionless f version, and the dotted curve is from the gas-dynamic m version. The dash-and-dotted curve is from the ff version (or "fully free" version), in which the ion–ion and electron–ion collisions are both switched off.

this coupling is accounted for by the quasineutrality condition. Because of this coupling, even in the absence of ion–ion and ion–electron collisions, the plasma electrons are significantly heated adiabatically (provided that the radiative cooling is neglected) during the implosion of a laser corona. In simulations in which all collisions are artificially "switched off," the energy yield in the Fe He$_\alpha$-line is lower by no more than a factor of about 2.5 (Fig. 6). The relatively weak sensitivity of the electron temperature to the shape of the ion distribution function is governed to a large extent by the quasineutrality condition, which is responsible for the strong coupling between the electron and ion plasma components. Strong kinetic effects can also be reduced by the spherical geometry of the target: during the spherical implosion of the plasma flow, the plasma density increases substantially, thereby increasing the rate of ion–ion collisions.

Before carrying out simulations with the KIN-MC code, we expected that, during the implosion of a laser corona plasma, the delocalization of the energy loss of high-energy ions in the low-density tail of the unloading wave of a laser corona in a large plasma volume should significantly decrease the total energy yield in the resonant Fe He$_\alpha$-line and increase the diameter of the generation region. However, the above results of kinetic and gas-dynamic simulations do not precisely confirm this expectation in full measure (Fig. 6). In Fig. 5, we can also see that the calculated diameter of the region where the resonant radiation is generated is about $D_{calc} \sim 300$ μm, which differs markedly from the experimentally measured diameter $D_{exp} \sim 450$–500 μm. Hence, in the case of an ideal spherically symmetric

implosion, the kinetic effects have no potential to explain the experimental data. Presumably, the lower hard X-ray yield and the larger generation region in experiments with TSTs are associated with two-dimensional and three-dimensional energy losses during the implosion of a laser corona plasma. These losses may come from the unstable character of plasma implosion as well as from non-one-dimensional implosion conditions in real targets [13].

4. CONCLUSION

(i) We have formulated the equations describing the ion kinetics in a simple multicomponent currentless ideal quasineutral plasma under the assumption than the electron distribution function is in local equilibrium. The ion–ion and ion–electron collisions are described by the Landau collision integrals. We have developed the combined model and designed the KIN-MC code for numerically solving the kinetic problems of a simple plasma. In the combined model, the kinetic equations are solved by the Monte Carlo method and the energy balance equations are solved in finite differences.

(ii) We have presented the results from kinetic simulations of the spherically symmetric implosion of a laser corona plasma under the conditions of experiments that were carried out in the Iskra-5 facility with thin-wall spherical targets with an internal input of laser energy [11, 13]. We have investigated the characteristic features of plasma implosion with allowance for ion–ion collisions. For a Fe-coated target with a diameter of about 1 mm in which about 4–5 kJ of the input energy of the pulse from an iodine laser is absorbed, we have calculated the effect of the nonequilibrium character of the ion velocity distribution function on the generation of the resonant Fe He$_\alpha$-line radiation during plasma implosion. The radiative cooling of the plasma was included in the model of internal radiative losses from the corona plasma. Our simulations show that the effect of the kinetics of ion–ion collisions on the generation of the resonant Fe He$_\alpha$-line radiation is relatively weak. Such a weak effect is explained by the strong integral influence of the shape of the ion distribution function on the electron temperature, strong coupling between the electron and ion plasma densities, the quasineutrality condition, and the functional dependence of the intensity of the resonant Fe He$_\alpha$-line emission in the corona approximation. Kinetic effects can also be reduced by the spherical geometry of the target: during spherical implosion, the plasma density in the converging flow increases substantially, thereby increasing the ion–ion collision frequency. In the one-dimensional approximation, kinetic effects fail to explain the experimental data that were obtained in [13] on X radiation spectra and on the diameter of the region where the resonant Fe He$_\alpha$-line radiation is generated.

(iii) Nevertheless, taking into account the kinetic effects of ion–ion collisions may be important when interpreting the detailed data from experiments with laser targets. First of all, this is true for the processes that are directly associated with the formation of the ion distribution function, such as the kinetics of fusion reactions and the formation of resonance lines in the radiation spectra. Our one-dimensional computations with the KIN-MC code show that the processes that have an indirect impact on the ion plasma component and are governed by, e.g., the electron temperature need not be so precisely incorporated into the detailed calculation of the ion distribution functions. The radiative characteristics of these processes in a high-temperature multicharged plasma can be calculated with a reasonable accuracy in the gas-dynamic approximation using the methods of nonequilibrium radiative gas dynamics. Hence, we can expect that using the gas-dynamic approximation is sufficient to calculate the influence of two-dimensional and three-dimensional effects on the plasma implosion and the generation of X radiation in TST targets.

ACKNOWLEDGMENTS

APPENDIX

1. Numerical Model and the KIN-MC Code

The set of Eqs. (4) and (12) is solved numerically by a combination of particle-in-cell and difference methods. The ion distribution function is modeled by an ensemble of particles whose evolution is traced by the MC method. The electron temperature is found by a finite-difference approximation to the electron energy balance equation (4) on a grid whose spacing is appropriately adjusted at each time step. In turn, each time step is divided into the following six substeps.

(i) At the first substep, the collisional ion motion and the convective transport of the electron temperature are calculated from the equations

$$\frac{\partial f_1}{\partial t} + v_1 \frac{\partial f_1}{\partial x} = 0,$$

$$\frac{\partial f_2}{\partial t} + v_1 \frac{\partial f_2}{\partial x} = 0,$$

$$\frac{\partial n_e T_e}{\partial t} + \frac{\partial n_e u_e T_e}{\partial x} = 0.$$

(ii) At the second substep, ion–ion collisions are taken into account by the MC method:

$$\frac{\partial f_1}{\partial t} = J_{11} + J_{12},$$

$$\frac{\partial f_2}{\partial t} = J_{22} + J_{21}.$$

(iii) At the third substep, the effect of the electron pressure on the ions and on the electron temperature is calculated from the equations

$$\frac{\partial f_1}{\partial t} - \frac{Z_1}{m_1 n_e} \frac{\partial P_e}{\partial x} \frac{\partial f_1}{\partial v_1} = 0,$$

$$\frac{\partial f_2}{\partial t} - \frac{Z_2}{m_2 n_e} \frac{\partial P_e}{\partial x} \frac{\partial f_2}{\partial v_1} = 0,$$

$$\frac{\partial n_e T_e}{\partial t} + \frac{2}{3} n_e T_e \frac{\partial u_e}{\partial x} = 0,$$

$$P_e = n_e T_e.$$

(iv) At the fourth substep, the change in the ion velocity due to the frictional forces associated with plasma electrons is calculated from the equations

$$\frac{\partial f_1}{\partial t} + \nu_{1u}(u_2 - u_1)\frac{\partial f_1}{\partial v_1} = 0,$$

$$\frac{\partial f_2}{\partial t} - \nu_{2u}(u_2 - u_1)\frac{\partial f_2}{\partial v_1} = 0,$$

$$\nu_{iu} = \frac{4\sqrt{2\pi}e^4 Z_1^2 Z_2^2}{3m_e^2} \frac{L_{e2}n_1 + L_{e1}n_2}{n_e} \frac{m_e}{m_i}\left(\frac{m_e}{T_e}\right)^{3/2} n_i.$$

(v) At the fifth substep, ion–electron collision frequency and the related change in the electron temperature are calculated from the equations

$$\frac{\partial f_1}{\partial t} = \nu_{1e}\left[\frac{T_e}{m_e}\Delta f_1 + \frac{m_1}{m_e}\frac{\partial}{\partial \mathbf{v}}(\mathbf{v} - \mathbf{u}_1)f_1\right],$$

$$\frac{\partial f_2}{\partial t} = \nu_{2e}\left[\frac{T_e}{m_e}\Delta f_2 + \frac{m_2}{m_e}\frac{\partial}{\partial \mathbf{v}}(\mathbf{v} - \mathbf{u}_2)f_2\right],$$

$$\frac{\partial n_e T_e}{\partial t} = 2\frac{m_1}{m_e}\nu_{1e}n_1(T_1 - T_e) + 2\frac{m_2}{m_e}\nu_{2e}n_2(T_2 - T_e),$$

$$\nu_{ie} = \frac{4\sqrt{2\pi}e^4 Z_i^2 L_{ei}n_e}{3 m_i^2}\left(\frac{m_e}{T_e}\right)^{3/2},$$

$$\mathbf{u}_i = (u_i, 0, 0).$$

(vi) At the sixth substep, the electron thermal diffusivity is calculated from the equations

$$\frac{\partial}{\partial t}(n_e T_e) = \frac{\partial}{\partial x}\lambda_e \frac{\partial T_e}{\partial x}, \quad \lambda_e = \frac{a T_e^{5/2}}{(Z + 3.44)\Lambda_{ie}}.$$

Now, we briefly describe how each of the substeps is implemented numerically.

At the first substep, the electron heat transport is calculated by a special procedure. First, each ion is assigned an additional variable equal to the electron temperature in the cell where the ion occurs. After the ions are displaced, a new grid is constructed so as to satisfy the condition that the number of ions in a cell be constant. Then, the new values of the density, mean velocity, and temperature of the ions and the electron temperature are calculated. In order to verify that the convective transport of the electron temperature is modeled correctly, it is sufficient to multiply the first two equations of this substep by $Z_1 T_e$ and the $Z_2 T_e$, respectively, and to integrate the resulting equations over ion velocities. Numerical experiments show that adjusting the grid in such a manner appreciably reduces statistical errors in calculating the ensemble-averaged quantities.

The second substep is most difficult to implement numerically. At this substep, Coulomb collisions are modeled by a specially developed version of the MC method [24]. Specifically, the Landau operator is approximated by the Boltzmann collision integral, and, then, the methods of the rarefied gas dynamics [25] are applied. The approximation error is controlled by appropriately choosing the dependence of the differential collision frequency on the time step. Fairly exact results can be obtained only when the time between model collisions is shorter than the time of relaxation to a locally Maxwellian distribution. Since this condition is difficult to satisfy for cells in which the ion mean free paths are short, the rate of model collisions is chosen to satisfy the condition for a particle to experience only one collision event per time step. This condition guarantees relaxation to a locally Maxwellian distribution in a cell on each time step, so that the method used in the second substep automatically starts to approximate the corresponding gas-dynamic equations of motion of a quasineutral two-component plasma.

At the third substep, the kinetic equations for the distribution functions f_i are replaced by the equivalent equations for the moments of the distribution functions:

$$\frac{\partial n_1}{\partial t} = 0, \quad \frac{\partial n_2}{\partial t} = 0,$$

$$\frac{\partial n_1 u_1}{\partial t} + \frac{Z_1 n_1}{m_1 n_e}\frac{\partial P_e}{\partial x} = 0,$$

$$\frac{\partial n_2 u_2}{\partial t} + \frac{Z_2 n_2}{m_2 n_e}\frac{\partial P_e}{\partial x} = 0.$$

These moment equations and the equations for $n_e T_e$ yield the equation

$$\frac{\partial}{\partial t}\left(\frac{\rho_1 u_1^2}{2} + \frac{\rho_2 u_2^2}{2} + \frac{3}{2}n_e T_e\right) + \frac{\partial u_e P_e}{\partial x} = 0, \quad \rho_i = m_i n_i,$$

which implies conservation of the total energy at this substep. This equation and the set of moment equations are solved numerically by the Godunov method [26], in which the required new electron velocities and pressures at the boundaries of the calculation cells are determined as follows. First, the following equations for u_e and P_e are constructed:

$$\frac{\partial u_e}{\partial t} + \left\langle\frac{Z}{m}\right\rangle\frac{\partial P_e}{n_e \partial x} = 0, \quad \left\langle\frac{Z}{m}\right\rangle\frac{\partial P_e}{\partial t} + n_e c^2 \frac{\partial u_e}{\partial x} = 0,$$

where

$$\left\langle\frac{Z}{m}\right\rangle = \frac{Z_1 Z_1 n_1}{m_1 n_e} + \frac{Z_2 Z_2 n_2}{m_2 n_e},$$

$$c^2 = \frac{2}{3}\left\langle\frac{Z}{m}\right\rangle\frac{P_e}{n_e} = \frac{2T_e}{3}\left\langle\frac{Z}{m}\right\rangle.$$

Then, the characteristic set of equations for these equations,

$$\left(\frac{\partial u_e}{\partial t} + \sqrt{\frac{6}{n_e}\left\langle\frac{Z}{m}\right\rangle}\frac{\partial\sqrt{P_e}}{\partial t}\right) + c\left(\frac{\partial u_e}{\partial x} + \sqrt{\frac{6}{n_e}\left\langle\frac{Z}{m}\right\rangle}\frac{\partial\sqrt{P_e}}{\partial x}\right) = 0,$$

$$\left(\frac{\partial u_e}{\partial t} - \sqrt{\frac{6}{n_e}\left\langle\frac{Z}{m}\right\rangle}\frac{\partial\sqrt{P_e}}{\partial t}\right) - c\left(\frac{\partial u_e}{\partial x} - \sqrt{\frac{6}{n_e}\left\langle\frac{Z}{m}\right\rangle}\frac{\partial\sqrt{P_e}}{\partial x}\right) = 0,$$

is used to solve the problem of the decay of the discontinuity at the boundaries of the calculation cells. The new values of the electron velocities and pressures are used to calculate the new ion velocities and the total energy and, then, to find the new electron temperature. The accuracy of the Godunov method is increased by linearly interpolating the values of the quantities at the boundaries of the calculation cells from their values at the centers of the cells.

In order to implement the fourth substep numerically, it is also convenient to switch to the equivalent set of moment equations:

$$\frac{\partial n_1}{\partial t} = 0, \quad \frac{\partial n_2}{\partial t} = 0,$$

$$\frac{\partial n_1 u_1}{\partial t} = +\nu_{1u}(u_2 - u_1)n_1,$$

$$\frac{\partial n_2 u_2}{\partial t} = -\nu_{2u}(u_2 - u_1)n_2.$$

These moment equations imply that the total mass velocity of the ions is conserved:

$$\rho_1 u_1 + \rho_2 u_2 = \rho u = \rho u_0,$$

$$\rho = \rho_1 + \rho_2.$$

These relationships give

$$u_1 = u_0 - \frac{\rho_1}{\rho}(u_{20} - u_{10})e^{-\nu t},$$

$$u_2 = u_0 + \frac{\rho_2}{\rho}(u_{20} - u_{10})e^{-\nu t},$$

$$\nu = \nu_{1u} + \nu_{2u}.$$

When implementing the fifth substep numerically, the collision rate ν_{ie} is calculated from the initial (at this substep) value of the electron temperature, while the electron temperature in front of the operator Δf_i is assigned its final (at this substep) value. This way guarantees that the energy is conserved. The final (at this substep) electron temperature is determined as follows. The moment equations that are constructed for the ion temperatures in each cell yield the following set of three ordinary differential equations for the ion and electron temperatures T_i and T_e:

$$\frac{\partial n_1 T_1}{\partial t} = \nu_{1\varepsilon} n_1 (T_e - T_1),$$

$$\frac{\partial n_2 T_2}{\partial t} = \nu_{2\varepsilon} n_2 (T_e - T_2),$$

$$\frac{\partial n_e T_e}{\partial t} = \nu_{1\varepsilon} n_1 (T_1 - T_e) + \nu_{2\varepsilon} n_2 (T_2 - T_e),$$

where $\nu_{i\varepsilon} = 2\dfrac{m_i}{m_e}\nu_{ie} = 2\dfrac{m_i}{m_e}\dfrac{4\sqrt{2\pi}}{3}\dfrac{e^4 Z_i^2 L_{ei} n_e}{m_i^2}\left(\dfrac{m_e}{T_e}\right)^{3/2}$.

The electron temperature obtained by solving this set of equations analytically is used for Monte Carlo simulations of ion–electron collisions by a Green's function approach [27].

At the sixth substep, the electron heat conduction equation is approximated by an implicit difference scheme, in which case the electron thermal diffusivity is calculated from the temperature found at the fifth substep. The resulting finite difference equations are solved by the sweep method.

The above model for solving the kinetic equations was implemented as the KIN-MC code. The code provides the possibility of switching off the ion–ion collisions; this version of simulations was referred to as a collisionless f version. Recall that, in the regions where the ion mean free paths are short, our scheme with model collisions results in the relaxation to a Maxwellian ion velocity distribution; consequently, in such regions, the scheme reduces to the solution of the corresponding gas-dynamic equations of motion of a quasineutral two-component plasma. With this circumstance in mind, we arranged the KIN-MC code so as to be able to perform calculations with the ion distribution functions that are artificially forced to be Maxwellian in all of the calculation cells at each time step and, accordingly, to solve the problems in the gas-dynamic approximation. This version of calculations was referred to as a "Maxwellian" m version.

It is well known that statistical errors always occur in Monte Carlo simulations. This is primarily true of the nonlinear problems that are solved using a comparatively small number of particles. The KIN-MC code provides the possibility of a diffusive smoothing of statistical errors; moreover, the parameters of the smoothing procedure can be changed during a run of the code.

## 2. Comparative Calculations of Planar Flows

The accuracy of the calculations of the Landau collision integral by Monte Carlo methods was checked by Ivanov and Kochubeĭ [24] for the problems of the thermalization of the nonequilibrium ion distribution functions in a homogeneous multicomponent plasma. The relevant Monte Carlo results were compared with the results obtained with the LAND code, which is based on a completely conservative difference scheme for solving the Landau equations. Ivanov and Kochubeĭ [24] found that there is a good agreement between the ion distribution function and its moments computed by different methods. They concluded that their numerical scheme constructed for modeling Coulomb collisions can also be used to calculate the spatial flows of a multicomponent plasma.

The scheme developed in [24] was tested in many studies on the gas-dynamic flows of an ideal gas. Numerical modeling of the gas-dynamic problems that admit analytic solutions (such as the problems of the planar and spherical reflections of shock waves and unloading waves) showed that this scheme gives correct numerical results, provided that the problems are solved numerically on spatial grids with relatively large spacings [28]. Moreover, the results of simulations in which the ion distribution function was artificially forced to be Maxwellian (see above) were found to coincide with the results obtained by modeling collisions in the gas-dynamic approximation. This is because the methods implemented in the corresponding numerical codes are, in fact, statistically analogous to the Godunov method [26].

Let us discuss the results obtained by simulating the interaction of plane unloading waves in a simple plasma by the KIN-MC code and, in the two-temperature gas-dynamic approximation, by the CC-9 code [21]. The calculations were carried out for the following initial parameter values: the thickness of the plasma corona is 40 μm ($0 < x < 0.004$ cm), the plasma density is $\rho = 0.1$ g/cm^3, the electron and ion temperatures are $T_e = T_i = 1.5$ keV, the plasma flow velocity is $u = 0$, the atomic weight of the Fe ions is $A_0 = 56$, and their ion charge number is $Z_0 = 26$. The boundary conditions at the left and right boundaries, $x = 0$ and $x = 0.03$ cm, assume ideal particle reflections. The radiative losses from the plasma are neglected. These parameters are characteristic of the problems associated with laser targets in which laser light is converted into X radiation (see Section 3). The simulations were carried out without (version a) and with (version b) allowance for the energy exchange between electrons and ions. The pro-
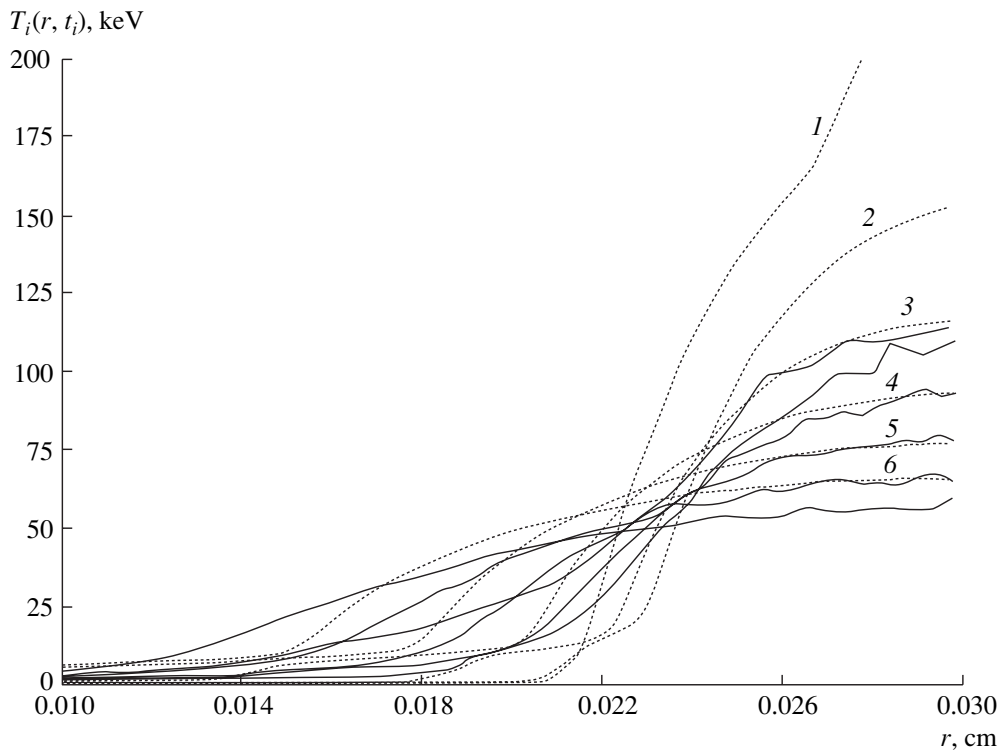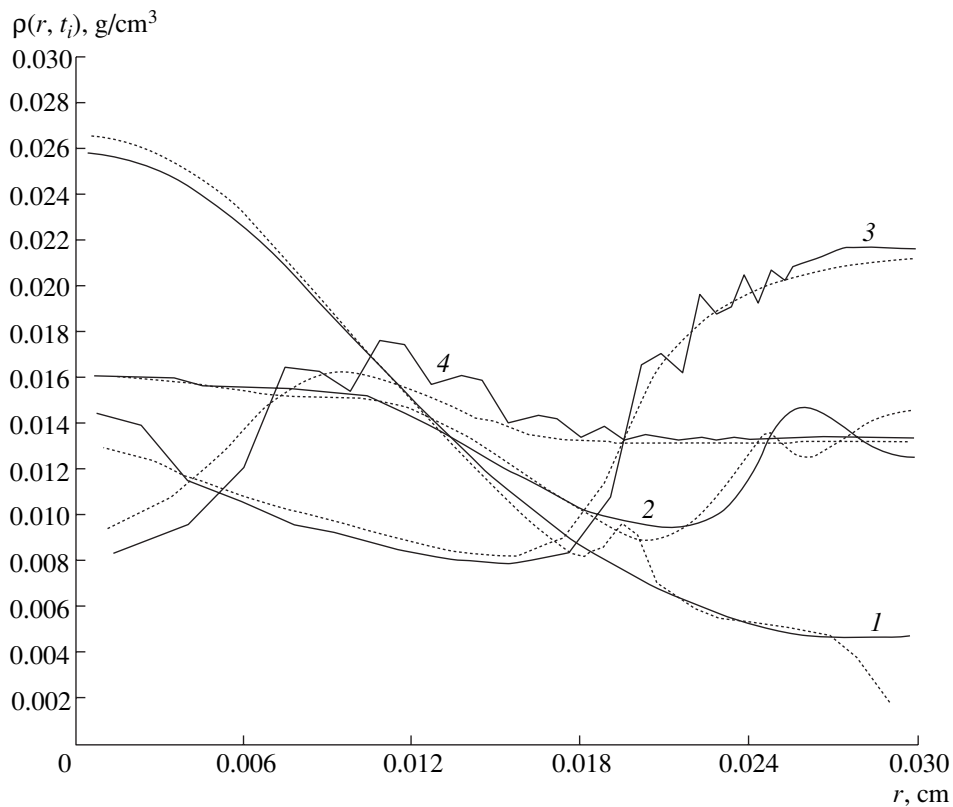
Fig. 7. Spatial profiles of the mean ion temperature $T_i(r, t_i)$ computed using the KIN-MC code (solid curves) and the CC-9 code (dotted curves) at the times $t_i = $ (*1*) 0.4, (*2*) 0.6, (*3*), 0.8, (*4*) 1.0, (*5*) 1.2, and (*6*) 1.4 ns without allowance for the energy exchange between the electron and ion subsystems.
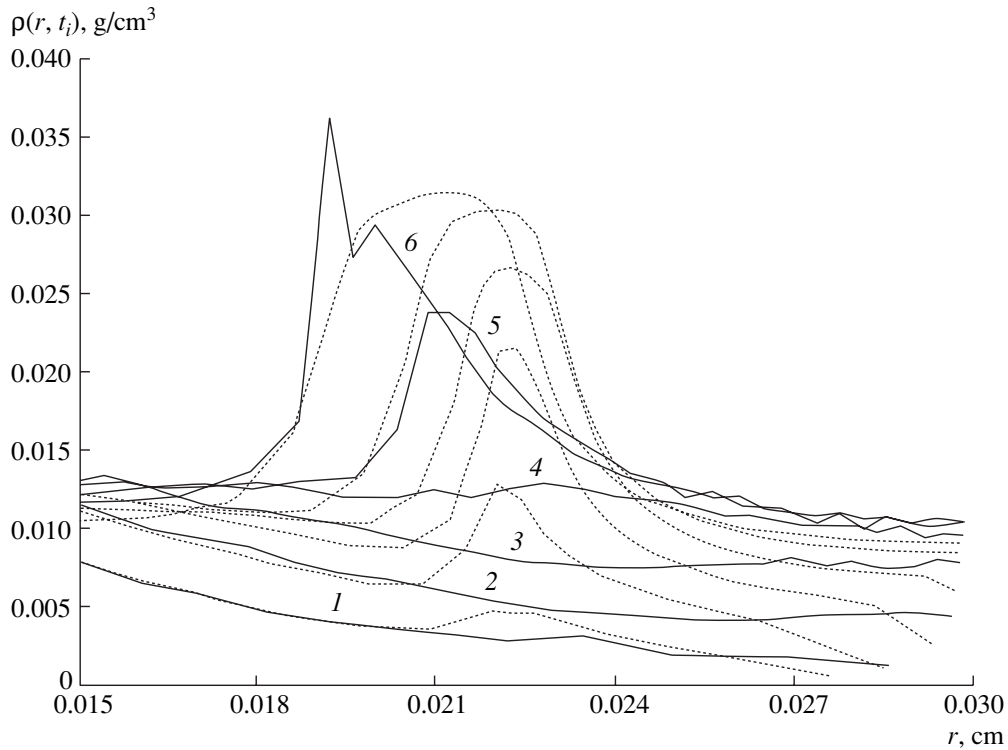
Fig. 8. Spatial profiles of the plasma density $\rho(r, t_i)$ computed using the KIN-MC code (solid curves) and the CC-9 code (dotted curves) at the times $t_i = $ (*1*) 0.3, (*2*) 0.4, (*3*) 0.5, (*4*) 0.6, (*5*) 0.7, and (*6*) 0.8 ns with allowance for the energy exchange between the electron and ion subsystems.

$T_i(r, t_i), T_p(r, t_i)$, keV
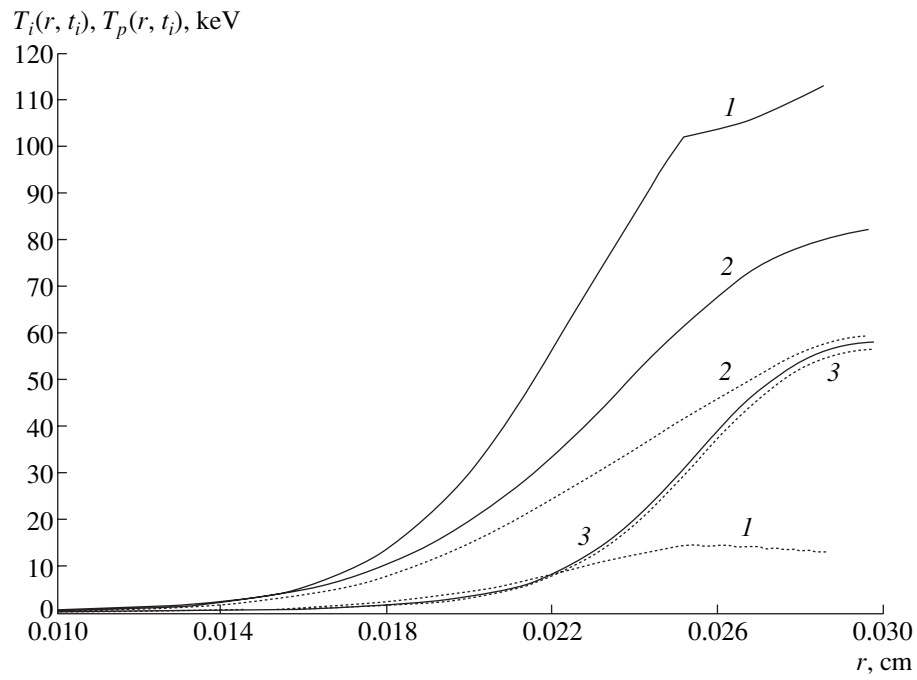
Fig. 9. Spatial profiles of the mean ion temperature $T_i(r, t_i)$ (solid curves) and the transverse ion temperature $T_p(r, t_i)$ (dotted curves) at the times $t_i =$ (*1*) 0.2, (*2*) 0.3, and (*3*) 0.4 ns computed without allowance for the energy exchange between the electron and ion subsystems.

$\rho(r, t_i)$, g/cm^3

Fig. 10. Spatial profiles of the plasma density $\rho(r, t_i)$ computed using the KIN-MC code (solid curves) and the CC-9 code (dotted curves) at the times $t_i =$ (*1*) 0.4, (*2*) 0.6, (*3*) 1.0, and (*4*) 1.5 ns with allowance for the energy exchange between the electron and ion subsystems.

files of the gas-dynamic quantities calculated in version *a* are shown in Figs. 7 and 8.

In a multicharged (quasineutral) plasma, the ion velocity in the tail of the unloading wave is proportional to $\sim \sqrt{(Z+1)/A}$ (at the expense of the electron pressure). In simulations, this velocity was found to be about 0.15 cm/ns, which corresponds to the ion kinetic energy $E_i \sim 0.6$ MeV/ion. Estimates of the mean free path of the ions with such energies with respect to Coulomb collisions show that it is comparable with the optical thickness of the expanding plasma, so that the kinetic effects can be expected to come into play after the plasma is reflected from the right boundary (i.e., in the interaction of waves). Figures 7 and 8 show the profiles of the ion temperatures and plasma density calculated at the times close to the time at which the plasma is reflected from the right boundary and the first shock wave forms. The thermalization time for the ion distribution function in the interaction region was determined from the relaxation time of the longitudinal and transverse ion temperatures and was found to be about 0.4–0.6 ns. As compared to the gas-dynamic simulations done with the help of the CC-9 code, which uses the standard transport coefficients, the reflected shock wave forms somewhat later and at a larger distance from the boundary. Since, in the calculations of version *a*, the ion–electron collisions are neglected, the ion temperature remains high throughout the computation time. It was found that, during the formation of a shock wave, about 50% of the kinetic energy acquired by the plasma during acceleration in the unloading wave is converted into the internal ion energy.

The numerical results obtained in the calculations of version *b* are illustrated in Figs. 9 and 10.

A comparison of Figs. 9 and 10 with Figs. 7 and 8 shows that, in versions *a* and *b*, the shock waves form in an essentially analogous fashion, thereby providing evidence that ion–ion collisions play a governing role in the problem under investigation. The profiles of the mean and transverse ion temperatures in Fig. 9 illustrate the thermalization of the ion distribution function in the interaction between unloading waves. In version *b*, the characteristic spatial scale on which the plasma is nonequilibrium (or, in other words, the front width of the shock wave) was found to be about 100 μm, the time during which the plasma is essentially nonequilibrium (i.e., the longitudinal and transverse ion temperatures are different) being about 0.2 ns. The development of gas-dynamic processes in later stages is illustrated by Fig. 10.

In the problem under consideration, an important role is also played by the energy exchange between ions and electrons. As compared to version *a*, the electron temperature in the region of interaction between unloading waves behind the front of the shock wave is higher by a factor of about three. The relaxation time of T_i and T_e is about 0.4 ns, which agrees with the results of gas-dynamic simulations with the CC-9 code. The

most profound difference between simulations with the CC-9 code and the KIN-MC code lies in the maximum values of the ion temperature T_i in the interaction between the plasma flows as well as in the width of the region where the ion temperature T_i is high. The ion temperature T_i computed from simulations with the standard transport coefficients using the CC-9 code is higher by a factor of about 1.5 to 2 and the width of the shock front is accordingly smaller. In order to adjust the results from gas-dynamic simulations to those from kinetic simulations, we varied the ion viscosity and ion thermal diffusivity in simulations with the CC-9 code. The above results from calculations of version *b* were obtained for the ion viscosity and ion thermal diffusivity that were increased by factors of 5 and 15, respectively, in order to describe the high penetrability of an anisotropic flow of fast ions in the tail of an unloading wave when the waves collide. Such a "fitting" provides a qualitative modeling of the effects revealed in kinetic simulations.

REFERENCES

1. J. D. Lindel, Phys. Plasmas **2**, 3933 (1995).
2. R. C. Elton, *X-Ray Lasers* (Academic, Boston, 1990; Mir, Moscow, 1994).
3. R. Bock, Europhys. News **23** (5), 83 (1992).
4. D. Shvarts, B. Yaakobi, P. Audebert, *et al.*, Proc. SPIE **831**, 283 (1988).
5. T. Bochly, P. Audebert, D. Shvarts, *et al.*, Proc. SPIE **831**, 306 (1987).
6. S. A. Bel'kov, A. V. Bessarab, A. V. Veselov, *et al.*, Zh. Éksp. Teor. Fiz. **97**, 834 (1990) [Sov. Phys. JETP **70**, 467 (1990)].
7. O. Larroche, Phys. Fluids B **5**, 2816 (1993).
8. F. Vidal, J. P. Matte, M. Casanova, and O. Larroche, Phys. Fluids B **5**, 3182 (1993).
9. C. Chenais-Popovics, O. Rancu, P. Renaudin, *et al.*, J. Quant. Spectrosc. Radiat. Transf. **54** (1/2), 105 (1995).
10. M. E. Jones, D. Winske, S. R. Goldman, *et al.*, Phys. Plasmas **3**, 1096 (1996).
11. P. D. Gasparyan, V. M. Gerasimov, Yu. K. Kochubey, *et al.*, in *Proceedings of the 5th International Colloquium on Atomic Spectra and Oscillator Strengths for Astrophysical and Laboratory Plasmas, Meudon, 1995*, Ed. by W.-U. Tchang-Brillet, J.-F. Wyart, and C. J. Zeippen (Publications de l'Observatoire de Paris, Meudon, 1996), p. 198.
12. G. V. Dolgaleva and V. A. Zhmaĭlo, Vopr. At. Nauki Tekh., Ser. MPMF, No. 2, 75 (1986).
13. S. A. Bel'kov, A. V. Bessarab, B. A. Voinov, *et al.*, in *Proceedings of the 5th International Zababakhin Scientific Talks, Snezhinsk, 1998*.
14. F. Hinton, in *Basic Plasma Physics*, Ed. by A. A. Galeev and R. N. Sudan (Énergoatomizdat, Moscow, 1983; North-Holland, Amsterdam, 1983), Vol. 1.
15. V. M. Zhdanov, *Transport Phenomena in Multicomponent Plasma* (Énergoatomizdat, Moscow, 1983).

16. V. P. Bashurin and É. M. Antonenko, in *Proceedings of the Conference on Numerical Methods of Gas Dynamics, Abrau-Dyurso, 1998.*

17. A. V. Brantov, V. Yu. Bychenkov, V. T. Tikhonchuk, and W. Rosmus, Zh. Éksp. Teor. Fiz. **110**, 1301 (1996) [JETP **83**, 716 (1996)].

18. A. V. Brantov, V. Yu. Bychenkov, V. T. Tikhonchuk, and W. Rosmus, Phys. Plasmas **5**, 2742 (1998).

19. L. Spitzer, *Physics of Fully Ionized Gases* (Interscience, New York, 1962).

20. Ya. B. Zel'dovich and Yu. P. Raizer, *Physics of Shock Waves and High-Temperature Hydrodynamic Phenomena* (Nauka, Moscow, 1966; Academic, New York, 1966).

21. B. A. Voinov, P. D. Gasparyan, Yu. K. Kochubeĭ, and V. I. Roslov, Vopr. At. Nauki Tekh., Ser. Mat. Model. Fiz. Protses., No. 2, 65 (1993).

22. S. A. Bel'kov, P. D. Gasparian, G. V. Dolgolyova, and Yu. K. Kochubey, J. Quant. Spectrosc. Radiat. Transf. **58**, 471 (1997).

23. S. A. Bel'kov, P. D. Gasparian, Yu. K. Kochubeĭ, and E. I. Mitrofanov, Zh. Éksp. Teor. Fiz. **111**, 496 (1997) [JETP **84**, 272 (1997)].

24. N. V. Ivanov and Yu. K. Kochubeĭ, Vopr. At. Nauki Tekh., Ser. Mat. Model. Fiz. Protses., No. 1, 3 (1998).

25. G. Berd, *Molecular Gas Dynamics* (Oxford Univ. Press, Oxford, 1976; Mir, Moscow, 1981).

26. S. K. Godunov, Mat. Sb. **47**, 271 (1959).

27. S. Chandrasekhar, *Stochastic Problems in Physics and Astronomy* (AIP, New York, 1943; Inostrannaya Literatura, Moscow, 1947).

28. N. V. Ivanov and P. D. Gasparyan, Vopr. At. Nauki Tekh., Ser. Mat. Model. Fiz. Protses., No. 1, 17 (1997).

Translated by G. V. Shepekina

<div align="center">

PLASMA
DYNAMICS

Dynamics of a Nonquasineutral Plasma in a Strong Magnetic Field

A. V. Gordeev

</div>

Russian Research Centre Kurchatov Institute, pl. Kurchatova 1, Moscow, 123182 Russia
Received September 28, 2000; in final form, April 2, 2001

Abstract—The motion of a nonquasineutral plasma in a strong magnetic field such that $B^2 \gg 4\pi n_i m_i c^2$ is analyzed. It is shown in simple examples that, when the plasma pressure and dissipation are neglected, the only dynamic process in a magnetized plasma is the evolution of the charge-separation electric field and the related magnetic field flux. The equations derived to describe this evolution are essentially the wave Grad–Shafranov equations. The solution to these equations implies that, in a turbulent Z-pinch, a steady state can exist in which the current at a supercritical level $J \gg m_i c^3/Ze$ is concentrated near the pinch axis. © 2001 MAIK "Nauka/Interperiodica".

1. Many problems in plasma theory are treated under the quasineutrality condition

$$n_e = Zn_i, \qquad (1)$$

where n_e and n_i are the electron and ion densities and Z is the ion charge number.

It is thought that this condition may fail to hold in the problems dealing with beams and diodes as well as in the problems of the interaction of high-frequency electromagnetic waves with plasmas [1, 2]. In recent years, interest has grown in various plasma objects in strong magnetic fields, in which case the quasineutrality condition is also violated; these are, e.g., ion diodes filled with magnetized electrons, electron vortices, and laser plasmas [3–8]. Gott and Yurchenko published a series of papers [9] in which they used an approach based on the dimensionality analysis of tokamak plasmas and showed that, under the quasineutrality condition, it is impossible to give a correct description of the full variety of possible modes of tokamak operation; in other words, the Debye radius should necessarily be take into consideration.

In investigating systems with a strong magnetic field, it is expedient to use, instead of the conventional Debye radius $r_D = \sqrt{T/4\pi e^2 n_e}$, the magnetic Debye radius $r_B = B/4\pi e n_e$, which is obtained from the Debye radius r_D by replacing the temperature T with the quantity $B^2/4\pi n_e$. The magnetic Debye radius r_B introduced in such a way describes the screening of the electric and magnetic fields in a plasma under the condition $B^2 \gg 4\pi n_e T$. An increase in the magnetic field causes the magnetization of the electrons and, then, of the ions, in which case the particle inertia can be neglected. Therefore, the electromagnetic force acting on the particle is equal to zero, so that the particles can be treated in the drift approximation. However, this approach is valid for a plasma that is in equilibrium; the deviation from equilibrium is usually described with allowance for the inertia of the heavier particles—the ions. However, in a sufficiently strong magnetic field, the inertial motion of the ions can be neglected. If we also ignore thermal effects and dissipation, we can describe the ions by the hydrodynamic equation

$$m_i \frac{d\mathbf{v}_i}{dt} = Ze\mathbf{E} + \frac{Ze}{c}[\mathbf{v}_i \times \mathbf{B}]. \qquad (2)$$

For strong magnetic fields, we can estimate the derivative d/dt as the ratio of the speed of light c to the characteristic scale length r_B in order to see that ion inertia can be neglected under the condition

$$B^2 \gg 4\pi n_i m_i c^2. \qquad (3)$$

For a hydrogen plasma density of $n = 10^{12}$ cm^{-3}, this condition corresponds to the magnetic field $B \gg 10$ T.

Below, we will show that, in such magnetic fields, the plasma in which the electrons and ions are both magnetized can exhibit evolution only if the quasineutrality condition is violated.

2. The basic set of equations used here consists of the drift equations for electrons and ions,

$$0 = -e\mathbf{E} - \frac{e}{c}[\mathbf{v}_e \times \mathbf{B}], \quad 0 = Ze\mathbf{E} + \frac{Ze}{c}[\mathbf{v}_i \times \mathbf{B}], \quad (4)$$

the electron and ion continuity equations,

$$\frac{\partial n_e}{\partial t} + \nabla \cdot (n_e \mathbf{v}_e) = 0, \quad \frac{\partial n_i}{\partial t} + \nabla \cdot (n_i \mathbf{v}_i) = 0, \quad (5)$$

Maxwell's equations

$$\nabla \times \mathbf{B} = \frac{4\pi e}{c}(Zn_i \mathbf{v}_i - n_e \mathbf{v}_e) + \frac{1}{c}\frac{\partial \mathbf{E}}{\partial t}, \qquad (6)$$

$$\nabla \times \mathbf{E} = -\frac{1}{c}\frac{\partial \mathbf{B}}{\partial t}, \tag{7}$$

and Poisson's equation

$$\nabla \cdot \mathbf{E} = 4\pi e(Zn_i - n_e). \tag{8}$$

Although Poisson's equation (8) is a consequence of Eqs. (5) and (6), we also include it in the basic set of equations because of its importance for further analysis.

Equation (4) implies that the electron and ion velocities are the same, $\mathbf{v}_e = \mathbf{v}_i \equiv \mathbf{v}$, so that we can introduce the common total time derivative

$$\frac{d}{dt} \equiv \frac{\partial}{\partial t} + \mathbf{v} \cdot \nabla. \tag{9}$$

First, we will consider a plasma system in which the magnetic field is directed along the z-axis and the electric field has two components: E_r and E_θ. If the magnetic field in such a system is sufficiently strong, then the most important dynamic processes occur in the plane perpendicular to the magnetic field, in which case, in describing the two-dimensional plasma dynamics, we can neglect the dependence on the longitudinal coordinate, $\partial/\partial z \equiv 0$.

Taking a curl of each of Eqs. (4) and using the corresponding continuity equations, we obtain

$$\frac{dI_e}{dt} = \frac{dI_i}{dt} = 0, \quad I_e = \frac{B_z}{n_e}, \quad I_i = \frac{B_z}{n_i}. \tag{10}$$

We see that the Lagrangian invariants I_e and I_i are conserved along the trajectories of a particle moving with velocity $\mathbf{v}$. The initial conditions are assumed to be such that the quantities ZI_e and I_i differ from one another, $ZI_e \neq I_i$; this assumption ensures that the quasineutrality condition fails to hold for all subsequent time.

In the analysis to follow, it is convenient to introduce the quantity R,

$$\frac{1}{R} \equiv 4\pi e\left(\frac{Z}{I_i} - \frac{1}{I_e}\right), \tag{11}$$

which has the dimensionality of length and obviously satisfies the equation

$$\frac{\partial R}{\partial t} + \mathbf{v} \cdot \nabla R = 0. \tag{12}$$

Below, when deriving the main equations of the approach presented here, we will restrict ourselves to cylindrically symmetric plasma states, $\partial/\partial\theta \equiv 0$, in which case the basic equations describing the plasma dynamics take the form

$$\frac{1}{r}\frac{\partial}{\partial r}(rE_r) = \frac{B_z}{R}, \tag{13}$$

$$\frac{E_\theta}{R} + \frac{1}{c}\frac{\partial E_r}{\partial t} = 0, \tag{14}$$

$$\frac{\partial B_z}{\partial r} = \frac{E_r}{R} - \frac{1}{c}\frac{\partial E_\theta}{\partial t}. \tag{15}$$

Hence, under the above assumptions, the plasma dynamics is completely described by Eqs. (12)–(15).

Note that, as was shown in [7], one of these equations, namely, Eq. (12), is equivalent to the induction equation.

3. Here, we derive the evolutionary equations for the plasma in the problem as formulated. Expressing velocity v_r from Eq. (4) in terms of E_θ and using Eqs. (13) and (14), we can readily transform Eq. (12) into the equation

$$\frac{\partial R}{\partial t}\frac{\partial}{\partial r}(rE_r) - \frac{\partial R}{\partial r}\frac{\partial}{\partial t}(rE_r) = 0, \tag{16}$$

which gives

$$rE_r = f(R) \equiv f, \tag{17}$$

where $f(R)$ is an arbitrary function of R. Using formula (17), we express R in terms of f and introduce the function $F(f)$ such that

$$R = R(f) \equiv \frac{\partial F}{\partial f}. \tag{18}$$

We substitute E_θ and B_z from Eqs. (13) and (14) into Eq. (15) to obtain the following equation for E_r:

$$\frac{\partial}{\partial r}\left\{R\frac{1}{r}\frac{\partial}{\partial r}(rE_r)\right\} = \frac{E_r}{R} + \frac{1}{c^2}\frac{\partial}{\partial t}\left(R\frac{\partial E_r}{\partial t}\right). \tag{19}$$

Using the identities

$$R\frac{\partial}{\partial r}(rE_r) \equiv \frac{\partial F}{\partial r}, \quad R\frac{\partial}{\partial t}(rE_r) \equiv \frac{\partial F}{\partial t},$$

we easily arrive at the final form of Eq. (19):

$$r\frac{\partial}{\partial r}\left(\frac{1}{r}\frac{\partial F}{\partial r}\right) - \frac{1}{c^2}\frac{\partial^2 F}{\partial t^2} = G(F), \quad G(F) \equiv \frac{f}{\partial F/\partial f}. \tag{20}$$

This is a one-dimensional Grad–Shafranov equation with an additional (second) term on the left-hand side. With this term, the Grad–Shafranov equation takes the form of an inhomogeneous wave equation.

Combining Eqs. (13) and (18) yields $F \equiv rA_\theta$, where A_θ is the azimuthal component of the vector potential. Of course, Eq. (20) can also be derived in a traditional way, by inserting the vector potential component A_θ into Maxwell's equations and using Eq. (12) to establish a relationship between the quantities rE_r and rA_θ. For a plasma with drifting electrons and ions, this relationship indicates the simultaneous wave dynamics of the magnetic flux, described by A_θ, and charge-separation electric field E_r.

Interestingly, the approach used here implies that $r_B/c \gg \omega_{pi}^{-1}$; in other words, the evolution of a non-

quasineutral plasma is much slower in comparison with the ion plasma oscillations. For the above parameter values, condition (3) yields $r_B \gg 10$ cm; consequently, the nonquasineutral plasma under consideration exhibits an evolution in the form of fairly large-scale oscillations of the electric fields on a characteristic time scale longer than 1 ns. In this case, fast plasma waves are suppressed, because the magnetic field is frozen in the ions.

4. Now, we derive an equation that is analogous to Eq. (20) and describes a plasma configuration with the magnetic field B_θ. This equation, which can be used for investigating plasma currents far above the Alfvén ion current, $J \gg J_{Ai} \equiv m_i c^3 / Ze$, will be derived using a different method, specifically, the method that was mentioned at the end of the previous section and in which all the quantities are regarded as functions of both the coordinate r and time t.

We turn to the z-component of Eq. (6):

$$\frac{1}{r}\frac{\partial}{\partial r}(rB_\theta) = \frac{4\pi e}{c}(Zn_i v_{iz} - n_e v_{ez}) + \frac{1}{c}\frac{\partial E_z}{\partial t}, \quad (21)$$

where

$$B_\theta = -\frac{\partial A_z}{\partial r}, \quad E_z = -\frac{1}{c}\frac{\partial A_z}{\partial t}.$$

With the electron and ion velocities deduced from Eq. (4) and with their z-components expressed as functions of the electric field, Eq. (21) becomes

$$\frac{1}{r}\frac{\partial}{\partial r}\left(r\frac{\partial A_z}{\partial r}\right) - \frac{1}{c^2}\frac{\partial^2 A_z}{\partial t^2} = -\frac{E_r}{rR^*}. \quad (22)$$

In terms of the new Lagrangian invariants I_e^* and I_i^*, the quantity R^* on the left-hand side of Eq. (22) takes a form similar to definition (11),

$$I_e^* = \frac{B_\theta}{rn_e}, \quad I_i^* = \frac{B_\theta}{rn_i}, \quad \frac{dI_e^*}{dt} = \frac{dI_i^*}{dt} = 0 \quad (23)$$

and satisfies Eq. (12),

$$\frac{1}{R^*} = 4\pi e\left(\frac{Z}{I_i^*} - \frac{1}{I_e^*}\right), \quad \frac{dR^*}{dt} = 0. \quad (24)$$

Note that the quantity R^* is a dimensionless one, while the quantity R has the dimensionality of length.

The r-component of Eq. (6) and Eq. (8) give the following two equations for A_z and rE_r:

$$\frac{\partial A_z}{\partial t} + R^*\frac{\partial}{\partial t}(rE_r) = 0, \quad \frac{\partial A_z}{\partial r} + R^*\frac{\partial}{\partial r}(rE_r) = 0. \quad (25)$$

Using Eq. (24), we can establish a relationship between R^* and rE_r. We substitute v_r found from Eq. (4) into Eq. (24), express E_z and B_θ in terms of A_z and use Eq. (25) to ascertain that R^* satisfies an equation that exactly coincides with Eq. (16). Consequently, we have $R^* = R^*(rE_r)$.

Inserting this functional expression into Eqs. (25) yields the relationship $rE_r = \Phi(A_z)$, which puts Eq. (22) in the final form

$$\frac{1}{r}\frac{\partial}{\partial r}\left(r\frac{\partial A_z}{\partial r}\right) - \frac{1}{c^2}\frac{\partial^2 A_z}{\partial t^2} = \frac{1}{r^2}\Phi(A_z). \quad (26)$$

This equation describes the dynamics of the magnetic and electric fields in a plasma with a current flowing along the z-axis. The characteristic currents whose dynamics is described by Eq. (26) can be estimated from condition (3) in which B is replaced by the expression $B_\theta = 2J/rc$, relating the magnetic field to the current:

$$J \gg J_{Ai} \equiv \frac{m_i c^3}{Ze}. \quad (27)$$

It is well known that, in turbulent regimes, plasma turbulence tends to equalize some of the Lagrangian invariants [4, 10]. If the current flowing in a plasma gives rise to turbulence, then, as a result of such turbulent equalization, we have $R^* = \text{const} \equiv 1/\nu$ and $\Phi(A_z) = \nu^2 A_z$, in which case Eq. (26) can be solved by separating the variables. Among the numerous possible solutions, we choose the solution

$$A_z \sim \int_0^\infty N_\nu(rs)\sin(cts)ds, \quad (28)$$

where $N_\nu(x)$ is the Neumann function. For an arbitrary value of ν, this solution is asymptotically (at $ct \gg r$) unsteady. However, in the important particular case $\nu = 1$, the chosen solution A_z has the form

$$A_z \equiv 0, \quad t < \frac{r}{c}, \quad A_z \sim \frac{ct}{r\sqrt{(ct)^2 - r^2}}, \quad t > \frac{r}{c}, \quad (29)$$

which implies that, for $ct \gg r$, the magnetic flux density near the plasma axis relaxes to a steady state such that $A_z \sim 1/r$. This particular case, in which we have $R^* = 1$, corresponds to a plasma configuration whose characteristic scale length is on the order of the magnetic Debye radius r_B. Let us estimate the magnetic Debye radius $r_B \sim B_\theta/(4\pi e n_e)$ for the current $J = 100$ MA and the electron density $n_e = 10^{20}$ cm^{-3}. Using the expression that relates the magnetic field B_θ to the current, we can estimate r_B as $r_B \sim \sqrt{J/2\pi e n_e c}$, which gives $r_B \sim 0.5 \times 10^{-2}$ cm.

It should be kept in mind that the drift approximation, in which expression (29) was obtained, becomes invalid near the axis and the solution has no singularity as $r \longrightarrow 0$. The characteristic radius of this axial region is on the order of the ion Larmor radius $r_{Li} \sim m_i c^2/(eB_\theta) \sim r_B 4\pi n_i m_i c^2/B_\theta^2 \ll r_B$.

An analysis of the stability of the supercritical currents flowing in a plasma yields the following equation for the perturbed radial electric field δE_r:

$$\frac{1}{\rho}\frac{d}{d\rho}\frac{\rho}{1+\rho^2}\frac{d}{d\rho}\delta E_r$$

$$+\left\{\frac{2\Omega}{(1+\rho^2)^2}+\frac{\Omega^2}{1+\rho^2}-\frac{1}{\rho^2}\right\}\delta E_r = 0, \tag{30}$$

where $\rho \equiv k_z r$, $\Omega \equiv \omega/k_z c$, ω is the perturbation frequency, and k_z is the wave vector in the propagation direction of the current.

In turn, an analysis of Eq. (30) shows that the inevitable localization of the perturbing currents near the axis results in steady-state electric-field oscillations with $\Omega = -1$. This corresponds to nonzero perturbations of the quantity R^*.

5. The unsteady dynamics of a magnetized plasma has been investigated under the assumption that the plasma is inertialess. It is shown that, in a strong magnetic field such that $B^2 \gg 4\pi n_i m_i c^2$, the only dynamic process in the plasma is the evolution of the charge-separation electric field and the related magnetic field flux.

The results obtained make it possible to qualitatively explain the results from simulations of laser plasmas in which very intense laser radiation ($\sim 10^{22}$ W/cm^2) gives rise to strong magnetic fields ($B \sim 10^5$ T) and the ions are accelerated to nearly the speed of light [11]. For electron densities of about $n_e \sim 10^{21}$ cm^{-3}, the magnetic Debye radius in such plasmas is estimated to be $r_B \sim$ 1 μm, which corresponds to characteristic time scales of about $\tau \sim 10^{-14}$ s. An important role of the localization of the plasma current in the axial region was revealed in simulations carried by Bulanov *et al.* [11].

REFERENCES

1. B. B. Kadomtsev, *Collective Phenomena in a Plasma* (Nauka, Moscow, 1988).

2. *Basic Plasma Physics*, Ed. by A. A. Galeev and R. N. Sudan (Énergoatomizdat, Moscow, 1984; North-Holland, Amsterdam, 1984).

3. G. A. Askar'yan, S. V. Bulanov, F. Pegoraro, and A. M. Pukhov, Pis'ma Zh. Éksp. Teor. Fiz. **60**, 240 (1994) [JETP Lett. **60**, 251 (1994)].

4. A. V. Gordeev, Fiz. Plazmy **23**, 108 (1997) [Plasma Phys. Rep. **23**, 92 (1997)].

5. A. V. Gordeev and S. V. Levchenko, Fiz. Plazmy **25**, 217 (1999) [Plasma Phys. Rep. **25**, 193 (1999)].

6. A. V. Gordeev and S. V. Levchenko, Pis'ma Zh. Éksp. Teor. Fiz. **67**, 461 (1998) [JETP Lett. **67**, 482 (1998)].

7. A. V. Gordeev and T. V. Loseva, Pis'ma Zh. Éksp. Teor. Fiz. **70**, 669 (1999) [JETP Lett. **70**, 684 (1999)].

8. T. Zh. Esirkepov, Y. Sentoku, K. Mima, *et al.*, Pis'ma Zh. Éksp. Teor. Fiz. **70**, 80 (1999) [JETP Lett. **70**, 82 (1999)].

9. Yu. V. Gott and É. I. Yurchenko, Fiz. Plazmy **22**, 16 (1996) [Plasma Phys. Rep. **22**, 13 (1996)]; Fiz. Plazmy **24**, 315 (1998) [Plasma Phys. Rep. **24**, 285 (1998)]; Fiz. Plazmy **25**, 899 (1999) [Plasma Phys. Rep. **25**, 827 (1999)].

10. A. V. Gordeev, Preprint No. 5884/6 (Russian Research Centre Kurchatov Institute, Moscow, 1995).

11. S. V. Bulanov, N. M. Naumova, T. Zh. Esirkepov, *et al.*, Pis'ma Zh. Éksp. Teor. Fiz. **71**, 593 (2000) [JETP Lett. **71**, 407 (2000)].

Translated by O. E. Khadin

Emission of Alfvén Waves from a Nonuniform MHD Waveguide

N. G. Mazur, E. N. Fedorov, and V. A. Pilipenko

Schmidt Joint Institute of Physics of the Earth, Russian Academy of Sciences,
ul. Bol'shaya Gruzinskaya 10, Moscow, 123995 Russia
Received February 15, 2001; in final form, April 15, 2001

Abstract—The efficiency of the wave energy loss from a nonuniform MHD waveguide due to the conversion of the trapped magnetosonic waveguide modes into runaway Alfvén waves is estimated theoretically. It is shown that, if the waveguide parameters experience a jumplike change along the waveguide axis, the interaction between the waveguide modes and Alfvén waves occurs precisely at this "jump." This effect is incorporated into the boundary conditions. A set of coupled integral equations with a singular kernel is derived in order to determine the transmission and reflection coefficients for the waveguide modes. The poles in the kernels of the integral operators correspond to the surface waves. When the jump in the waveguide parameters is small, analytic expressions for the frequency dependence of the transformation coefficients are obtained by using a model profile of the Alfvén velocity along the magnetic field. For the jump characterized by the small parameter value $\varepsilon = 0.3$, the wave-amplitude transformation coefficient can amount to 5–10%. Under the phase synchronization condition (when the phase velocities of the waveguide modes on both sides of the jump are the same), the wave-energy transformation coefficient is much higher: it increases from a fraction of one percent to tens of percent. The transformation of fast magnetosonic waves into Alfvén waves is resonant in character, which ensures the frequency and wavelength filtering of the emitted Alfvén perturbations. © 2001 MAIK "Nauka/Interperiodica".

1. INTRODUCTION

In research on controlled nuclear fusion in tokamaks, auxiliary heating by RF fields at Alfvén frequencies [1–3] is successfully applied in addition to ohmic heating. The maximum auxiliary heating power is achieved when the Alfvén mode is strongly absorbed during the resonant excitation of a surface wave at a steep gradient of the plasma parameters [4, 5]. The highly nonuniform Alfvén velocity distribution and the related surface waves also occur at the interfaces between the plasma media in astrophysical plasmas. The excitation and dissipation of surface waves may play a role in the heating of the solar chromosphere [6]. In the Earth's magnetosphere, surface waves at the plasmapause are observed as a sort of pulsations of the geomagnetic field [7].

The mathematical formalism for describing the conversion of fast magnetosonic (FMS) modes into Alfvén waves is essentially identical to that for describing the conversion of electromagnetic waves into plasma oscillations [8, 9]. The excited surface wave plays an important role in the temporal evolution of the process of conversion of the electromagnetic wave into plasma oscillations at a steep plasma density gradient [10].

All of the above wave processes in laboratory and space plasmas were studied using one-dimensional models, which significantly simplify theoretical analysis. On the other hand, it is worth noting that the regions with an increased plasma density often form MHD waveguides, which are frequently encountered in space

plasmas. Such waveguides are able to absorb and accumulate the energy of hydrodynamic perturbations. Dense plasma sheets exist in the equatorial planes of the magnetospheres of the giant planets, such as Jupiter and Saturn [11, 12]. Near the Earth, the plasma density is increased in the equatorial plane of the magnetosphere [13] and in high-altitude cusps [14]. One of the characteristic plasma configurations in which hydrodynamic waveguide modes can propagate is the plasma sheet in the Earth's magnetotail [15, 16].

Information on the processes by which the wave energy is accumulated in the MHD waveguides near the Earth can be obtained by ground-based observations or by satellite observations. This is possible because the modes trapped in a waveguide are converted into Alfvén waves capable of propagating over large distances along the magnetic field lines without being scattered in space. In attempting to interpret the data from actual observations in terms of the conversion mechanism, it is necessary to estimate the wave energy loss from an MHD waveguide due to the conversion of the trapped magnetosonic waves into Alfvén waves. Fedorov *et al.* [17] considered a waveguide where FMS waves are converted into Alfvén waves at smooth plasma inhomogeneities to which the Wentzel–Kramers–Brillouin (WKB) approximation can be applied. Here, we analyze the conversion of FMS waves into Alfvén waves in a waveguide whose parameters change along the axis in a stepwise manner.

2. HYDROMAGNETIC WAVEGUIDE FOR FMS WAVES

We consider an inhomogeneous plasma in a constant magnetic field $\mathbf{B}_0$. We assume that, in a certain plasma layer, the plasma density is increased at the center and decreased monotonically away from the center, so that the Alfvén velocity $V_A(z)$ at the center is minimum. Since there is a "well" in the Alfvén velocity distribution, the layer serves as a waveguide for FMS perturbations. We choose a Cartesian coordinate system (x, y, z) with the z- and x-axes directed along the magnetic field $\mathbf{B}_0$ and the waveguide axis, respectively, and assume that the plasma is homogeneous along the y-axis (Fig. 1).

We neglect thermal and kinetic effects in order to describe the plasma perturbations by the ideal MHD equations. According to [17, 18], it is convenient to introduce the potentials ψ and φ for FMS and Alfvén perturbations, respectively, in which case the electric and magnetic fields, $\mathbf{E}$ and $\mathbf{B}$, can be represented as $\mathbf{E} = \mathbf{E}_A + \mathbf{E}_M$ and $\mathbf{B} = \mathbf{B}_A + \mathbf{B}_M$, where

$$\mathbf{E}_A = -\nabla_\perp \varphi, \quad \mathbf{E}_M = [\mathbf{e}_z \times \nabla]\psi,$$
$$\partial_t \mathbf{B}_A = [\mathbf{e}_z \times \nabla]\partial_z \varphi, \quad \partial_t \mathbf{B}_M = \nabla_\perp \partial_z \psi - (\nabla_\perp^2 \psi)\mathbf{e}_z. \tag{1}$$

Here, we use the notation $\nabla_\perp = \mathbf{e}_x \partial_x + \mathbf{e}_y \partial_y$. Substituting expressions (1) into Maxwell's equations gives the equations for the potentials.

We start by considering a simple case in which the Alfvén velocity V_A is uniform along the waveguide axis and depends only on z, $V_A = V_A(z)$. For such a waveguide, the potentials satisfy the equations [17]

$$(\partial_{zz} - V_A^{-2}\partial_{tt})\varphi = 0,$$
$$(\nabla_\perp^2 + \partial_{zz} - V_A^{-2}\partial_{tt})\psi = 0. \tag{2}$$
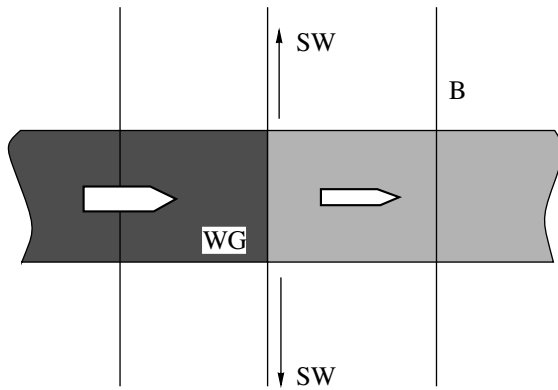
Fig. 1. Geometry of a model MHD waveguide. The arrows show the propagation directions of the waveguide mode (WG) and surface wave (SW).

If the potentials obey the dependence $\propto \exp(-i\omega t)$, Eqs. (2) reduce to

$$L_A \varphi = 0, \quad (\nabla_\perp^2 + L_A)\psi = 0, \tag{3}$$

where $L_A = \partial_{zz} + k_A^2$ is the Alfvén operator and $k_A = \omega/V_A$ is the Alfvén wavenumber. If the Alfvén velocity is independent of the transverse coordinates x and y, then Eqs. (3) for the potentials of FMS and Alfvén waves are decoupled, so that the waves do not interact.

Let us describe the structure of the modes that can propagate in the waveguide under consideration. To simplify the model, we assume that $k_A(z) \longrightarrow k_\infty > 0$ as $z \longrightarrow \pm\infty$. We introduce the function $U(z) = k_\infty^2 - k_A^2(z)$, which is negative and obeys the relationships $U(-\infty) = U(\infty) = 0$. Since the plasma is homogeneous in the y direction, different harmonics of the perturbed potentials, $\propto \exp(ik_y y)$, can be treated separately. The equation for ψ, the second one in Eqs. (3), takes the form

$$[\partial_{xx} - k_y^2 + k_\infty^2 + \partial_{zz} - U(z)]\psi(x, z) = 0.$$

Since this equation is uniform in x, it has the solutions $\psi(x, z) = \exp(i\kappa x)e(z)$, in which the profile $e(z)$ along the z-axis is described by the following spectral problem with the parameter ν:

$$[-\partial_{zz} + U(z)]e_\nu(z) = \nu^2 e_\nu(z). \tag{4}$$

The wavenumber $k_\perp = (\kappa^2 + k_y^2)^{1/2}$ is related to the spectral parameter ν by $k_\perp^2 = k_\infty^2 - \nu^2$, which yields $\kappa^2 = k_\infty^2 - k_y^2 - \nu^2$.

Equation (4) is a one-dimensional Schrödinger equation with the potential $U(z)$, which has one minimum, e.g., $U(z = 0) = U_0$. If the function $U(z)$ decreases sufficiently sharply at infinity, then the spectrum of problem (4) consists of a finite number of discrete eigenvalues ν_n^2 within the interval $U_0 < \nu_n^2 < 0$ and a continuum of eigenvalues ν^2 in the positive z-axis $(0, +\infty)$. The properties of the continuous spectrum in the spectral problem (4) that are required for further analysis are described in Appendix A. Here, we are interested in the eigenfunctions $e_n(z)$ ($n = 1, \ldots, N$) corresponding to the eigenvalues $\nu_n^2 < 0$, because these eigenfunctions describe the waveguide modes with the potentials $\psi_n(x, z) = \exp(i\kappa_n x)e_n(z)$ ($\kappa_n^2 = k_\infty^2 - k_y^2 - \nu_n^2$), which are trapped in the layer with a depressed Alfvén velocity. The eigenfunctions $e_n(z)$ decrease exponentially with distance from the waveguide layer: $e_n(z) \propto \exp(-|\nu_n z|)$ for $|z| \longrightarrow \infty$. We assume that these eigenfunctions satisfy the conventional normalization condition $\int_{-\infty}^{+\infty} e_m \bar{e}_n dz = \delta_{mn}$.

3. GENERAL THEORY OF THE EMISSION OF SURFACE WAVES FROM AN MHD WAVEGUIDE WITH A SHARP PLASMA INHOMOGENEITY

In a longitudinally nonuniform waveguide such that $V_A = V_A(x, z)$, the FMS waveguide modes propagating along the waveguide axis can generate Alfvén waves. In this case, instead of the decoupled equations (2) for the potentials, we are faced with a far more complicated set of coupled equations [17, 18]:

$$\nabla_\perp(\partial_{zz} + k_A^2)\nabla_\perp\varphi = (\nabla_\perp k_A^2 \cdot [\mathbf{e}_z \times \nabla]\psi),$$

$$\nabla_\perp(\nabla_\perp^2 + k_A^2)\nabla_\perp\psi = -(\nabla_\perp k_A^2 \cdot [\mathbf{e}_z \times \nabla]\varphi).$$

From these equations, we see that FMS waves (with the potential $\propto \psi$) can generate Alfvén perturbations (with the potential $\propto \varphi$) if the Alfvén velocity V_A changes along the waveguide axis. Here, we are interested in the situation when the Alfvén velocity changes sharply over the wavelength of FMS waves, in which case the emitted Alfvén waves are similar in structure to the surface waves. Let the Alfvén velocity change in a step-wise manner from $V_A^-(z)$ to $V_A^+(z)$ at $x = 0$:

$$V_A(x, z) = \begin{cases} V_A^-(z) & \text{for} \quad x < 0 \\ V_A^+(z) & \text{for} \quad x > 0. \end{cases}$$

In each of the half-spaces $x < 0$ and $x > 0$, the Alfvén velocity is uniform in x. Consequently, the electromagnetic field on both sides of the boundary $x = 0$ can be described by simple equations (3). Since FMS waves interact with Alfvén perturbations only at the boundary between the half-spaces, the coupling between Eqs. (3) can be incorporated into the boundary conditions. Hence, the potential ψ satisfies the conditions

$$\psi = \psi^-, \quad (\nabla_\perp^2 + k_-^2 - L_-)\psi^- = 0 \quad \text{for} \quad x < 0,$$
$$\psi = \psi^+, \quad (\nabla_\perp^2 + k_+^2 - L_+)\psi^+ = 0 \quad \text{for} \quad x > 0, \tag{5}$$

where $L_\mp = -\partial_{zz} + U_\mp(z)$, $U_\mp(z) = k_\mp^2 - (k_A^\mp)^2$, and $k_A^\mp(-\infty) = k_A^\mp(+\infty) = k_\mp$.

The electromagnetic field components tangential to the boundary between the half-spaces, namely, the components $\mathbf{E}_\tau$ and $\mathbf{B}_\tau$, are related by the conditions

$$\mathbf{E}_\tau|_{x=+0} - \mathbf{E}_\tau|_{x=-0} = 0,$$
$$\mathbf{B}_\tau|_{x=+0} - \mathbf{B}_\tau|_{x=-0} = \mu_0\mathbf{I} \times \mathbf{e}_x, \tag{6}$$

where $\mathbf{I}$ is the surface current flowing along the boundary. In what follows, we need only two of the four conditions (6) imposed on the field components. In fact, one of the conditions, specifically, the condition that the longitudinal component of the electric field be continuous, holds automatically, because, in ideal magnetohydrodynamics, we have $E_z = E_\parallel = 0$. The relationship

$B_y|_{x=+0} - B_y|_{x=-0} = \mu_0 I_z$ serves to determine the field-aligned surface current at the boundary. The remaining two conditions have the form

$$E_y|_{x=+0} - E_y|_{x=-0} = 0,$$
$$B_z|_{x=+0} - B_z|_{x=-0} = 0. \tag{7}$$

In order to transform these relationships into the boundary conditions for the potential ψ, we turn to Eqs. (1), which yield the following expressions for the components E_y and B_z of the electromagnetic field of FMS waves: $E_y = \partial_x\psi$ and $i\omega B_z = \nabla_\perp^2\psi$. We substitute these expressions into conditions (7) and take into account Eqs. (5) to obtain

$$\partial_x\psi^-|_{x=-0} = \partial_x\psi^+|_{x=+0},$$
$$(L_- - k_-^2)\psi^-|_{x=-0} = (L_+ - k_+^2)\psi^+|_{x=+0}. \tag{8}$$

Now, we should specify the wave process that serves as an energy source for an Alfvén wave generated at the boundary between the semi-infinite homogeneous plasma media. As was shown in Section 2, the equations for a medium that is homogeneous in the x direction have solutions describing the waveguide modes. An FMS perturbation propagating along the waveguide is generally a superposition of all possible waveguide modes; for our purposes here, it is sufficient to consider only one of them, specifically, the mode that is incident on the boundary, e.g., from the left (Fig. 1). At the boundary, this mode is partly reflected back into the original medium and partly transmitted into the second medium. Also, this mode may excite other waveguide modes, which propagate away from the boundary in both media. However, since we are interested in wave generation along the boundary between two homogeneous plasma media (in the direction of $\mathbf{B}_0$), we restrict ourselves, for simplicity, to analyzing the situation in which only one waveguide mode exists on both sides of the boundary.

In order to describe the wave process in question, we solve the boundary-value problem (5) with the boundary conditions (8). According to the method for separating the Fourier variables, we expand the desired solution in the spectra of the operators $L_\mp$:

$$\psi^-(x, z) = [\exp(i\kappa_1^- x) + R_1\exp(-i\kappa_1^- x)]e_1^-(z)$$
$$+ \int_{-\infty}^{+\infty} R_\nu\exp(-i\kappa_\nu^- x)e_\nu^-(z)d\nu,$$
$$\psi^+(x, z) = D_1\exp(i\kappa_1^+ x)e_1^+(z) \tag{9}$$
$$+ \int_{-\infty}^{+\infty} D_\nu\exp(i\kappa_\nu^+ x)e_\nu^+(z)d\nu.$$

Here, $(\kappa_1^{\mp})^2 = k_{\mp}^2 - k_y^2 - (\nu_1^{\mp})^2$, $(\kappa_\nu^{\mp})^2 = k_{\mp}^2 - k_y^2 - \nu^2$; R_1 and D_1 are the reflection and transmission coefficients for the waveguide mode, respectively; and the analogous coefficients R_ν and D_ν refer to the continuum. The functions $e_n(z)$ of the discontinuous spectrum of the operator L were described in Section 2, and the continuum is discussed in detail in Appendix A.

We substitute expressions (9) for the potential ψ into conditions (8) at the boundary $x = 0$ to obtain the relationships

$$\kappa_1^-(1 - R_1)e_1^-(z) - \int\limits_{-\infty}^{+\infty} \kappa_\mu^- R_\mu e_\mu^-(z)d\mu$$

$$= \kappa_1^+ D_1 e_1^+(z) + \int\limits_{-\infty}^{+\infty} \kappa_\mu^+ D_\mu e_\mu^+(z)d\mu,$$

$$\lambda_1^-(1 + R_1)e_1^-(z) + \int\limits_{-\infty}^{+\infty} \lambda_\mu^- R_\mu e_\mu^-(z)d\mu$$

$$= \lambda_1^+ D_1 e_1^+(z) + \int\limits_{-\infty}^{+\infty} \lambda_\mu^+ D_\mu e_\mu^+(z)d\mu,$$

(10)

where $\lambda_1^{\mp} = k_{\mp}^2 - (\nu_1^{\mp})^2$ and $\lambda_\nu^{\mp} = k_{\mp}^2 - \nu^2$. To simplify the formulas, we use the notation $k_\perp^2 = \lambda$ with the corresponding indices.

Taking the scalar product of relationships (10) with e_1^- and e_ν^- and carrying out simple but rather laborious manipulations, which are presented in Appendix B, we arrive at the final set of equations for the coefficients R_1, D_1, R_ν, and D_ν:

$$R_1 = R_1^{(0)} + \int\limits_{-\infty}^{+\infty} F_R(\nu)D_\nu d\nu, \tag{11}$$

$$D_1 = D_1^{(0)} + \int\limits_{-\infty}^{+\infty} F_D(\nu)D_\nu d\nu, \tag{12}$$

$$R_\nu = R_\nu^{(0)} + \int\limits_{-\infty}^{\infty} K_R(\nu, \mu)D_\mu d\mu, \tag{13}$$

$$D_\nu = D_\nu^{(0)} + \int\limits_{-\infty}^{\infty} K_D(\nu, \mu)D_\mu d\mu. \tag{14}$$

The free terms and the kernels of these equations are represented by formulas (B.2), (B.3), (B.8), and (B.9) in Appendix B. We direct attention to the general structure of the equations derived: Eq. (14) is an integral equation of the second kind for the function D_ν. Having

found a solution to this equation, we can determine the remaining coefficients R_1, D_1, and R_ν, because Eqs. (11)–(13) relate them to D_ν.

It is important to note that the quantities $D_\nu^{(0)}$, K_D, $R_\nu^{(0)}$, and K_R contain the resonant denominator

$$\Delta(\nu) = \lambda_\nu^+ \kappa_\nu^- + \lambda_\nu^- \kappa_\nu^+$$

$$= (k_+^2 - \nu^2)\sqrt{k_-^2 - k_y^2 - \nu^2} + (k_-^2 - \nu^2)\sqrt{k_+^2 - k_y^2 - \nu^2},$$

which is the dispersion function of the surface wave generated at the boundary $x = 0$. The roots $\nu = \pm\nu_s$ of the equation $\Delta(\nu) = 0$ are the wavenumbers of this wave, in which case the values of $|\nu_s|$ lie between k_- and k_+. The representation of the wave field in the form of Eq. (12) was obtained by expanding the solution in the discrete and continuous spectra of the transverse operators $L_{\mp}$. The surface perturbations are described in terms of the potentials ψ_- and ψ_+ of the wave fields that are similar in structure to FMS perturbations in each half-space. However, since these potentials obey different conditions at the boundary $x = 0$, it is impossible to introduce a unified potential ψ, which would be continuous over the entire space. This indicates that the potentials ψ_- and ψ_+ describe the coupled FMS and Alfvén perturbations. The discontinuity $(\psi_+ - \psi_-)|_{x=0}$ corresponds to the field-aligned surface current I_z of a surface wave propagating along the jump in the Alfvén velocity, i.e., along the boundary $x = 0$. The field of the surface wave will be explicitly calculated below by closing the integration contour in Eq. (12) in the plane of the complex variable ν. As a result, the field will be represented as the sum of the residues at the poles of the integrands (i.e., at the points $\pm\nu_s$) and the integrals along contours along both sides of the cuts drawn from the branch points. The integrals along both sides of the cuts describe FMS waves propagating away from the boundary in both media, while the residues describe the surface waves that are localized in x and represent the coupled FMS and Alfvén perturbations. We emphasize that the surface waves experience no reflection and propagate away from the boundary in both directions along the z-axis.

The kernels K_D and K_R possess an important property: each of them can be represented as a sum of the degenerate component (the product of the functions of ν and μ) and the nondegenerate component, which determines the singular operator with a Hilbert kernel:

$$K_D(\nu, \mu) = -\frac{1}{2}D_\nu^{(0)}\Phi(\mu) + \frac{C_D(\nu, \mu)}{\mu^2 - \nu^2},$$

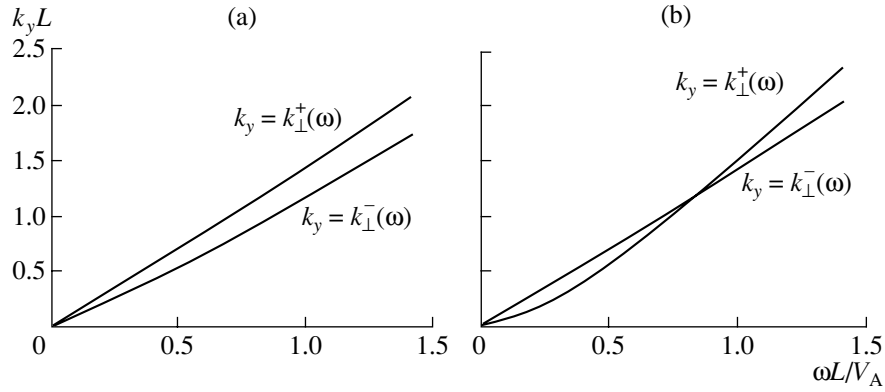$$K_R(\nu, \mu) = -\frac{1}{2}R_\nu^{(0)}\Phi(\mu) + \frac{C_R(\nu, \mu)}{\mu^2 - \nu^2},$$

(15)

Fig. 2. Phase diagrams and synchronization conditions of the waveguide modes.

where

$$\Phi(\mu) = \left(\frac{\lambda_\mu^+}{\lambda_1^-} + \frac{\kappa_\mu^+}{\kappa_1^-}\right)(e_\mu^+, e_1^-), \qquad (16)$$

and the quantities $D_\nu^{(0)}$, $R_\nu^{(0)}$, C_D, and C_R are described by fairly involved explicit expressions (B.9) and (B.8) given in Appendix B.

The efficiency for conversion of the waveguide mode into a surface wave can be characterized by the quantities

$$K = \int_{-\infty}^{\infty} [S_z^{(SW)}(x, +\infty) - S_z^{(SW)}(x, -\infty)]$$
$$\times dx \left[\int_{-\infty}^{\infty} S_x^{(WG)}(z)dz\right]^{-1} \qquad (17)$$

and

$$b_\pm = \max\left|\mathbf{B}_\pm^{(SW)}\right|(\max|\mathbf{B}^{(WG)}|)^{-1}, \qquad (18)$$

which will be referred to as the wave-energy and wave-magnetic-field conversion coefficients, respectively. Here, $\mathbf{S}^{(WG)}$ and $\mathbf{B}^{(WG)}$ are, respectively, the averaged Poynting vector $\mathbf{S} = (2\mu_0)^{-1}\mathrm{Re}[\mathbf{E} \times \bar{\mathbf{B}}]$ and the magnetic induction vector of the incident waveguide mode and $\mathbf{S}^{(SW)}$ and $\mathbf{B}^{(SW)}$ are the same vectors of the surface wave far from the waveguide axis.

It is important to note that the very formulation of the problem implies the existence of the waveguide mode with the potential $\psi^{(WG)} = e_1^-(z)\exp(i\kappa_1^- x)$, which propagates in the medium to the left from the jump in the Alfvén velocity. In other words, the parameters ω and k_y should belong to the transmission band of the entrance channel of the waveguide. In a uniform waveguide, the wavenumber is a function of frequency, $k_\perp = k_\perp(\omega)$. Here, we speak of a particular waveguide

mode, e.g., the mode with $k_\perp^2 = k_\infty^2 - \nu_1^2$. In the x direction, the waveguide can transmit modes with $k_y < k_\perp(\omega)$. Recall that the waveguide under investigation consists of two homogeneous plasma media, each with its own dependence of $k_\perp$ on ω. Depending on the relative shapes of the longitudinal profiles of $V_A(z)$ on both sides of the boundary between the media, the boundaries of the transmission bands, $k_y = k_\perp^-(\omega)$ and $k_y = k_\perp^+(\omega)$, either do not intersect (Fig. 2a) or intersect at a certain point (ω_*, k_*) (Fig. 2b). The latter case is of particular interest because, at the frequency $\omega = \omega_*$, the wavenumbers of the waveguide mode in both media coincide, which indicates synchronization of the entrance and exit channels of the waveguide. This situation can take place only under the following condition: the difference of the background Alfvén velocities far from the waveguide, $V_A^+(\pm\infty) - V_A^-(\pm\infty)$, and that at the waveguide center, $V_A^+(0) - V_A^-(0)$, should have opposite signs (Fig. 3). If these differences have the same signs, then synchronization of the entrance and exit channels of the waveguide is impossible.

4. PERTURBATION THEORY FOR A WEAKLY NONUNIFORM WAVEGUIDE

In a general formulation, the problem is very difficult to solve mathematically. In order to give insight into the characteristic features of the wave process, we consider the limiting case of a small jump in the Alfvén velocity at the boundary between two homogeneous plasma media:

$$\left|\frac{V_A^+}{V_A^-} - 1\right| \ll 1.$$

In this case, we can derive explicit expressions for all of the quantities of interest to us. We set $U_+(z) - U_-(z) =$
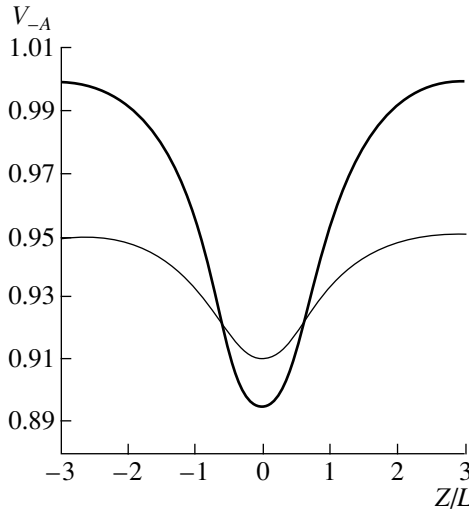
Fig. 3. Model profile of the Alfvén velocity along the magnetic field.

$\varepsilon h(z)$ and $k_+^2 - k_-^2 = \varepsilon d$, where ε is a small parameter. The function $\varepsilon h(z)$ can be regarded as a perturbation of the operator L_- across the boundary $x = 0$; i.e., we can set $L_+ = L_- + \varepsilon h(z)$. The corrections to the eigenvalues and eigenfunctions of the discrete spectra can be found using the standard Schrödinger perturbation theory [19]; the corresponding estimates for the continuum are presented in Appendix A.

The potential $\psi^{(SW)}(x, z)$ of the surface wave far from the waveguide axis can be calculated from the coefficients D_ν and R_ν, which should be found in advance by solving Eqs. (14) and (13), and from the asymptotic estimates (for $z \longrightarrow \pm\infty$) of the integrals over the continuum in expansion (9). In this case, the perturbation of the original waveguide mode is determined by the coefficients D_1 and R_1.

It follows from further analysis that the efficiency with which the waveguide mode is converted into a surface wave is the highest near the boundary of the transmission band of the entrance channel of the waveguide, i.e., for $\kappa_1^-(\omega, k_y) \longrightarrow 0$. Consequently, it is necessary to obtain uniform asymptotic estimates for D_ν and R_ν that are valid for $\varepsilon \longrightarrow 0$ up to the boundary of the transmission band. In order to simplify matters, we denote κ_1^- by κ.

For $\varepsilon \longrightarrow 0$ at fixed κ, the free terms $D_\nu^{(0)}$ and $R_\nu^{(0)}$ in Eqs. (14) and (13) are first-order quantities. The nondegenerate components of the kernels K_D and K_R, i.e., the second terms on the right-hand sides of representations (15), are also proportional to ε; moreover, the corresponding proportionality coefficients are uniform in the parameter κ. On the other hand, the estimate $\Phi(\mu) = O(\varepsilon)$, which follows from expression (16) at fixed κ and

the relationship $(e_\mu^+, e_1^-) = O(\varepsilon)$, is nonuniform as $\kappa \longrightarrow 0$, because the function $\Phi(\mu)$ contains the term proportional to $\propto \kappa^{-1}$.

Hence, although the degenerate components of the kernels K_D and K_R are on the order of ε^2, they should be taken into account in obtaining uniform asymptotic estimates, whereas the nondegenerate components can be neglected. The leading-order terms of the uniform asymptotic estimates can be found from the following set of equations with nondegenerate kernels:

$$D_\nu = D_\nu^{(0)} - \frac{1}{2}\int\limits_{-\infty}^{+\infty} D_\nu^{(0)}\Phi(\mu)D_\mu d\mu,$$

$$R_\nu = R_\nu^{(0)} - \frac{1}{2}\int\limits_{-\infty}^{+\infty} R_\nu^{(0)}\Phi(\mu)D_\mu d\mu. \tag{19}$$

These equations have the solution

$$D_\nu = AD_\nu^{(0)}, \quad R_\nu = AR_\nu^{(0)},$$

$$A = \left(1 + \frac{1}{2}\int\limits_{-\infty}^{+\infty} \Phi(\nu)D_\nu^{(0)}d\nu\right)^{-1}. \tag{20}$$

By exploiting the smallness of ε, we can significantly simplify expressions (B.8), (B.9), and (16) for $D_\nu^{(0)}$, $R_\nu^{(0)}$, and $\Phi(\nu)$. When analyzing the situation near the boundary of the transmission band, we can also replace the quantities that remain finite as $\kappa \longrightarrow 0$ by their values at $\kappa = 0$. As a result, we obtain

$$D_\nu^{(0)} = -R_\nu^{(0)} = \frac{\varepsilon C_0 k_\perp^2 h_\nu^-}{2(\nu^2 + a^2)(\nu^2 - \nu_s^2)},$$

$$\Phi(\nu) = -\frac{i\varepsilon \overline{h_\nu^-}}{\kappa\sqrt{\nu^2 + a^2}}, \tag{21}$$

where we introduced the notation

$$h_\nu^- = (e_\nu^-, he_1^-), \quad a^2 = -(\nu_1^-)^2 > 0, \quad k_\perp^2 \equiv \lambda_1^- = k_-^2 + a^2,$$

$$C_0 = 2(1 + \sqrt{1 + \kappa^{-2}\varepsilon P_1})^{-1} \quad (\lambda_1^+ - \lambda_1^- = \varepsilon P_1 + O(\varepsilon^2)).$$

Using expressions (21), we find the coefficient A in solution (20):

$$A = \left\{1 - \frac{i\varepsilon^2 C_0 k_\perp^2}{4\kappa}\int\limits_{-\infty}^{+\infty} \frac{|h_\nu|^2 d\nu}{(\nu^2 + a^2)^{3/2}[\nu^2 - (k_- + i0)^2]}\right\}^{-1}. \tag{22}$$

Now, we estimate the integrals over the continuum in expressions (9), restricting the analysis to the wave

field far from the waveguide axis. For example, we consider

$$\psi_{\text{cont}}^-(x, z) = \int_{-\infty}^{\infty} R_\nu \exp(-i\kappa_\nu^- x)e_\nu^-(z)d\nu. \qquad (23)$$

To be specific, we analyze the limit $z \longrightarrow +\infty$, in which we take into account expressions (A.5) and (A.6) to obtain

$$\psi_{\text{cont}}^-(x, z) = \int_{-\infty}^{\infty} \alpha_\nu^- R_\nu \exp(-i\kappa_\nu^- x + i\nu z)d\nu$$

$$+ \int_{-\infty}^{\infty} \beta_\nu^- R_\nu \exp(-i\kappa_\nu^- x - i\nu z)d\nu. \qquad (24)$$

In order to take the integrals on the right-hand side of expression (24), we close the integration contours for the first and second integrals through the upper and lower half-planes of the plane of the complex variable ν, respectively. The integrands have poles at the points $\nu = \pm(\nu_s + i0)$ (we displace the poles from the real axis by infinitely small distances in order to take into account an arbitrarily small dissipation and thus to obtain a physically correct result). The calculation of the integrals in expression (24) reduces to the calculation of the residues at the indicated poles and integration along contours along both sides of the cuts, which are necessary in order to deal with the single-valued branch of the integrand. For the first integral in expression (24), the cut is drawn from the branch point $\nu = i\sqrt{k_y^2 - k_-^2}$ upward along the imaginary axis around the pole $\nu = ia$, in which case, when considering the region adjacent to the boundary of the transmission band, we can restrict ourselves to the inequality $k_y > k_-$; i.e., we can assume that the branch point of the function κ_ν^- lies on the imaginary axis. For the second integral in expression (24), the cut is drawn in a similar way— from the branch point $\nu = -i\sqrt{k_y^2 - k_-^2}$ downward along the imaginary axis.

For $z \longrightarrow +\infty$, the integrals along contours along both sides of the cuts are negligibly small. Hence, we are left with the problem of calculating the residues at the points $\nu = \pm(\nu_s + i0)$. The integral $\psi_{\text{cont}}^+(x, z) = \int_{-\infty}^{\infty} D_\nu \exp(i\kappa_\nu^+ x)e_\nu^+(z)d\nu$ can be treated in a similar way. As a result, we obtain

$$\psi_{\text{cont}}^{\mp}(x, z) = \pm\frac{\varepsilon\pi}{2ik_-}AC_0(\alpha_{k_-}^- h_{k_-}^- + \overline{\beta_{k_-}^- h_{k_-}^-})$$

$$\times \exp(-k_y|x| + ik_- z). \qquad (25)$$

Here, we take into account the fact that $\nu_s^2 \longrightarrow k_-^2$ as $\varepsilon \longrightarrow 0$; recall that the value of ν_s^2 is intermediate between the values of k_-^2 and k_+^2, and that $k_+^2 - k_-^2 = \varepsilon d \longrightarrow 0$. In the limit $z \longrightarrow -\infty$, we arrive at analogous formulas:

$$\psi_{\text{cont}}^{\mp}(x, z) = \pm\frac{\varepsilon\pi}{2ik_-}AC_0(\gamma_{k_-}^- h_{k_-}^- + \overline{\delta_{k_-}^- h_{k_-}^-})$$

$$\times \exp(-k_y|x| - ik_- z). \qquad (26)$$

Using expressions (25) and (26) for the potentials of the surface wave, we can calculate the conversion coefficients (17) and (18):

$$K = \varepsilon^2 C_0^2|A|^2 \frac{k_y}{k_- \kappa_1^- k_\perp^2}(q_+ + q_-),$$

$$b_\pm^2 = \varepsilon^2 C_0^2|A|^2 \frac{k_y^2}{k_\perp^5 \max w(z)}q_\pm, \qquad (27)$$

where

$$q_+ = \frac{\pi^2}{2}\left|\alpha_{k_-}^- h_{k_-}^- + \overline{\beta_{k_-}^- h_{k_-}^-}\right|^2,$$

$$q_- = \frac{\pi^2}{2}\left|\gamma_{k_-}^- h_{k_-}^- + \overline{\delta_{k_-}^- h_{k_-}^-}\right|^2,$$

$$w(z) = k_\perp^{-3}(\partial_z e_1^-)^2 + k_\perp^{-1}(e_1^-)^2.$$

The coefficients α_ν, β_ν, γ_ν, and δ_ν are given by formulas (A.6) in Appendix A; the minus superscript indicates that these coefficients are calculated from the "unperturbed" potential $U_-(z)$. Note that, for a symmetric longitudinal profile $V_A(z)$, we obviously have $q_+ = q_-$.

5. COEFFICIENTS FOR CONVERSION OF THE WAVEGUIDE MODE INTO A SURFACE ALFVÉN WAVE

Let us consider in more detail the structure of expressions (27) for the conversion coefficients $K(\omega, \kappa, \varepsilon)$ and $b(\omega, \kappa, \varepsilon)$. The factors $q_\pm$ depend only on the frequency ω; consequently, when studying the behavior of K and b near the cutoff frequency, they can be regarded as being constant. The calculations carried out in Section 6 for a particular example show that each of the functions $q_\pm(\omega)$ vanishes in both limits $\omega \longrightarrow 0$ and $\omega \longrightarrow \infty$ and has one or several maxima.

When estimating different factors in expressions (27), we normalize them to the characteristic transverse scale length L of the waveguide layer. In order of magnitude, the factor $q_\pm L^3$ is fairly small: it is about 0.1 or even smaller. Because of the smallness of the quantity ε^2, the coefficient K, which contains the small denominator κL, is essentially nonzero only near the boundary

of the transmission band. As for the coefficient b, it obeys the relationship $b \propto \varepsilon \sqrt{q_\pm L^3}$, so that the region where it is not too small is wider.

Unlike the factor $q_\pm L^3$, the factors $k_y k_-^{-1} k_\perp^{-2} L^{-2}$ and $k_y^2 k_\perp^{-5} L^{-3}/\max w(z)$ in expressions (27) are easy to estimate analytically. They remain finite as $\kappa \longrightarrow 0$ ($k_y = \sqrt{k_\perp^2 - \kappa^2}$). For moderate frequencies, $\omega \sim V_A L^{-1}$, they are typically on the order of unity. Finally, we turn to the factor $F = \varepsilon^2 C_0^2 |A|^2$ in expressions (27). This factor depends in a fairly complicated fashion on the three parameters ω, κ, and ε and plays an important role (especially in combination with the factor κ in the denominator of K) in determining the behavior of K and b near the boundary of the transmission band (as $\kappa \longrightarrow 0$). An analysis of the dependence of F on κ shows that the functions $C_0(\kappa)^2$ and $|A(\kappa)|^2$ increase monotonically from zero at $\kappa = 0$ to unity for $\kappa \longrightarrow \infty$. The transition occurs near the boundary of the transmission band, in a narrow region whose width depends on the value of the small parameter ε. The quantity C_0 is a function of the dimensionless combination $\xi = \kappa(\varepsilon P_1)^{-1/2}$: $C_0 = 2\xi(\xi + \sqrt{\xi^2 + 1})^{-1}$. We can see that, for $\kappa \longrightarrow 0$, the function C_0^2 is proportional to κ^2 and thus cancels the factor κ in the denominator in $K(\kappa)$, even without recourse to the function $|A|^2$. As a result, the conversion coefficient $K(\kappa)$ decreases to zero as $\kappa \longrightarrow 0$, and, near the boundary of the transmission band, it has a maximum on the order of $\varepsilon^{3/2} P_1^{-1/2} L^{-1}$ at $\kappa \sim \sqrt{\varepsilon P_1}$.

Note that, at the zero argument, the slope of the function $C_0(\kappa)$ increases without bound as $P_1 \longrightarrow 0$. For $P_1 = 0$, the function $C_0(\kappa)$ is identically unity. Consequently, if the function $P_1(\omega)$ vanishes at a certain value $\omega = \omega_*$ (in Section 3, this situation was called the synchronization of the entrance and exit channels of the waveguide), then an increase in $K(\kappa)$ as $\kappa \longrightarrow 0$ is now restricted by the factor $|A(\kappa)|^2$. For $C_0 \equiv 1$, this factor is a function of the combination $\eta = \kappa L/\varepsilon^2$:

$$ A = \left(1 + \frac{\alpha + i\beta}{\eta}\right)^{-1}, \quad |A|^2 = \frac{\eta^2}{(\eta + \alpha)^2 + \beta^2}. $$

Here, the meaning of the quantities $\alpha(\omega)$ and $\beta(\omega)$ can be understood by reference to expression (22). Consequently, for $\omega = \omega_*$, the conversion coefficient $K(\kappa)$ reaches its maximum at $\kappa L \sim \varepsilon^2$, the maximum value being independent of ε! As ω approaches ω_*, the above case with $\max K \sim \varepsilon^{3/2} P_1^{-1/2} L^{-1}$ transforms gradually (for $L^2 P_1(\omega) \sim \varepsilon^3$) to the case with $\max K \sim 1$.

6. NUMERICAL ESTIMATES FOR A MODEL WAVEGUIDE

Let the longitudinal profile $V_A(z)$ in the region $x < 0$ of the incident waveguide mode be specified as

$$ V_A^2(z) = V_-^2[1 + \gamma^2/\cosh^2(z/L)]^{-1}, $$

where L is the characteristic thickness of the plasma layer. This shape of the profile $V_A(z)$ (see Fig. 2) is chosen in such a way that the potential $U(z)$ in the Schrödinger equation (4) admits an explicit solution of the eigenvalue problem [19]. The parameter γ characterizes the relative depth of the well of the profile $V_A(z)$: $1 - \min(V_A/V_-)^2 = \gamma^2/(1 + \gamma^2)$. In calculations, we normalize the frequency ω to the background Alfvén frequency, thus introducing the dimensionless parameter $\Omega = \omega L/V_-$. After renormalization of the linear scale length, $\zeta = z/L$, the Schrödinger equation (4) becomes

$$ [\partial_{\zeta\zeta} + \gamma^2 \Omega^2 (\cosh \zeta)^{-2} + (\nu L)^2] E_{(\nu L)}^-(\zeta) = 0, $$

where the eigenfunctions are related to the original eigenfunctions e_ν^- by $E_{(\nu L)}^-(\zeta) = e_\nu^-(L\zeta)$ for the continuum and by $E_1^-(\zeta) = \sqrt{L} e_1^-(L\zeta)$ for the discrete spectrum. In this waveguide model, the eigenvalue of the main state (the main waveguide mode) and the corresponding eigenfunction are represented as $(\nu_1^- L)^2 = -\tau^2$, and $E_1^-(\zeta) = N(\cosh \zeta)^{-\tau}$, where $\tau = \frac{1}{2}(\sqrt{1 + 4\gamma^2 \Omega^2} - 1)$ and the normalizing coefficient N is defined according to the condition $\int_{-\infty}^{\infty} |E_1|^2 d\zeta = 1$ and is expressed in terms of the Γ function as $N^2 = \pi^{-1/2}\Gamma(\tau + 1/2)/\Gamma(\tau)$.

For numerical calculations, we normalize expressions (27) to the linear scale length L in such a way that they represent the dependence of K and b on the dimensionless parameters Ω, γ, and $k_y L$.

Figure 4 shows the conversion coefficients K and b calculated as functions of the frequency Ω for different values of the parameter $k_y L$ in the case when it is impossible to synchronize the wave parameters of the entrance and exit channels of the waveguide. This calculation was carried out for the model parameter values $\gamma_- = 1$, $\gamma_+^2/\gamma_-^2 = 1.383$, and $V_-^2/V_+^2 = 0.940$, which correspond to $\varepsilon = 0.3$. The conversion coefficients are seen to be very sensitive functions of the frequency. As k_y decreases, the peaks in the profiles $K(\omega)$ and $b(\omega)$ become lower. As k_y increases, the peaks are displaced to the right. The maximum values of the magnetic-field conversion coefficient are about $b(\omega) \simeq 2$–4%, and the maximum values of the energy conversion coefficient amount to at most fractions of one percent.
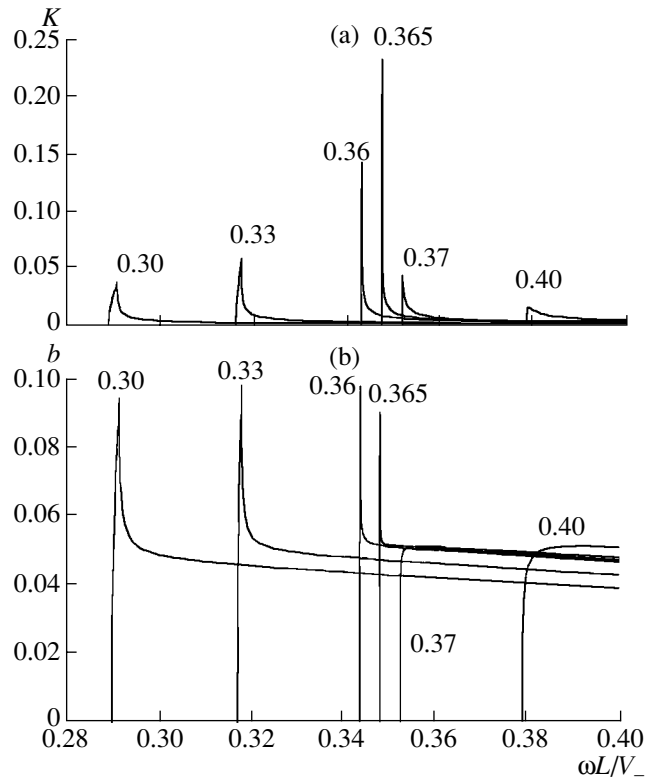
When synchronization of the wave parameters of the entrance and exit channels of the waveguide is possible (Fig. 5), the conversion efficiency is significantly
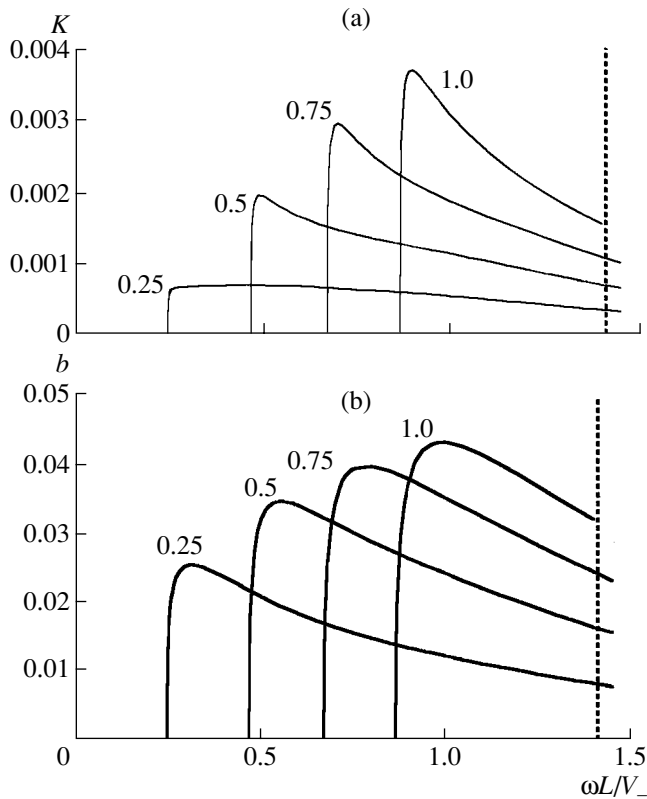
Fig. 4. Dependence of the (a) wave-energy and (b) wave-magnetic-field conversion coefficients on the dimensionless frequency in a model waveguide without phase synchronization. Numerals above the curves denote different values of the parameter k_yL.

Fig. 5. Profiles of the (a) wave-energy and (b) wave-magnetic-field conversion coefficients in a model waveguide with phase synchronization for k_yL values close to k_*L.

higher. The maximum values of $K(\omega)$ amount to several tens of percent; however, this is true of k_y values in a narrow region near the value $k_* = k_\perp(\omega_*)$. In this case, the coefficient b is also somewhat higher and the decrease in the maxima of $b(\omega)$ as k_y decreases is far more gradual.

The case $k_y < k_*$ can be described as follows. As the frequency decreases, the exit channel of the waveguide stops transmitting waves before the cutoff of the entrance channel. The peak in the profile $b(\omega)$ is approximately two times higher than that in the case $k_y > k_*$ and is far more pronounced. The peak in the profile $K(\omega)$ also becomes markedly higher. These effects are associated with the total reflection of the waveguide mode; as a result, the amplitudes of the waves in the conversion region double. The profiles in Fig. 5 were obtained for the model parameter values $\gamma_- = 1$, $\gamma_+^2/\gamma_-^2 = 0.438$, and $V_-^2/V_+^2 = 1.600$, which also correspond to $\varepsilon = 0.3$. The conversion process acts as a kind of band-pass filter that permits only narrow-band Alfvén oscillations to reach the waveguide output.

7. SUMMARY AND CONCLUSIONS

We have shown that the plasma layer can serve as a waveguide for FMS waves, which are insignificantly damped when propagating along the layer. The FMS waves are converted into localized Alfvén waves at small but sharp plasma inhomogeneities along the waveguide axis. The conversion efficiency increases with the parameter k_yL and becomes maximum when the parameter reaches values corresponding approximately to the cutoff frequency of the waveguide mode, $\omega \simeq k_yV_A$. Note that, in the one-dimensional case, the absorption of the energy of the incident wave at a steep plasma density gradient ($\rho_+ \gg \rho_-$) is enhanced near the frequency $\omega_s \simeq \sqrt{2}k_zV_A^+$ of the standing surface wave [7]. On the whole, in a plasma that is inhomogeneous in two directions and in which surface waves can escape along the boundary between two different plasma media, the efficiencies for conversion and absorption of the energy of the incident waveguide mode are lower than those in a plasma that is inhomogeneous in one direction and where there are regimes in which the incident wave can be absorbed essentially completely.

The resonant character of the conversion of FMS waves into surface Alfvén waves is responsible for fre-

quency and wavelength filtering of the emitted Alfvén perturbations. The phase synchronization condition can take place only for non-self-similar jumps in the profile $V_A(z)$. Phase synchronism takes place in the situation in which the phase velocities of the waveguide mode with frequency ω_* along the waveguide axis are the same on both sides of the jump in the Alfvén velocity. Under the phase synchronization condition, the conversion efficiency is high: even in the case of a slight jump, it amounts to about ten percent.

ACKNOWLEDGMENTS

APPENDIX A

Eigenfunctions of the Continuous Spectrum of the Schrödinger Equation

We represent the electromagnetic fields in a waveguide as a superposition of the fields of normal waves propagating along the waveguide axis. To do this, we solve the equation for ψ in set (3) by the method of expansion in the spectrum of the Alfvén operator $L_A = \partial_{zz} + k_A^2(z)$. In Section 2, we somewhat modified the problem at hand; specifically, we switched from the operator L_A to the operator $L = -L_A + k_\infty^2 = -\partial_{zz} + U(z)$ in order to deal with the standard one-dimensional Schrödinger equation (4). In Section 2, we also discussed the properties of the eigenfunctions of the discrete spectrum of the operator L in connection with the waveguide modes. Here, we analyze in detail the eigenfunctions of the continuum.

The continuous spectrum of Eq. (4) is doubly degenerate. Accordingly, we choose two linearly independent solutions to Eq. (4) in the following way. As ν^2 runs the positive axis $\nu^2 > 0$, each of the two values of ν runs the entire real axis (except for the point $\nu = 0$). At a given value of ν, we single out the solution $u_\nu(z)$ to Eq. (4) by imposing the conditions

$$u_\nu \approx d_\nu \exp(i\nu z) \quad (z \longrightarrow +\infty),$$
$$u_\nu \approx \exp(i\nu z) + r_\nu \exp(-i\nu z) \quad (z \longrightarrow -\infty). \tag{A.1}$$

If $\nu > 0$, then the quantities r_ν and d_ν in conditions (A.1) have the meaning of the reflection and transmission coefficients of the potential well $U(z)$ for a plane wave. We can assume that the coefficients r_ν and d_ν for a particular potential are known functions, because they can be obtained by integrating Eq. (4) numerically. Note that the functions $u_\nu(z)$ and $u_{-\nu}(z)$ are solutions to the differential equation (4) with the same parameter ν^2.

Consequently, since the coefficients of this equation are real, conditions (A.1) yield

$$u_{-\nu}(z) = \overline{u_\nu(z)}, \tag{A.2}$$

where the overbar denotes the complex conjugate.

The corresponding manipulations (which are omitted here for brevity) show that

$$\int_{-\infty}^{\infty} u_\mu(z)\overline{u_\nu(z)}dz = 2\pi[\delta(\mu - \nu) + r_\mu\delta(\mu + \nu)].$$

We see that the functions $u_\nu(z)$ are not orthonormal. Consequently, in place of these functions, it is expedient to use the functions $e_\nu(z)$ satisfying the conditions

$$\int_{-\infty}^{\infty} e_\mu(z)\overline{e_\nu(z)}dz = \delta(\mu - \nu), \tag{A.3a}$$

$$e_\nu(z) = \overline{e_{-\nu}(z)}. \tag{A.3b}$$

Here, the latter condition is analogous to condition (A.2) and makes it possible to unambiguously determine the functions $e_\nu(z)$. Each of the functions $e_\nu(z)$, being a solution to Eq. (4), can be represented as a linear combination of the functions $u_\nu(z)$ and $u_{-\nu}(z)$ with the coefficients determined from conditions (A.3a) and (A.3b):

$$e_\nu = \frac{1}{2\sqrt{\pi}d_\nu}[(1 + |d_\nu|)^{1/2}u_\nu - r_\nu(1 + |d_\nu|)^{-1/2}u_{-\nu}]. \tag{A.4}$$

The coefficients in the asymptotic expressions

$$e_\nu(z)$$

$$\simeq \begin{cases} \alpha_\nu\exp(i\nu z) + \beta_\nu\exp(-i\nu z) & \text{for } z \longrightarrow +\infty \\ \gamma_\nu\exp(i\nu z) + \delta_\nu\exp(-i\nu z) & \text{for } z \longrightarrow -\infty \end{cases} \tag{A.5}$$

are found by comparing expressions (A.1) and (A.4):

$$\alpha_\nu = \frac{1}{2\sqrt{\pi}}(1 + |d_\nu|)^{1/2},$$

$$\beta_\nu = -\frac{1}{2\sqrt{\pi}}r_\nu\overline{d_\nu}(d_\nu)^{-1}(1 + |d_\nu|)^{-1/2},$$

$$\gamma_\nu = \frac{1}{2\sqrt{\pi}}|d_\nu|(d_\nu)^{-1}(1 + |d_\nu|)^{1/2}, \tag{A.6}$$

$$\delta_\nu = \frac{1}{2\sqrt{\pi}}r_\nu|d_\nu|(d_\nu)^{-1}(1 + |d_\nu|)^{-1/2}.$$

Now, we consider two operators, $L_+ = -\partial_{zz}u + U_+(z)$ and $L_- = -\partial_{zz}u + U_-(z)$. We denote by $e_\nu^+(z)$ and $e_\nu^-(z)$ the solutions to the differential equation (4) with the

potentials $U_+(z)$ and $U_-(z)$, respectively. We have to determine the Fourier coefficients

$$(e_\mu^+, e_\nu^-) = \int\limits_{-\infty}^{\infty} e_\mu^+(z)\overline{e_\nu^-(z)}dz.$$

Omitting the intermediate manipulations, we write out the final expression

$$(e_\mu^+, e_\nu^-) = \varrho_1(\nu)\delta(\mu - \nu) \\ + \varrho_2(\nu)\delta(\mu + \nu) + \gamma_{\mu\nu}. \tag{A.7}$$

Here, $\gamma_{\mu\nu} = -h_{\mu\nu}(\mu^2 - \nu^2)^{-1}$, $h_{\mu\nu} = ((U_+ - U_-)e_\mu^+, e_\nu^-)$, and the integrals resulting from the integration of (e_μ^+, e_ν^-) over the spectral parameter μ and containing $\gamma_{\mu\nu}$ are understood in terms of the Cauchy principal value. The coefficients in front of the δ functions depend on the coefficients d_ν and r_ν in the asymptotic expressions (A.1) in a fairly complicated fashion:

$$\varrho_1(\nu) = \frac{1}{4\sqrt{Z}}\left[\left(1 + \frac{|d_\nu^-||d_\nu^+|}{d_\nu^+ \overline{d_\nu^-}}\right)(r_\nu^+ \overline{r_\nu^-} + Z)\right. \\ \left. - r_\nu^+ \overline{r_\nu^-}\left(1 - \frac{d_\nu^- \overline{d_\nu^+}}{d_\nu^+ \overline{d_\nu^-}}\right)\right], \tag{A.8}$$

$$\varrho_2(\nu) = \frac{1}{4\sqrt{Z}\overline{d_\nu^-}d_\nu^+}[(\overline{r_\nu^+} - \overline{r_\nu^-})(\delta + |r_\nu^-|^2 - \overline{r_\nu^-}r_\nu^+ \\ + |d_\nu^-|^2 - \overline{d_\nu^-}d_\nu^+)(1 + |d_\nu^-|) - \overline{r_\nu^-}\delta^2 \\ + \overline{r_\nu^-}(1 + |d_\nu^+|)(|d_\nu^+ - d_\nu^-|^2 + |r_\nu^+ - r_\nu^-|^2) \\ + \overline{r_\nu^-}\delta(\overline{r_\nu^-}r_\nu^+ - |r_\nu^-|^2 + \overline{d_\nu^-}d_\nu^+ - |d_\nu^-|^2)], \tag{A.9}$$

where $Z = (1 + |d_\nu^-|)(1 + |d_\nu^+|)$ and $\delta = |d_\nu^+| - |d_\nu^-|$.

For a small jump in the Alfvén velocity, the differences $r_\nu^+ - r_\nu^-$ and $d_\nu^+ - d_\nu^-$ and the quantity δ are all on the order of ε. From dependence (A.9), we immediately see that $\varrho_2(\nu) = O(\varepsilon^2)$. Using dependence (A.8) and the relationship $|r_\nu^-|^2 = 1 - |d_\nu^-|^2$ and taking the limit $\varepsilon \longrightarrow 0$, we arrive at the asymptotic expression

$$\varrho_1(\nu) \longrightarrow \frac{1}{4(1 + |d_\nu^-|)}\left(1 + \frac{|d_\nu^-|^2}{|d_\nu^-|^2}\right) \\ \times [1 - |d_\nu^-|^2 + (1 + |d_\nu^-|^2)] = 1,$$

which gives $\varrho_1(\nu) = 1 + O(\varepsilon)$.

APPENDIX B

Derivation of the Set of Equations for the Coefficients R_1, D_1, R_ν, and D_ν

Taking the scalar product of relationships (10) with e_1^- and e_ν^- and using expression (A.7), we obtain the set of equations

$$\kappa_1^- R_1 + \kappa_1^+ p_{11} D_1 = \kappa_1^- - \int\limits_{-\infty}^{+\infty} \kappa_\mu^+ p_\mu D_\mu d\mu,$$

$$\lambda_1^- R_1 - \lambda_1^+ p_{11} D_1 = -\lambda_1^- + \int\limits_{-\infty}^{+\infty} \lambda_\mu^+ p_\mu D_\mu d\mu,$$

$$\kappa_\nu^- R_\nu + \kappa_\nu^+[\varrho_1(\nu)D_\nu + \varrho_2(\nu)D_{-\nu}] \\ = -\kappa_1^+ q_\nu D_1 - \int\limits_{-\infty}^{+\infty} \kappa_\mu^+ \gamma_{\mu\nu} D_\mu d\mu, \tag{B.1}$$

$$\lambda_\nu^- R_\nu - \lambda_\nu^+[\varrho_1(\nu)D_\nu + \varrho_2(\nu)D_{-\nu}] \\ = \lambda_1^+ q_\nu D_1 + \int\limits_{-\infty}^{+\infty} \lambda_\mu^+ \gamma_{\mu\nu} D_\mu d\mu,$$

where we introduced the notation

$$(e_1^+, e_1^-) = p_{11}, \quad (e_\nu^+, e_1^-) = p_\nu, \quad (e_1^+, e_\nu^-) = q_\nu.$$

Resolving the first two equations from set (B.1) in R_1 and D_1 and the last two equations in R_ν and the combination $\varrho_1(\nu)D_\nu + \varrho_2(\nu)D_{-\nu}$, we transform Eqs. (B.1) to

$$R_1 = (\lambda_1^+ \kappa_1^- - \lambda_1^- \kappa_1^+)\Delta_{11}^{-1} \\ + \int\limits_{-\infty}^{+\infty} (\lambda_\nu^+ \kappa_1^+ - \lambda_1^+ \kappa_\nu^+)\Delta_{11}^{-1} p_\nu D_\nu d\nu, \tag{B.2}$$

$$D_1 = 2p_{11}^{-1}\lambda_1^- \kappa_1^- \Delta_{11}^{-1} \\ - \int\limits_{-\infty}^{+\infty} p_{11}^{-1}\Delta_{11}^{-1}(\lambda_\nu^+ \kappa_1^- + \lambda_1^- \kappa_\nu^+)p_\nu D_\nu d\nu, \tag{B.3}$$

$$R_\nu = (\lambda_1^+ \kappa_\nu^+ - \lambda_\nu^+ \kappa_1^+)\Delta(\nu)^{-1} q_\nu D_1 \\ + \int\limits_{-\infty}^{+\infty} (\lambda_\mu^+ \kappa_\nu^+ - \lambda_\nu^+ \kappa_\mu^+)\Delta(\nu)^{-1} \gamma_{\mu\nu} D_\mu d\mu, \tag{B.4}$$

$$\varrho_1(\nu)D_\nu + \varrho_2(\nu)D_{-\nu} + \frac{\lambda_1^+\kappa_\nu^- + \lambda_\nu^-\kappa_1^+}{\Delta(\nu)}q_\nu D_1$$
$$+ \int_{-\infty}^{+\infty} \frac{\lambda_\mu^+\kappa_\nu^- + \lambda_\nu^-\kappa_\mu^+}{\Delta(\nu)}\gamma_{\mu\nu}D_\mu d\mu = 0, \tag{B.5}$$

where $\Delta_{11} = \lambda_1^+\kappa_1^- + \lambda_1^-\kappa_1^+$ and $\Delta(\nu) = \lambda_\nu^+\kappa_\nu^- + \lambda_\nu^-\kappa_\nu^+$. Equation (B.5) contains both of the coefficients D_ν and $D_{-\nu}$. In order to eliminate the coefficient $D_{-\nu}$ in (B.5) and to keep D_ν, we replace ν by $-\nu$. Taking into account the relationships $q_{-\nu} = \overline{q_\nu}$, $\lambda_{-\nu}^\pm = \lambda_\nu^\pm$, and $\kappa_{-\nu}^\pm = \kappa_\nu^\pm$, we find

$$\varrho_1(-\nu)D_{-\nu} + \varrho_2(-\nu)D_\nu + \frac{\lambda_1^+\kappa_\nu^- + \lambda_\nu^-\kappa_1^+}{\Delta(\nu)}\overline{q_\nu}D_1$$
$$+ \int_{-\infty}^{+\infty} \frac{\lambda_\mu^+\kappa_\nu^- + \lambda_\nu^-\kappa_\mu^+}{\Delta(\nu)}\gamma_{\mu,-\nu}D_\mu d\mu = 0. \tag{B.6}$$

We subtract Eq. (B.6) multiplied by $\varrho_2(-\nu)$ from Eq. (B.5) multiplied by $\varrho_1(\nu)$ to obtain the relationship

$$\Delta_\rho(\nu)D_\nu + \frac{\lambda_1^+\kappa_\nu^- + \lambda_\nu^-\kappa_1^+}{\Delta(\nu)}f(\nu)D_1$$
$$+ \int_{-\infty}^{+\infty} \frac{\lambda_\mu^+\kappa_\nu^- + \lambda_\nu^-\kappa_\mu^+}{\Delta(\nu)}g(\mu,\nu)D_\mu d\mu = 0, \tag{B.7}$$

where

$$\Delta_\rho(\nu) = \varrho_1(\nu)\varrho_1(-\nu) - \varrho_2(\nu)\varrho_2(-\nu),$$

$$f(\nu) = q_\nu\varrho_1(-\nu) - \overline{q_\nu}\varrho_2(\nu),$$

$$g(\mu,\nu) = \gamma_{\mu\nu}\varrho_1(-\nu) - \gamma_{-\mu,\nu}\varrho_2(\nu).$$

Finally, inserting Eq. (B.3) into Eqs. (B.4) and (B.7), we arrive at the formula

$$R_\nu = \frac{2\lambda_1^-\kappa_1^-(\lambda_1^+\kappa_\nu^+ - \lambda_\nu^+\kappa_1^+)q_\nu}{p_{11}\Delta_{11}\Delta(\nu)}$$
$$+ \int_{-\infty}^{+\infty} \left[-\frac{(\lambda_1^+\kappa_\nu^+ - \lambda_\nu^+\kappa_1^+)q_\nu(\lambda_\mu^+\kappa_1^- + \lambda_1^-\kappa_\mu^+)p_\mu}{p_{11}\Delta_{11}\Delta(\nu)} \right. \tag{B.8}$$
$$\left. - \frac{(\lambda_\mu^+\kappa_\nu^+ - \lambda_\nu^+\kappa_\mu^+)h_{\mu\nu}}{\Delta(\nu)(\mu^2 - \nu^2)} \right] D_\mu d\mu,$$

which relates R_ν to D_ν, and at the following integral equation of the second kind for the function D_ν:

$$D_\nu = -\frac{2\lambda_1^-\kappa_1^-(\lambda_1^+\kappa_\nu^- + \lambda_\nu^-\kappa_1^+)f(\nu)}{p_{11}\Delta_{11}\Delta(\nu)\Delta_\rho(\nu)}$$
$$+ \int_{-\infty}^{+\infty} \left[\frac{(\lambda_1^+\kappa_\nu^- + \lambda_\nu^-\kappa_1^+)f(\nu)(\lambda_\mu^+\kappa_1^- + \lambda_1^-\kappa_\mu^+)p_\mu}{p_{11}\Delta_{11}\Delta(\nu)\Delta_\rho(\nu)} \right. \tag{B.9}$$
$$\left. + \frac{(\lambda_\mu^+\kappa_\nu^- + \lambda_\nu^-\kappa_\mu^+)\tilde{h}_{\mu\nu}}{\Delta(\nu)\Delta_\rho(\nu)(\mu^2 - \nu^2)} \right] D_\mu d\mu,$$

where $\tilde{h}_{\mu\nu} = h_{\mu\nu}\varrho_1(-\nu) - h_{\mu,-\nu}\varrho_2(\nu)$. Hence, we must, first, solve Eq. (B.9) to obtain the coefficient D_ν, and, then, from Eqs. (B.2), (B.3), and (B.8), we can determine the remaining coefficients R_1, D_1, and R_ν.

REFERENCES

1. L. Chen and A. Hasegawa, Phys. Fluids **17**, 1399 (1974).
2. J. A. Tataronis, J. Plasma Phys. **13**, 87 (1975).
3. A. V. Timofeev, Usp. Fiz. Nauk **100** (2), 185 (1970) [Sov. Phys. Usp. **13**, 51 (1970)].
4. J. A. Tataronis and W. Grossmann, Nucl. Fusion **16**, 667 (1976).
5. V. E. Golant and V. I. Fedorov, *High-Frequency Methods of Plasma Heating in Toroidal Fusion Facilities* (Énergoatomizdat, Moscow, 1986).
6. J. Heyvaerts and E. R. Priest, Astron. Astrophys. **117**, 220 (1983).
7. L. Chen and A. Hasegawa, J. Geophys. Res. **79**, 1033 (1974).
8. K. N. Stepanov, Zh. Éksp. Teor. Fiz. **35** (6), 1002 (1965) [Sov. Phys. JETP **10**, 773 (1965)].
9. Yu. M. Aliev, S. Vukovic, O. M. Gradov, and A. Yu. Kure, Pis'ma Zh. Éksp. Teor. Fiz. **25**, 351 (1977) [JETP Lett. **25**, 326 (1977)].
10. T. A. Davydova, Fiz. Plazmy **7**, 921 (1981) [Sov. J. Plasma Phys. **7**, 507 (1981)].
11. K. K. Khurana and M. G. Kivelson, J. Geophys. Res. **94**, 5255 (1989).
12. R. Cramm, K.-H. Glassmeier, M. Stellmacher, and C. Othmer, J. Geophys. Res. **103**, 11951 (1998).
13. A. V. Gul'el'mi, *Magnetohydrodynamic Waves in Near-Earth Plasma* (Nauka, Moscow, 1982).
14. E. N. Fedorov, N. G. Mazur, V. A. Pilipenko, and S. Lepidi, Geomagn. Aéron. **38** (2), 60 (1998).
15. P. M. Edwin, B. Roberts, and W. J. Hughes, Geophys. Res. Lett. **13**, 373 (1986).
16. W. Allan and A. N. Wright, J. Geophys. Res. **103**, 2359 (1998).
17. E. Fedorov, N. Mazur, V. Pilipenko, and K. Yumoto, J. Geophys. Res. **103**, 26595 (1998).
18. E. N. Fedorov, N. G. Mazur, and V. A. Pilipenko, Fiz. Plazmy **21**, 333 (1995) [Plasma Phys. Rep. **21**, 311 (1995)].
19. L. D. Landau and E. M. Lifshitz, *Quantum Mechanics: Non-Relativistic Theory* (Nauka, Moscow, 1986; Pergamon, New York, 1977).

Translated by I. A. Kalabalyk

Influence of Electromagnetic Radiation on the Shock Structure Formation in Complex Plasmas

S. I. Popel*, A. A. Gisko*, A. P. Golub'*, T. V. Losseva*, and R. Bingham**

*Institute for Dynamics of Geospheres, Russian Academy of Sciences, Leninskiĭ pr. 38-6, Moscow, 117979 Russia
**Rutherford Appleton Laboratory, Chilton, Didcot, Oxfordshire, OX11 OQX, UK

Abstract—Electromagnetic radiation effects are calculated for the case of the solar radiation spectrum in the vicinity of the Earth. The influence of the photoelectric effect on the propagation of nonlinear waves in complex plasmas is studied when the dust grains acquire large positive charges. Exact solutions to nonlinear equations in the form of steady-state shocks that do not involve electron–ion collisions are found, and the conditions for their existence are obtained. In contrast to the classical collisionless shock waves, the dissipation due to the dust charging involves the interaction of the electrons and ions with the dust grains in the form of microscopic grain currents and the photoelectric current. The nonsteady problem of the evolution of a perturbation and its transformation into a nonlinear wave structure is considered. The evolution of an intense, initially nonmoving region with a constant increased ion density is investigated. It is shown that the evolution of a rather intense nonmoving region with a constant increased ion density can result in the formation of a shock wave. In addition to the compressional wave, a rarefaction region (dilatation wave) appears. The presence of a dilatation wave finally leads to the destruction of the shock structure. The possibility is discussed of the observation of shock waves related to dust charging in the presence of electromagnetic radiation in active rocket experiments, which involve the release of a gaseous substance in the Earth's ionosphere in the form of a high-speed plasma jet at altitudes of 500–600 km. © 2001 MAIK "Nauka/Interperiodica".

1. INTRODUCTION

At present, a large number of plasma investigations are devoted to multicomponent plasmas containing electrons, ions, charged microspheres (dust grains), and neutrals. Such plasmas are usually referred to as "complex plasmas." Complex (dusty) plasma cannot usually survive in the absence of either external sources of electrons and ions (e.g., due to ionization) or plasma particle fluxes from dust-free regions. The fluxes of electrons and ions are absorbed by dust grains, which results in variations in their charges. Variations in the dust grain charge can also be caused by an external electromagnetic radiation via the photoelectric effect. The strong dissipativity of the complex plasma due to dust grain charging [1] points to the exceptional role of dissipative structures (such as shock waves) in complex plasmas.

Shock waves often arise in nature because of the balance between the wave breaking nonlinear force and the wave damping dissipative force. Collisional and collisionless shock waves can appear due to friction between the particles [2] and the wave–particle interaction [3], respectively. In complex plasmas, an anomalous dissipation due to dust charging results in the existence of a new kind of shock wave related to this dissipation. These waves are collisionless in the sense that they do not involve electron–ion collisions. However, in contrast to classical collisionless shock waves, the dissipation due to dust charging involves the interaction of

the plasma electrons and ions with dust grains in the form of microscopic grain currents. The case in which the shock waves related to dust grain charging are rather intense corresponds to the ion acoustic wave propagation. The main results concerning this new kind of ion acoustic shocks are presented in [4–6]. Recently, the first results of laboratory experiments confirming the effect of negatively charged dust on the formation of ion acoustic shocks were obtained [7, 8].

The importance of shock waves in complex plasmas is associated with different astrophysical applications [5]. For example, according to modern concepts [9], the formation of stars occurs mainly in interstellar dust–molecular clouds after compressional shock waves have propagated through them, thus creating an initial density condensation for further gravitational contraction. The presence of dust in interstellar clouds can significantly influence the sound velocity, not to mention the shock wave propagation. The investigation of shock waves related to the dissipation caused by dust grain charging can also be important [5, 10] for the description of shocks in supernova explosions, particle acceleration in shocks, the explanation of the effects in active geophysical and space experiments involving the release of a gaseous substance in the Earth's ionosphere and magnetosphere, etc.

In astrophysical applications, the effect of electromagnetic radiation (as well as the influence of the photoelectric effect on the dust grain charge) cannot often

be ignored. This effect can lead to new qualitative results in comparison with the situation in which this effect is neglected. In particular, the photoelectric effect can result in the positive charge of dust grains, while in the case where the dust grain charge is varied only due to microscopic electron and ion currents, the dust grain charge is negative (see, e.g., [11]).

This paper deals with the case where the photoelectric effect strongly influences the dust grain charge. The electromagnetic radiation effects are calculated for the solar radiation spectrum in the vicinity of the Earth. We investigate solutions in the form of dust ion acoustic shock waves. In particular, we consider the nonsteady problem of the evolution of a perturbation and its transformation into a nonlinear wave structure. In Section 2, we describe the basic assumptions and equations and present steady-state shock wave solutions. In Section 3, we consider the evolution of an intense, initially non-moving region with a constant, increased ion density using a numerical method analogous to that developed in [12]. In Section 4, we discuss the possibility of observing the shock waves under consideration in active space rocket experiments that involve the release of a gaseous substance in the Earth's ionosphere. A summary of our findings and conclusions are given in Section 5.

2. STEADY-STATE SHOCK WAVE SOLUTIONS

The average radius a of grains in a typical complex plasma is much smaller than the electron Debye length λ_D, the spatial scale of perturbations, and the distance between the plasma particles. Since the dust grains are massive ($m_i Z_d \ll m_d$, where m_i and m_d are the ion and grain masses, respectively), they can be considered immobile and their density n_d can be assumed to be constant on the ion acoustic time scale [13]. Furthermore, in the absence of perturbations, the quasineutrality condition $n_{i0} = n_{e0} + Z_{d0} n_d$ holds. Here, $q_d = -Z_d e$ is the mean dust grain charge; $-e$ is the electron charge; n_i and n_e are the ion and electron densities, respectively; and the subscript 0 denotes unperturbed quantities.

We will assume that the grain charge varies due to both the photoelectric electron current and the microscopic electron and ion grain currents (originating from the potential difference between the plasma and the grain surface). The photoelectric electron current is due to the photoelectric effect, which results in the separation (and removal) of the electrons from the dust grain surface. When electromagnetic radiation is sufficiently intense, the photoelectric effect leads to the positive charge of dust grains. In this paper, we restrict ourselves to the case in which the dust grain charge is positive. This case differs qualitatively from the case in which the photoelectric current is absent [4, 5, 12]; its consideration allows us to distinguish the effects caused by the influence of electromagnetic radiation on the shock wave propagation.

According to the orbit-limited probe model [14, 15], for equilibrium electrons and ions, we have the following expressions for the microscopic currents to the grain surface (cf. [11, 16–18]):

$$I_e \approx -\pi a^2 e \left(\frac{8 T_e}{\pi m_e}\right)^{1/2} n_e \left(1 + \frac{e q_d}{a T_e}\right), \qquad (1)$$

$$
\begin{aligned}
I_i = \sqrt{\frac{\pi}{2}} a^2 v_{Ti} e n_i \\
\times \left\{ 2 \exp\left(-\frac{v_i^2 + v_{\min,i}^2(q_d)}{2 v_{Ti}^2}\right) \cosh\left(\frac{v_i v_{\min,i}(q_d)}{v_{Ti}^2}\right) \right. \\
+ \sqrt{\frac{\pi}{2}} \frac{v_{Ti}}{v_i}\left(1 + \frac{v_i^2}{v_{Ti}^2} - \frac{2 e q_d}{a m_i v_{Ti}^2}\right) \\
\left. \times \left[\mathrm{erf}\left(\frac{v_{\min,i}(q_d) + v_i}{\sqrt{2} v_{Ti}}\right) - \mathrm{erf}\left(\frac{v_{\min,i}(q_d) - v_i}{\sqrt{2} v_{Ti}}\right)\right] \right\},
\end{aligned}
\qquad (2)
$$

where m_e is the electron mass, T_j and $v_{Tj} = (T_j/m_j)^{1/2}$ are the temperature and thermal velocity of particles of species j ($j = i, e$), v_i is the ion fluid velocity, $v_{\min,i}(q_d) = (2 e q_d/a m_i)^{1/2}$, and erf$(x)$ is the error function. Here, we take into account that, when q_d is positive (in contrast to the situation with $q_d < 0$), only the ions with velocities $|\mathbf{v}| > v_{\min,i}(q_d)$ can reach the grain surface, while there is no limitation on the absolute value of the electron velocity. We emphasize that this fact results in different (from the case of $q_d < 0$ considered, e.g., in [4]) expressions for the electron (I_e) and ion (I_i) currents.

The photoelectric current produced by the electrons emitted from the dust grain surface in the presence of external electromagnetic radiation with spectrum $\Phi(\omega)$, where $\Phi = \int \Phi(\omega) d\omega$ is the luminous flux, is given by the formula

$$I_{ph} = \frac{\pi \beta e a^2}{\hbar} \int_{\omega_R - e^2 Z_d/a\hbar}^{\infty} \frac{\Phi(\omega)}{\omega} d\omega. \qquad (3)$$

Here, β is the probability of the emission of an electron under the action of one photon on the dust particle surface, $\hbar$ is Planck's constant, and $\hbar \omega_R$ is the photoelectric work function. The limits of integration are determined by the fact that photons with frequencies $\omega > \omega_R - (e^2 Z_d/a\hbar)$ can only produce the photoelectric current. As was mentioned above, in this paper, electromagnetic radiation effects are calculated for the solar radiation spectrum in the vicinity of the Earth. For simplicity, the spectrum is approximated by the black body spectrum $\Phi(\omega) = \Phi_0 \omega^3/[\exp(\hbar\omega/T_s) - 1]$ with an effective temperature of $T_s = 6000$ K and $\Phi_0 = 5.5 \times 10^{-55}$ g s

(in this case, $\Phi_s = \int \Phi(\omega)d\omega = 1.4 \times 10^6$ erg/(cm^2 s) is the solar constant).

The mean charge of immobile dust grains is governed by the charge conservation equation

$$\partial_t q_d = I_e(q_d) + I_i(q_d) + I_{ph}(q_d). \qquad (4)$$

The unperturbed mean charge q_{d0} satisfies the equation $I_e(q_{d0}) + I_i(q_{d0}) + I_{ph}(q_{d0}) = 0$. The typical parameters of the Earth's ionosphere at altitudes of 500–600 km (see, e.g., [19]) are $n_{e0} = 10^3$ cm^{-3}, $n_{i0} = 8 \times 10^2$ cm^{-3}, $T_e = 2$ eV, and $T_i = 0.5$ eV. Then, for the dust parameters (see, e.g., [20]) $a = 10^{-4}$ cm, $\lambda_R \equiv 2\pi c/\omega_R = 2 \times 10^{-5}$ cm (which is typical for most materials), and $\beta = 0.1$, the unperturbed grain charge is equal to $Z_{d0} \approx -1.92 \times 10^3$, which confirms the above assumption $q_d = -Z_d e > 0$.

The electron density is assumed to obey a Boltzmann distribution $n_e = n_{e0}\exp(e\varphi/T_e)$ with a constant electron temperature T_e. We note that, in the vicinity of a dust grain, the Boltzmann distribution for the electron density can fail to hold because of the attraction between the electrons and the dust grain. However, for $T_i < T_e$ (which is satisfied in the above example, in which $T_e = 2$ eV and $T_i = 0.5$ eV), the electron density distribution can be considered to be Boltzmann at distances longer than or on the order of the ion Debye length. In all subsequent considerations, the minimum characteristic parameter of the problem is the electron Debye length, which is larger than the ion Debye length.

In the situation under consideration, in which the photoelectric effect results in a positive grain charge (cf. [11]), the ion current I_i is several orders of magnitude lower than I_e and I_{ph}. Thus, on a time scale characteristic of ion acoustic waves, we can neglect the change in the number of ions and the loss of the ion momentum due to dust charging and can use the ion continuity equation and the ion momentum equation. Furthermore, we use Poisson's equation for the electrostatic potential

$$\partial_x^2 \varphi = 4\pi e(n_e + Z_d n_d - n_i). \qquad (5)$$

In this paper, the problem is solved in one-dimensional plane geometry, which is applicable when the width of the shock front is far less than the characteristic transverse scale on which the parameters of the problem vary. All of the parameters are assumed to depend only on the time variable t and the spatial variable x.

We consider a quasi-steady structure propagating with velocity V in the x direction and assume that the condition $v_{Ti} < V \ll v_{Te}$ is satisfied, which is characteristic of the ion acoustic wave propagation. Thus, all the

parameters depend only on the variable $\xi = x - Vt$. From the ion conservation equations, we obtain

$$n_i = Mn_{i0}(M^2 - 2\varphi)^{-1/2}, \qquad (6)$$

$$v_i = c_s(M - \sqrt{M^2 - 2\varphi}), \qquad (7)$$

where we use the normalization $e\varphi/T_e \longrightarrow \varphi$, $V/c_s \longrightarrow M$, and $\xi/\lambda_D \longrightarrow \xi$. Here, $c_s = (T_e/m_i)^{1/2}$ is the ion acoustic speed in the absence of dust.

From Poisson's equation, we obtain

$$d_\xi^2 \varphi = \exp(\varphi) + \left(1 + \frac{\delta z}{z_0}\right)Z_{d0}d - \frac{M(1 + Z_{d0}d)}{\sqrt{M^2 - 2\varphi}}, \quad (8)$$

where $d = n_{d0}/n_{e0}$ and $z_0 = Z_{d0}e^2/aT_e$. The normalized perturbed charge $\delta z = -e\delta q_d/aT_e$, where $\delta q_d = q_d - q_{d0}$ is governed by the equation

$$d_\xi \delta z = j(\varphi) = j_e(\varphi) + j_i(\varphi) + j_{ph}(\varphi), \qquad (9)$$

with

$$j_e = -\frac{A}{M(1 + Z_{d0}d)}\sqrt{\frac{8m_iT_e}{\pi m_e T_i}}\exp(\varphi)(1 - z_0 - \delta z), \quad (10)$$

$$j_i = \frac{A}{\sqrt{M^2 - 2\varphi}}\left\{\sqrt{\frac{2}{\pi}}\exp[-(\alpha^2 + \gamma^2)]\cosh(2\alpha\gamma)\right.$$
$$+ \frac{1}{2\sqrt{2}}\left[1 + 2\gamma^2 + 2(z_0 + \delta z)\frac{T_e}{T_i}\right] \qquad (11)$$
$$\left.\times \left[\frac{\text{erf}(\alpha + \gamma)}{\gamma} - \frac{\text{erf}(\alpha - \gamma)}{\gamma}\right]\right\},$$

$$j_{ph} = \frac{J_{ph}}{M}\int\limits_{w > w_R(\delta z)}\frac{w^2}{\exp(T_e w/T_s) - 1}dw. \qquad (12)$$

Here, $A = a[(1 + Z_{d0}d)/4\lambda_D](T_i/T_e)^{1/2}$, $J_{ph} = \pi\beta e^2 a^2 T_e^{3/2} m_i^{1/2}\Phi_0(\lambda_D/a)/\hbar^4$, $\gamma = [M - (M^2 - 2\varphi)^{1/2}](T_e/2T_i)^{1/2}$, $\alpha = [-(z_0 + \delta z)]^{1/2}(T_e/T_i)^{1/2}$, $w_R(\delta z) = w_{R0} - (z_0 + \delta z)$, and $w_{R0} = \hbar\omega_R/T_e$. We also used relationships (6) and (7). Note that j is the normalized perturbed total current density. Clearly, all of the solutions must satisfy the inequality $\varphi \le M^2/2$. Equations (8) and (9) can be numerically integrated provided that the existence conditions for nonlinear wave solutions are known. The solutions to equations (8) and (9) cannot simultaneously satisfy the condition that $\varphi \longrightarrow 0$ as ξ tends to $+\infty$ or $-\infty$. This means that, in the problem as formulated, there are no nonlinear solitary waves. For a shock wave solution to exist, there must be two different asymptotic φ values at $\xi \longrightarrow \pm\infty$ and the derivatives

of the perturbed quantities must vanish there. In this case, from (8) and (9) we obtain the relationship for the perturbed grain charge

$$\delta z = -z_0 + \frac{z_0}{Z_{d0}d}\left[\frac{M(1 + Z_{d0}d)}{\sqrt{M^2 - 2\varphi}} - \exp(\varphi)\right], \quad (13)$$
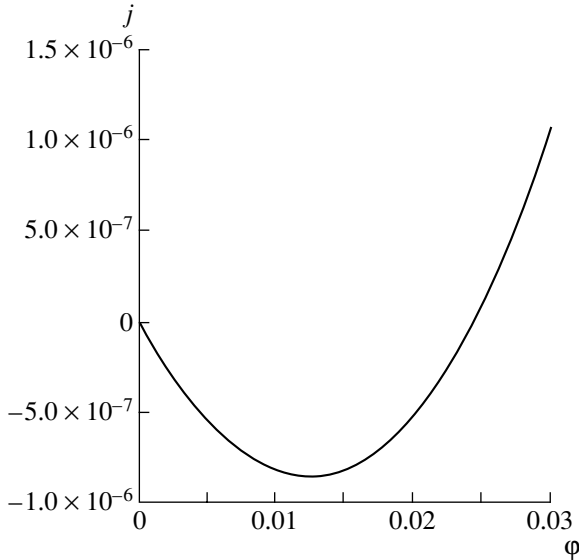
and the current balance condition $j = 0$. The qualitative behavior of the solution to the equation $j = 0$ is the same as that of the function $f_2(\varphi)$ in [4] (see Fig. 2 in [4]).

The set of equations (13) and $j = 0$ has two different solutions $\varphi = 0$ and $\varphi = \varphi_A$ only if the following condition is satisfied:

$$M^2 > M_0^2 \equiv \left(1 + \frac{1 + Z_{d0}d}{Z_{d0}d}z_0 G\right)\left(\frac{z_0 G}{Z_{d0}d} + E\right)^{-1}, \quad (14)$$

where

$$G = \frac{\exp(z_0 T_e/T_i)(T_e/T_i)(2 + z_0 T_e/T_i) + (1 + Z_{d0}d)^{-1}\sqrt{m_i T_e/m_e T_i} + F_{ph}}{\exp(z_0 T_e/T_i)(1 + z_0 T_e/T_i)},$$

$$E = \frac{(1 + Z_{d0}d)^{-1}\sqrt{m_i T_e/m_e T_i}(1 - z_0)}{\exp(z_0 T_e/T_i)(1 + z_0 T_e/T_i)},$$

$$F_{ph} = \sqrt{\pi/8}(J_{ph}/A)(w_{R0} - z_0)^2/\{\exp[T_e(w_{R0} - z_0)/T_s] - 1\}.$$

Figure 1 presents the current density j [obtained with allowance for relationship (13)] for $M = 0.894$ (we emphasize that M is normalized to the ion acoustic speed c_s without dust) and the typical parameter values $n_{e0} = 10^3$ cm^{-3}, $n_{i0} = 8 \times 10^2$ cm^{-3}, $T_e = 2$ eV, $T_i = 0.5$ eV, $a = 10^{-4}$ cm, $\lambda_R = 2 \times 10^{-5}$ cm, $\beta = 0.1$, and $\Phi = \Phi_s = 1.4 \times 10^6$ erg/(cm^2 s). For these parameters, we have $z_0 \approx -1.41$ and $\varphi_A \approx 0.024$. We note that, in this case, $\varphi_A \ll M^2/2$. The calculations carried out with luminous fluxes two orders of magnitude higher and

two orders of magnitude less than that of solar radiation in the vicinity of the Earth show that the inequality $\varphi_A \ll M^2/2$ also remains valid in these cases. When this inequality is valid, we can neglect j_i as compared to j_e and j_{ph} within the entire range of the potential φ corresponding to the nonlinear wave solution (i.e., for $0 < \varphi < \varphi_A$). In this case, inequality (14) is simplified to

$$M^2 > M_0^2 \approx \frac{(H + J_{ph}w_R^2)(1 + Z_{d0}d)z_0}{J_{ph}w_R^2 z_0 - H[(Z_{d0}d - 1)z_0 - Z_{d0}d]}, \quad (15)$$

where

$$H = A\sqrt{\frac{8m_i T_e}{\pi m_e T_i}}\left[\exp\left(\frac{T_e w_R}{T_s}\right) - 1\right].$$

Inequality (14) is necessary for the existence of two asymptotic solutions, namely, $\varphi = 0$ and $\varphi = \varphi_A$ (e.g., at $\xi \longrightarrow +\infty$ and $-\infty$, respectively).

The requirement that the set of equations (13) and $j = 0$ have a solution with the asymptotic values $\varphi = 0$ and $\varphi = \varphi_A$ at $\xi \longrightarrow \pm\infty$ results in the inequality

$$M^2 \leq M_1^2 \equiv 1 + Z_{d0}d. \quad (16)$$

Condition (16) can be obtained in a way analogous to that in the case where the dust grain charge varies only due to the microscopic electron and ion currents and the photoelectric effect is ignored [4]. When deriving this condition, it is taken into account that the inequality $j < 0$ remains valid for $0 < \varphi < \varphi_A$ (see Fig. 1).

We note that $\varphi = 0$ and $\varphi = \varphi_A$ are also exact solutions to Eqs. (8) and (9), because these differential equations are homogeneous. Furthermore, both solutions correspond to $E \equiv -\nabla\varphi = -d_\xi\varphi = 0$. Now, we can find a solution bridging these two asymptotic solutions. Figures 2a and 2b show the profiles of the potential $\varphi(\xi)$ and the electric field $E = -d_\xi\varphi$, respectively. A similar

Fig. 1. Current density j vs. φ for $M = 0.894$ and the parameter values $n_{e0} = 10^3$ cm^{-3}, $n_{i0} = 8 \times 10^2$ cm^{-3}, $T_e = 2$ eV, $T_i = 0.5$ eV, $a = 10^{-4}$ cm, $\lambda_R = 2 \times 10^{-5}$ cm, $\beta = 0.1$, and $\Phi = \Phi_s = 1.4 \times 10^6$ erg/(cm^2 s). The solutions to the equation $j = 0$ are $\varphi = 0$ and $\varphi_A \approx 0.024$.

profile for the normalized perturbed charge δz can be deduced from Eq. (9) taking into account that j is always negative in the region of interest (see Fig. 2c). Figure 2d shows the profile of the ion density n_i normalized to the unperturbed electron density n_{e0}.

In Figs. 2a and 2b, oscillation regions that correspond to the separation of the electron and ion charges cannot be distinguished (see, e.g., [12]). However, this effect actually takes place. Figure 3 presents a portion of the profile of the electric field E on an enlarged scale. The effect of charge separation increases when the luminous flux decreases and/or M increases.

The solution presented in Figs. 2a and 2b corresponds to the balance between the wave breaking nonlinear force and the wave damping dissipative force in a uniform complex plasma with Boltzmann electrons, inertial ions, and immobile but *variable-charge* dust grains. This solution can be treated as a steady-state shock wave solution. The dissipativity in this wave is related to variations in dust grain charges due to the microscopic electron and ion grain currents and the photoelectric electron current. The width of the shock front can be expressed in terms of the charging rate ν_q and the ion acoustic speed as $\Delta\xi\lambda_D \sim c_s/\nu_q$, where

$$\nu_q \equiv -\left.\frac{\partial(I_e + I_i + I_{ph})}{\partial q_d}\right|_{q_d = -Z_{d0}e}$$

$$= \frac{\omega_{pi}^2 a}{\sqrt{2\pi}v_{Ti}}\exp\left(\frac{z_0 T_e}{T_i}\right)\left(2 + \frac{z_0 T_e}{T_i}\right) + \frac{\omega_{pe}^2 a}{\sqrt{2\pi}v_{Te}} \quad (17)$$

$$+ \frac{\pi\beta a e^2 \Phi_0 T_e^2}{\hbar^4}\frac{(w_{R0} - z_0)^2}{\exp[T_e(w_{R0} - z_0)/T_s] - 1}.$$

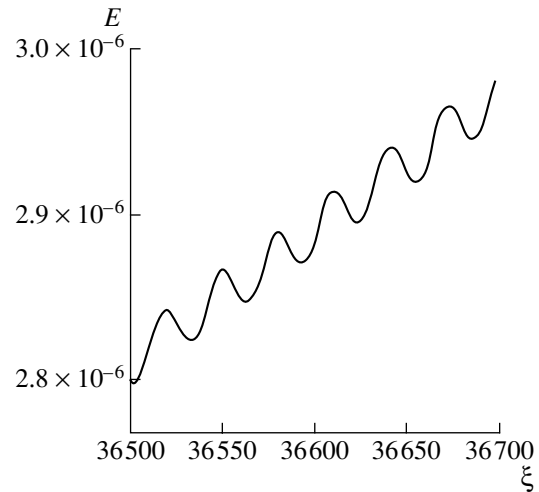For example, for $n_{e0} = 10^3$ cm^{-3}, $n_{i0} = 8 \times 10^2$ cm^{-3}, $T_e = 2$ eV, $T_i = 0.5$ eV, $a = 10^{-4}$ cm, $\lambda_R = 2 \times 10^{-5}$ cm, $\beta = 0.1$, and $\Phi = \Phi_s = 1.4 \times 10^6$ erg/(cm^2 s), the width of the shock front is $\Delta\xi\lambda_D \sim 10^4\lambda_D \approx 3 \times 10^5$ cm, while $c_s/\nu_q \sim 10^5$ cm. We emphasize that, for the above plasma parameters, the charging rate in the presence of electromagnetic radiation ($\nu_q \approx 20$ s^{-1}) is much higher than the charging rate in the absence of radiation ($\nu_q \approx 0.3$ s^{-1}).

The shock speed M must simultaneously satisfy inequalities (14) and (16). For the majority of complex plasmas in which $n_{e0} \sim n_{i0}$, this speed is close to the ion acoustic speed $(T_e/m_i)^{1/2}$. The range of M in which shock solutions exist is fairly narrow. For the above parameters, we have $M_0 \approx 0.879$ and $M_1 \approx 0.8944$.

In the above considerations, we neglected the effect of Landau damping on the shock wave formation. This is valid when dissipation due to dust charging is stronger than that due to Landau damping. On time scales characteristic of ion acoustic wave propagation in the presence of electromagnetic radiation, the condition for

dissipative effects due to dust charging to dominate over those due to Landau damping is

$$(a^2/\lambda_D^2)\lambda_D^3 n_{e0} \gg (m_e/m_i)(\nu_q/\omega_{pi}), \quad (18)$$

where $\omega_{pi} = (4\pi n_{i0}e^2/m_i)^{1/2}$ is the ion plasma frequency. For $n_{e0} = 10^3$ cm^{-3}, $n_{i0} = 8 \times 10^2$ cm^{-3}, $T_e = 2$ eV, $T_i =$
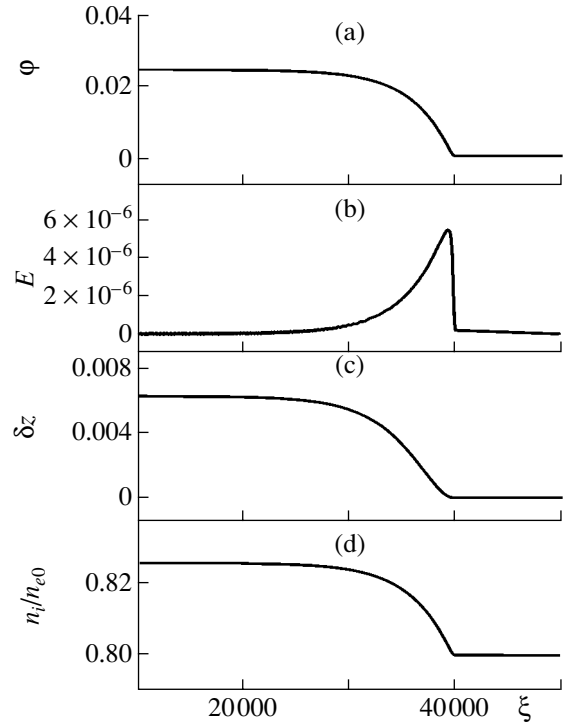
Fig. 2. Profiles of (a) the potential $\varphi(\xi)$, (b) electric field $E = -d_\xi\varphi$, (c) perturbation of the normalized charge δz, and (d) ion density n_i normalized to the unperturbed electron density n_{e0} in a shock wave structure for the parameters of Fig. 1.

Fig. 3. A portion of the profile of the electric field E on an enlarged scale. The range of ξ corresponds to the wave front region.

0.5 eV, $a = 10^{-4}$ cm, $\lambda_R = 2 \times 10^{-5}$ cm, $\beta = 0.1$, and $\Phi = \Phi_s = 1.4 \times 10^6$ erg/(cm^2 s), inequality (18) is easily satisfied (the left-hand side is three orders of magnitude larger than the right-hand side).

The shock waves discussed here are collisionless in the sense that they do not involve electron–ion collisions (the source of dissipation for ordinary collisional ion acoustic shock waves). However, in contrast to classical collisionless shock waves [3], in which dissipation is only related to the turbulent wave–particle interaction, dissipation due to dust charging involves the interaction of electrons and ions with dust grains in the form of microscopic grain currents and the photoelectric current. A similar situation takes place in the absence of electromagnetic radiation [4]. This is because, for the majority of complex plasmas, the charging rate ν_q is much higher than the ion–ion collision frequency and the electron collision frequency. We emphasize that dust shocks have unique conditions of existence. Thus, they can be useful in studying astrophysical complex plasmas.

3. EVOLUTION OF AN INITIALLY NONMOVING REGION WITH A CONSTANT INCREASED ION DENSITY

The above investigation concerned the problem of the existence of steady-state shock wave solutions. However, in order to understand whether shock wave structures are significant nonlinear wave structures in dusty plasmas in the presence of electromagnetic radiation, it is necessary to answer the question of whether the evolution of a perturbation leads to the formation of shocks in a dusty plasma with a variable grain charge. Furthermore, the solution of the problem of the evolution of a perturbation and the possibility of its transformation into a shock wave is important from the standpoint of the description of real phenomena like supernova explosions, as well as laboratory experiments and active space and geophysical experiments.

In order to investigate the problem of the evolution of a perturbation and its transformation into a nonlinear wave structure in a dusty plasma with a variable grain charge in the presence of electromagnetic radiation, we used a computational method analogous to that developed in [12].

To solve the ion continuity equation and the ion momentum equation, we use the LCPFCT modification of the flux-corrected transport (FCT) algorithm with fourth-order phase accuracy, second-order time accuracy, and minimum residual diffusion [21]. The FCT algorithm is monotonic, conservative, and positivity-preserving. This means that the algorithm is accurate and resolves steep gradients (including scales on the order of the grid size). When a convected quantity (such as the ion density) is initially positive, it remains positive and no new maxima or minima are introduced due to numerical errors during convection.

The LCPFCT transport algorithm consists of the following four sequential steps:

(i) the computation of the transported and diffused values and the choice of the diffusion coefficients to satisfy monotonicity,

(ii) the computation of the raw antidiffusive fluxes,

(iii) the correction or limitation of these fluxes to assure monotonicity, and

(iv) the performance of the antidiffusive correction.

To solve Eq. (4) for dust grain charging, we use the fourth-order Runge–Kutta method [22]. Poisson's equation is solved numerically using the sweep method [21].

The total set of equations is solved using the following sequence of operations (at each time step):

(i) the integration of conservation equations,

(ii) the integration of the equation for dust grain charging, and

(iii) the integration of Poisson's equation.

These three stages are related to each other by an iteration process that is verified by the charge density convergence.

Now, we consider the situation in which the evolution of an initial perturbation can result in the formation of a shock wave structure that is close to the exact steady-state shock wave solution. For simplicity, we consider a nonmoving region with a constant increased ion density as an initial perturbation. The amplitude of the initial perturbation φ_0 should be larger than that of the steady-state shock φ_A. Otherwise, a quasi-steady shock does not form; the amplitude of the evolving perturbation progressively decreases; and, finally, the perturbation disappears.

The results of calculations describing the evolution of an initially nonmoving region with a constant increased ion density that corresponds to the initial amplitude $\varphi_0 = 0.048$ for the plasma parameters $n_{e0} = 10^3$ cm^{-3}, $n_{i0} = 8 \times 10^2$ cm^{-3}, $T_e = 2$ eV, $T_i = 0.5$ eV, $a = 10^{-4}$ cm, $\lambda_R = 2 \times 10^{-5}$ cm, $\beta = 0.1$, and $\Phi = \Phi_s = 1.4 \times 10^6$ erg/(cm^2 s) are presented in Figs. 4 and 5. It is assumed that the initial charge of dust grains is equal to its equilibrium value in the absence of wave perturbations ($z_0 \approx -1.41$). We use the normalization $x/\lambda_D \longrightarrow x$ for the spatial variable and $tc_s/\lambda_D \longrightarrow t$ for time. The evolution of the perturbation results in the formation of a quasi-steady structure propagating at $t > 100$ with a constant speed corresponding to the Mach number $M \approx 0.894$. Figure 4 shows the profiles of the potential $\varphi(x)$, the normalized charge perturbation δz, the ion speed v_i normalized to c_s, and the ion density n_i normalized to the unperturbed electron density n_{e0} at the instants $t = 100$, 10000 and 20000. The initial profiles (at $t = 0$) of the potential φ and the normalized ion density n_i/n_{e0} are shown by the light curves on the left of the corresponding panels. The light curves on the right of the panels
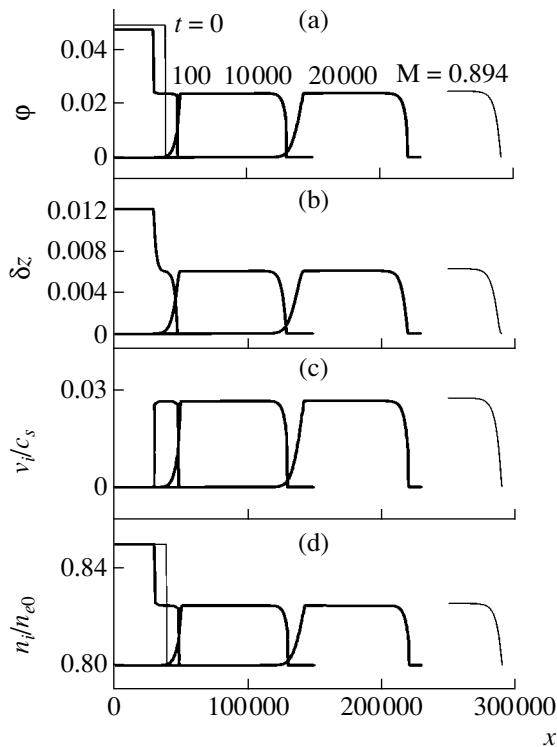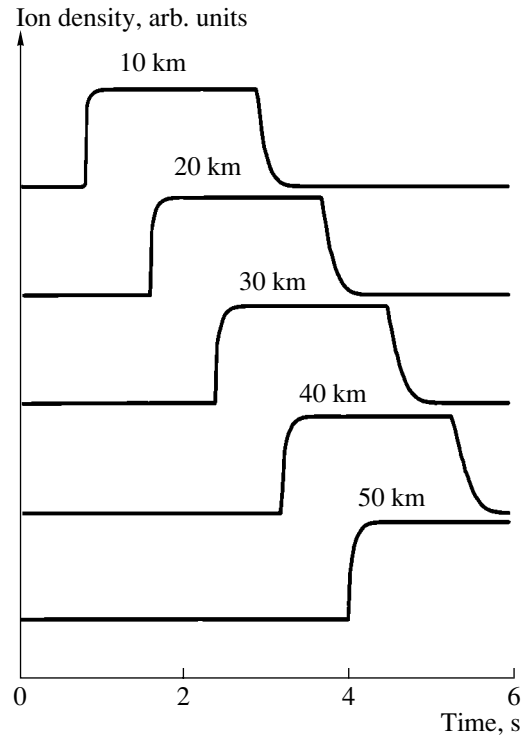
Fig. 4. Profiles of (a) the potential $\varphi(x)$, (b) normalized charge perturbation δz, (c) ion speed v_i normalized to c_s, and (d) ion density n_i normalized to the unperturbed electron density n_{e0} at the instants $t = 100$, 10000 and 20000 for the following parameters: $\varphi_0 = 0.048$, $n_{e0} = 10^3$ cm^{-3}, $n_{i0} = 8 \times 10^2$ cm^{-3}, $T_e = 2$ eV, $T_i = 0.5$ eV, $a = 10^{-4}$ cm, $\lambda_R = 2 \times 10^{-5}$ cm, $\beta = 0.1$, and $\Phi = \Phi_s = 1.4 \times 10^6$ erg/(cm^2 s). The initial charge of dust grains is equal to the equilibrium grain charge in the absence of wave perturbations ($z_0 \approx -1.41$). The initial profiles (at $t = 0$) of the potential φ and the normalized ion density n_i/n_{e0} are shown by the light curves on the left of the corresponding panels. The light curves on the right of the panels (a)–(d) show the profiles corresponding to the exact steady-state shock wave solution with $M = 0.894$.

Fig. 5. Evolution of the initial perturbation of the ion density on the real spatial and time scales. The parameters are the same as in Fig. 4.

show the corresponding profiles of the exact steady-state shock wave solution with $M = 0.894$.

In Fig. 4, we can see that the evolution of an intense, initially nonmoving region with a constant increased ion density results in the formation of a shock wave similar to the exact steady-state shock wave solution with the Mach number $M = 0.894$. The difference between these two solutions is the presence in the former of a rarefaction region (dilatation wave) in addition to a compression region. In the course of the shock wave evolution, the distance between the rarefaction and compression regions decreases. Finally, the presence of the dilatation wave leads to the destruction of the shock structure.

Figure 5 illustrates the spatial evolution of the initial perturbation of the ion density at real spatial and time

scales. In this figure, the regions corresponding to the compression and dilatation waves are clearly seen.

We have also studied the influence of the initial dust grain charge on the evolution of an initially nonmoving region with a constant increased ion density. Analogously to [12], the evolution of an initial perturbation for different initial grain charges is almost the same at $t > 100$. This is related to the fact that the characteristic charging time of dust grains is far less than the time during which a structure similar to the exact steady-state shock wave solution is formed.

4. ACTIVE EXPERIMENTS AND THE POSSIBILITY OF SHOCK WAVE OBSERVATION

Let us discuss the possibility of the observation of shock waves related to dust charging in the presence of electromagnetic radiation. As was shown above, the width of the front of a shock wave related to dust charging for ionospheric plasma parameters at altitudes of 500–600 km and dust grain sizes on the order of 10^{-4} cm can attain several kilometers. Thus, it is of interest to investigate the possibility of both the appearance of charged dust grains in active rocket experiments that involve the release of a gaseous substance in the Earth's ionosphere and the formation of shock waves related to dust charging in such experiments. The idea of shock wave observations was forwarded in con-

nection with active space experiments carried out by the Active Magnetospheric Particle Tracer Explorers (AMPTE). One of the main purposes of the AMPTE experiment (see, e.g., [23]) was to study collisionless shock waves with very wide fronts. We pay main attention to experiments conducted in the daytime (when electromagnetic radiation makes an important contribution). We assume that the experiments are carried out at altitudes of 500–600 km and the scheme of experiments is analogous to that of the Fluxus-1 and Fluxus-2 experiments, which were carried out at an altitude of 140 km [24, 25]. In those experiments, the source of charged particles was the generator of high-speed plasma jets. The shock wave front is associated with the fore part of the jet, i.e., the boundary between the jet plasma and the ionospheric plasma. The possibility of observing shocks related to the dissipation caused by dust charging in the absence of electromagnetic radiation (when experiments are carried out at night) was discussed in [10].

In experiments conducted at altitudes of 500–600 km, aerosols (dust grains) appear as a result of condensation [26]. The period of the formation of the centers of condensation is very short, and all the drops have approximately the same size a. The size a was estimated for two situations [10]. In the first case, calculations were performed by N.A. Artem'eva for an air jet. The characteristic expansion velocity of molecular nitrogen is $U = 0.3$–0.5 km/s. Condensation starts when the jet passes a distance on the order of 10 cm. The degree of condensation is equal approximately to 0.72, and the grain size is $a = 1.5 \times 10^{-4}$ cm. In the second case, the gaseous substance was iron. The estimates were obtained with the use of data from [26]. In this case, the degree of condensation is $x \approx 0.44$. The important result here is that the size a decreases significantly as the jet velocity increases ($a = 6 \times 10^{-3}$ cm for $U = 9.2$ km/s; $a = 3.3 \times 10^{-5}$ cm for $U = 15.5$ km/s; $a = 6 \times 10^{-7}$ cm for $U = 21.4$ km/s; and $a = 10^{-8}$ cm for $U = 27.2$ km/s). We see that, for the U values exceeding 25 km/s, the size a is on the order of the characteristic size of a molecule. This means that, at sufficiently high jet velocities, condensation does not lead to the formation of grains.

The charge acquired by dust grains can be estimated as an unperturbed dust grain charge from the balance condition for the microscopic electron and ion grain currents and the photoelectric electron current. For ionospheric parameters at altitudes of 500–600 km ($n_{e0} = 10^3$ cm^{-3}, $n_{i0} = 8 \times 10^2$ cm^{-3}, $T_e = 2$ eV, $T_i = 0.5$ eV, and $\Phi = \Phi_s = 1.4 \times 10^6$ erg/(cm^2 s)), the parameters $\lambda_R \equiv 2\pi c/\omega_R = 2 \times 10^{-5}$ cm and $\beta = 0.1$, and the above values of the jet velocity U, we found the values of the charge number Z_{d0}, the charging rate ν_q, and the characteristic distance $L \sim U/\nu_q$ over which the dust grain acquires the charges $q_d \sim -Z_{d0}e$.

The main results of this investigation are the following:

(a) For velocities U lower than 10 km/s, the effect of dust charging is significant and the characteristic distance L over which the grain acquires a significant charge does not exceed the width of the shock front (which, in our case, is on the order of 1 km). For example, for a molecular nitrogen jet propagating with a velocity of $U = 0.5$ km/s, we have $Z_{d0} \approx -2.98 \times 10^3$ and $L \sim 10^3$ cm; for an iron jet and $U = 9.2$ km/s, we obtain $Z_{d0} \approx -1.19 \times 10^5$ and $L \sim 10^3$ cm.

(b) The increase in the velocity U results in the weakening of the effect of dust charging and an increase in the distance L. For an iron jet velocity of $U = 15.5$ km/s, we obtain $Z_{d0} \approx -6.55 \times 10^2$ and $L \sim 3 \times 10^5$ cm (which is on the order of the shock front width). For $U = 21.4$ km/s, we have $Z_{d0} \approx -12$ and $L \sim 10^7$ cm.

For the above parameters, the ion acoustic speed, which determines the speed of the shock front, is $c_s \sim 10$ km/s. Thus, the optimum velocities U for manifesting the dust charging effect and observing the related shock waves do not exceed 10 km/s. The distances L corresponding to these velocities are reasonable from the standpoint of active experiments. By analogy to the AMPTE experiment [23], we can expect that the active experiments will make it possible to study the structure of the shock wave front and the physical processes occurring at the front. Furthermore, the active experiments described here and in [10] can help to model different physical phenomena occurring in nature, e.g., during a large meteoroid impact with the Moon's surface [27]. The evolution of the impact plume can lead to the formation of a shock wave structure associated with the appearance of charged grains produced due to the condensation of both the plume substance and the vapor thrown from the crater and the surrounding regolith layer.

5. SUMMARY

We have studied the influence of the photoelectric effect on the propagation of nonlinear waves in complex plasmas. The photoelectric effect results in the appearance of electrons emitted from the surface of dust grains, which, in turn, leads to the generation of the photoelectric electron current in addition to the usually considered microscopic electron and ion currents. We have calculated the electromagnetic radiation effects for the solar radiation spectrum in the vicinity of the Earth. In complex plasmas, an important role is played by nonlinear shock wave structures. The physical reason for their existence is an anomalous dissipation originating from the dust charging. In contrast to the case in which radiation is absent, the dust grains acquire large positive charges. We have found exact solutions to nonlinear equations in the form of steady-state shocks and have obtained the conditions for their existence. These shock waves are collisionless in the sense that they do not involve electron–ion collisions. However, in contrast to classical collisionless shock waves, in which

dissipation is only due to the turbulent wave–particle interaction, the dissipation due to dust charging involves the interaction of electrons and ions with dust grains in the form of the microscopic grain current and the photoelectric current. In the case under consideration, ion acoustic shocks can exist within a rather narrow range of the shock wave velocities determined by inequalities (14) and (16). For the majority of complex plasmas, the shock wave velocity is close to the ion acoustic speed $(T_e/m_i)^{1/2}$. We have considered the nonsteady problem of the evolution of a perturbation and its transformation into a nonlinear wave structure. We have investigated the evolution of an intense, initially nonmoving region with a constant increased ion density. The evolution of such a region can result in the formation of a shock wave solution that is similar to the exact steady-state solution. The difference between these two solutions is that, in the former, there is a rarefaction region (dilatation wave) in addition to a compression region. Finally, the presence of the dilatation wave leads to the destruction of the shock structure. We have discussed the possibility of observing shock waves related to dust charging in the presence of electromagnetic radiation in active rocket experiments that are based on the scheme of the Fluxus-1 and Fluxus-2 experiments [24, 25] and involve the release of a gaseous substance in Earth's ionosphere in the form of a high-speed plasma jet at altitudes of 500–600 km. For the shock waves related to dust charging to be observed, the jet velocity should not exceed 10 km/s. Because of the unique conditions of the existence of dust shock waves in the presence of electromagnetic radiation, they can be useful in studying astrophysical complex plasmas.

ACKNOWLEDGMENTS

REFERENCES

1. V. N. Tsytovich, Usp. Fiz. Nauk **167**, 57 (1997) [Phys. Usp. **40**, 53 (1997)].
2. Ya. B. Zel'dovich and Yu. P. Raizer, *Physics of Shock Waves and High-Temperature Hydrodynamic Phenomena* (Nauka, Moscow, 1966, 2nd ed.; Academic, New York, 1966).
3. R. Z. Sagdeev, in *Reviews of Plasma Physics*, Ed. by M. A. Leontovich (Atomizdat, Moscow, 1964; Consultants Bureau, New York, 1968), Vol. 4.
4. S. I. Popel, M. Y. Yu, and V. N. Tsytovich, Phys. Plasmas **3**, 4313 (1996).
5. S. I. Popel, V. N. Tsytovich, and M. Y. Yu, Astrophys. Space Sci. **256**, 107 (1998); S. I. Popel, V. N. Tsytovich, and M. Y. Yu, in *Plasma Physics*, Ed. by P. Martin and J. Puerta (Kluwer, Dordrecht, 1998), p. 107.
6. S. I. Popel, A. P. Golub', T. V. Losseva, and R. Bingham, Pis'ma Zh. Éksp. Teor. Fiz. **73**, 258 (2001) [JETP Lett. **73**, 223 (2001)].
7. Y. Nakamura, H. Bailung, and P. K. Shukla, Phys. Rev. Lett. **83**, 1602 (1999).
8. Q.-Z. Luo, N. D'Angelo, and R. L. Merlino, Phys. Plasmas **6**, 3455 (1999).
9. S. A. Kaplan and S. B. Pikel'ner, *The Interstellar Medium* (Nauka, Moscow, 1963; Harvard Univ. Press, Cambridge, 1970).
10. S. I. Popel and V. N. Tsytovich, Astrophys. Space Sci. **264**, 219 (1999).
11. O. Havnes, U. de Angelis, R. Bingham, *et al.*, J. Atmos. Terr. Phys. **52**, 637 (1990).
12. S. I. Popel, A. P. Golub', T. V. Losseva, *et al.*, Fiz. Plazmy **27**, 483 (2001) [Plasma Phys. Rep. **27**, 455 (2001)].
13. S. I. Popel and M. Y. Yu, Phys. Rev. E **50**, 3060 (1994); Contrib. Plasma Phys. **35**, 103 (1995).
14. F. F. Chen, *Plasma Diagnostic Techniques*, Ed. by R. H. Huddlestone and S. L. Leonard (Academic, New York, 1965), Chap. 4.
15. M. S. Barnes, J. H. Keller, J. C. Forster, *et al.*, Phys. Rev. Lett. **68**, 313 (1992).
16. L. Spitzer, Jr., *Physical Processes in the Interstellar Medium* (Wiley, New York, 1978; Mir, Moscow, 1981).
17. B. T. Draine and E. E. Salpeter, Astrophys. J. **312**, 77 (1979).
18. O. Havnes, T. W. Hartquist, and W. Pilipp, in *Physical Processes in Interstellar Clouds*, Ed. by G. E. Morfill and M. Scholer (D. Reidel, Dordrecht, 1987).
19. D. Bilitza, *International References Ionosphere 1990*, Science Data Center, NSSDC/WDC-A-R&S 90-20 (Greenbelt, Maryland, 1990).
20. E. C. Whipple, Rep. Prog. Phys. **44**, 1206 (1981).
21. E. S. Oran and J. P. Boris, *Numerical Simulation of Reactive Flow* (Elsevier, New York, 1987).
22. G. E. Forsythe, M. A. Malcolm, and G. B. Moler, *Computer Methods for Mathematical Computations* (Prentice-Hall, Englewood Cliffs, 1977).
23. R. Bingham, V. D. Shapiro, V. N. Tsytovich, *et al.*, Phys. Fluids B **3**, 1728 (1991).
24. B. G. Gavrilov, A. I. Podgorny, I. M. Podgorny, *et al.*, Geophys. Res. Lett. **26**, 1549 (1999).
25. R. E. Erlandson, P. K. Swaminathan, C.-I. Meng, *et al.*, Geophys. Res. Lett. **26**, 1553 (1999).
26. Yu. P. Raĭzer, Zh. Éksp. Teor. Fiz. **37**, 1741 (1959) [Sov. Phys. JETP **10**, 1229 (1960)].
27. I. V. Nemtchinov, R. E. Spalding, V. V. Shuvalov, *et al.*, in *Proceedings of the 31st Lunar and Planetary Science Conference, Houston, TX, 2000*, p. 1334.

Translated by the authors

EDGE
PLASMA

Structure of Fluctuations in the Floating Potential and Ion Saturation Current in the Edge Plasma of the L-2M Stellarator

Yu. V. Kholnov

Institute of General Physics, Russian Academy of Sciences, ul. Vavilova 38, Moscow, 119991 Russia
Received November 2, 2000; in final form, January 18, 2001

Abstract—Results are presented from the measurements of the ion saturation current, the floating potential, and their fluctuations in the edge plasma of the L-2M stellarator. Distinguishing features in the distribution of the ion saturation current and the floating potential near the separatrix are revealed and examined. Based on the cross correlation measurements with probes positioned at different toroidal angles, it is concluded that fluctuations in the ion saturation current are related to fast vertical displacements of the plasma column, whereas fluctuations in the floating potential have the form of waves propagating in the radial direction. © *2001 MAIK "Nauka/Interperiodica".*

1. INTRODUCTION

In order to better understand transport mechanisms in tokamaks and stellarators, it is necessary to study the edge plasma processes in these devices. Here, edge plasma means a plasma region near the separatrix. Outside the separatrix, the magnetic field lines terminate at the limiter, divertor plates, or vacuum chamber wall. Near the chamber wall, all of the edge plasma parameters are strongly inhomogeneous. In the presence of a limiter, the direction of the poloidal rotation near the chamber wall changes from the electron to ion diamagnetic drift direction [1]. The strong plasma inhomogeneity is the main reason for the increased level of fluctuations in the plasma parameters.

The edge plasma is usually investigated with Langmuir probes. The validity of the probe measurements is confirmed by reflectometry, electron-cyclotron emission measurements, and other diagnostics. At present, studies of the edge plasma turbulence are in progress. Thus, a new line of investigation—the study of the statistical properties of turbulence in toroidal devices—has been developed. Nevertheless, a number of problems that have been attacked for the last twenty years still remain unresolved. First of all, this concerns the theoretical description of the edge plasma turbulence.

In a number of studies on fluctuations in the floating potential and ion saturation current in the edge plasma of toroidal devices (see, e.g., [2–4]), it was found that, if the temperature fluctuations are ignored, then the behavior of fluctuations in the plasma density and plasma potential cannot be adequately described by the Boltzmann formula $\tilde{n} \sim \dfrac{\tilde{\phi}}{kT_e}$. In [5], it was shown that only 45% of the density fluctuations correlated with the Boltzmann distribution.

In this paper, we present results from the studies of the radial distributions of the floating potential and ion saturation current, fluctuations in these parameters, and the cross correlation functions for probes positioned at different toroidal and poloidal angles in the L-2M stellarator.

2. EXPERIMENTAL SETUP

The main parameters of the L-2M stellarator are the following: the major radius is $R = 100$ cm, the mean plasma radius (the mean radius of the vacuum separatrix) is $r_s = 11.5$ cm, and the toroidal magnetic field is $B_T = 1.2$–1.4 T [6].

The rotational transform of the L-2M magnetic configuration can be written in the form

$$\iota^* \approx 0.175 + 0.26(r/r_s)^2 + 0.27(r/r_s)^4, \quad \iota^* = 1/q,$$

where r is the mean radius of a magnetic surface and q is the safety factor. The plasma was created and heated with a gyrotron operating at a frequency of 75 GHz. A microwave beam (180–250 kW) was launched at the toroidal angle $\varphi = 0°$. The maximum electron temperature was $T_e \sim 1$ keV, the average plasma density was $n_e \sim 1.5 \times 10^{13}$ cm^{-3}.

The parameters of the edge plasma in the L-2M stellarator were measured with several probe sets positioned at different toroidal angles: in the top port at $\varphi \simeq 347°$ and in the bottom ports at $\varphi = 0°$, $\varphi \simeq 231°$ and $\varphi = 90°$ (in Fig. 1, the corresponding probe sets are denoted as a, b, c, and d, respectively). Note that the microwave power was launched in the cross section in which probe set c was installed; however, we did not observe that this had any influence on the results of probe measurements.

Each probe set consisted of several individual probes; with these probes, we measured the poloidal and radial correlations. The probes had 2-mm-long molybdenum electrodes 0.5 mm in diameter. The probe wires were isolated with quartz pipes. The ion saturation current was measured using load resistances of 3 or 10 Ω. The recording system allowed us to analyze signals with frequencies up to 1 MHz.

The rotational transform at the last magnetic surface was equal to $\sim 0.7 \times 2\pi$. Thus, probes a and c separated by an interval equal to ~ 0.7 of the major circumference were located on nearly the same magnetic field line. The distance between probes b and c along the magnetic field line was longer than the major circumference by a factor of 1.5. The position of the last magnetic surface $r = 113$ mm in the cross section of probes b was determined previously with magnetic measurements. Calculations show that, in the regions under study, the outward shift of the separatrix due to the plasma pressure is relatively small (~ 5 mm). Note that, a similar outward shift may be produced by an external vertical magnetic field of $B_p \simeq 40$ G. Unfortunately, the data from magnetic measurements for the other angles under study are lacking.

In [7], the parameters of the edge plasma were measured with a probe positioned in the inner port in the cross section $\varphi \simeq 90°$. It was shown that the edge plasma consists of three characteristic regions: a wall region, a region with a high gradient of the electron density, and the edge of the plasma column. The plasma density in the wall region was on the order of $n_e \simeq 10^9$ cm^{-3}, the electron temperature was $T_e \sim 2$–4 eV, and the floating potential V_f was close to zero. Near the separatrix, the plasma density increased by three orders of magnitude. At the edge of the plasma column, the plasma density increased only slightly, but the temperature increased substantially.
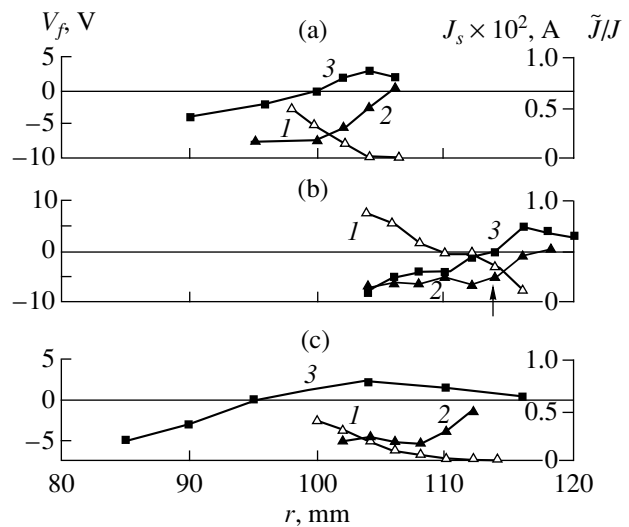
3. MEASUREMENTS OF THE ION SATURATION CURRENT AND FLOATING POTENTIAL

Figure 2 shows typical distributions of the ion saturation current J_s, fluctuations $\tilde{J}_s/J_s$, and the floating potential V_f near the last magnetic surface in the cross sections corresponding to probes a, b, and c. It can be seen in these figures that the profiles measured in these cross sections are somewhat different, but their behavior is similar: the ion saturation current arises at a certain distance from the chamber wall and increases as the probe is displaced into a plasma, whereas the current fluctuations increase toward the plasma edge, as was also observed in other devices. The floating potential at the edge is positive (below 10 V) and varies only slightly with radius; deeper in the plasma, it becomes negative and increases in magnitude.

The vertical arrow in Fig. 2b shows the position of the separatrix for probe b. The position of the separatrix
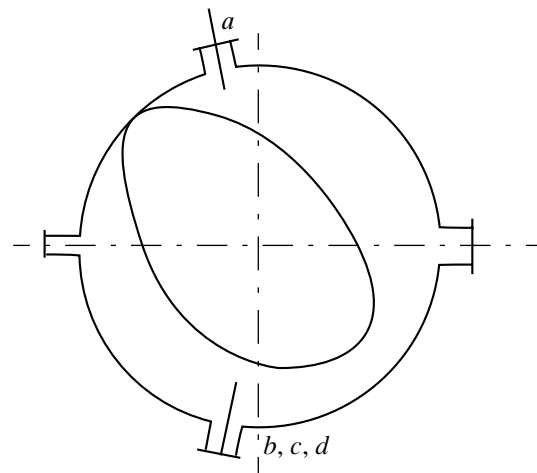

Fig. 1. Arrangement of the probes in the cross section of the vacuum chamber of the L-2M stellarator. Probe a is positioned at the toroidal angle $\varphi \approx 347°$, probe b is at $\varphi \approx 231°$, probe c is at $\varphi = 0°$, and probe d is at $\varphi = 90°$. The last closed magnetic surface is schematically shown inside the vacuum chamber.

Fig. 2. Distributions of (1) the ion saturation current J_s, (2) $\tilde{J}_s/J_s$ fluctuations, and (3) floating potential V_f at the plasma edge. The measurements were carried out (a) in the top port by probe a, (b) in the bottom port by probe b, and (c) in the bottom port by probe c. The load in J_s measurements is 10 Ω.

can be seen to almost coincide with the region in which the potential changes its sign. This was also observed in previous experiments in which the last closed magnetic surface was measured with probes in different cross sections.

The difference between the edge plasma profiles at different toroidal angles seems to be related, first of all,
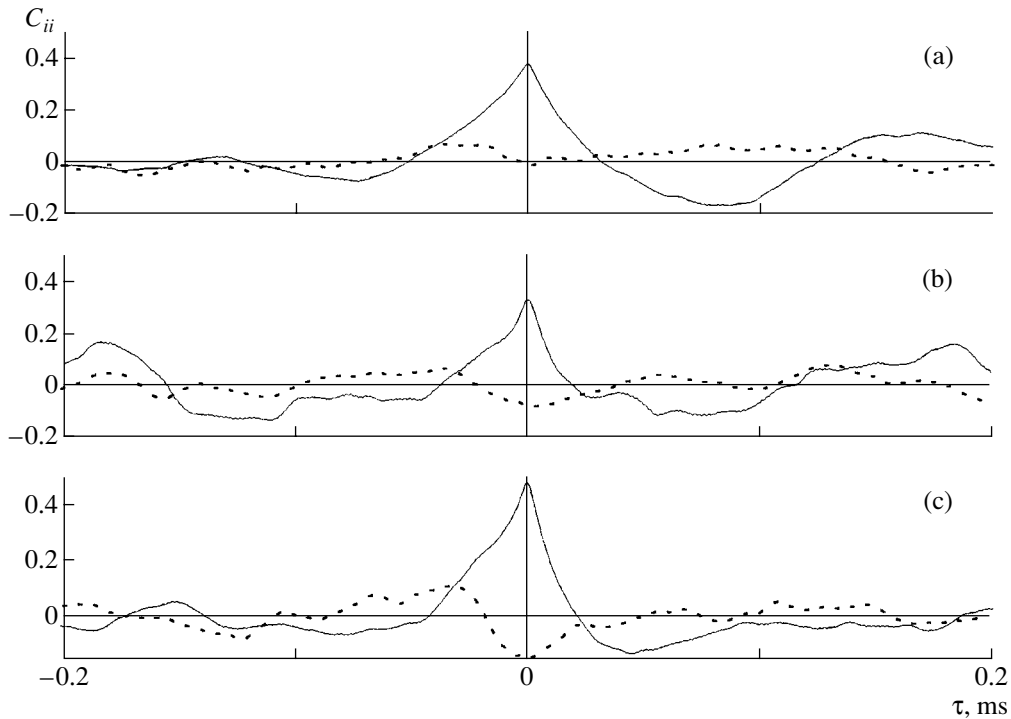
Fig. 3. Cross correlation functions between fluctuations in the ion saturation current at probes b and c (solid line) and probes a and c (dashed line) under different experimental conditions: (a) the heating power is $P = 200$ kW and the vertical magnetic field is $B_p = 40$ G, (b) $P = 200$ kW and $B_p = 0$, and (c) $P = 250$ kW and $B_p = 0$.

to an error in determining the coordinate with respect to the chamber wall. Second, the difference may be due to the presence of the resonant magnetic surface with $m/n = 2/1$. The vacuum magnetic measurements showed that this resonance takes place at a distance of ~2 cm from the last magnetic surface; however, in the presence of the plasma, the magnetic structure somewhat changes because of the plasma pressure.

4. FLUCTUATIONS IN THE ION SATURATION CURRENT

The aim of the fluctuation measurements was to determine the structure of fluctuations in the plasma of the L-2M stellarator. To do this, we measured the correlation between the probe signals.

Figure 3 shows the cross correlation functions measured under different experimental conditions (for different heating powers with and without applying an external vertical magnetic field, which leads to the shift of the plasma edge by several millimeters). The figure demonstrates a rather good correlation of fluctuations in the ion saturation current measured with probes b and c, both located in the bottom ports. For probes a (located in the top port) and c, the correlation level is substantially lower; nevertheless, the results of three different experiments show that, in this case, anticorrelation is observed. The correlation function C_{ii} was calculated by superimposing the functions measured in

several shots, which allowed us to enhance the contrast. However, even this procedure did not reveal any correlation between probes a and b, although the distance between them along the magnetic field line was shorter.

Figure 4 shows the results of measurements in which probe b was shifted radially with respect to probe c. We can see that the correlation function varies slightly; i.e., the size of the region in which fluctuations are localized is at least ~1 cm. As can be seen in Figs. 3 and 4, the time delay in the cross correlation function is absent, which indicates that the oscillation phase of the fluctuation signal does not change.

The coefficient of correlation between the fluctuations measured by the bottom probes b and c is higher than that for probes a and b, although the distance between the latter probes along the magnetic field line is shorter. This indicates that long-wavelength fluctuations along the magnetic field lines are absent. As is seen from Figs. 3 and 4, the maximum value of the correlation coefficient usually varies in the range 0.2–0.4 and, in some cases, attains 0.6. However, in some shots, the correlation between the bottom probes was significantly lower, which indicated to the absence of a correlation between these probes. In this case, the relative fluctuation $\tilde{J}_s / J_s$ increased from 10–15 to 30–40%. It may be supposed that, when the correlation between the signals from the probes separated by a large distance along the torus was high, the oscillation modes

with small $k_\parallel$ were excited. When no correlation was observed, this mode, probably, was suppressed.

## 5. FLUCTUATIONS IN THE FLOATING POTENTIAL

The behavior of fluctuations in the floating potential differs substantially from that in the ion saturation current. We recall that no correlation was observed for the ion saturation currents of probes a and b. At the same time, the cross correlation function between the floating potentials measured with these probes C_{vv} was rather high, as is seen from Fig. 5. Figure 5a shows how the cross correlation function C_{vv} varies as the top probe shifts by ~3 cm. The results correspond to two positions of probe b. We note that C_{vv} varies with radius by a sinusoidal law. A similar situation is observed in Fig. 5b, which shows a fragment of such sinusoidal oscillations as the bottom probe c shifts relative to probe b, and in Fig. 5c, which represents another series of experiments in which the bottom probe d positioned at $\varphi = 90°$ shifts relative to probe b. It should be noted that the same distribution was observed independent of whether the measurements of the ion saturation current were carried out; i.e., this effect cannot be attributed to plasma perturbation caused by the measurements of the ion saturation current.

Variations in the cross correlation function C_{vv} with radius can be interpreted as variations in the oscillation phase, i.e., as the radial propagation of a wave. As follows from Fig. 5a, the characteristic wavelength of the wave propagating in the transverse direction is ~3 cm and the characteristic period, which is determined by the correlation time, is ~100–150 μs.

To understand the character of the radial wave propagation (i.e., to determine whether the wave is standing or running), we measured the correlation functions for two probes of set b that were spaced by 4 mm in the radial direction. Figure 6 shows the correlation functions calculated using the results of four series of experiments. In all four series, the delay times in the correlation functions point to the radial propagation of fluctuations. The sign of the delay time corresponds to the outward propagation, and the velocity estimated from the delay time of the correlation function (3–5 μs) is ~10^5 cm/s.

6. DISCUSSION OF THE RESULTS

The measurements of the distributions of the average values of the ion saturation current and the floating potential showed that the last magnetic surface calculated with account for the plasma pressure nearly coincides with the boundary of the region in which we observe the increase in the ion saturation current. The floating potential in this region remains positive and varies slightly in magnitude. Deeper in the plasma, the potential drops sharply. In [8], it was shown that, as the
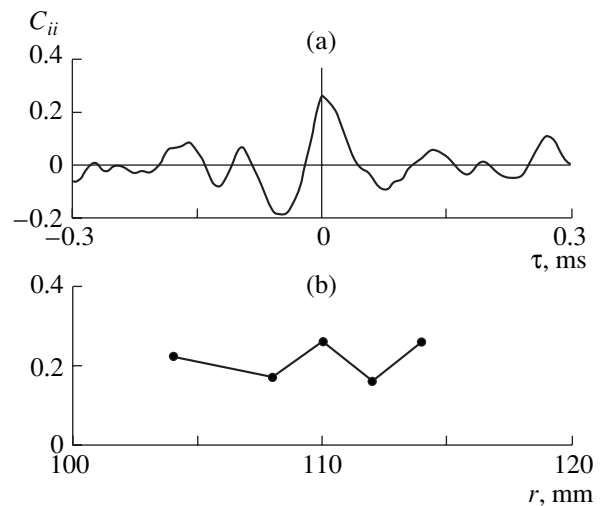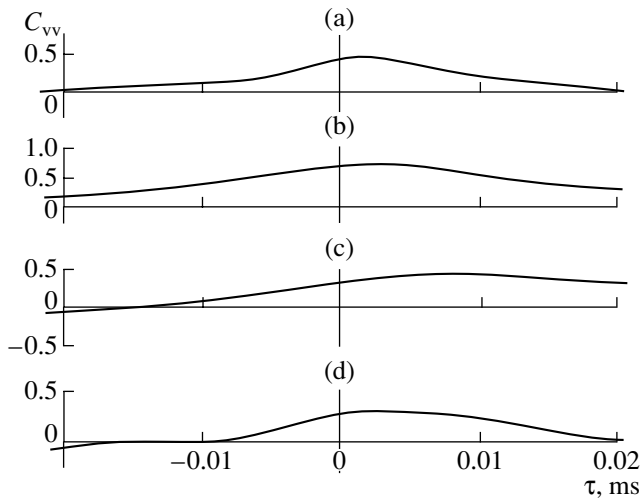

Fig. 4. (a) Cross correlation function $C_{ii}(\tau)$ between fluctuations in the ion saturation current measured with probes b and c positioned in bottom ports ($r_b = 110$ mm, $r_c = 95$ mm) and (b) $C_{ii}(0)$ vs. the radial position of probe b for $r_c = 95$ mm.
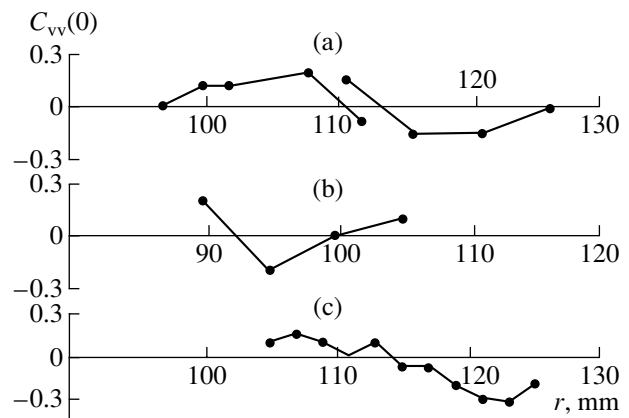
Fig. 5. Cross correlation function $C_{vv}(0)$ between the floating potential signals from (a) probes a and b vs. the position of probe a for two positions of probe b, $r_{b1} = 110$ mm (left curve) and $r_{b2} = 108$ mm (right curve); (b) probes b and c vs. the position of probe c for the fixed probe b ($r_b = 110$ mm); and (c) probes b and d vs. the position of probe d for the fixed probe b ($r_b = 100$ mm).

neutral gas flux from the wall increases, the point at which V_f changes its sign shifts toward the plasma center. This allows us to suppose that the region in which the potential is positive and varies only slightly with radius is associated with ionization processes in the plasma. Previous measurements of the electron temperature showed that the increase in T_e correlates with the decrease in V_f.

There is another plausible explanation of the difference between the observed J_s and V_f distributions. The stable last closed magnetic surface is produced by the

Fig. 6. Cross correlation functions $C_{vv}(\tau)$ between the floating potential signals from two probes in set *b* that are spaced by 4 mm in the radial direction for different positions of the first probe: (a) $r_1 = 106$ mm, (b) $r_2 = 104$ mm, (c) $r_3 = 102$ mm, and (d) $r_4 = 110$ mm.

external magnetic field, and the behavior of V_f outside this surface depends on the high plasma conductivity along the magnetic field lines. As for the electron density, the diffusion density distribution at these radii may be related to the particle loss across (rather than along) magnetic field lines.

Fluctuation measurements confirmed that the spatial distributions of fluctuations in the ion saturation current and fluctuations in the floating potential are different, as was observed in many devices. The correlation between J_s fluctuations measured by the bottom probes, the weak dependence of this correlation on the radius, and the anticorrelation between the signals from the top and bottom probes allow us to suggest that the effects observed can be attributed to the displacement of the plasma column. The characteristic time of correlation between the signals from the top and bottom probes decreases during discharge (~10 ms) from 60–100 to 15–30 μs and increases after the heating pulse ends. Hence, we may suppose that the fluctuations are fast vertical displacements of the plasma column.

As was shown above, V_f fluctuations have the form of waves propagating in the radial direction. The possibility of the radial propagation of fluctuations is confirmed by the results of [9], in which it was shown that the coupling between modes can provide a mechanism for such propagation. Unfortunately, we cannot certainly state whether these waves are running or standing, because the shifted correlation functions in Fig. 6 may correspond to other oscillation modes that are not

related to the effects observed with the probes positioned at different toroidal angles.

7. CONCLUSION

(i) It is shown that, at any toroidal angle, the distribution of the floating potential V_f in the edge plasma is the same. Two radial regions may be distinguished: the region in which the potential is positive and varies only slightly and the region in which the potential is negative and its magnitude increases toward the plasma center. The plasma density becomes measurable in the region where the potential is positive.

(ii) It is shown that, in the edge plasma of the L-2M stellarator, the distributions of $\tilde{n}/n$ (which corresponds to J_s fluctuations) and $\tilde{\phi}/kT_e$ (which corresponds to V_f fluctuations) are different. This indicates that fluctuations are not electrostatic drift fluctuations. The correlation between J_s fluctuations at different radii evidences the fast vertical displacements of the plasma column as a whole.

REFERENCES

1. C. Hidalgo, M. Pedrosa, B. van Milligen, *et al.*, J. Plasma Fusion Res. **1**, 96 (1998).

2. S. J. Levinson, J. M. Beal, E. J. Powers, and R. D. Bengtson, Nucl. Fusion **24**, 527 (1984).

3. H. Zushi, T. Mzuuchi, O. Motojima, *et al.*, Nucl. Fusion **28**, 433 (1988).

4. R. R. Domínguez and R. E. Waltz, Nucl. Fusion **27**, 65 (1987).

5. V. Pericoli-Ridolfini, A. Pietropaolo, R. Cesario, and F. Zonca, Nucl. Fusion **38**, 1745 (1998).

6. V. V. Abrakov, D. K. Akulina, E. D. Andryukhina, *et al.*, Nucl. Fusion **37**, 233 (1997).

7. M. S. Berezhetskii, V. P. Budaev, and R. S. Ivanov, J. Nucl. Mater. **162/164**, 831 (1989).

8. G. M. Batanov, L. V. Kolik, A. E. Petrov, *et al.*, Pis'ma Zh. Éksp. Teor. Fiz. **68**, 560 (1998) [JETP Lett. **68**, 585 (1998)].

9. X. Garbet, L. Laurent, A. Samain, and J. Chinardet, Nucl. Fusion **34**, 963 (1994).

Translated by N. F. Larionova

LOW-TEMPERATURE PLASMA

Structures of the Plasma Channels in a Besselian Beam

L. N. Pyatnitsky

Associated Institute for High Temperatures, Russian Academy of Sciences, Izhorskaya ul. 13/19, Moscow, 127412 Russia

Received February 28, 2001

Abstract—A mechanism for the formation of the structure of an optical discharge in Besselian laser beams is proposed on the basis of analyzing numerous experiments. The discharge structure is determined by the periodicity of the field of a Besselian beam in the radial and longitudinal directions and also depends on the power and duration of the heating pulse. In the initial stage of the plasma channel formation, the configuration of the channel inhomogeneities follows the discharge structure. If the spatial scale of the discharge structure is small, then the developing channel evolves into a homogeneous state. The time required for the structural inhomogeneities of the plasma channel to be smoothed out is estimated as a function of their scale length. © 2001 MAIK *"Nauka/Interperiodica"*.

1. INTRODUCTION

The problems related to laser spark plasmas have been widely discussed in the literature (see, e.g., [1, 2]). Laser sparks are usually produced by a spherical lens, which focuses laser light into a small-diameter Gaussian beam. However, the distance L over which the intensity of such a beam can be assumed to be constant is restricted by the phenomenon of diffractive spreading. The divergence angle γ of the beam depends on the ratio of the laser wavelength λ to the beam radius a_0, $\gamma \sim \lambda/a_0$, so that, over distances $L \gg a_0$, the beam radius can be represented as $a = \gamma L$.

The diffractive spreading, which is in principle unavoidable, can, nonetheless, be compensated by forming a laser beam with a conical wave front converging toward the beam symmetry axis at an angle γ. A conical wave front is produced by a conical lens, or an axicon (see, e.g., [3]). Over the focal distance $L = R/\tan\gamma$ behind an axicon with an aperture R, the beam radius a_0 is independent of the wavelength and remains essentially constant. The radial distribution of the laser field is described by the Bessel function $J_0(x)$ [4], where $x = kr\sin\gamma$, $k = 2\pi/\lambda$, and r is the distance from an arbitrary spatial point to the beam axis.

The field of such a Besselian beam has maximums in the cylindrical regions whose boundaries x_m are the zeros of the Bessel function, $J_0(x_m) = 0$. The radius of the central region is equal to $x_0 = 2.40$, which gives $\gamma \approx 0.4\lambda/a_0$. Thus, for $\lambda \approx 1$ μm, $2a_0 = 50$ μm, and $2R = 4.5$ cm, we have $\gamma \approx 1°$. A comparison between these two beams for $2a_0 = 50$ μm shows that the cross-sectional area of a Gaussian beam increases tenfold over a distance of $L \sim 2$ mm, while the cross section of a Besselian beam remains constant over the entire focal distance $L \approx 130$ cm. A photograph of a laser spark in a Besselian beam with the above parameters is shown in Fig. 1 [5].

The very high axial symmetry of Besselian beams makes it possible to overcome several challenging problems in developing new plasma-based technologies [5–9], such as super-high-speed commutation, the generation of short-wavelength laser pulses, the plasma acceleration of charged particles, and inertial confinement fusion. In the latter case, the use of Besselian laser beams should automatically provide a uniform irradiation of laser targets (recall that, in spherical geometry, the degree of nonuniformity should be no higher than 1–2% in order for instabilities not to develop [10]).

However, the matter is not so simple as it was originally thought to be. The photograph shown in Fig. 1 was taken with a long exposure time (the camera shutter was held open) in the intrinsic light from a plasma
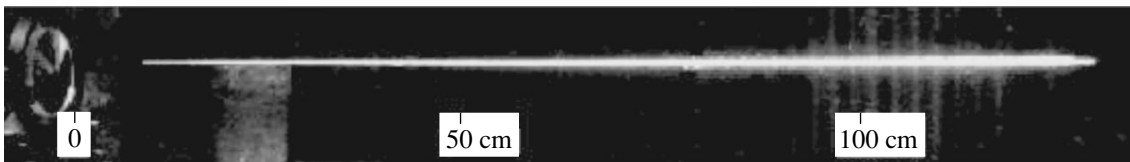
Fig. 1. Laser spark produced by a Besselian beam with the parameters $\gamma = 1°$, $\lambda = 1.06$ μm, and $R = 2.25$ cm.

heated by a 200-J, 50-ns laser pulse. Further investigations revealed several different regimes of breakdown of a gas by a Besselian beam (including the running-focus regime [6]) and the formation of structures with unusual configurations in the developing plasma channel. The formation and evolution of such structures indicate the onset and development of instabilities. In order to gain insight into the nature of this phenomenon, the structures of plasma channels at different stages were investigated in a number of gases at pressures from 0.05 to 10 atm (see, e.g., [7, 9]). It was established that the structures observed depend on the properties of Besselian beams [4]. The objective of this study is to clarify the mechanism for the formation of structures with different configurations.

2. STRUCTURES OF THE PLASMA CHANNELS

The structures of plasma channels were investigated using laser plasma diagnostics. The distribution of optical inhomogeneities in a plasma channel was visualized by shadowgraphy, schlieren photography, and interferometry. The optical inhomogeneities were recorded by image converter cameras and charge-coupled device (CCD) cameras. In the initial stage of the process, when the elements of the structure were still small-scale and the breakdown centers were opaque to probing radiation, the structure of the plasma channels was determined from the scattering of heating or probing radiation.

When comparing the plasma channels formed in Besselian beams with different parameters, it should be kept in mind that the longitudinal profile $I(z)$ of the beam intensity depends on the form of the axicon generatrix and the radial profile of the intensity of the incident radiation. For a straight-line generatrix and a rectangular (or Gaussian) profile, the longitudinal profile $I(z)$ is peaked at $z \approx L$ (or, respectively, at $z = L/2$). An exact expression for the beam intensity will be analyzed below. To compare the results obtained under different conditions, we can use the approximate formulas for the radiation intensity $w \sim (E/\tau)\gamma^3$ and the specific energy $\varepsilon \sim E\gamma^3$, where E is the laser pulse energy, τ is the full width at half-maximum (FWHM) of the laser pulse, and $a^2 L \sim \gamma^{-3}$.

Figure 2 shows two instantaneous shadowgraphs of parts of the plasma channels produced by a laser pulse with the energy $E = 70$ J and duration $\tau = 40$ ns in a Besselian beam with the convergence angle $\gamma = 7.5°$ ($L = 17$ cm). The shadowgraph of a channel in Fig. 2a was recorded 10 ns after the breakdown of air at atmospheric pressure, and the shadowgraph in Fig. 2b shows an analogous channel at the same pressure but in argon 20 ns after the breakdown. It can be seen that the plasma channel that forms in air (Fig. 2a) is continuous and uniform; it also remains uniform throughout all subsequent stages of the discharge. In contrast, the channel in argon (Fig. 2b) has a beaded structure even 20 ns after the breakdown; to a greater or lesser extent, the channel remains beaded throughout its lifetime.

This structural difference can only be explained by the fact that the intensity of the Besselian beam in argon is far above the threshold level, because, under the same conditions, the threshold for breakdown in argon is lower in comparison with that in air. If this explanation is true (i.e., if the structure of the forming plasma channel is actually affected by the intensity of the Besselian beam), this characteristic feature should also persist in other gases. This important conclusion was verified in a special series of experiments with a step profile of the specific power along the beam.

These experiments were carried out with a profiled axicon capable of producing beams with a conical wave front whose convergence angle γ varied in the range $13° \le \gamma \le 20°$. Over a focal distance of $L \approx 10$ cm, the axicon focused approximately one-quarter of the laser energy onto a 1-cm-long interval, thereby providing the conditions under which the heating radiation intensities at the neighboring sites of the focal region differed by several times in the course of a discharge. Also, in these experiments, the laser pulse energy was increased to $E = 150$ J (which corresponded to $\tau = 40$ ns). In Fig. 3, which shows a schlieren photograph of part of the plasma channel in air at atmospheric pressure, the zone of elevated pulse intensity is indicated by two small strips, installed in advance under the Besselian beam.

(a)   (b)

2 mm   2 mm
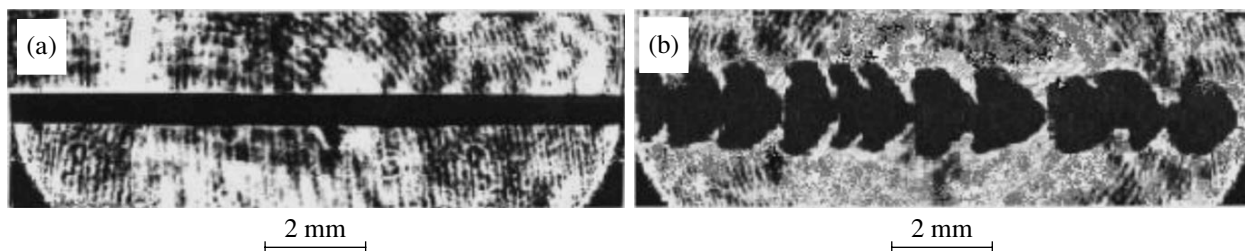
Fig. 2. Plasma channels (a) 10 ns after the breakdown in air at a pressure of 1 atm and (b) 20 ns after the breakdown in argon at the same pressure for $E = 70$ J, $\tau = 40$ ns, and $\gamma = 7.5°$.
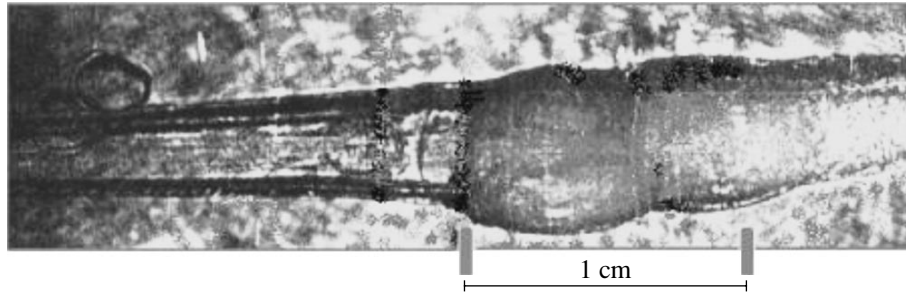
Fig. 3. Plasma channel in a beam focused by a profiled axicon ($13° \leq \gamma \leq 20°$).
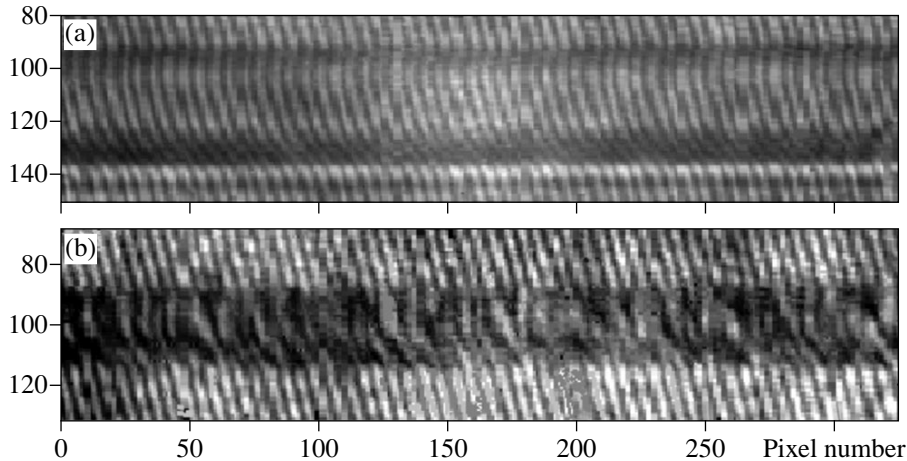
Fig. 4. Interferograms of a channel produced in N_2O at pressures of (a) 0.27 and (b) 0.67 atm for $E = 0.6$ J, $\tau = 100$ ps, and $\gamma = 18°$.

The schlieren photograph was taken 180 ns after the beginning of the heating pulse. On the left side of the photograph, one can distinctly see a transparent homogeneous channel with a sharp boundary. Approaching the indicated region, the increase in the specific input energy is accompanied by a gradual increase in the plasma channel diameter. However, in the indicated region, where the pulse intensity is elevated, this tendency is far more pronounced: the diameter of the channel increases abruptly and the channel itself becomes opaque to probing radiation, thereby indicating the change in the structure. We can thus conclude that the channel structure may actually change when the laser intensity becomes significantly higher than the threshold intensity.

In Fig. 3, we can also see a perturbation that emerges from the region of elevated pulse intensity and propagates to the left along the channel. Judging from the image of the projection of the perturbation onto the plane of observation, the perturbation is spherical in shape and develops near the boundary of the indicated region. The distance the perturbation passed over a time of about 160 ns is estimated to be about 0.3 cm, which indicates that the perturbation propagated at a mean velocity of $v \sim 2 \times 10^6$ cm/s. These results make it possible to identify the perturbation as a wave driven in the zone where the intensity of the heating radiation changes in a jumplike manner. In what follows, we will assume that the perturbation waves may also be driven in local zones of elevated radiation intensity.

In a relatively late stage of the channel evolution (about 160 ns after the beginning of breakdown and later), it is impossible to recognize the original seed small-scale perturbations, which, presumably, had enough time to damp. On the other hand, they may influence the channel structure, in which case, however, the heating pulse should be long enough so that, over the time of its action, the perturbation wave can travel a distance comparable with the characteristic scale length of the Besselian beam. Thus, for a pulse duration of $\tau = 40$ ns and velocity $v \sim 2 \times 10^6$ cm/s, this distance is about $r \approx 1$ mm; this indicates that, for the primary perturbations to be observable in a beam of radius $a = 10$ μm, the pulse should be made shorter by at most two and a half orders of magnitude.

Plasma channels created by short laser pulses were investigated in a device [11] operating at the laboratory headed by Prof. H.M. Milchberg (University of Maryland, USA) in joint experiments with the participation of L.Ya. Margolin and the author of this paper. The channels shown in Fig. 4 were produced in nitrous

oxide, which was chosen as the working medium because of the low threshold for optical breakdown and thus provided the possibility of investigating the formation of the channels in a broad pressure range. The parameters of the Besselian beams were as follows: $\lambda = 1.06 \ \mu m$, $E = 0.6 \ J$, $\tau = 100 \ ps$, and $\gamma = 18°$. The diameter of the central part of such beams was $2a_0 = 2.6 \ \mu m$, and the beam length was $L = 1.5 \ cm$. The state of the channels illuminated with 70-ps, 0.53-μm laser pulses was monitored by a Mach–Zehnder interferometer. The magnified interferogram images were recorded by a 512-μm-long CCD camera. In Fig. 4, the numerals denote the numbers of the pixels of the CCD camera, each of the pixels being 1.6 μm in size.

The interferograms shown in Figs. 4a and 4b were taken at pressures of 0.27 and 0.67 atm, respectively. The contours of the plasma channels are seen against the background of the interference fringes of equal inclination. The amount by which the fringes are displaced reflects the value of the plasma density. The channels were created by identical Besselian beams and were recorded 250 ps after the beginning of the heating pulse. Nevertheless, the channel in Fig. 4a appears to be completely uniform, while the interferogram of the channel in Fig. 4b provides evidence for highly developed perturbations. The threshold for breakdown at a pressure of 0.67 atm (Fig. 4b) should be lower than that at a pressure of 0.27 atm (Fig. 4a). Thus,

we again arrive at the conclusion that, for short heating pulses, the channel structure should change when the beam intensity becomes higher than the threshold intensity.

Note that the pattern of the displaced fringes in Fig. 4b provides evidence for numerous discrete primary breakdown centers. Therefore, we can assume that, on the whole, the channel is formed against the background of the perturbation waves driven by the primary breakdown centers and that the onset and the configuration of these centers play a dominant role in the formation of the channel structure.

3. CONFIGURATIONS OF THE OBSERVED BREAKDOWN CENTERS

It was most expedient to display the configuration of the primary breakdown centers in the scattered laser light. This made it possible to visualize, first of all, perturbations in which the electron density is the highest and to automatically satisfy the synchronization conditions. The representative images of the distribution of the primary breakdown centers in Besselian beams with different parameters during breakdown in air and argon are shown in Fig. 5, in which the wave front propagates from left to right.

Figure 5a illustrates the breakdown in argon at a pressure of 0.2 atm in a Besselian beam with the param-
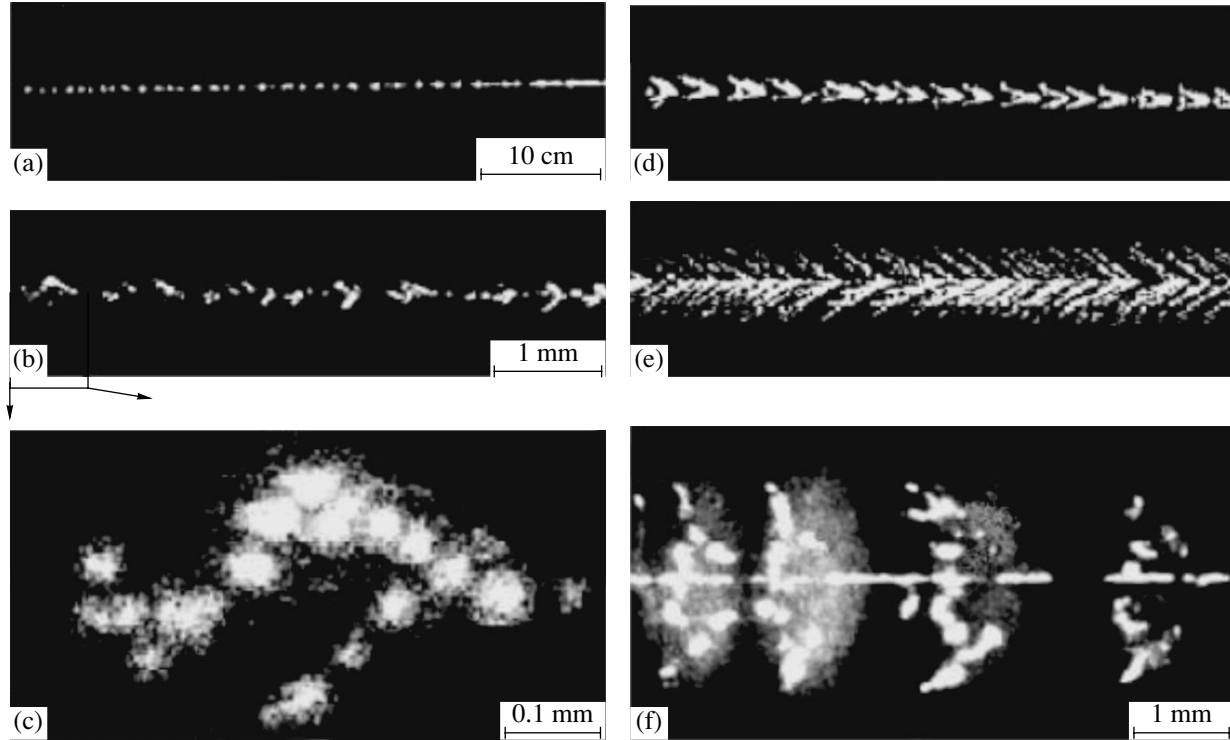
Fig. 5. Primary breakdown centers in (a) argon at a pressure of 0.2 atm ($E = 10 \ J$, $\tau = 0.8 \ ns$, $\gamma = 1°$), (b) air at a pressure of 1 atm ($E = 17 \ J$, $\tau = 0.8 \ ns$, $\gamma = 2.5°$), (d) air at a pressure of 1 atm ($E = 20 \ J$, $\tau = 20 \ ns$, $\gamma = 5°$), (e) air at a pressure of 1 atm ($E = 70 \ J$, $\tau = 40 \ ns$, $\gamma = 7.5°$), and (f) argon at a pressure of 1 atm ($E = 70 \ J$, $\tau = 40 \ ns$, $\gamma = 7.5°$). Frame (c) is a magnified fragment of image (b).

eters $E = 10$ J, $\tau = 0.8$ ns, and $\gamma = 1°$. The images cover a beam portion of length 50 cm, the total length of the beam being about $L \approx 130$ cm. Closer to the axicon (on the left side of the figure), the beam intensity is slightly above the threshold and is about one-quarter of the beam intensity averaged over the beam length. In this region, the breakdown centers occur at the beam axis and form a periodic sequence of points with a spatial separation of about $l \approx 7$ mm. Farther away from the axicon, the beam intensity increases and the individual breakdown centers start to merge, tending to form a continuous breakdown channel.

Figure 5b illustrates an optical discharge in air at atmospheric pressure in a beam with the parameters $E = 17$ J, $\tau = 0.8$ ns, and $\gamma = 2.5°$ ($L \approx 52$ cm), the beam intensity being two orders of magnitude higher than that for a discharge in argon. Judging from the image in Fig. 5b, we may speak of the structural blocks rather than of the breakdown centers. The spatial separation between the blocks along the beam axis is about $l \approx 1.1$ mm. In turn, each block consists of smaller cells with a size of 0.02–0.05 mm. Figure 5c is a magnified fragment of the image shown in Fig. 5b. We can distinctly see the individual cells and the lines formed by them. The angle β at which the lines are inclined to the beam axis is significantly larger than γ. For this reason, the appearance of the lines of cells cannot be explained as being due to the propagation of the breakdown front upward laser radiation, as is usually done when investigating optical discharges at the focus of a spherical lens.

The images shown in Figs. 5a–5c were obtained with relatively short heating pulses in Besselian beams with small convergence angles γ. Next, Figs. 5d–5f illustrate the action of beams with modified parameters and longer pulses. Thus, Fig. 5d shows the image of the structure of a plasma channel created in air at atmospheric pressure by a Besselian beam with the parameters $E = 20$ J, $\tau = 20$ ns, and $\gamma = 5°$ ($L \approx 26$ cm). As compared to the experiment illustrated in Fig. 5b, the beam intensity is lower by a factor of about three, but the specific energy of radiation is one order of magnitude higher. The structure of the breakdown discharge is again periodic in the axial direction, but the spatial period is shorter ($l \approx 0.28$ mm) and the structural blocks, which again occurred in the axial region, are now continuous plasma formations.

For a higher specific energy of radiation and longer laser pulses, the configuration of a breakdown discharge in air at atmospheric pressure becomes radically different. Figure 5e shows the image of an optical discharge driven in a Besselian beam with the parameters $E = 70$ J, $\tau = 40$ ns, and $\gamma = 7.5°$ ($L \approx 17$ cm). As compared to Fig. 5d, the beam intensity in this discharge is higher by a factor of 6 and the specific energy is higher by a factor of 12. The channel structure is characterized by the appearance of extensions, which are inclined to the symmetry axis at an angle of $\beta \gg \gamma$; as a result, the

channel structure is herringbone-shaped. The spatial period of the extensions in the axial direction is about $l \approx 0.12$ mm, and the extensions themselves are separated from the discrete breakdown centers.

The structure of the plasma channels is most peculiar in optical discharges in argon. Figure 5f illustrates an optical discharge driven in argon by a Besselian beam with the same parameters as in Fig. 5e ($E = 70$ J, $\tau = 40$ ns, $\gamma = 7.5°$). The most pronounced structural inhomogeneities of the channel are funnel-shaped or beaded, the spatial separation between them being larger than 1 mm. It is well known [1] that, in argon, the threshold intensity for breakdown ($I_{th} = 1.5 \times 10^{10}$ W/cm^2) is lower than that in air ($I_{th} = 8 \times 10^{10}$ W/cm^2) by a factor of 5.3. That is why, for the same beam parameters, the excess of the beam intensity above the threshold in argon plays a greater role and the structure of the plasma channels in argon (Fig. 5f) differs radically from that in air (Fig. 5e). However, from Fig. 5f, we can see that, in argon, the breakdown centers also form a periodic structure whose period in the axial direction ($l \approx 0.12$ mm) coincides with the period of the channel structure in air (Fig. 5e).

According to the above experimental data, the structure of the plasma channels was always observed to be periodic in the longitudinal direction. The spatial scale of the structure is independent of the sort of gas, the gas pressure, and the energy and duration of the heating pulse and is determined exclusively by the convergence angle γ of the conical wave front of a Besselian beam. Other types of structures, with larger and smaller characteristic scale lengths, were also observed. It was established that the properties of a larger scale structure depend not only on the parameters of the Besselian beam but also on the sort of gas. For a smaller scale structure, this dependence is far less obvious. However, a detailed analysis of the experimental data shows that, to a greater or lesser extent, the smaller scale structure always manifests itself in plasma channels produced by Besselian beams. For this reason, we briefly address the structure of the Besselian beam itself.

4. STRUCTURE OF THE BESSELIAN BEAM

The formation of a periodic sequence of breakdown centers along the symmetry axis was observed when the first attempt was made to create a plasma channel in the field of a Besselian beam [3]. Originally, the point breakdown centers were explained as a result of misalignment. Only after the analysis of the streak images of breakdown propagation [12], was the appearance of the breakdown centers attributed to the laser field distribution formed behind the axicon in a nonlinear medium.

The properties of the medium are determined by its dielectric function

$$\varepsilon = \varepsilon_0 + i\varepsilon'' + \varepsilon_{NL}(|E|^2), \tag{1}$$
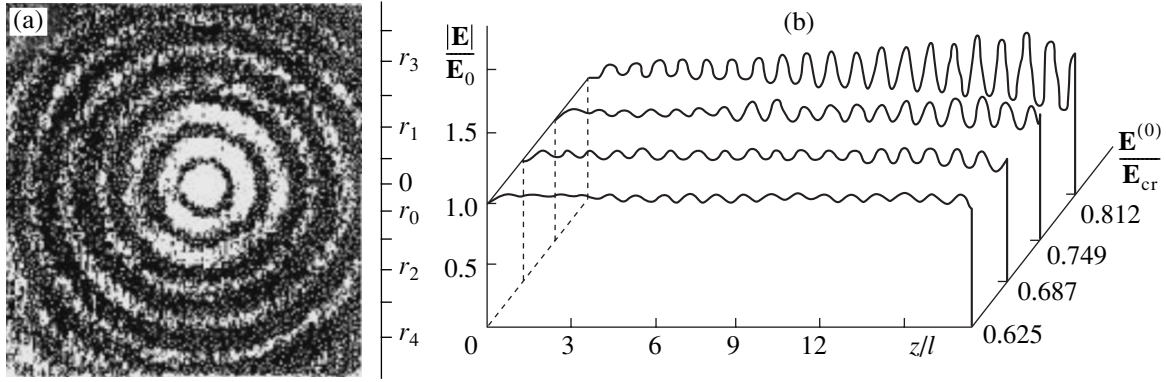
Fig. 6. Field structure of a Besselian beam with $\gamma = 5°$: (a) the measured radial field distribution and (b) the longitudinal field profiles calculated for a cubic nonlinearity of the gas.

where the imaginary part ε'' describes the wave damping and the nonlinear functional ε_{NL} is determined by the equation of state of the matter and describes the characteristic features of the interaction.

By analogy with the focusing of a Gaussian beam [13], we describe the field distribution behind the axicon in a medium with the nonlinear dielectric function (1) by the following equation for the complex field amplitude $\mathbf{E}(r, t) = \mathrm{Re}\{\mathbf{e}E(r, z)\exp[-i(\omega t - kz)]\}$ [4]:

$$2ik\frac{\partial E}{\partial z} + \frac{1}{r}\left(r\frac{\partial E}{\partial r}\right) + \left(\frac{\omega}{c}\right)^2[i\varepsilon'' + \varepsilon_{NL}(|E|^2)]E = 0, \quad (2)$$

where $k^2 = (\omega/c)^2\varepsilon_0$. We supplement this equation with the following boundary condition for the focusing of laser radiation by an axicon with aperture R:

$$E(r, z = 0) = E_{\mathrm{in}}(r)\exp(-ikr\sin\gamma). \quad (3)$$

Here, $E_{\mathrm{in}}(r > R) = 0$ and $E_{\mathrm{in}}(r \le R) = I^{1/2}(r)$, where $I(r)$ is the radial profile of the intensity of the incident beam.

In the axial ($r < z\sin\gamma$, $kr^2 < z$) zone of the focal region of the axicon ($\lambda/\sin^2\gamma \ll z < L$), the linear ($\varepsilon'' = \varepsilon_{NL} = 0$) solution $E^{(0)}$ to Eq. (2) with the boundary condition (3) has the form

$$E^{(0)}(r, z) = E_a f(k, r, a, z)$$
$$+ E_0(z)\exp(-i(kz/2)\sin^2\gamma) \quad (4)$$
$$\times [J_0(kr\sin\gamma) - irJ_1(kr\sin\gamma)/2z\sin\gamma].$$

Here, the first term $E_a f$, which accounts for the diffraction at the edge of the axicon, is as small as $(\lambda/z)^{1/2}$ compared to the second term, which describes, to within a small term on the order of $r/(2z\sin\gamma)$, the beam field behind the axicon. The transverse (with respect to the beam axis) component of the wave vector of the beam field is equal to $k_\perp = k\sin\gamma$ (and, accordingly, $\delta k_\parallel = 1/2k\sin^2\gamma$), and the amplitude $E_0(z)$ of the field varies

gradually in the axial direction,

$$E_0(z) = 2\pi(z/\lambda)^{1/2}\sin\gamma E_{\mathrm{in}}(z\sin\gamma)\exp(-i\pi/4). \quad (5)$$

Consequently, behind the axicon, the field distribution can be described with good accuracy by the Bessel function $J_0(kr\sin\gamma)$:

$$|E^{(0)}(r, z)| = |E_0(z)|J_0(kr\sin\gamma), \quad (6)$$

in which case the beam intensity can be represented as $I \sim E_0^2(z)J_0^2(kr\sin\gamma)$. The photograph of the beam field distribution in the experiment with a Besselian beam ($\gamma = 5°$) is shown in Fig. 6a, where the calculated values of the zeros of the Bessel function r_m (where m is the number of the ring) are indicated at the scale on the right.

The properties of a Besselian beam in a nonlinear interaction with the medium are determined by the nonlinear component $\varepsilon_{NL}(|E|^2)$ of the dielectric function of the medium. The particular form of the expression for ε_{NL} depends on the degree of ionization, the electron temperature, the relationship between the electron mean free path and the scale on which the beam field varies, etc. In the strong field of a Besselian beam, the dielectric function of the gas with excited atoms can be considered to be a locally nonlinear power function because of the multiphoton transitions from the metastable state in gas atoms. According to [14], for the nonlinear effects to come into play when the beam intensity at the axis is about 10^{11} W/cm^2, it is sufficient that the fraction of the atoms in the excited metastable state be 10^{-3} of the total number of gas atoms.

During the avalanche ionization of the gas, the nonlinear effects depend on the properties of the produced plasma. In a weakly ionized plasma, the electron temperature changes as a result of the electron heating due to inverse-bremsstrahlung absorption and the energy loss associated mainly with electron–neutral collisions. If, in this case, the electron mean free path λ_e is small

compared to the scale length L_E on which the electromagnetic field varies, $\lambda_e/L_E < \delta_e^{1/2}$ (where δ_e is the fraction of the energy of an electron that is transferred to a neutral atom in a collision event), then the nonlinear part of the dielectric function ε depends on the extent to which the electron density n_e deviates from its initial quasisteady value n_0, $\delta n = n_e - n_0$, so that the nonlinear part $\varepsilon_{NL} = -\delta n/n_c$ of the dielectric function can be written as

$$\varepsilon_{NL} = \frac{n_0}{n_c}|\mathscr{E}|^2. \qquad (7)$$

Here, $\mathscr{E} = E/E_T$, where $E_T = (12\pi\delta_e n_c T)^{1/2}$ is the plasma field characteristic of thermal nonlinearity, $n_c = m_e\omega^2/4\pi e^2$, and n_0 and T are the quasisteady electron density and temperature. For $\delta_e^{1/2} < \lambda_e/L_E < 1$, the nonlinear effects become nonlocal, in which case the dependence of the nonlinear functional ε_{NL} on $\mathscr{E}$ can be determined from the electron heat-conduction equation. Expression (7) is also valid for a relatively hot plasma such that $\lambda_e > L_E$ ($|\delta n/n_0| < 1$), in which case, however, the field amplitude $\mathscr{E}$ should be normalized to the plasma field $E_s = (16\pi n_c T)^{1/2}$ characteristic of the instability related to ponderomotive effects.

For different power-law local nonlinearities (as well as for a nonlocal response function of the medium), an analysis of the solution to Eq. (2) [4] shows that, in the longitudinal profile $E_0(z)$ of the field amplitude, there is a longitudinal structure with the characteristic scale length

$$l = 2\pi/\delta k_\parallel = 2\lambda/\sin^2\gamma. \qquad (8)$$

This structure forms when the radiation power in the central region and, accordingly, in each ring region of the radial distribution (6) corresponds to the value of $|\mathscr{E}|$ that is close to the critical value $\mathscr{E}_{cr}$ for self-focusing. Thus, for the dielectric function with the nonlinear part (7), this value lies in the parameter range

$$0.2 \lesssim \frac{n_0}{n_c - n_0}\frac{1}{\sin^2\gamma}\frac{|E^{(0)}|^2}{E_{cr}^2} \leq 1, \qquad (9)$$

where $E^{(0)}$ is the value of the linear solution to Eq. (2) at the axis and $E_{cr} = E_T$.

For the experimental conditions of Fig. 5d, the numerical solution to Eq. (2) with the boundary condition (3) and the dielectric function with the nonlinear part (7) is illustrated in Fig. 6b, which shows the longitudinal profiles of the dimensionless field $|E|/E_0$ calculated as a function of the dimensionless length z/l at the symmetry axis for four values of the parameter $|E^{(0)}|/E_{cr}$. We can see that, in the parameter range (9), the electric field in the plasma channel produced by a Besselian beam actually possesses a longitudinal periodic structure whose period $l = 0.28$ mm coincides with the period l obtained from the experimental data illustrated in Fig. 5d.

For a particular nonlinear dielectric function, the field of a Besselian beam may be either below or far above the critical field. The weaker the beam field, the smaller the modulation depth of the structure is. In contrast, as the beam field increases above the critical level, a large-scale structure with a period of $l_1 \sim 10l$ [4] forms simultaneously with the main structure with period (8). The configuration of a breakdown discharge in Fig. 5f corresponds precisely to this doubly periodic structure with the periods $l \approx 0.13$ mm and $l_1 \approx 1.4$ mm (on average), which are close to the calculated periods $l \approx 0.124$ mm and $l_1 = 1.24$ mm. According to Fig. 5f and theoretical predictions, the large-scale modulation manifests itself not only in the axial focal region of the beam but also in the ring regions of the radial distribution of the beam field intensity. For this reason, the diameter of the doubly periodic structure is larger than that in the absence of the large-scale modulation; this conclusion is confirmed by a comparison of the breakdown structures illustrated in Figs. 5e and 5f.

5. MECHANISM FOR THE FORMATION OF THE STRUCTURE OF AN OPTICAL DISCHARGE

We begin our analysis of the structure of an optical discharge by considering a plasma channel produced by a 0.6-J laser pulse with $\tau = 100$ ps. The structure of this plasma channel is shown in Fig. 4b. Because of the small dimensions of the primary perturbations and very short times during which they developed, we failed to record their positions and measure their parameters. Hence, let us turn to the interferogram shown in Fig. 4b and try to reconstruct the discharge structure by calculations.

In the interferogram, the amount by which the fringes of equal inclination are displaced reflects the structure of the perturbations. The interferogram obtained with the CCD camera contains 56 fringes along the z-axis, so that, for a given radius r, we can construct the displacement of the interference fringes $\delta(N)$ as a function of $N = z/h$ (the z-coordinate normalized to the fringe spacing h). This dependence reflects the distribution of the density perturbations along the channel. Figure 7 displays the dependence $\delta(N)$ calculated for different values of the ratio r/R, where $2R = 41.0$ μm is the mean diameter of the plasma channel shown in Fig. 4b. In Fig. 7, the upper plot characterizes the displacement of the fringes far from the channel (at $r/R = 5$) and demonstrates that the fringes are in fact spaced periodically. The middle plots (from top to bottom) show the displacement of the fringes at the channel axis ($r/R = 0$) and at the relative radii $r/R = 0.25$, 0.50, and 0.75. The lower plot (at $r/R = 1$) characterizes

Displacement of the fringes, pixel number
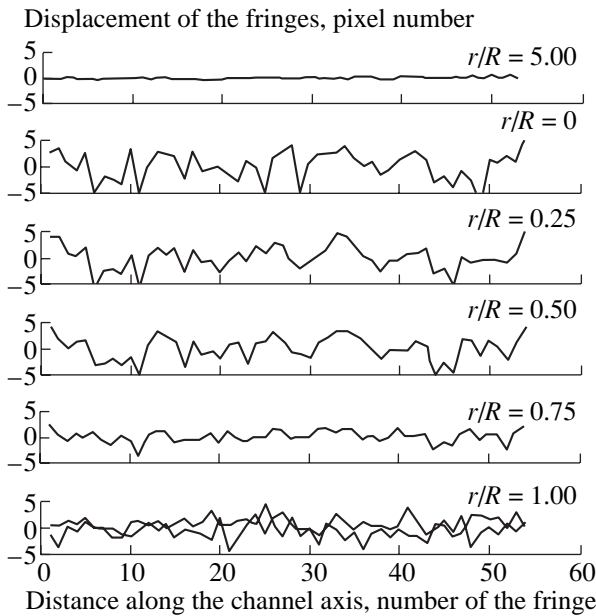
Fig. 7. Longitudinal profiles of the amplitude of pulsations of the plasma density in the channel shown in Fig. 4b at different dimensionless radii r/R.

the radial displacements of the upper and lower boundaries of the channel.

This distribution of the density perturbations confirms the discrete nature of gas breakdown. Every breakdown center gives rise to a region in which the plasma temperature and density are both elevated and which starts expanding as a spherical ionization wave. In turn, every spherical wave is an expanding spherical layer with pulsating hydrodynamic parameters [15]. The superposition of these waves gives rise to the observed pulsations of the plasma density. It seems reasonable to suppose that the breakdown centers form at the points at which the beam intensity is maximum.

According to Section 4, the symmetry properties of the problem enable us to describe the structure of a Besselian beam by two coordinates, specifically, the longitudinal and radial coordinates, z and r. The longitudinal structure of the beam is characterized by a sequence of points at which the beam intensity is maximum and which are separated by the distance $l = 2\lambda/\sin^2\gamma$ (or $l \approx 21$ μm for the case of Fig. 4b). The radial structure of the beam is characterized by a sequence of rings whose dimensionless (normalized to the channel radius $R = 20.5$ μm) radii ($a = 0.063, 0.145, 0.227, ...$) correspond to the zeros of the Bessel function. The question then arises: what are the rings at which the breakdown occurs? This question can be answered by reference to numerical modeling [16].

We assume that the breakdown centers appear either in the central focal region of the beam or at a structural ring with the corresponding diameter $2a_m$. We also assume that, in the longitudinal direction, the break-

down centers are dispersed among the beam intensity maxima (there are 24 points over a distance equal to 512 μm). For convenience, when comparing the calculated results with the measured data, we normalize the z coordinate and the amplitude of pulsations of the plasma density to the fringe spacing h in the z direction and investigate the channel structure over the same interval $\{z_1, z_2\} = \{0, 55\}$ that was observed experimentally. We also take into account the fact that the displacement of the interference fringes corresponds to the total phase increment along a chord of the cylindrical channel. We specify the chord by the coordinates $z = (z_2 - z_1)/2$ and $r_0 = R/2$, in which case, along half of the chord, the y coordinate changes from 0 to $r_0\tan\varphi$, where φ is the azimuthal angle. The summation along the entire chord should include all perturbations that are driven at the points pz within the interval $\{z_1, z_2\}$ on the axis. Over a time interval t_0 less than the duration τ of the heating pulse, the points pz may obey a random temporal distribution pt. We normalize the quantities pt, t_0, and τ to the time of observation of the channel, 250 ps, so the dimensionless duration of the pulse is equal to $\tau = 0.4$.

Let us write out the complete set of initial parameter values for our problem:

$$a = \{0.063, 0.145, 0.227\}, \quad k = 25, \quad \tau = 0.4,$$
$$t_0 = 0.4, \quad \{z_1, z_2\} = \{-1, 56\},$$
$$\{y_1, y_2\} = \{0, r_0\tan(\pi/3)\}, \quad f(r) = 1, \tag{10}$$
$$m = 11, \quad Q = 1, \quad q = 0.$$

Along with the values specified above, this set includes the following parameters: the number k of perturbations and the length of the interval of the channel under consideration, $\{z_1, z_2\}$ (with allowance for the processes at the ends); the profiles $f(r)$ ($r \le a$) of the parameters of the primary perturbations; the number m of terms in the summation along the chord; the displacement Q of the entire uniform sequence of the points pz of primary perturbations ($Q < h$); and the range q of random deviations of the coordinates pz of the points in a partially destroyed periodic sequence of primary perturbations. Since the time required for the wave front of a Besselian beam to cross the interval $\{z_1, z_2\}$ is equal to 1.6 ps ($t = 0.01$), we neglect the delay between the heating pulse and the breakdown discharge driven by it and assume that the energy release in the breakdown is instantaneous.

Let us consider an initial ($t = 0$) breakdown center in the form of a ball of radius a. Let the ball be centered at the origin of the coordinates. Inside the ball ($r < a$), the perturbed density is described by an arbitrary function $f(r)$. Outside the ball ($r > a$), the unperturbed density is $\rho_0 = 1$ and the excess density is $\rho = 0$. According to
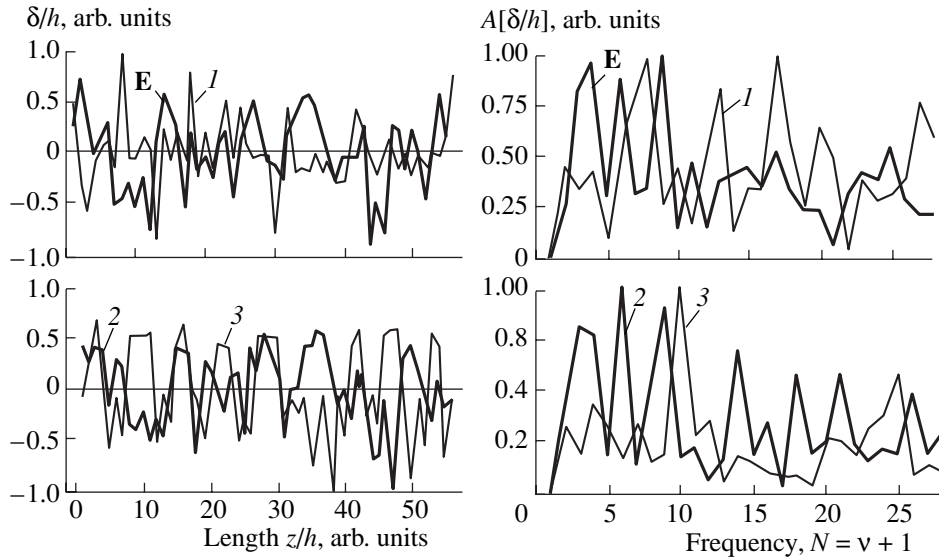
Fig. 8. Longitudinal (at $r_0 = 0.5$) structure of pulsations of the plasma density in a plasma channel according to the experimental data (curves **E**) and the calculational results for $a =$ (*1*) 0.063, (*2*) 0.145, and (*3*) 0.227.

[15], for a perturbation propagating at the speed of sound c, we have

$$|r - ct| > a \quad \text{for} \quad \rho = 0,$$

$$|r - ct| \leq a \quad \text{for} \quad \rho \sim f(|r - ct|)\frac{(r - ct)}{r}. \quad (11)$$

At $r \gg a$, a perturbation of an arbitrary initial shape becomes a spherical layer of thickness $2a$, in which the density pulsations are described by the function $f(|r - ct|)$. Consequently, formula (11) determines the configuration and the internal structure of a propagating perturbation wave. The problem of the superposition of perturbation waves with the initial conditions (10) was solved by means of the Mathematica-4 software package.

Figure 8 illustrates the results calculated for the initial perturbations with the radii $a = 0.063$, 0.145, and 0.227, which correspond to the first three roots of the Bessel function (i.e., to the axial region and the first and second rings); the related profiles are denoted by *1*, *2*, and *3*, respectively. The figure also shows the experimentally obtained dependences of **E** corresponding to the perturbations illustrated in Fig. 7 for the relative radius $r/R = 0.5$, which corresponds to the r_0 value adopted for simulations. The experimental profiles of **E** and the profiles computed for $a = 0.145$ are displayed by the heavy curves. Shown on the left and on the right of Fig. 8 are the longitudinal density profiles and their spatial spectra, respectively.

A comparison of numerical results with the experimental data shows that the profiles calculated for $a = 0.063$ and 0.227 contradict the measured dependence. For $a = 0.063$, the scale of the structure is too small, and, for $a = 0.227$, the scale is too large. In the latter case, the resonance phenomena begin to manifest themselves. Agreement between the results obtained for the first ring ($a = 0.145$) and the experimental data is much better. For this reason, the characteristics of the structure of the plasma channels were refined and the initial parameters were adjusted precisely for $a = 0.145$. The adjustable parameters were as follows: the number k of the initial perturbations, the distribution pz (including the displacement Q of the entire sequence of the initial perturbations and the range q of random deviations), the time interval t_0 during which the breakdown centers originate, and the shape of the function $f(r)$.

It was found that the structure of perturbations in a plasma channel was described most exactly for the following values of the adjustable parameters: $k = 25$, $t_0 = 0.2$, $Q = 0.17$, $q = 0$, and $f(r) = 1$. It is these parameter values for which profiles *2* in Fig. 8 were calculated. Hence, during the time interval $t_0 = 0.2$ (about 50 ps), the perturbations originate at each longitudinal maximum in the intensity of a Besselian beam and the spacing between the perturbations coincides with $l = 21$ µm to within several percent. For a heating pulse with the duration $\tau = 100$ ps and energy $E = 0.6$ J, the zone of perturbations extends to the second ring (of radius 2.9 µm) of the distribution of the Besselian beam intensity. At rings with larger radii, the beam intensity is insufficient to produce the breakdown centers. Note that the value $t_0 = 0.2$ indicates a breakdown at a level of 0.8 of the maximum beam intensity.

Having checked the assumption of the localization of the breakdown centers at the points of the maximum intensities of a Besselian beam, we turn to the analysis of the structure of an optical discharge, which can be affected by the breakdown propagation. A rich store of data on particular breakdown processes was acquired in
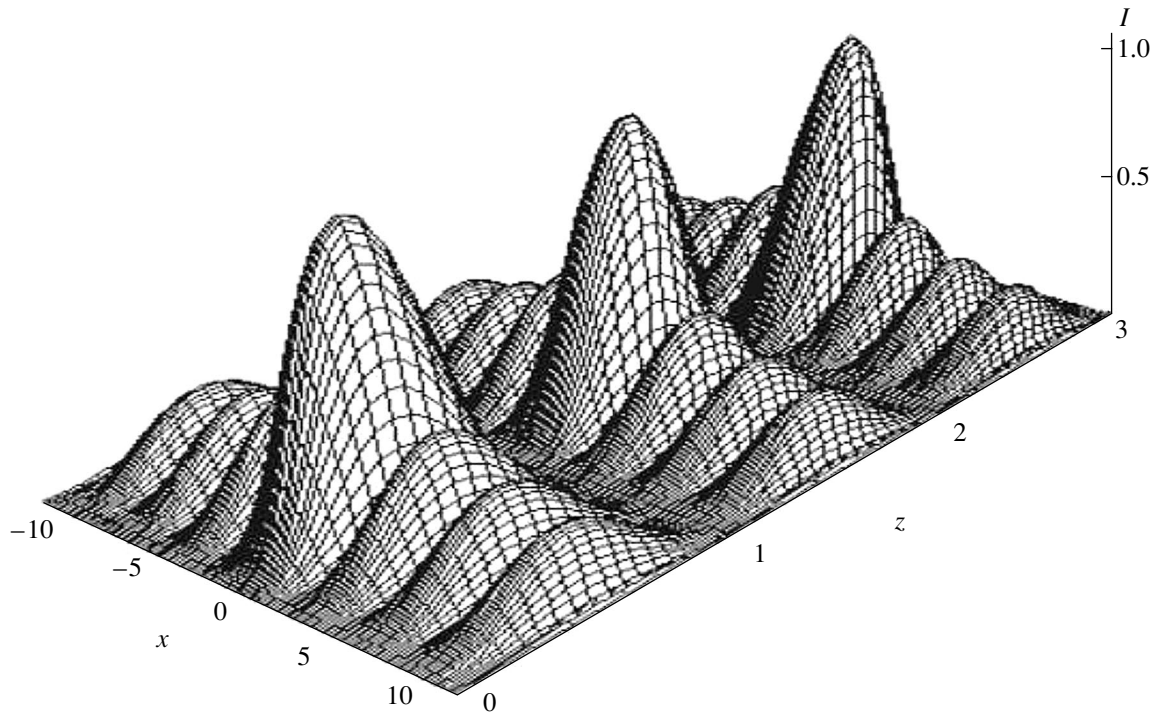
Fig. 9. Schematic structure of a Besselian beam.

experiments aimed at investigating laser sparks in the focal region of a spherical lens [1, 2]. According to these data, the threshold intensity for breakdown is proportional to the ionization potential and decreases with increasing pressure, diameter of the focal region, and laser pulse duration. The breakdown front can propagate at a velocity of 10^7–10^8 cm/s upward laser radiation as an ionization wave, a breakdown wave, or a light detonation wave. The optical discharge develops nonuniformly, because the velocity with which it expands in the radial direction is close to the speed of sound in the plasma produced and is thus appreciably lower than the propagation velocity upward laser radiation.

Analogous phenomena can also take place in an optical discharge that is driven by a laser pulse focused by an axicon. In this case, the formation of the structure of the discharge is, as before, affected by the energy and duration of the pulse. However, it is also necessary to take into account the field structure of a Besselian beam. To make the interpretation of the experimental data more illustrative, we show in Fig. 9 a fragment of the beam structure. In the figure, the beam radius is characterized by the argument $x = kr\sin\gamma$ of the Bessel function and the beam length z is specified as the number of the peak in the longitudinal profile of the beam intensity. In order to make the effect of interest to us more pronounced, the figure shows the varying component of the beam intensity I rather than the total intensity. The value $x = 0$ corresponds to the symmetry axis of the beam. The spacings between the neighboring

peaks in the radial and longitudinal directions can be estimated as $\delta a \approx \lambda/2\sin\gamma$ and $l = 2\lambda/\sin^2\gamma$, respectively.

When the beam intensity is only slightly above the threshold, the breakdown occurs exclusively in the focal region of the beam ($x = 0$). Under condition (9) (or a similar condition), the intensity profile of the beam becomes modulated with period l along the z-axis and the beam evolves to the structure shown in Fig. 9. In contrast, a beam with an intensity below the threshold either remains unmodulated or becomes modulated very slightly (Fig. 6b). However, even under condition (9), the sequence of breakdown centers occurs in the focal region of the smallest diameter ($x_0 = 2.4$), and the perturbations are damped over short distances. Accordingly, after the neighboring breakdown centers merge together, the plasma channel rapidly becomes uniform. These two scenarios of the development of the process are illustrated by Figs. 2a and 4a and by the left part of the channel shown in Fig. 3.

As the laser energy increases, the beam becomes sufficiently intense for the breakdown centers to originate at the next inner cylindrical surfaces at which the beam intensity is maximum, so that the zone of the primary breakdown successively extends to the rings of larger radii ($x_m = 5.52, 8.65, \ldots$). As the diameter of the primary perturbation zone increases, the distance over which the primary perturbation can affect the channel structure becomes longer (in proportion to a_m/a_0). However, for a short laser pulse ($\tau = 0.1$ ns), the plasma produced by the breakdown does not have enough time

to expand to the larger rings of the beam structure. As the pulse comes to an end, the interaction of the heating radiation with the perturbations that it itself generates does not influence the discharge structure, so that the plasma channel forms as a result of the spontaneous propagation of perturbations. The channel structure shown in Fig. 4b was obtained by simulating precisely this mechanism.

The structure of the plasma channel is formed by this mechanism when the heating pulse is sufficiently short ($\tau \leq 0.1$ ns). Now, we consider the channel structures in the case of nanosecond laser pulses (Fig. 5). In Fig. 5a, which illustrates the experiment on laser pulses with $\tau = 0.8$ ns in argon at a pressure of 0.2 atm, one can distinctly see that pronounced breakdown centers occur precisely at the points of the central maxima of the intensity of a Besselian beam. The spatial structure of the forming plasma channel was resolved by recording optical inhomogeneities in the scattered laser light and by using a beam with a small convergence angle, $\gamma = 1°$ ($l \approx 7$ mm). Although, in this experiment, the pulse duration was almost one order of magnitude longer, the distance to the next row of the maximum intensities in the first ring of a Besselian beam was also found to increase by approximately the same amount ($\delta a \approx 30$ μm).

In the channel region that is closer to the axicon (on the left side of Fig. 5a), the beam intensity is about threshold intensity and its value actually corresponds to the pulse energy $E \approx 2.5$ J. Let us use this value of the beam intensity when comparing the breakdown conditions in different experiments. Note that the threshold intensity for breakdown in argon at a pressure of 0.2 atm is lower than that in air at atmospheric pressure by a factor of 2.6 [2]. For this reason, we adopt the following threshold parameter values for the beam in air: $E = 6.5$ J, $\gamma = 1°$, and $\tau = 0.8$ ns, assuming that, for these values, the breakdown centers in air at atmospheric pressure originate in the central focal region of the beam at the points at which the beam intensity is maximum and which are separated by the distance l given in formula (8).

In order to estimate the conditions for the formation of a structured plasma channel, we determine the ratios of the power and energy densities of radiation in the beams that produce the plasma channels shown in Fig. 5 to their threshold values. To do this, we use the above relationships $w \sim E\gamma^3/\tau$ and $\varepsilon \sim E\gamma^3$. We also present the radii r_i of the breakdown zone, which can be obtained from the data of Fig. 5 (the subscripts a–f correspond to the frames of this figure). Setting $w_a = \varepsilon_a = 1$ and taking into account the fact that the threshold intensity for breakdown in argon at a pressure of 0.2 atm is lower than that at atmospheric pressure by a factor of 5.3, we obtain ($w_b = w_c$, $\varepsilon_b = \varepsilon_c$, $r_b = r_c$)

$$w_b = 40.6,\ \varepsilon_b = 40.6,\ r_b = 0.1\ \text{mm};$$

$$w_d = 15.4,\ \varepsilon_d = 384,\ r_d = 0.08\ \text{mm};$$

$$w_e = 91.2,\ \varepsilon_e = 4.56 \times 10^3,\ r_e = 0.31\ \text{mm};$$

$$w_f = 1250,\ \varepsilon_f = 6.3 \times 10^4,\ r_f = 1.1\ \text{mm}.$$

From the experimental data on w_i, the Mathematica-4 software package makes it possible to determine the number m of the ring at which the relative laser power is sufficient for breakdown and the argument $x = kr\sin\gamma$ of the Bessel function:

$$x_b = 25.7,\ m_b = 8;\ x_d = 10.0,\ m_d = 3;$$

$$x_e = 59.0,\ m_e = 19;\ x_f = 803,\ m_f = 251.$$

However, the same parameters can also be determined from the experimental data on the radii r_i:

$$x_b = 25.8,\ m_b = 8;\ x_d = 51.7,\ m_d = 16;$$

$$x_e = 238,\ m_e = 74;\ x_f = 850,\ m_f = 266.$$

For the same pulse duration, the power density in the channels in Figs. 5b and 5c is higher than that in the channel in Fig. 5a by a factor of 41. As a result, the channels in Figs. 5b and 5c are more complicated in structure. Instead of individual breakdown centers, there are numerous centers, which combine into groups. The distances between the centers of the groups are equal to the period of the longitudinal beam structure, $l = 1.1$ mm (for the convergence angle $\gamma = 2.5°$). Note that both of the methods yield the same number of the ring of the radial structure of a Besselian beam: $m_b = 8$.

From Fig. 5c, we can see that the structural groups of the breakdown centers lie within a cylindrical region with a radius of about 0.1 mm and a length of about 0.5 mm. In the middle of the cylindrical region, the breakdown centers concentrate at the periphery (near the cylindrical surface), while, near the edges, they concentrate in the axial region. This distribution of the breakdown centers is similar to the distribution of the beam field at a longitudinal maximum in the beam intensity. We can thus conclude that the breakdown centers most likely originate at the points where the longitudinal maxima in the beam intensity occur at the outermost ring of the radial beam structure at which the beam intensity is still above the threshold. It should be noted that, in the experiment at hand, the laser pulse had a peculiar shape: for $\tau = 0.8$, the rise time of the pulse front was 100 ps.

The period $l = 0.28$ mm of the longitudinal structure of the plasma channel shown in Fig. 5d coincides exactly with the period computed for a beam with the convergence angle $\gamma = 5°$. However, the above two methods give different numbers of the rings of the radial structure of a Besselian beam: $m_d = 3$ and 16. Clearly, this discrepancy is associated with the pulse duration, which is equal to $\tau = 20$ ns and exceeds the duration of the beam in the previous experiment by a factor of more than 20. Accordingly, for a low specific radiation power, $w_d = 15.4$, the pulse energy is higher by a factor of approximately 10; i.e., $\varepsilon_d = 384$. Presum-

ably, for such a power, the primary breakdown centers actually originate at the first three inner rings of the radial beam structure ($m_d = 3$). However, a heating pulse with a length of 6 m maintains plasma production by breakdown even after the primary breakdown centers have already originated.

Under these conditions, the breakdown front in the focal region of a spherical lens moves upward laser radiation at the velocity $v \sim 10^7$ cm/s. The velocity of the simultaneous thermal expansion of the plasma in other directions is far lower, $u \sim 10^6$–5×10^6 cm/s. The plasma is produced by the ionization wave. In the case of beam focusing by an axicon, the front of the primary breakdown can also propagate upward laser radiation. However, unlike the case of spherical focusing, the intensity of a Besselian beam can also be maximum at the points on the outside of the breakdown zone (Fig. 9). At each such point, the beam field has the potential to maintain plasma production by breakdown. When passing through the point of maximum beam intensity, the ionization wave (which reduces the threshold for breakdown) gives rise to a new breakdown center. We thus arrive at a certain combination of the radiative (ionizational) mechanism and the breakdown-wave mechanism.

Let v be the propagation velocity of the breakdown front upward laser radiation, u be the radial velocity of the ionization wave, δr_m be the radial distance between the neighboring cylindrical surfaces of the radial structure of a Besselian beam, and $\delta r_\gamma = \delta r_m / \sin\gamma$ be the distance between the same surfaces but along the laser "ray" (i.e., upward laser radiation, along a line directed at the angle γ). Since the angle γ is small and $\delta r_m \ll \delta r_\gamma$, the front of the spherical ionization wave passes through the neighboring ring earlier than the breakdown front propagating upward laser radiation. Hence, the angle at which the breakdown wave propagates deviates from γ. In addition, the beam intensity decreases along the laser ray because of the finite length of the axial structure maximum. As a result, the breakdown wave propagates at an angle $\beta \gg \gamma$ from point to point in the structure of a Besselian beam.

The longitudinal and radial components of the total velocity can be represented as $v_z \approx v\cos\gamma$ and $v_r \approx v\sin\gamma + u$. Then, the angle β is determined by the relationship

$$\tan\beta \approx \frac{v\sin\gamma + u}{v\cos\gamma}. \qquad (12)$$

For example, for $v = 10^7$ cm/s and $u = 2 \times 10^6$ cm/s, we have $\beta = 16°$, which agrees with the inclination angle $\beta = 13°$–$17°$ measured from the image of the channel in Fig. 5d.

For a long heating pulse, the ionization wave, which lowers the intensity threshold for breakdown, passes through the region between the primary breakdown centers, in which the beam field can be below the

threshold level. However, if the breakdown centers arise before the intensity of the heating pulse becomes maximum and if the maximum intensity of the beam is sufficiently high, then the breakdown centers merge into continuous plasma formations. In Fig. 5d, these formations are seen as side extensions. In the experiment illustrated in Fig. 5d, the pulse duration is $\tau = 20$ ns, so that the beam intensity remains nearly maximum at least over a time interval of $t \sim 0.1\tau = 2$ ns. During this time, the region where the intensity threshold for breakdown is lowered extends (at a velocity of $u \approx 2 \times 10^6$ cm/s) for $\delta r \sim 40$ μm, which satisfies the main condition for the process to occur, $\delta r > \delta r_m$, because, in the case at hand, we have $\delta r_m = 6$ μm.

The channel structure in Fig. 5e quantitatively (rather than qualitatively) differs from that in Fig. 5d. Indeed, the method for determining the number of the ring of the radial structure of the Besselian beam from the measured radiation intensity gives $m_e = 19$ ($x_e = 59.0$), while the method for determining the same number from the measured radius of the breakdown zone yields $m_e \approx 74$ ($x_e = 238$). Of course, the channel structure forms by the same mechanisms as in the previous case, and the larger number of rings on which the breakdown centers originate is associated with the higher power and energy densities of radiation. Therefore, the side extensions of the channel structure are longer than those in Fig. 5d. The higher specific power of radiation and the larger convergence angle γ lead to the larger inclination angle of the extensions (the angle β). However, the large angle γ hinders the merging of the breakdown centers, which are thus observed to merge together only in the axial region of the channel structure. Using relationship (12), we can estimate the velocity ratio u/v. For the channel structure shown in Fig. 5e, the inclination angle of the extensions is $\beta \approx 36°$, which gives (u/v) ≈ 0.56.

In the context of the mechanism under discussion, we consider the configuration of an optical discharge illustrated in Fig. 5f. In the relevant experiment, the specific power $w_b = 1250$ and the specific energy $\varepsilon_b = 6.3 \times 10^4$ were both one order of magnitude higher than those in Fig. 5e, the pulse duration being the same. Accordingly, the beam intensity is far above the threshold, so that the breakdown zone includes the ring number $m_f \approx 250$ (which corresponds to $x_f = 803$). On the other hand, measurements of the radius of the breakdown zone yield $m_f \approx 266$ and $x_f = 851$. Hence, we may suppose that the channel structure is formed by basically the same mechanism. However, such a high excess of the beam intensity above the threshold has important consequences.

In Fig. 5f, the breakdown centers resemble large bright spots and occur at the peripheral rings of the radial beam structure. Presumably, such factors as high electron plasma density in the spots and their large dimensions are, to a great extent, responsible for the screening of the central regions of the plasma channel

from radiation. For this reason, it was possible to detect only fragments of the side extensions of the channel structure; moreover, these fragments were observed to terminate radially without reaching the axial region of the beam. From Fig. 5f, one can see that the beam intensity at the center of the channel is sufficient to ensure breakdown only along discrete intervals in the axial focal region of the axicon. The screening may also be responsible for wide spacing between the structural groups of the breakdown centers.

Let us estimate the velocity ratio u/v. By measuring the angle β from the inclination of the contours of the extensions, we find $\beta \approx 48°$, which corresponds to the ratio $(u/v) \approx 1$, thereby providing evidence for the detonation breakdown mechanism. Hence, we can conclude that, when the beam intensity is far above the threshold intensity, the structure of an optical discharge degenerates into a sequence of coaxial breakdowns and the forming breakdown centers evolve according to the detonation mechanism.

6. CONCLUSION

A conical lens makes it possible to focus laser light in such a way as to prevent the diffractive spreading of laser pulses. In this case, the radial profile of the laser field is described by the Bessel function and the longitudinal extension of the field is independent of the laser wavelength. Such Besselian beams can be used to create an extended uniform plasma channel. However, such a channel is subject to instabilities resulting in various structural inhomogeneities.

The presence of structural inhomogeneities is associated primarily with the field structure of the Besselian beam, which is characterized by radially (m) and axially (k) ordered sets of the points of the field intensity maximums. The radial ordering is determined by the rings whose radii correspond to the zeros of the Bessel function. The longitudinal structure (z_k) forms due to the nonlinear interaction of a Besselian beam with a gas. If this interaction is only slightly nonlinear, the beam gives rise to a uniform plasma channel. In a strongly nonlinear interaction, an optical discharge develops from breakdown centers that originate at the longitudinal maxima z_k in the beam intensity.

The channel structure depends on the duration of the heating pulse and the excess of the beam intensity above the threshold intensity. The pulse is assumed to be short if its duration is insufficient for the produced plasma to reduce the threshold intensity for breakdown at the neighboring structural elements of the beam. A short pulse gives rise to breakdown centers at every structural inhomogeneity in the axial direction, in which case the diameter of the breakdown zone (the number m of rings) depends on the pulse energy. The minimum diameter $2a_0$ is the diameter of the central region of a Besselian beam. In this case, the perturbation waves driven by the breakdown centers are damped

over short distances, so that, during a time interval of $t \sim 5 \times 10^{-11} \sin^{-2}\gamma$ s, the breakdown centers merge together, giving rise to a uniform plasma channel. When the diameter of the primary breakdown zone is large ($m > 0$), the distance over which perturbations can affect the channel structure increases in proportion to a_m/a_0, so that, as the pulse comes to an end, the plasma channel forms as a result of spontaneous propagation of the perturbations.

If the laser pulse is long, the breakdown front moves upward laser radiation, as in the case of focusing by a spherical lens. Simultaneously, the plasma is produced by a spherical ionization wave. However, unlike the case of spherical focusing, there may be other maxima of the intensity of a Besselian beam on the outside of the breakdown zone. At each of these points, the beam field has the potential to maintain plasma production by breakdown. When passing through a point of the maximum beam intensity on the outside of the breakdown zone, the ionization wave lowers the threshold for breakdown and gives rise to a new breakdown center. We can thus conclude that the breakdown front propagates in a jumplike manner, because of the peculiar combination of the radiative (ionizational) mechanism and the breakdown-wave mechanism.

The radial expansion velocity of the plasma is markedly lower than the velocity of the breakdown wave. However, the spatial scale of the radial structure of a Besselian beam is smaller than the period of the longitudinal beam structure, $(r_{m+1,k} - r_{mk}) \ll (r_{m,k+1} - r_{mk})$. As a result, the breakdown front propagates from the points r_{0k} along trajectories whose directions are determined by the ratio of the expansion velocity of the spherical ionization wave to the velocity of the breakdown wave. The length of the trajectories depends on the intensity and duration of the heating pulse.

For intensities far above the threshold level, the breakdown centers can originate at rings with large radii, in which case the breakdown front propagates as a light detonation wave, producing large plasma domains. High plasma electron density in the domains may be responsible for the screening of the central regions of the Besselian beam from radiation and for the onset of conical breakdown fronts. The radii a_m of the conical fronts depend on the beam intensity, and the distances between the fronts are determined by the inclination angle of their generatrix.

The configuration of inhomogeneities of the plasma channel follows the structure of an optical breakdown for a long time. The inhomogeneities may be smoothed out only as a result of interpenetration and intermixing. The duration t of this smoothing depends on the scale length δr of the inhomogeneities and can be easily estimated from the propagation velocity u of the perturbations in the channel: $t \sim \delta r/u$. The larger the scale of the channel structure, the longer the time interval is during which the inhomogeneities are smoothed out and damped. Thus, for the velocity $u = 2 \times 10^6$ cm/s, the

structural inhomogeneities with the characteristic dimensions $\delta r \leq 0.1$ mm are smoothed out during the time interval $t \leq 5$ ns, while, for $\delta r \sim 1$ mm, this time interval increases at least up to $t \sim 50$ ns.

REFERENCES

1. Yu. P. Raĭzer, Usp. Fiz. Nauk **132**, 549 (1980) [Sov. Phys. Usp. **23**, 789 (1980)]; *Laser-Induced Discharge Phenomena* (Nauka, Moscow, 1974; Consultants Bureau, New York, 1977).

2. G. V. Ostrovskaya and A. N. Zaĭdel', Usp. Fiz. Nauk **111**, 579 (1973) [Sov. Phys. Usp. **16**, 834 (1973)].

3. F. V. Bunkin, V. V. Korobkin, Yu. A. Kurinyĭ, *et al.*, Kvantovaya Élektron. (Moscow) **10**, 443 (1983).

4. N. E. Andreev, Yu. F. Aristov, L. Ya. Polonsky, and L. N. Pyatnitsky, Zh. Éksp. Teor. Fiz. **100**, 1756 (1991) [Sov. Phys. JETP **73**, 969 (1991)].

5. L. Ya. Polonsky and L. N. Pyatnitsky, Opt. Atmos. **1**, 86 (1988); *The Most Important Results of Research Engineering of Institute of High Temperatures, USSR Academy of Sciences* (Nauka, Moscow, 1987), p. 93.

6. S. S. Bychkov, M. Yu. Marin, and L. N. Pyatnitsky, Tr. Inst. Obshch. Fiz. Akad. Nauk **50**, 166 (1995); S. Bychkov, M. Marin, and L. Pyatnitsky, Inst. Phys. Conf. Ser. **125**, 439 (1992).

7. L. N. Pyatnitsky and L. Ya. Polonsky, in *Invited Papers of the XIX International Conference on Phenomena in Ionized Gases, ICPIG, Belgrade, 1989*, p. 342.

8. V. V. Korobkin and M. Yu. Romanovskiĭ, Tr. Inst. Obshch. Fiz. Akad. Nauk **50**, 3 (1995).

9. V. V. Korobkin, L. Ya. Polonsky, and L. N. Pyatnitsky, Tr. Inst. Obshch. Fiz. Akad. Nauk **41**, 23 (1992).

10. S. Yu. Luk'yanov and N. G. Koval'skiĭ, *Hot Plasma and Controlled Nuclear Fusion* (Mosk. Inzh.-Fiz. Inst., Moscow, 1999), p. 408.

11. R. Clark and H. M. Milchberg, Phys. Rev. E **57**, 3417 (1998); J. Fan, T. R. Clark, and H. M. Milchberg, Appl. Phys. Lett. **73**, 3064 (1998).

12. V. V. Korobkin, M. Yu. Marin, V. I. Pil'skiĭ, *et al.*, Kvantovaya Élektron. (Moscow) **12**, 959 (1985); Preprint, IVTAN (Institute of High Temperatures, USSR Academy of Sciences, Moscow, 1984).

13. V. N. Lugovoĭ and A. M. Prokhorov, Usp. Fiz. Nauk **111**, 203 (1973) [Sov. Phys. Usp. **16**, 658 (1973)].

14. N. E. Andreev, S. V. Kuznetsov, and L. N. Pyatnitsky, Fiz. Plazmy **17**, 1123 (1991) [Sov. J. Plasma Phys. **17**, 652 (1991)].

15. L. D. Landau and E. M. Lifshitz, *Fluid Mechanics* (Nauka, Moscow, 1988; Pergamon, New York, 1987).

16. L. N. Pyatnitsky, Zh. Éksp. Teor. Fiz. **113** (1), 191 (1998) [JETP **86**, 107 (1998)].

Translated by G. V. Shepekina

<center>LOW-TEMPERATURE
PLASMA</center>

Investigation of the Electron Energy Distribution Function in Hollow-Cathode Glow Discharges in Nitrogen and Oxygen

V. Yu. Bazhenov, A. V. Ryabtsev, I. A. Soloshenko, A. G. Terent'eva, V. A. Khomich, V. V. Tsiolko, and A. I. Shchedrin

Institute of Physics, National Academy of Sciences of Ukraine, pr. Nauki 144, Kiev, 03039 Ukraine

Received February 15, 2001

Abstract—The mechanism for the formation of the inverse electron distribution function is proposed and realized experimentally in a nitrogen plasma of a hollow-cathode glow discharge. It is shown theoretically and experimentally that, for a broad range of the parameters of an N_2 discharge, it is possible to form a significant dip in the profile of the electron distribution function in the energy range $\varepsilon = 2–4$ eV and, accordingly, to produce the inverse distribution with $df(\varepsilon)/d\varepsilon > 0$. The formation of a dip is associated with both the vibrational excitation of N_2 molecules and the characteristic features of a hollow-cathode glow discharge. In such a discharge, the applied voltage drops preferentially across a narrow cathode sheath. In the main discharge region, the electric field E is weak ($E < 0.1$ V/cm at a pressure of about $p \sim 0.1$ torr) and does not heat the discharge plasma. The gas is ionized and the ionization-produced electrons are heated by a beam of fast electrons (with an energy of about 400 eV) emitted from the cathode. A high-energy electron beam plays an important role in the formation of a dip in the profile of the electron distribution function in the energy range in which the cross section for the vibrational excitation of nitrogen molecules is maximum. A plasma with an inverted electron distribution function can be used to create a population inversion in which more impurity molecules and atoms will exist in electronically excited states. © *2001 MAIK "Nauka/Interperiodica"*.

1. INTRODUCTION

In recent years, numerous technological applications of low-pressure gas discharges in nitrogen and nitrogen-containing mixtures have stimulated active experimental and theoretical investigations of the electron energy distribution function (EEDF) in order to gain a better insight into the physics of the plasmochemical processes occurring in various plasma devices (see, e.g., [1–8]).

First of all, we should note that the shape of the EEDF is highly sensitive to the type of discharge and its parameters even in experiments with the same gas mixtures. Thus, in [1–4], the EEDF in N_2 and N_2–O_2 mixtures was studied under conditions such that the electric field was stronger than the breakdown field and was the only factor responsible for the heating of plasma electrons. In those papers, the EEDF $f(\varepsilon)$ was found to be monotonic ($df(\varepsilon)/d\varepsilon < 0$), but with different temperatures in different energy ranges. Such a shape of the EEDF is associated with the fact that, under those conditions, the distribution of the plasma electrons rapidly becomes Maxwellian under the action of the electric field.

On the contrary, in [5–8], it was shown that, in a weak electric field in the post-discharge plasmas of repetitive discharges in N_2 and Ar–N_2 mixtures, an important role in the formation of the EEDF is played by superelastic collisions, because, during the period between successive discharges, the electrons are heated

only by energy transfer from vibrationally and electronically excited molecules to the plasma. As a result, the EEDF becomes peaked at energies that correlate with the excitation energies of the vibronic (vibrational–electronic) levels of molecules.

Our paper is devoted to an experimental and theoretical investigation of the EEDF in discharges that differ radically from both those studied in [1–4] and those studied in [5–8]. Specifically, we are interested in steady hollow-cathode glow discharges in nitrogen and oxygen. In such discharges, which are widely used in various technological applications, the applied voltage drops preferentially across a narrow cathode sheath. According to our measurements, the electric field E in the main discharge region was at most 0.1 V/cm (at a pressure of about $p \sim 0.1$ torr), which is one order of magnitude weaker than that in [1–4]. In our experiments, the gas was ionized and the plasma electrons were heated by a beam of fast electrons (with an energy of about 400 eV) emitted from the cathode. We show that, in such discharges in nitrogen, the formation of a significant dip in the EEDF in the energy range 2–4 eV and, accordingly, the inversion of the EEDF ($df(\varepsilon)/d\varepsilon > 0$) are attributed to the vibrational excitation of N_2 molecules. In contrast, in discharges in oxygen, the EEDF is monotonic because, on the one hand, it is cut off at low threshold energies for the excitation of the lowest lying electronically excited metastable states of O_2 molecules and, on the other hand, the cross sections for the excita-

tion of the vibrational levels of oxygen molecules are small.

2. EXPERIMENTAL SETUP AND MEASUREMENT RESULTS

The experiments were carried out with a hollow cylindrical cathode 280 mm in diameter and 400 mm in length. A 230-mm-diameter anode was placed near one end of the cathode. The vacuum chamber was pre-evacuated by a forepump to a residual pressure of 5×10^{-3} torr. Then, the chamber was filled with the working gas (nitrogen or oxygen) in the pressure range from 3×10^{-2} to 1×10^{-1} torr. The discharge current and applied voltage were varied in the ranges 0.5–0.9 A and 400–600 V, respectively. The plasma density, electric fields, and EEDF were measured by a pair of single Langmuir probes [9] made of tungsten wires 100 μm in diameter, the receiving sections being from 10 to 15 mm in length. The probes were designed so as to provide measurements along and across the symmetry axis of the cathode. In order for the measured current–voltage (I–V) characteristics of the probes to be immune to probe-surface contamination, the probes were cleaned after each measurement by heating them to a temperature of about 800° C with a dc source.

The EEDF was determined numerically by differentiating the I–V characteristics twice with (if necessary) preinterpolation of the measured data. The measurement accuracy was increased using the modified method described in [2], which is based on a specially devised programmable diagnostic system controlled by a personal computer. At each step of a measurement cycle, the controlling computer code specified the probe current with an accuracy of 0.1 μA and provided simultaneous measurements of the probe voltage relative to the anode, the anode voltage, and the discharge current. The change in the probe current at each step was calculated automatically during the measurements with the help of a specially developed algorithm for optimizing the signal-to-noise ratio over the entire range of measured currents (a complete cycle of measurements of one I–V characteristic included from 1500 to 2000 steps). The measurements were carried out in the stroboscopic regime at a rate of 100 Hz synchronously with the oscillations of the supply voltage, thereby making it possible to avoid the influence of these oscillations on the experimental results. The gating time of the measured signals was 1 μs. The time delay (7 ms) of the measurement with respect to the beginning of the half-wave of the supply voltage was chosen so as to optimize the signal-to-noise ratio. After performing the measurements over the prescribed range of probe current variations, the measured data in the form of a dependence of the probe current on the probe potential for a given discharge current and given discharge voltage were stored as a computer file. With fixed experimental parameters, the I–V characteristic was measured up to 30 times. Thereafter, the data stored in the corresponding files were averaged over the measurement cycles.

The plasma potential was assumed to be equal to the probe potential at which the second derivative of the probe current with respect to the probe voltage vanishes. The plasma density was computed from the electron saturation current to the probe.
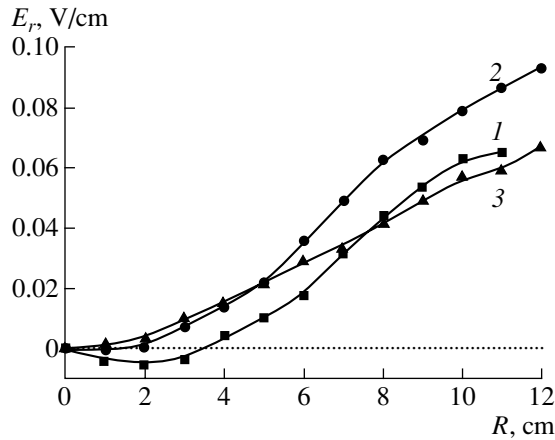
Figure 1 shows the radial profiles of the plasma density for different nitrogen pressures. We can see that the shape of the profiles is highly sensitive to the working gas pressure. For $p = 0.1$ torr, the plasma density is minimum at the cathode axis and increases gradually in the radial direction, reaching a maximum value at $R \approx$ 11 cm. At lower pressures ($p = 0.03, 0.06$ torr), the situation is radically different: the plasma density n_e is maximum at the axis of the system and decreases monotonically with radius. This dependence is peculiar to hollow-cathode discharges. At a pressure of 0.1 torr, essentially all of the energy of the fast primary electrons emitted from the cathode is expended on the excitation and ionization of the working gas within a distance of several centimeters from the cathode; consequently, the gas at the system axis is ionized mainly by the electrons that diffuse from the region where the plasma has already been produced. As a result, the plasma density is the highest not at the cathode axis but in the region where the loss of fast electrons is maximum and, accordingly, the plasma production is most intense. As the working gas pressure decreases, the maximum of the plasma density profile shifts toward smaller radii and, at $p \approx 0.05$ torr, it becomes bell-shaped.

Recall that, in gas discharges, a very important role is played by the electric field, which heats the plasma electrons and thus can substantially influence the shape
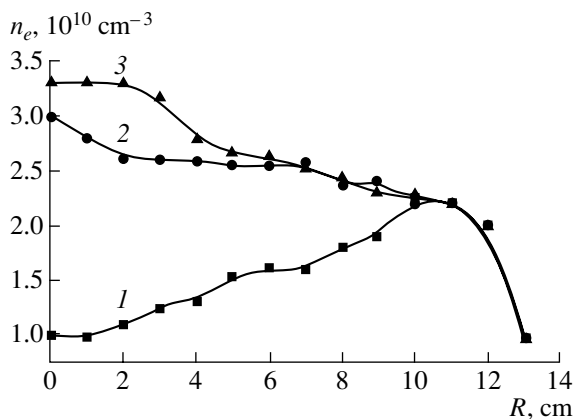
Fig. 1. Radial profiles of the electron density for different nitrogen pressures: (*1*) $p = 0.1$ torr, $I_d = 0.63$ A, and $U_d = 470$ V; (*2*) $p = 0.06$ torr, $I_d = 0.73$ A, and $U_d = 580$ V; and (*3*) $p = 0.03$ torr, $I_d = 0.77$ A, and $U_d = 615$ V.

Fig. 2. Radial profiles of the radial electric field for different nitrogen pressures: (*1*) $p = 0.1$ torr, $I_d = 0.63$ A, and $U_d = 470$ V; (*2*) $p = 0.06$ torr, $I_d = 0.73$ A, and $U_d = 580$ V; and (*3*) $p = 0.03$ torr, $I_d = 0.77$ A, and $U_d = 615$ V.

of the EEDF. Figure 2 displays the experimentally measured radial profiles of the radial electric field E_r for different nitrogen pressures. The radial behavior of E_r is seen to be analogous to that of the plasma density. At low nitrogen pressures, the radial electric field is positive and increases monotonically with the radius. For $p = 0.1$ torr, the component E_r is negative in the axial region (where the plasma density is the lowest); at larger radii, it passes through zero and starts increasing monotonically. The maximum value of E_r does not exceed 0.1 V/cm. The longitudinal electric field E_z was found to be even weaker: the measurements showed that $E_z \approx 1$–2×10^{-2} V/cm for $p = 0.1$ torr, $E_z \approx 0.5$–$1 \times$

10^{-2} V/cm for $p = 0.06$ torr, and $E_z < 10^{-2}$ V/cm for $p = 0.03$ torr. Below, we will show that such longitudinal and radial electric fields are too weak to significantly affect the shape of the EEDF.

The EEDF was measured at different points inside the vacuum chamber at different pressures of the working gas. Figures 3 and 4 show typical EEDFs measured at nitrogen pressures of 0.1 and 0.03 torr. We can see that the EEDF is strongly non-Maxwellian: it has a pronounced dip in the energy range 2–4 eV. Moreover, at a lower pressure (Fig. 3), there are two dips in the EEDF in this energy range.

We also established that, at low pressures, the EEDF is essentially independent of the radius, while, at $p = 0.1$ torr, the EEDF experiences fairly strong variations in the radial direction. Moreover, at the chamber axis (i.e., in the region where the reduced electric field E/N is minimum), the dip in the EEDF is the smallest. This radial behavior of the EEDF is not associated with the presence of an electric field, because the action of the electric field should result in the formation of an EEDF that depends on the radius in the opposite manner—the dip in the EEDF would be smallest at the discharge periphery, where the field is maximum. The observed reduction in the dip in the EEDF near the axis of a hollow cathode at high pressures (Fig. 4) may be attributed to the decrease in the number of high-energy electrons (which serve as the major energy source in the plasma) and, accordingly, to an increasingly important role of the processes that force the EEDF to evolve into a Maxwellian function. As was mentioned above (Fig. 1), it is precisely this pressure range in which the plasma density n_e is minimum at the chamber axis.
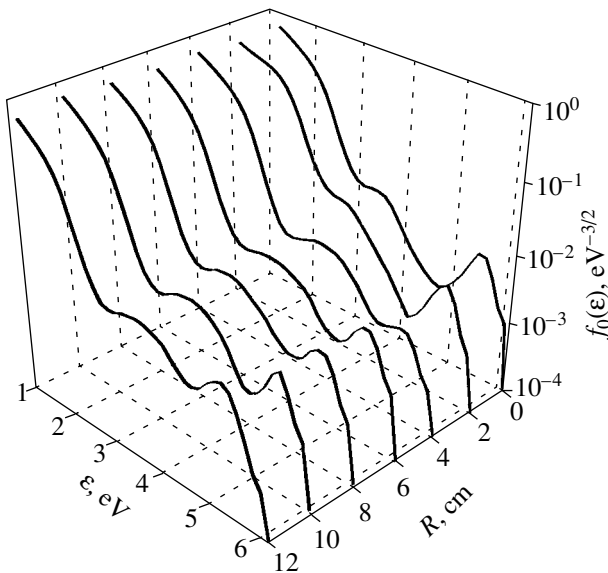
Fig. 3. EEDFs measured in nitrogen at a pressure of $p = 0.03$ torr at different radial positions R.
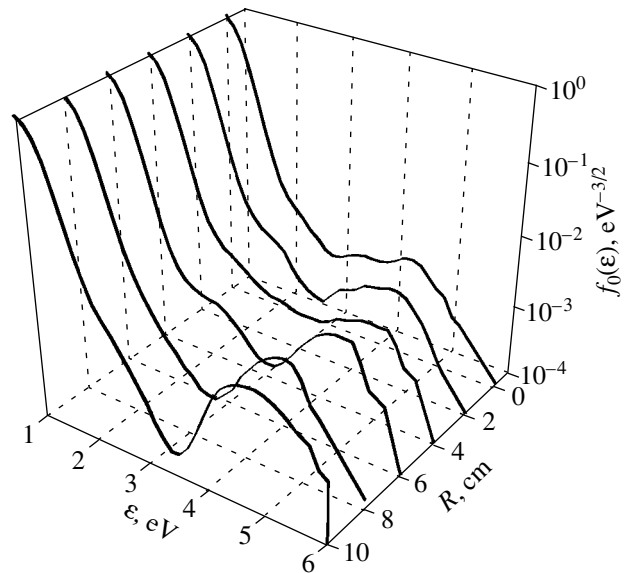
Fig. 4. EEDFs measured in nitrogen at a pressure of $p = 0.1$ torr at different radial positions R.
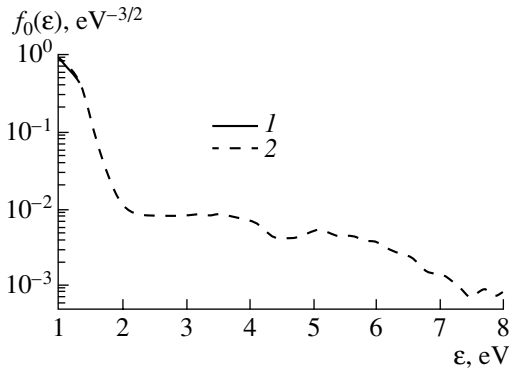
Fig. 5. EEDF measured in oxygen at a pressure of $p = 0.06$ torr at $R = $ (*1*) 0 and (*2*) 9 cm.

The EEDF in an oxygen plasma is illustrated in Fig. 5, which shows that it is qualitatively different from the EEDF in N_2, although measurements were carried out in discharges with the same parameters. To a good accuracy, the EEDF in O_2 can be described by a Maxwellian function, but with different temperatures in the energy ranges $\varepsilon = 0$–2.5 eV and $\varepsilon > 2.5$ eV.

The physical reasons for such a large discrepancy between the EEDFs in N_2 and O_2 will be discussed in the next section.

3. THEORY

We calculated the EEDF by solving the Boltzmann equation in the two-term approximation [10]:

$$
\frac{1}{n_e N}\left(\frac{m}{2e}\right)^{1/2}\varepsilon^{1/2}\frac{\partial(n_e f_0)}{\partial t} - \frac{1}{3}\left(\frac{E}{N}\right)^2\frac{\partial}{\partial\varepsilon}\left(\frac{\varepsilon}{Q_T}\frac{\partial f_0}{\partial\varepsilon}\right)
$$
$$
- \frac{\partial}{\partial\varepsilon}\left[2\frac{m}{M}Q_T\varepsilon^2\left(f_0 + T\frac{\partial f_0}{\partial\varepsilon}\right)\right] = S_{eN} + S_{ee} + A(\varepsilon),
$$

(1)

where $f_0(\varepsilon)$ is the symmetric part of the EEDF; T is the gas temperature (in eV); $e = 1.602 \times 10^{-12}$ erg/eV; M is the mass of a molecule; N is the gas density; Q_T is the transport cross section; m is the mass of an electron; n_e

Table 1

No.	Reaction	Threshold energy ε_{sh}, eV
1	$N_2 + e \longrightarrow N_2(v) + e,\ v = 1...8$	1.5
2	$N_2 + e \longrightarrow N_2(A^3\Sigma_u^+) + e$	6.7
3	$N_2 + e \longrightarrow N_2(a^1\Pi_g) + e$	8.55
4	$N_2 + e \longrightarrow N_2(B^3\Pi_g) + e$	11.5
5	$N_2 + e \longrightarrow N_2^+ + e + e$	15.6
6	$N_2 + e \longrightarrow N + N + e$	9.76

is the electron density; S_{eN} is the integral of electron–neutral inelastic collisions; S_{ee} is the integral of electron–electron collisions; and $A(\varepsilon)$ is the ionization term, which includes the source of primary electrons. The expressions for the terms S_{eN}, S_{ee}, and $A(\varepsilon)$ were taken from [11].

The EEDF $f_0(\varepsilon)$ was normalized to satisfy the condition

$$
\int_0^\infty \varepsilon^{1/2} f_0(\varepsilon)d\varepsilon = 1.
$$

(2)

The electron processes that were taken into account when solving the Boltzmann equation for discharges in nitrogen and oxygen are listed in Tables 1 and 2. The superelastic scattering of electrons by vibrationally excited molecules was neglected, because, for the discharges under investigation, the specific input power and, accordingly, the vibrational temperature T_v were both much lower than those in the experiments of [4–8].

The cross sections for elastic and inelastic scattering of electrons by N_2 and O_2 molecules were taken from [12].

The calculations were carried out with the values of the electric field and electron density that were measured experimentally at different regions of the discharge chamber. The energy ε_n of the beam of primary electrons was assumed to be on the order of the potential drop across the cathode sheath, $\varepsilon_n \approx 400$ eV.
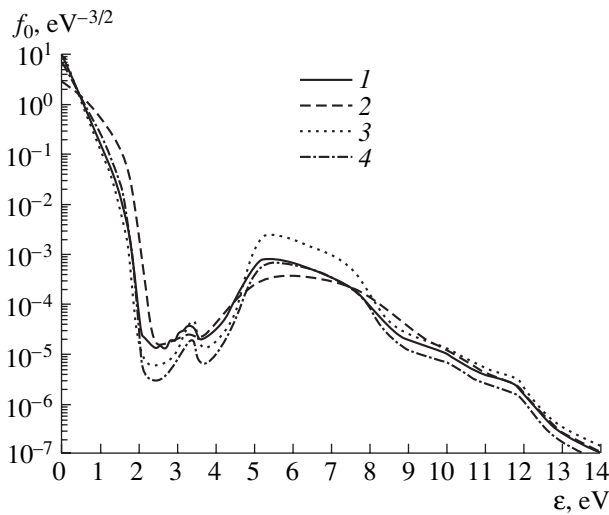
Equation (1) was solved using the same methods as in [10].

Figure 6 shows the EEDFs obtained theoretically for a hollow-cathode discharge in nitrogen. The EEDF was calculated for the parameter range (n_e, E) corresponding to the intervals of variation of n_e and E in the radial direction in the discharge chamber. For all values of the discharge parameters, there are two pronounced dips in the EEDF in the energy range $\varepsilon = 2$–4 eV. The dips are associated with the sharp peaks in the cross section for the vibrational excitation of N_2 molecules in this energy range. The EEDF calculated without allowance for the vibrational excitation of N_2 molecules is monotonic. Another factor that causes the dips in the EEDF to vanish is an artificial increase in E/N by an order of magnitude, up to the values that correspond to the experiments of [1–4] and are large enough for the EEDF to become Maxwellian.

Figure 7 shows the EEDFs calculated for an oxygen plasma. An important property in which oxygen differs from nitrogen is the presence of the metastable excited states of O_2 molecules, $O_2(^1\Delta_g)$ and $O_2(b^1\Sigma_g^+)$, with low threshold energies (0.95 and 1.64 eV, respectively). The EEDF calculated with allowance for the excitation of these states is cut off at energies of about 1–2 eV; this effect is especially pronounced for weak electric fields (Fig. 7). As for the processes of the vibrational excita-

Fig. 6. EEDFs in nitrogen calculated for the parameter values (*1*) $p = 0.03$ torr, $n_e = 10^{10}$ cm^{-3}, and $E = 0.01$ V/cm; (*2*) $p = 0.03$ torr, $n_e = 10^{10}$ cm^{-3}, and $E = 0.1$ V/cm; (*3*) $p = 0.1$ torr, $n_e = 10^{10}$ cm^{-3}, and $E = 0.01$ V/cm; and (*4*) $p = 0.1$ torr, $n_e = 2 \times 10^{10}$ cm^{-3}, and $E = 0.06$ V/cm.
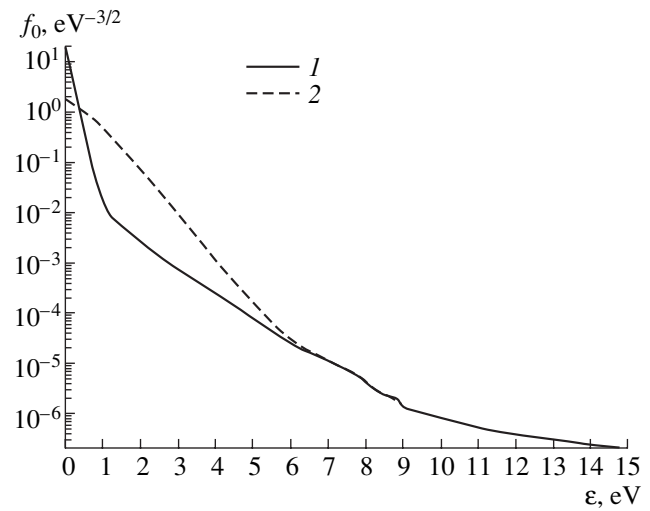

Fig. 7. EEDFs in oxygen calculated for $p = 0.06$ torr, $n_e = 10^{10}$ cm^{-3}, and $E =$ (*1*) 0.01 and (*2*) 0.1 V/cm.

tion of O_2 molecules, they have essentially no influence on the EEDF because the vibrational excitation cross section for O_2 molecules is much smaller than that for N_2 molecules: up to the threshold energies for the excitation of electronic levels, the EEDF in an oxygen plasma can be described with good accuracy by a Maxwellian function with one or two (depending on the electric field magnitude) temperatures in different energy ranges.

4. DISCUSSION OF THE RESULTS

A comparison between the EEDFs measured experimentally in a nitrogen plasma at low pressures (Fig. 3) and the related EEDFs calculated theoretically (Fig. 6) shows that the experimental data agree well with theoretical predictions both qualitatively and quantitatively. In the energy range 2–4 eV, the positions of the measured and calculated dips in the EEDF coincide within an accuracy of 10–20%. In the measured EEDF, the dip that is closer to the right peak coincides with the relevant calculated dip within the limits of experimental error.

It should be noted that our experimental technique does not provide correct measurements of the EEDF in the energy range below 1 eV. Presumably, this is the reason why, in the range $\varepsilon < 1$ eV, the measured EEDF $f(\varepsilon)$ decreases to a lesser extent than the calculated EEDF. However, a comparison between the calculated and measured extents to which the EEDF decreases relative to its value at an energy of 1 eV also shows good agreement between theory and experiment.

At higher pressures, the agreement between the calculated and measured EEDFs is somewhat worse

(Fig. 4), because, as was noted above, the radial energy distribution of the beam of fast electrons emitted by the cathode is highly nonuniform. In turn, the radial nonuniformity of the beam may be responsible for the nonlocal character of the EEDF, thereby giving rise to the loss of high-energy electrons at the axis of the discharge chamber. However, our calculations were carried out under the assumption that all of the parameters governing the EEDF are spatially uniform.

To within experimental error, the EEDF measured in an oxygen plasma (Fig. 5) also agrees well with the EEDF calculated for the electric field $E = 0.01$ V/cm with allowance for the above scattering cross sections (Fig. 7). Note that, in discharges in oxygen, the electric field was measured to be weaker than 0.02 V/cm. To a first approximation, the experimental EEDF can be described by two Maxwellian functions with different

Table 2

No.	Reaction	Threshold energy ε_{sh}, eV
1	$O_2 + e \longrightarrow O_2(v) + e$, $v = 1\ldots10$	1.95
2	$O_2 + e \longrightarrow O_2(^1\Delta_g) + e$	0.98
3	$O_2 + e \longrightarrow O_2(b^1\Sigma_g^+) + e$	1.64
4	$O_2 + e \longrightarrow O_2(A^3\Sigma_u^+) + e$	4.5
5	$O_2 + e \longrightarrow O_2(*) + e$	6.0
6	$O_2 + e \longrightarrow O_2(**) + e$	8.0
7	$O_2 + e \longrightarrow O_2(***) + e$	9.7
8	$O_2 + e \longrightarrow O_2^+ + e + e$	12.2
9	$O_2 + e \longrightarrow O + O + e$	6.0
10	$O_2 + e \longrightarrow O^- + O$	3.6

temperatures. Up to an energy of about 7 eV, the EEDF calculated theoretically for $E = 0.1$ V/cm is a one-temperature Maxwellian function; however, in our experiments with discharges in oxygen, such strong electric fields were not observed.

5. CONCLUSION

Hence, we have investigated the EEDF in hollow-cathode glow discharges in which the plasma is preferentially heated by fast electrons that are emitted from the cathode and are accelerated by the space charge electric field in the cathode sheath. We have revealed the following features of the EEDF:

(i) In discharges in nitrogen, there is a significant dip in the EEDF in the energy range $\varepsilon = 2$–4 eV. The dip is associated with the vibrational excitation of N_2 molecules.

(ii) In discharges in oxygen, the monotonic nature of the EEDF stems from the following two factors: first, the cross section for the vibrational excitation of oxygen molecules is smaller than that for nitrogen molecules and, second, the threshold energies for the excitation of the lowest lying metastable states of oxygen molecules are low.

The results of theoretical calculations agree well with the experimental data.

The measured and calculated EEDFs can be used to model the plasma kinetics and, accordingly, to determine the densities of all plasma components, thereby providing a good way to optimize the technologies based on hollow-cathode glow discharges. In addition, since the electric fields in such discharges are low, the EEDF adequately reflects inelastic electron processes and thus may give both qualitative and quantitative information about the cross sections for the corre-

sponding processes in more complicated plasma-forming media.

REFERENCES

1. N. L. Aleksandrov, A. M. Konchakov, and É. E. Son, Fiz. Plazmy **4**, 169 (1978) [Sov. J. Plasma Phys. **4**, 98 (1978)].
2. V. Guerra and J. Loureiro, J. Phys. D **28**, 1903 (1995).
3. V. Guerra and J. Loureiro, Plasma Sources Sci. Technol. **6**, 373 (1997).
4. C. M. Ferriera and J. Lourero, Plasma Sources Sci. Technol. **9**, 528 (2000).
5. C. Gorse, M. Capitelli, and A. Ricard, J. Chem. Phys. **82**, 1900 (1985).
6. N. A. Gorbunov, N. B. Kolokolov, and A. A. Kudryavtsev, Zh. Tekh. Fiz. **58**, 1817 (1988) [Sov. Phys. Tech. Phys. **33**, 1104 (1988)].
7. N. A. Gorbunov, N. B. Kolokolov, and A. A. Kudryavtsev, Zh. Tekh. Fiz. **61** (6), 52 (1991) [Sov. Phys. Tech. Phys. **36**, 616 (1991)].
8. N. A. Oyatko, Yu. Z. Ionikh, N. B. Kolokov, *et al.*, J. Phys. D **33**, 2010 (2000).
9. Yu. A. Ivanov, Yu. A. Lebedev, and L. S. Polak, *Contact Diagnostics in Nonequilibrium Plasmochemistry* (Nauka, Moscow, 1981).
10. A. I. Shchedrin, A. V. Ryabtsev, and D. Lo, J. Phys. B **29**, 915 (1996).
11. J. P. Shkarofsky, T. W. Johnston, and M. P. Bachynski, *The Particle Kinetics of Plasmas* (Addison-Wesley, Reading, 1966; Atomizdat, Moscow, 1969).
12. I. A. Soloshenko, V. V. Tsiolko, V. A. Khomich, *et al.*, Fiz. Plazmy **26**, 845 (2000) [Plasma Phys. Rep. **26**, 792 (2000)].

Translated by I. A. Kalabalyk